Exploring Relativistic Accretion Flow Around Black Holes and Wormholes

Gargi Sen

A thesis
submitted for the degree of

Doctor of Philosophy

Supervisor

Prof. Santabrata Das

Co-supervisor

Prof. Debaprasad Maity

Department of Physics
Indian Institute of Technology Guwahati
Guwahati - 781039, Assam, India

Exploring Relativistic Accretion Flow Around Black Holes and Wormholes

A thesis submitted by

Gargi Sen

to

Indian Institute of Technology Guwahati
in partial fulfillment of the requirements
for the award of the degree of
Doctor of Philosophy in Physics

Supervisor

Prof. Santabrata Das

Co-supervisor

Prof. Debaprasad Maity

Department of Physics
Indian Institute of Technology Guwahati
Guwahati - 781039, Assam, India

To

My Best Friend Swapnendu Jethu

&

My Doctor Jethu,

who are unfortunately now in

'The Undiscovered Country'

"The pursuit of truth and beauty is a sphere of activity in which we are permitted to remain children all our lives."

-Albert Einstein

Declaration

I hereby declare that works presented in the thesis entitled "**Exploring Relativistic Accretion Flow Around Black Holes and Wormholes**" has been carried out by me under the supervision of Prof. Santabrata Das and Prof. Debaprasad Maity at the Department of Physics, Indian Institute of Technology Guwahati, India. The thesis has not been submitted anywhere else for any degree. Works presented in the thesis are all my own unless referenced to the contrary in the thesis.

Gargi Sen.

Gargi Sen
Roll No. 196121011
Department of Physics
Indian Institute of Technology Guwahati
Guwahati, India
E-mail: g.sen@iitg.ac.in

Date: March 27, 2026

Certificate

It is certified that the work contained in the thesis entitled "**Exploring Relativistic Accretion Flow Around Black Holes and Wormholes**" by Miss. Gargi Sen (Roll No - 196121011), a Ph.D. student in the Department of Physics, Indian Institute of Technology, Guwahati is carried out under our supervision and has not been submitted elsewhere for the award of any other degree.

Dr. Santabrata Das
Professor
Department of Physics
Indian Institute of
Technology Guwahati
Guwahati, India
E-mail: sbdas@iitg.ac.in

Dr. Debaprasad Maity
Professor
Department of Physics
Indian Institute of
Technology Guwahati
Guwahati, India
E-mail: debu@iitg.ac.in

Date: March 27, 2026

Acknowledgements

As the chapter of my PhD journey comes to the end, I realize how much this path has been shaped by the people around me. Their care, support, advice, and encouragement have been my strength. I am truly grateful to everyone who supported, guided, and stood by me through challenges and achievements. I wish to wholeheartedly acknowledge the invaluable contributions of each and every person who stood by me during this time.

First and foremost, I express my heartfelt gratitude to my PhD supervisors, Prof. Santabrata Das and Prof. Debaprasad Maity, for their unwavering support, insightful guidance, and constant encouragement throughout my PhD journey. Their detailed discussions, valuable suggestions, and emphasis on critical thinking have immensely enriched my understanding of relativistic accretion physics. Their discipline, dedication, and time management have always inspired me, while their concern for my well-being encouraged me to take care of my health.

It is a great pleasure to acknowledge my doctoral committee members, Prof. Sayan Chandrabarti (Chairperson), Prof. Bibhas Ranjan Majhi, and Prof. Sovan Chakraborty, for their valuable time, insightful feedback, and constructive suggestions on my research throughout this journey. Their feedback during the Annual Progress Seminars helped me to improve the way of approaching problems, and they also gave important ideas for future directed work. I sincerely thank Sayan Sir for the academic discussions in his office, where he always welcomed me without any time constraints. I am deeply grateful to him for inspiring and encouraging me during the hardest time of my PhD life. I also wish to express my heartfelt gratitude to Bibhas Sir for always keeping his door open for me and for generously sharing the detailed academic discussions, valuable insights and suggestions. I am deeply thankful to Dr. Anuj Nandi for his insightful comments on my research work, which significantly enhanced its quality.

I am grateful to my collaborators, Prof. Sayan Chandrabarti, Prof. Sudip Bhattacharyya, Prof. Chandrachur Chakraborty, and Dr. Avijit Chowdhury, for their valuable inputs and suggestions that greatly improved the quality of my work. I would like to express my special thanks to Chandrachur da and Avijit da, who were always approachable, open to discussions, and sharing their insights. Working with them has been an invaluable learning experience, and I feel fortunate to have had the opportunity to collaborate with them.

I am sincerely grateful to Prof. Kazuharu Bamba for hosting me as a visitor at Fukushima University. I am grateful to Prof. Rajibul Shaikh for hosting my visit to ISI, and to Prof. Rajibul Shaikh and Prof. Suddhasattwa Brahma for the valuable and insightful academic discussions. I also extend my heartfelt thanks to Prof. Ranjeev Misra and Dr. Chiranjeeb Singha for hosting my visit to IUCAA, and to Prof. Ranjeev Misra, Prof. Dipanjan Mukherjee, and Dr. Chiranjeeb Singha for the engaging academic interactions.

I am also thankful to Prof. Subhaditya Bhattacharya, Prof. Arunansu Sil, Prof. Subhradip Ghosh, Prof. Soumitra Nandi, Prof. Padma K. Padmanabhan, Prof. Uday Narayan Maiti and Prof. Meduri C. Kumar of IIT Guwahati for their warm welcome, kind support, and friendly discussions on a wide range of topics.

I sincerely acknowledge the financial support provided by the University Grants Commission (UGC), Government of India, that helped me to conduct my research work smoothly.

I would like to thank the Department of Physics, IIT Guwahati, for providing all the necessary resources, infrastructure, and supportive environment for my research. I am grateful to the Heads of the Department during my PhD tenure, Prof. Subhradip Ghosh, Prof. Perumal Alagarsamy, and Prof. Bosanta R. Boruah, for their support and encouragement.

I was fortunate to be a part of the 'Gravity Journal Club', which broadened my understanding of diverse aspects of gravity apart from accretion physics.

I sincerely thank our technical staff members, Basab da, Hemanta da, Avijit da, Gautam da, Aditya da, Lokesh Sir, Prasenjit da, and Radha di, for their friendly support and constant cooperation in resolving technical issues related to desktops, Wi-Fi, printers, and projectors, which ensured the smooth continuation of our day-to-day academic work.

I extend my gratitude to the administrative staff members, Ambarish da, Jyoti Sir, and Monojit Sir, for their kind assistance in ensuring the smooth handling of all official works.

I am deeply grateful to Anupama Ma'am, who has been like a local guardian to me during my stay here. Her heartfelt warmth, guidince, and hospitality, together with the comfort of her lovingly prepared food during stressful times, truly made me feel at home away from home.

I feel privileged to acknowledge my teachers beyond IIT Guwahati, who have guided and encouraged me from my early education through my formative years. I am especially grateful to my school and college teachers, Ruchira Ma'am, Aparna Ma'am, Shipra Ma'am, Dipanwita Ma'am, Sujay Sir, Prabhash Sir, Purnendu Sir, Sanoar Sir, Ajanta Ma'am, and Sudipta Ma'am, who have been constant sources of knowledge and inspiration and have continued to stay in touch with me to this day. Their encouragement and positivity have left a lasting impression on my life and academic journey.

I am immensely grateful to my senior group members, Biplob da, Ramiz da, Indu da, Aneesha di, Pradeep da, Monu da, Rajesh da, Riajul da, and Sovan da, for their insightful discussions, valuable guidance, and constant encouragement throughout my PhD journey. Their constructive suggestions and shared experiences have greatly enriched my research and learning. I am equally thankful to my friends and juniors in our research group, Samik, Seshadri, Sourav, Banashree, Camelia, Amit, Akhil, Sreetama, Surendra, Mostak, Ayan, Subhasis, Rajesh, Jitumani, and Sitesh, for sharing not only academic discussions but also personal moments of companionship and support, which have left cherished memories with me. I sincerely thank Subhankar for our insightful and productive discussions on physics.

Beyond my research group, I am thankful to my seniors, Surojit da, Subhajit da, Kuntal da, Rony da, Lopa di, Modhurima di, Shilpi di, Ipshita di, Priyanka di, Partha da, Arghyajit da, Dibyendu da, Devabrat da, Sumit da, Golam da, Sanket da, Samit da, Sudip da, and Suvikrant da, Tanima di, Bhaswati di, for their constant support and valuable guidance. I am also thankful to my friends, Dipankar (Dipu), Sudipta, Shantanu, Chinmoy, Suruj, Lipika, Mijanur, Koushik, Debabrata, Swarup, Soumen, Shafeeque, Sunil, Roson, Ravinder, Prateechee, Debarun, Arko, Sourav Pal, Ankit, Setabuddin, Rahul, Usman, Prajjwal, Sree, and Suchismito, for

their encouragement and cheerful companionship. I extend my thanks to my juniors, Abhik, Niloy, Bhoomika, Indrajit, Nayan, Himanshu, Dipankar Barman, Sanu, Arpita, Madan, Shailesh, Dipendu Bhandari, Fatima, Anirban, Dipendu Halder, Sourav, Tandrima, Joya, Koustav, Srijata, Urmimala, Swati, Gunjan, Hemanta, Nalinikanta, Niraj, Rajat, Samir, Sanjoy, Tulsiram, Tarun, Disha, Bhera, Rajesh Pramanik, Debalina, Gourab, Sonakshi, Sandip, Arkadip, and Dikshit, for creating a vibrant and warm environment.

I am also deeply grateful to my 'girls group', Alolika, Amalika, Pooja, Saraswati, Esha, and Sonali, who have always been there for me during tough times and shared my happiest moments with equal warmth and joy. Their unwavering support, laughter, and friendship have made my journey memorable and truly special.

I wish to convey my sincere gratitude to Rajesh Da, whose encouragement, guidance, and kindness extended far beyond academic support. His thoughtful advice, unwavering motivation, and genuine care have not only enriched my research but also made my journey more meaningful and enjoyable.

My heartfelt thanks go to my MSc friend, Dipu, who has been a steadfast and inspiring companion throughout my PhD journey. His support and encouragement have been invaluable. I am blessed with the enriching discussions I used to have at CCD with Dipu and Abhik.

I also deeply cherish the companionship of my juniors, Nihar, Shreya, Arko, and Subhajit, whose presence has added joy and created memorable moments at the last phase of my PhD journey. Their warm and friendly support has made this experience more lively, which leaves lasting memories that I will always treasure.

I am grateful to my two childhood brothers, Akash and Sayan, my school friends, Sanchayita, Sneha, Suchitra, Anwesha, and Susmita, and my college friends, Suvashis, Dilruba, Manjistha, Paromita, Chayan, and Sayan, who have been a constant source of encouragement and support throughout my journey.

I owe my deepest gratitude to my best friend, Sahabub, who has been a constant pillar of support throughout this journey. He has stood by my side through every challenge, offering constant encouragement, patience, and faith in me. His thoughtful guidance, comforting presence, and boundless positivity have helped me to overcome negativity and to move forward with renewed hope, strength, and determination.

Finally, my profound and heartfelt acknowledgment goes to my family, my beloved grandmother, my parents, and my brother Sonai for their unwavering love, constant support, and boundless encouragement throughout my life. I am also deeply grateful to Babita aunty for her unconditional love and support from my childhood to the present day. I am who I am today because of the endless sacrifices, love, and guidance of my Maa and Baba. Their patience, understanding, and belief in me have been the foundation upon which I could build my dreams and pursue this challenging journey. From my earliest steps in education to the completion of my PhD, they have always stood by me, celebrated my successes, and comforted me in every time of difficulty. The values, discipline, and resilience they taught me have been my guiding light. Therefore, this PhD is not only my achievement, it is theirs, a heartfelt tribute to their unwavering love, boundless care, and endless sacrifices.

Acronyms

WD	:	White Dwarf
NS	:	Neutron Star
BH	:	Black Hole
SMBH	:	Supermassive Black Hole
AGN	:	Active Galactic Nuclei
XRB	:	X-ray Binary
GBH	:	Galactic Black Hole
GMM	:	Gravitomagnetic Monopole
WH	:	Wormhole
DSWH	:	Damour Solodukhin Wormhole
RDSWH	:	Rotating Damour Solodukhin Wormhole
ECO	:	Exotic Compact Object
DM	:	Dark Matter
WIMP	:	Weakly Interacting Massive Particle
CDM	:	Cold Dark Matter
CMB	:	Cosmic Microwave Background
PAMELA	:	Payload for Antimatter Matter Exploration and Light-nuclei Astrophysics
Fermi-LAT	:	Fermi Large Area Telescope
EoS	:	Equation of State
NFW	:	Navarro-Frank-White
SPH	:	Smooth Particle Hydrodynamics
GW	:	Gravitational Wave
Cyg X-1	:	Cygnus X-1
ULX	:	Ultraluminous X-ray Sources
ADAF	:	Advection Dominated Accretion Flow

RIAF	:	Radiatively Inefficient Accretion Flow
CDAF	:	Convection Dominated Accretion Flow
TCAF	:	Two Component Advective Flow
CENBOL	:	CENtrifugal pressure supported BOundary Layer
PSC	:	Post-shock Corona
PDS	:	Power Density Spectra
SED	:	Spectral Energy Distribution
QPO	:	Quasi Periodic Oscillations
MHD	:	Magnetohydrodynamic
MRI	:	Magneto Rotational Instability
MAD	:	Magnetically Arrested Disk
SANE	:	Standard and Normal Evolution
Sgr A	:	Sagittarius A
M87	:	Messier 87
GRMHD	:	General Relativistic Magneto Hydrodynamic
EHT	:	Event Horizon Telescope
LT	:	Lense-Thirring
BP	:	Bardeen-Petterson
RPM	:	Relativistic Precession Model
ISCO	:	Innermost Stable Circular Orbit
KTN	:	Kerr-Taub-NUT

Notations

Φ_G: Gravitational potential.

M_*: Mass of the compact object.

$\mathscr{R}$: Radius of the compact object.

$M_\odot$: Solar mass.

p: Gas pressure.

ρ: Mass density of the flow.

ρ_∞: Density of gas cloud at infinity.

L: Luminosity.

$R_{\mu\nu}$: Ricci tensor.

$g_{\mu\nu}$: Metric tensor.

R: Ricci scalar.

$T_{\mu\nu}$: The energy momentum tensor of the matter distributions.

G: Gravitational constant.

c : Speed of light.

$G_{\mu\nu}$: Einstein tensor.

$r_{\rm Sh}$: Event horizon of the Schwarzschild BH or Schwarzschild radius.

$M_{\rm BH}$: Mass of the BH.

X^μ, ξ^μ, η^μ: Killing vectors.

K: Kretschmann scalar.

$R_{\mu\nu\alpha\beta}$: Riemann tensor.

$r_{\rm ISCO}$: Innermost stable circular orbit for Schwarzschild BH.

$r_{\rm ph}$: Unstable photon circular orbit for Schwarzschild BH.

$b_{\rm ph}$: Impact parameter corresponding to $r_{\rm ph}$.

b: Impact parameter of photon.

$a_{\rm k}$: Kerr parameter or spin parameter.

$r_{\rm H}$: Event horizon of the Kerr BH.

$r_{\rm C}$: Cauchy horizon of the Kerr BH.

$r_{\rm E}^+$: Outer ergosurface of the Kerr BH.

$r_{\rm E}^-$: Inner ergosurface of the Kerr BH.

$\Omega_{\rm H}$: Angular momentum at the event horizon of Kerr BH.

$r_{\rm ISCO}^+$: ISCO radius for prograde orbit of Kerr BH.

$r_{\rm ISCO}^-$: ISCO radius for retrograde orbit of Kerr BH.

$r_{\rm ph}^+$: Prograde circular photon orbit of Kerr BH.

$r_{\rm ph}^-$: Reprograde circular photon orbit of Kerr BH.

n: NUT parameter or GMM.

$r_{\rm H}^{\rm KTN}$: Event horizon of the KTN BH.

$r_{\rm C}^{\rm KTN}$: Cauchy horizon of the KTN BH.

$r^{\rm KTN}_{\rm E(+)}$: Outer ergosurface of the KTN BH.

$r^{\rm KTN}_{\rm E(-)}$: Inner ergosurface of the KTN BH.

β: Dimensionless parameter of the WH.

$r_{\rm Th}$: Throat radius of WH.

$M_{\rm WH}$: Mass of the WH.

$\Omega_{\rm Th}$: Aangular momentum of the WH at throat.

$\mathscr{M}$: Mass in the cluster.

$\rho_{\rm DM}$: Density of the DM distribution.

$M_{\rm halo}$: Halo mass of the DM distribution.

a_0: Characterized length scale of the DM distribution.

P_t: Tangential pressure of DM distributions.

$\tilde{r}_c$: Cut off radius of DM distributions.

Ψ: Compactness of DM distributions.

$E_{\rm acc}$: Released gravitational potential energy due to accretion.

$E_{\rm nuc}$: Energy due to nuclear fusion reaction.

$\dot{M}$: Mass accretion rate.

$F_{\rm rad}$: Radiation pressure force.

σ_T: Thomson scattering cross-section.

m_e: Mass of the electron.

m_p: Mass of the proton.

$F_{\rm grav}$: Gravitational force.

$L_{\rm Edd}$: Eddington luminosity.

$\dot{M}_{\rm Edd}$: Eddington mass accretion rate.

ϱ_e: Efficiency factor of energy generation due to accretion.

$\tilde{L}$: Length of the accreting system.

$\tilde{l}$: The mean free path of the accreted fluid.

T: Temperature of the flow.

v: velocity of the flow.

C_s: Sound speed of the flow.

$r_{\rm B}$: Bondi radius.

$T_{r\phi}$: Tangential stress.

p_r: Radiation pressure.

$P_{\rm tot}$: Total pressure including the gas pressure and the radiation pressure.

α: Dimensionless viscosity parameter.

$\tilde{\nu}$: Kinematic viscosity.

$Q_{\rm vis}$: Viscous heating.

$Q_{\rm rad}$: Radiative cooling.

T_i: Ion temperature.

T_e: Electron temperature.

n_i: Number density of ions.

n_e: Number density of electrons.

H: Half thickness of the accretion disk.

$t_{\rm diff}$: Photon diffusion time scale.

$t_{\rm acc}$: Accretion timescale.

$t_{\rm cool}$: Cooling time scale.

$\tilde{\beta}$: Tilted angle between the directions of spin and angular momentum of the accretion disk.

ν_1: Kinematic viscosity related to the shear within the plane.

ν_2: Kinematic viscosity related to the shear perpendicular to the disk.

$r_{\rm BP}$: BP radius.

ν_r: Radial epicyclic frequency.

ν_θ: Vertical epicyclic frequency.

ν_ϕ: Keplerian frequency.

$\nu_{\rm LT}$: LT precession frequency.

$\nu_{\rm per}$: Periastron precession frequency.

k_B: Boltzmann constant.

Γ: Adiabatic index.

N: Polytropic index.

c_p: Specific heats at constant pressure.

c_v: Specific heats at constant volume.

$\mathcal{E}$: Bernoulli constant.

$\mathcal{L}$: Angular momentum.

λ: Specific angular momentum.

r_s: Shock location.

R: Compression ratio.

S: Shock strength.

$r_{\rm edge}$: Outer edge of accretion disk.

Φ: Magnetic flux.

I: Isorotation parameter.

$T^{\mu\nu}$: Energy-momentum tensor accretion flow.

j^μ: Mass flux of the accretion flow.

e: Local energy density of accretion flow.

h: Specific enthalpy accretion flow.

$F^{\mu\nu}$: Faraday electromagnetic tensor.

${}^*F^{\mu\nu}$: Hodge dual of the Faraday electromagnetic tensor.

e^μ: Electric field in the rest frame of fluid.

b^μ: Magnetic field in the rest frame of fluid.

B: Total magnetic field.

$p_{\rm mag}$: Magnetic Pressure.

$p_{\rm tot}$: Total pressure including gas pressure and magnetic pressure.

plasma-β: Ratio of gas pressure to magnetic pressure.

$h_{\rm tot}$: Total specific enthalpy of the magnetized fluid.

C_a: Alfvén velocity of the magnetized accretion flow.

$C_{\rm f}$: Fast Magnetosonic Speed.

u^μ: Four-velocity of fluid.

h^i_μ: Projection operator.

$\Phi^{\rm eff}$: Effective potential.

$\Phi^{\rm eff}_{\rm e}$: Effective potential on the equatorial plane.

r_c: Critical point.

$r_{\rm in}$: Inner critical point.

$r_{\rm mid}$: Middle critical point.

$r_{\rm out}$: Outer critical point.

M: Mach number.

$\dot{\mathcal{M}}$: Entropy accretion rate.

Θ: Dimensionless temperature.

Σ: Surface density.

$\tilde{e}$: Charge of the electron.

h: Planck's constant.

ν: Frequency of the photon.

Z_i: Charge of ion.

g_{br}: Gaunt factor.

T_e: Electron temperature.

ν_o: Observed frequency.

ν_e: Emitted frequency.

z: Redshift factor.

$n^{\max}$: Maximum NUT parameter for shock.

$\epsilon(\nu)$: Bremsstrahlung emissivity at frequency ν.

L_S: Luminosity of Cyg X-3.

λ_K: Keplerian angular momentum.

$\tilde{\tau}$: Optical depth.

τ_s: Optical depth due to Thompson scattering.

τ_a: Absorption optical depth.

$\kappa_{\rm s}$: The opacity coefficient of Thompson Scattering.

$k_{\rm R}^{\rm ff}$: Rosseland mean opacity coefficient for free-free emission.

a_*: $a_{\rm k}/M_{\rm BH}$.

n_*: $n/M_{\rm BH}$.

$\Omega_{\rm LT}^{\rm KTN}$: LT precession frequency around KTN BH.

$\Omega_{\rm LT}$: LT precession frequency around Kerr BH.

$\Omega_{\rm p}$: Approximate LT precession frequency around KTN BH.

$\tilde{r}_0$: $\Omega_{\rm p}$ vanishes at this radius.

$\mathscr{L} = |\mathbf{L}|$: Angular momentum per unit surface area on each annulus.

$r_{\rm align}$: Disk remains aligned up to that radius.

$r_{\rm warp}$: LT effect dominates inside this radius.

Abstract

The origin of high energy radiation from quasars, active galactic nuclei (AGNs), and X-ray binaries (XRBs) has drawn attention to the scientific community. Accretion onto compact object has emerged as one of the fundamental mechanisms in explaining the observed luminosity from these sources. Since the emitted radiation due to accretion carries imprints of the spacetime geometry near the compact object, the dynamics of accretion flows provide crucial insights into both the nature of the central object and the accreting matter. In the vicinity of compact objects, the gravitational field is so strong that we consider an appropriate effective potential to mimic the relativistic effects of the underlying spacetime geometry. Moreover, as the thermodynamical state of accretion flows undergoes a transition from non-relativistic to relativistic close to compact objects, we incorporate the relativistic equation of state (EoS). A subsonic flow at large distances from the black hole (BH) becomes supersonic as it approaches the BH under the influence of strong gravity. The infalling matter may also encounter a centrifugal barrier, and depending on the shock conditions, a post-shock corona (PSC) of hot, dense electrons can form. PSC is capable of reprocessing the soft disk photons to high energy radiations via inverse Comptonization process and such high energy radiation are commonly observed from BH XRBs.

To begin with, in Chapter 2, we present relativistic shock-induced accretion flows around Kerr-Taub-NUT (KTN) BHs, which is a broader class of stationary and axisymmetric vacuum solutions of Einstein's equations characterized by mass ($M_{\rm BH}$), spin ($a_{\rm k}$), and NUT charge (n). We solve the relativistic hydrodynamic equations to obtain both shock-free and shock-induced accretion solutions. Standing shocks form when the flow experiences a centrifugal barrier and satisfies the relativistic Rankine-Hugoniot shock conditions. Indeed, the shock-induced accretion solutions are physically more viable due to their higher entropy, and they produce significantly higher disk luminosity compared to the shock-free accretion solutions.

BHs are not the only possible accreting compact objects, exotic compact objects such as wormholes (WHs) remain theoretically viable. Therefore, in Chapter 3, we investigate the relativistic accretion flow in a stationary axisymmetric Kerr-like WH, which is characterized by spin parameter ($a_{\rm k}$), dimensionless parameter (β), and its mass ($M_{\rm WH}$). WH is defined by a throat that connects the two regular spacetimes. By solving the hydrodynamical equations, we identify four types of transonic accretion flows in addition to subsonic flows. The transonic accretion solutions are more viable than the subsonic ones due to their higher entropy. We further compute the disk luminosities and demonstrate that our model reproduces the observed luminosity of Cygnus X-3 in its hypersoft state.

Observational evidence from flat galaxy rotation curves, galaxy velocities, and the Cosmic Microwave Background (CMB) indicates to the existence of dark matter (DM) in the Universe. The Standard Model of particle physics cannot account for the nature of DM, which plays a crucial role in large scale structure formation and the growth of supermassive BHs at galactic centers. DM also influences the spacetime geometry. Consequently, the DM halos around the BHs have critical impact on the accretion flow. To address this, we study relativistic accretion around galactic BHs surrounded by cold DM halos in the steady state in Chapter 4. We consider several DM profiles, including Hernquist, Navarro-Frenk-White (NFW), Einasto, and DM spike.

Our results show that DM halo shifts the critical point of the transonic accretion flow inward and enhances disk luminosity depending on DM distribution. Since major contribution of luminosity originates from the inner disk, this would help to probe the nature of DM near BHs

Moreover, magnetic fields also play a crucial role in the dynamics and emission properties of accretion flows around compact objects. Motivated by the recent Event Horizon Telescope (EHT) observations of Sagittarius A* (Sgr A*), in Chapter 5, we investigate relativistic accretion flows around Kerr BH using a general relativistic magnetohydrodynamics (GRMHD) framework in the steady state, and examine the magnetic field strengths constrained by the EHT. By solving the GRMHD equations with constant flow parameters, such as energy ($\mathcal{E}$), angular momentum ($\mathcal{L}$), magnetic flux (Φ), and isorotation parameter (I), we obtain global accretion solutions. For a wide range of parameter space, these solutions reproduce magnetic field strengths within $\pm 10\%$ of the EHT reported values. This provides a theoretical framework that explains the complex dynamics of the magnetized accretion flows around Sgr A*.

In astrophysical scenarios, tilted accretion disks form when the angular momentum of the accretion disk is misaligned with that of a rotating compact object. Such misalignment induces Lense-Thirring (LT) precession due to frame dragging, which strongly influences the observable signatures. Therefore, we extend our analysis to a tilted, thin accretion disk around a slowly spinning KTN BH. In Chapter 6, we compute the radial tilt profile up to the innermost stable circular orbit (ISCO), which takes into account the interplay between LT torque and viscous torque. Our results show that the inner disk may either align or remain tilted depending on KTN BH parameters ($M_{\rm BH}$, $a_{\rm k}$, n) and viscosity. This analysis further indicates the imprint of the NUT parameter in the spacetime.

In summary, this thesis presents a detailed analysis of relativistic hydrodynamic flows around compact objects, exotic compact objects, and compact objects embedded within DM halos, in the steady state. Furthermore, GRMHD flows are studied in light of EHT observations. Finally, we examine the dynamics of tilted accretion disk around KTN BH.

List of publications

[I]. Study of relativistic accretion flow around KTN black hole with shocks.

Gargi Sen, Debaprasad Maity, Santabrata Das.

JCAP 08 (2022) 048, arXiv: 2204.02110.

Content of Chapter 2 is based on this paper.

[II]. Study of relativistic hot accretion flow around Kerr-like Wormhole.

Gargi Sen, Debaprasad Maity, Santabrata Das.

JCAP 10 (2024) 068, arXiv: 2405.11453.

Content of Chapter 3 is based on this paper.

[III]. Effect of generic dark matter halo on transonic accretion onto galactic black holes.

Avijit Chowdhury, Gargi Sen, Sayan Chakrabarti, Santabrata Das.

Phys. Rev. D 112, 064041 (2025), arXiv: 2503.08528.

Content of Chapter 4 is based on this paper.

[IV]. GRMHD modelling of accretion flow around Sagittarius A* constrained by EHT measurements.

Gargi Sen, Debaprasad Maity, Santabrata Das.

Phys. Rev. D 112, 083047 (2025), arXiv:2510.03602

Content of Chapter 5 is based on this paper.

[V]. Study of a Tilted Thin Accretion Disk around a Kerr-Taub-NUT black hole.

Gargi Sen, Chandrachur Chakraborty, Sudip Bhattacharyya, Debaprasad Maity, Sayan Chakrabarti, Santabrata Das.

JCAP 12 (2024) 030, arXiv: 2408.03270.

Content of Chapter 6 is based on this paper.

Conferences/Workshop/School attended

- Presented a talk (online) titled "Study of relativistic accretion flow around KTN black hole with shock" at **NEMA-VII, 2022**, Rajib Gandhi University, India.
- Presented a talk (online) titled "Study of relativistic accretion flow around KTN black hole with shock" at **COSPAR, 2022**, Athens, Greece.
- Presented a *e*-poster titled "Study of relativistic accretion flow around KTN black hole with shock" at **YAM, 2022**, ARIES, India.
- Presented a talk titled "Study of relativistic accretion flow in a Kerr-like wormhole" at **PANE,2022**, Manipur University, India.
- Presented a talk titled "Study of relativistic accretion flow around KTN black hole with shock" at **32nd meeting of IAGRG, 2022**, IISER Kolkata, India.
- Presented a talk titled "Study of relativistic accretion flow around KTN black hole with shocks" at **RETCO-V, 2023**, Kodaikanal Solar Observatory, India.
- Presented a poster titled "Properties of relativistic advective accretion flow in a Kerr-like wormhole" at **ICGC, 2023**, IIT Guwahati, India.
- Presented a poster titled "Study of the relativistic accretion flow in a Kerr-like wormhole" at **Gravity 2025: New Horizon of Black Hole Physics, 2025**, Kyoto University, Japan.
- Attended a school named **Beyond the Horizon: Testing the black hole paradigm** at ICTS Bengaluru, India, 2025.

Contents

List of Figures

List of Tables

Chapter 1

Introduction

The innocent wonder of *Twinkle, Twinkle, Little Stars* of the infinite midnight sea above us has astonished and inspired human hearts from childhood to present day with their own mystery. As we grow older, we learn that the night sky is not a mere collections of living stars but also many dead stars are there. From the imaginative worlds of science-fiction tales about black holes, wormholes to the groundbreaking discovery of the bright ring around a black hole, the cosmos has become one of the most mesmerizing subjects for all humanity. This naturally leads us to the questions related to the nature of these objects, their origin and activities within this immense cosmic ocean, and most importantly about their detection directly or indirectly. These questions form the central focus of this thesis. In the introduction, we will discuss them one by one as we proceed.

1.1 Compact objects

A supernova explosion causes the catastrophic end of a massive star's life when there is insufficient energy production due to nuclear fusion. As a result, the pressure gradient provided by radiation becomes inadequate to prevent the gravity, which in principle leads to the gravitational collapse. Through this process, a tremendous amount of gravitational energy is released in the form of high energy radiation and the dense compact objects are left behind, which represent the final evolutionary stages of stars. Depending on the initial mass of the progenitor stars, the compact remnants lead to the formation of white dwarfs (WDs), neutron stars (NSs), or black holes (BHs). Unlike main-sequence stars, compact objects do not generate energy through nuclear fusion. Therefore, WDs and NSs are supported by electron and neutron degeneracy pressure, respectively, whereas BHs are the ultimate collapse products, where nothing is left to resist the formation of the singularity. As the high mass is concentrated in a small region, the density and gravitational potential ($\Phi_G \propto \frac{M_*}{\mathscr{R}}$, M_* and $\mathscr{R}$ being the

mass and radius of the compact object) are extremely high for these objects. Therefore, general relativity plays a crucial role in describing their structure and behavior accurately. Moreover, these compact objects serve as natural laboratories for studying the properties of matter in a strong gravity regime, and act as source of electromagnetic as well as gravitational radiation in astrophysical contexts. In the following, we will briefly discuss the properties of these compact objects (WDs, NSs and BHs).

1.1.1 White dwarfs

White dwarfs (WDs) represent the final evolutionary stage of low and intermediate mass stars (with initial mass $M_* < 8 - 10 M_\odot$). These compact objects possess a mass of the order of one solar mass ($M_\odot$) with characteristic radii comparable to the Earth. As a result, the density becomes very high. The companions of 40 Eridani (Herschel, 1785; Russell, 1914; Hertzsprung, 1915) and Sirius (Bessel, 1844; Bond, 1862) played important role in the history of WDs, as they are recognized as a distinct class of subluminous stars. Adams (1914) found that the spectral nature of these stars is not the same as that of main sequence A-type stars. The unusual mass luminosity properties of 40 Eridani B (companion of 40 Eridani) (Bond et al., 2017), and Sirius B (companion of Sirius) (Adams, 1915) lead to interest in studying faint stars. Because of this uniqueness, these stars are named as 'faint white stars', 'white stars with low apparent magnitude' and 'white dwarf' (Luyten, 1922a,b, 1923). For these objects, Fowler (1926) showed that electron degeneracy pressure provides the force necessary to counteract the gravitational collapse. In the non-relativistic limit, the pressure (p) is proportional to the 5/3 power of its density (ρ), *i.e.*, $p \propto \rho^{5/3}$, whereas $p \propto \rho^{4/3}$ in case of the relativistic equation of state (EoS). Chandrasekhar (1931) considered the relativistic effects and discovered the maximum mass of WDs $\sim 1.4 M_\odot$, which is known as the Chandrasekhar mass limit. However, the exact value depends on the composition of the matter. WDs emit thermal radiation from residual heat, and fades them over time. Therefore, we can analyze their properties by using the Hertzsprung-Russell (HR) diagram, which is a plot of luminosity (L) vs. effective temperature (T) (Shapiro & Teukolsky, 1983). For higher dense WDs, the degenerate pressure also becomes high, which in turn increases the thermal conductivity. The high densities of WDs yield higher the surface gravity ($\sim 10^8$cm s^{-2}, whereas the Sun's surface gravity is $\sim 10^4$ cm s^{-2}). Moreover, WDs serve as age indicators for stellar populations like the Galactic disk (Oswalt et al., 1996) and globular clusters (Renzini et al., 1996). Binary systems containing WDs provide valuable laboratories for investigating accretion processes, binary evolution, and gravitational wave (GW) dynamics.

1.1.2 Neutron stars

Neutron stars (NSs) represent another important class of compact objects formed under extreme conditions of the interplay between nuclear physics and gravity. Baade & Zwicky (1934) proposed the first idea of NSs by showing the transformation of ordinary stars into compact objects of very tightly packed neutrons via supernova explosions. At the core of these compact objects, density goes up to $\sim 10^{13} - 10^{15}$ g/cm^3 (Frolov & Zelnikov, 2011) and protons transform into neutrons via inverse beta decay. As a result, the neutron degeneracy pressure in the neutron rich core prevents further gravitational contraction and forms NSs. Oppenheimer & Volkoff (1939) found

that stable static NSs could not have masses larger than $\sim 0.7M_\odot$ by assuming the matter of an ideal gas of non interacting neutrons. Later, the maximum mass of NSs was found to be $\sim 2M_\odot$ considering nucleon-nucleon interaction (Cameron, 1959). Structurally, the interior of a NS can be divided into two main parts, *i.e.*, the liquid core and solid crust. The core is uniformly distributed, whereas the crust is non-uniform and composed of nuclear clusters. Various EoSs of NSs have been proposed with compositions including mesons, hyperons, baryons, leptons, pion condensates, or even quark matter (Cameron, 1959; Ambartsumyan & Saakyan, 1960; Ivanenko & Kurdgelaidze, 1965; Migdal, 1972; Sawyer, 1972). When the rotating NSs are coupled with a strong magnetic field, they can emit electromagnetic radiation and high energy accelerated particles (Pacini, 1967; Gold, 1969). These neutron rich nuclei of mass $\sim 1-2M_\odot$ and radii of about $10-12$ km are observed as pulsars or the sources of X-ray and γ-ray. The discovery of first X-ray pulsar Cygnus X-1 by the Uhuru satellite (Oda et al., 1971), radio pulsars (Hewish et al., 1968), accreting pulsars (Giacconi et al., 1971; Tananbaum et al., 1972), and binary pulsars (Hulse & Taylor, 1975) provide the opportunity to measure the nature and mass of NSs. Moreover, the GW signal from the merger of two NSs (Abbott et al., 2017), and the emitted neutrinos from supernova explosion carry information about the formation, structure and evolution of NSs.

1.1.3 Black holes

We have already discussed that the WDs and NSs hold themselves from gravitational collapse via electrons and neutrons degenerate pressure, respectively. On the other hand, there is no mechanism for black holes (BHs) to withstand the inward pull of gravity and finally collapse into a singularity. This compact object is a profound prediction of Einstein's theory of general relativity (Einstein, 1916a,b; Einstein, 1918). Gravity is so intense near the BH that no matter or light can come out from it. BH is a region of spacetime that is disconnected from the external Universe via a surface called the event horizon. As the Newtonian gravity fails to understand the nature of the BH, the general theory of relativity becomes important to explain this. In this theory, the geometry of spacetime is related to the presence of matter through Einstein's field equation as,

$$R_{\mu\nu} - \frac{1}{2}g_{\mu\nu}R = G_{\mu\nu} = \frac{8\pi G}{c^4}T_{\mu\nu}, \tag{1.1}$$

where $R_{\mu\nu}$ is the Ricci tensor, $g_{\mu\nu}$ denotes metric tensor, R is the Ricci scalar of the background metric, $T_{\mu\nu}$ represents the energy momentum tensor of the matter distributions in the spacetime, G is the universal gravitational constant, c is the speed of light, and $G_{\mu\nu}$ denotes the Einstein tensor. Wheeler (1968) first coined the term 'black hole' and Michell and Laplace independently predicted that if the star's mass is so high, light can not emerge from it (Montgomery et al., 2009). Based on the Newtonian theory, they obtained the size of such a 'dark star', which later coincides with the gravitational radius ($r_{\rm Sh} = 2GM_*/c^2$) of Schwarzschild BH calculated in Einstein's theory of gravity. The progenitor star with mass $> 10M_\odot$ (Shapiro et al., 1976) becomes a BH at the end of its evolution. Depending on BH mass, they are classified as stellar mass BHs ($\sim 3M_\odot$ to several tens $M_\odot$), intermediate mass BHs ($10^2M_\odot < M_* < 10^5M_\odot$), and supermassive BHs ($M_* > 10^5M_\odot$) that power active galactic nuclei (AGNs) and quasars. Another kind of BHs are the primordial BHs, which may form in the early Universe due to perturbations in the homogeneous background density. As we cannot directly

observe a BH, we have to rely on several powerful indirect methods to study them, such as BH shadow (Cunningham & Bardeen, 1973; Luminet, 1979; Chandrasekhar, 1983), electromagnetic waves (such as X-rays, γ-rays and radio waves) (Schreier et al., 1971; Lynden-Bell & Rees, 1971; Pringle & Rees, 1972; Pringle, 1981), and the GWs (Einstein, 1916a; Einstein, 1918). The first compelling observational evidence for the existence of BHs came from studies of the X-ray binary (XRB) Cygnus X-1 (Bolton, 1972; Webster & Murdin, 1972), which has a mass larger than the NS's maximum mass limit. In the following part, we elaborately discuss the properties of BHs.

A. Schwarzschild black hole

The Schwarzschild BH solution is the first exact vacuum solution of Einstein's field equations, and its metric illustrates the exterior gravitational field of a spherically symmetric mass distribution. Astronomer Karl Schwarzschild obtained the first spherically symmetric solution (known as Schwarzschild solution)[1] of vacuum Einstein's field equations (Schwarzschild, 1916). In the Schwarzschild coordinates, the metric is expressed as,

$$\begin{aligned} ds^2 =& g_{tt}dt^2 + g_{rr}dr^2 + g_{\theta\theta}d\theta^2 + g_{\phi\phi}d\phi^2, \\ =& -\left(1 - \frac{2M_{\rm BH}G}{c^2 r}\right)dt^2 + \frac{1}{\left(1 - \frac{2M_{\rm BH}G}{c^2 r}\right)}dr^2 + r^2(d\theta^2 + \sin^2\theta d\phi^2). \end{aligned} \tag{1.2}$$

Here, G is the universal gravitational constant, c is the speed of light, and $M_{\rm BH}$ is the mass of the BH. Shortly after, Droste (1917) also got the same Schwarzschild solution separately. Later, Birkhoff theorem (Birkhoff & Langer, 1923) also tells that the Schwarzschild solution is the unique spherically symmetric static vacuum solution of Einstein's field equations. A schematic diagram of a Schwarzschild BH is illustrated in Fig. 1.1. In the following analysis, we adopt the geometric unit system by setting $G = c = 1$, unless otherwise stated. In this coordinate system, the singularity occurs at the radius, where $g^{rr} = 1/g_{rr} = 0$ (see Eq. (1.2)). This radius is identified as the event horizon of the Schwarzschild BH or the Schwarzschild radius ($r_{\rm Sh} = 2M_{\rm BH}$), and this coordinate singularity can be removed by the proper choice of coordinate. The surface at $r_{\rm Sh} = 2M_{\rm BH}$ acts as a one way surface, from where nothing (massive or massless) can come out. For an static infinite observer, a particle takes an infinite time to reach the event horizon. Therefore, this surface ($r = r_{\rm Sh}$) is also called an infinite redshift surface ($g_{tt} = 0$). On the event horizon, tangent vectors are light-like or null, therefore, it is a null hypersurface. Furthermore, the symmetries of spacetime and conserved quantities for particles in that spacetime are encoded in the Killing vectors, which leave the spacetime unchanged while moving along these. The Killing vector (X^μ) satisfies the relation $\nabla_\nu X_\mu + \nabla_\mu X_\nu = 0$, which is known as Killing equation. This Killing vector (X^μ) is time-like ($X^\mu X_\mu < 0$) outside the event horizon ($r > r_{\rm Sh}$), null ($X^\mu X_\mu = 0$) at the event horizon ($r = r_{\rm Sh}$) and space-like ($X^\mu X_\mu < 0$) inside the event horizon ($r < r_{\rm Sh}$). Therefore, the event horizon is otherwise stated as the Killing horizon. Another singularity exists at $r = 0$. If we calculate the Kretschmann scalar (K) (one of the curvature invariants) for the Schwarzschild metric, we get $K =$

[1] Schwarzschild solution was derived in the hospital, where Schwarzschild was admitted due to an acute skin disease after joining the first World War at the end of 1915.

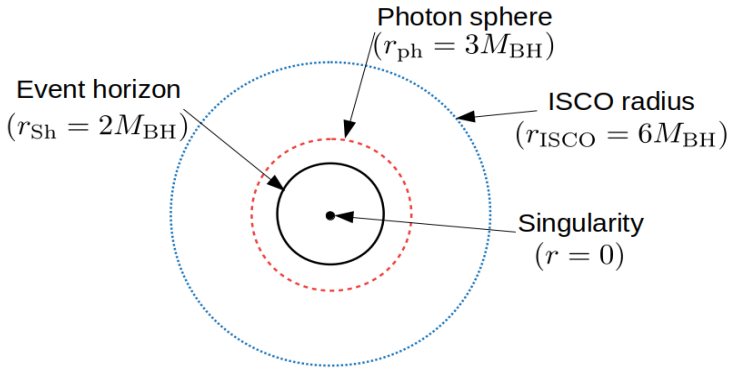

Figure 1.1: A schematic diagram of a Schwarzschild black hole.

$R_{\mu\nu\alpha\beta}R^{\mu\nu\alpha\beta} = \frac{12r_{\rm Sh}^2}{r^6}$, where $R_{\mu\nu\alpha\beta}$ is Riemann tensor. Therefore, the Kretschmann scalar is finite at $r = r_{\rm Sh}$. On the other hand, K is infinite at $r = 0$ and it is called the curvature singularity or physical singularity, which is not removable by a coordinate transformation. Furthermore, it is worth mentioning that a massive particle would be stable upto the innermost stable circular orbit (ISCO) ($r_{\rm ISCO} = 6M_{\rm BH}$) (Landau & Lifschits, 1975), and beyond that it freely falls into the BH, whereas the unstable photon (massless particle) circular orbit is located at $r_{\rm ph} = 3M_{\rm BH}$. So, there exists a critical impact parameter $b_{\rm ph} = 3\sqrt{3}M_{\rm BH}$ corresponding to $r_{\rm ph}$, such that any light ray with $b < b_{\rm ph}$ will be captured by the BH and photons with $b > b_{\rm ph}$ will be deflected away from the BH (Landau & Lifschits, 1975; Luminet, 1979).

B. Kerr black hole

In an astrophysical scenario, most of the celestial objects are rotating in nature and it is obvious that due to gravitational collapse of the stars, the angular momentum is retained in the remnant compact objects. Therefore, after Karl Schwarzschild's formulations of the exact vacuum solution of Einstein's field equations of a non-rotating spherically symmetric static BH (Schwarzschild, 1916), Roy Kerr discovered an exact vacuum solution of the Einstein field equations for the case of a rotating BH (Kerr, 1963), which is known as Kerr solution. Later, it was shown that the Kerr solution uniquely describes any spinning and uncharged BH in Einstein's theory. Ruffini & Wheeler (1971) proposed the no-hair conjecture, which affirms that the most general stationary BH solution to the Einstein-Maxwell equations is the Kerr-Newman solution (Newman et al., 1965), that depends only on the mass, angular momentum and electric charge of the BH. The line element of a stationary axisymmetric spacetime is given by,

$$ds^2 = g_{tt}dt^2 + g_{rr}dr^2 + g_{\theta\theta}d\theta^2 + g_{\phi\phi}d\phi^2 + 2g_{t\phi}dtd\phi. \tag{1.3}$$

In terms of Boyer-Lindquist coordinates, the components of the Kerr metric are expressed as (Boyer & Lindquist, 1967),

$$\begin{aligned} g_{tt} &= -\left(1 - \frac{2M_{\rm BH}r}{\Sigma}\right), \; g_{\theta\theta} = \Sigma, \; g_{rr} = \frac{\Sigma}{\Delta}, \\ g_{t\phi} &= -\frac{2M_{\rm BH}a_{\rm k}r\sin^2\theta}{\Sigma}, \; g_{\phi\phi} = \left(r^2 + a_{\rm k}^2 + \frac{2M_{\rm BH}ra_{\rm k}^2\sin^2\theta}{\Sigma}\right)\sin^2\theta, \end{aligned} \tag{1.4}$$

with,

$$\Sigma = r^2 + a_{\rm k}^2 \cos^2\theta,$$
$$\Delta = r^2 - 2M_{\rm BH} r + a_{\rm k}^2.$$

Here, $a_{\rm k}$ is the spin parameter or Kerr parameter, and $M_{\rm BH}$ is the BH mass. We use $(-,+,+,+)$ sign convention and the geometric unit system ($G = c = 1$). Setting $a_{\rm k} = 0$, we get back the Schwarzschild metric. The metric has coordinate singularity, where $g_{rr} = \infty$ or $g^{rr} = 0$, which in turns gives the radii $r_\pm = M_{\rm BH} \pm \sqrt{M_{\rm BH}^2 - a_{\rm k}^2}$. Here, r_+ is called event horizon ($r_{\rm H}$) and r_- is called Cauchy horizon ($r_{\rm C}$). For $a_{\rm k} < M_{\rm BH}$, we get BH, and $a_{\rm k} > M_{\rm BH}$ gives the naked singularity case. Moreover, curvature singularity is located at $r = 0$ and $\theta = \pi/2$, which is known as ring singularity and the Kretchmann scalar $K = R_{\mu\nu\alpha\beta}R^{\mu\nu\alpha\beta}$ diverges here, whereas at the event horizon and the Cauchy horizon, K is finite. Therefore, these are the removable singularities. Another important concept for rotating BHs is the ergosphere. The eargosurface is the surface of infinite redshift, *i.e.*, $g_{tt} = 0$, located at $r_{\rm E}^\pm = M_{\rm BH} \pm \sqrt{M_{\rm BH}^2 - a_{\rm k}^2 \cos^2\theta}$. The outer ergosurface $r_{\rm E}^+$ (inner ergosurface $r_{\rm E}^-$) coincides with event horizon $r_{\rm H}$ (Cauchy horizon $r_{\rm C}$) on the axis of rotation $\theta = 0$ and π. In the region between the outer ergosurface and the event horizon, no one can stand still. This region is called the ergosphere or ergoregion. Fig. 1.2 pictorially illustrates a Kerr BH. As the Kerr spacetime is stationary and axisymmetric, it has two Killing vectors, such as the time translation Killing vector (ξ_t^μ) and the azimuthal Killing vector (ξ_ϕ^μ). Therefore, their combination $\xi^\mu = \xi_t^\mu + \Omega_{\rm H}\xi_\phi^\alpha$ is also a Killing vector, where $\Omega_{\rm H}$ is the angular momentum at the horizon. At $r_{\rm H}$, $\xi^\mu\xi_\mu = 0$, which signifies that the Killing vector is null at the horizon. The time-like trajectory ($\xi^\mu\xi_\mu < 0$) at $r > r_{\rm H}$ becomes null trajectory ($\xi^\mu\xi_\mu = 0$) at $r = r_{\rm H}$, and at $r < r_{\rm H}$, it turns to space-like ($\xi^\mu\xi_\mu > 0$). At the ergosurface, the norm of the time translation Killing vector vanishes, *i.e.*, $g_{\mu\nu}\xi_t^\mu\xi_t^\nu = 0$. Inside the ergosphere, the particles are forced to corotate with the BH's spin due to the frame dragging effect. Penrose (1969) proposed a mechanism for extracting energy from a rotating BH due the presence of an ergosphere. If a particle of energy E_0 is thrown from infinity to the ergosphere, it splits into two particles. One of them comes back to the infinity with energy $E_1 = E_0 - E_2$, whereas the another one goes into the BH with energy E_2, which is negative with respect to the infinite observer, and this ingoing particle will corotate with the BH. For $E_1 > E_0$, the rotational energy of the BH is being extracted in this process, which is known as the 'Penrose process'. Therefore, the spin of the BH slows down. Moreover, using the metric components (Eq. (1.4)), the ISCO radius on the equatorial plane is calculated as (Bardeen et al., 1972),

$$r_{\rm ISCO}^\pm = M_{\rm BH}\left[3 + Z_2 \mp \sqrt{(3 - Z_1)(3 + Z_1 + 2Z_2)}\right],$$

where Z_1 and Z_2 are given by,

$$Z_1 = 1 + \left(1 - \frac{a_{\rm k}^2}{M_{\rm BH}^2}\right)^{1/3}\left[\left(1 + \frac{a_{\rm k}}{M_{\rm BH}}\right)^{1/3} + \left(1 - \frac{a_{\rm k}}{M_{\rm BH}}\right)^{1/3}\right],$$

and,

$$Z_2 = \sqrt{3\frac{a_{\rm k}^2}{M_{\rm BH}^2} + Z_1^2}.$$

Here, $r_{\rm ISCO}^+$ and $r_{\rm ISCO}^-$ represent the ISCO radius for prograde orbits and retrograde orbits, respectively. The unstable photon circular orbit around a Kerr BH is obtained

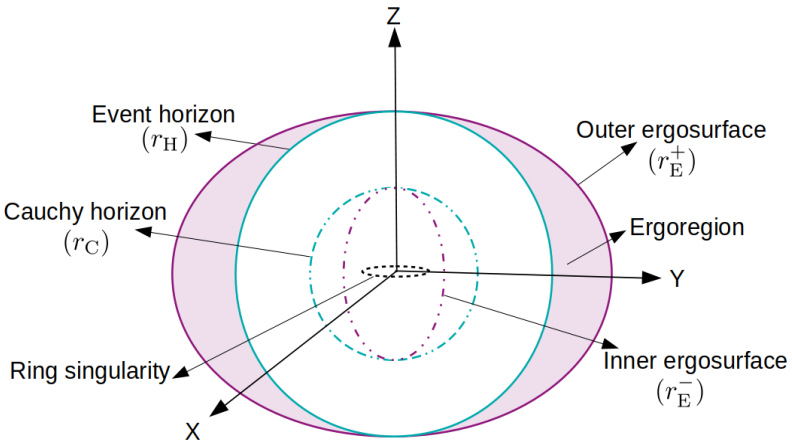

Figure 1.2: A pictorial representation of a Kerr black hole.

as (Chandrasekhar, 1983),

$$r_{\rm ph}^{\pm} = 2M_{\rm BH}\left[1+\cos\left\{\frac{2}{3}\arccos\left(\mp\frac{a_{\rm k}}{M_{\rm BH}}\right)\right\}\right].$$

For the maximally rotating BH ($M_{\rm BH} = a_{\rm k}$), the prograde and retrograde circular photon orbits are located at $r_{\rm ph}^{+} = M_{\rm BH}$ and $r_{\rm ph}^{-} = 4M_{\rm BH}$, respectively.

C. Kerr-Taub-NUT black hole

Newman, Unti, and Tamburino (Newman et al., 1963) introduced a new class of stationary and spherically symmetric spacetime, which is known as the Taub-NUT solution (Misner, 1963). Thereafter, Miller (1973) proposed the Kerr-Taub-NUT (KTN) metric, which is a stationary and axisymmetric solution of the vacuum Einstein-Maxwell equations. Subsequently, Plebanski & Demianski (1976) presented a general form of the stationary and axisymmetric vacuum solutions of Einstein's field equation known as Plebanski-Demianski (PD) metric, which encompasses a wide range of well known vacuum solution of Einstein's equations, such as Schwarzschild, Kerr, Kerr-Newman, Taub-NUT, KTN, and Reissner-Nordström. In presences of NUT charge, Schwarzschild spacetime transforms into Taub-NUT spacetime, while Kerr spacetime gives rise the KTN spacetime. The spacetime interval in the KTN spacetime is given by (Miller, 1973),

$$ds^2 = -\frac{\Delta}{\Sigma}(dt - Ad\phi)^2 + \frac{\Sigma}{\Delta}dr^2 + \Sigma d\theta^2 + \frac{1}{\Sigma}\sin^2\theta(a_{\rm k}dt - Bd\phi)^2, \tag{1.5}$$

with $\Sigma = r^2 + (n + a_{\rm k}\cos\theta)^2$, $\Delta = r^2 - 2M_{\rm BH}r + a_{\rm k}^2 - n^2$, $A = a_{\rm k}\sin^2\theta - 2n\cos\theta$, and $B = r^2 + a_{\rm k}^2 + n^2$, where $a_{\rm k}$ and n are the Kerr parameter and NUT parameter, respectively. Fig. 1.3 is the pictorial illustration of KTN BH. The KTN spacetime contains two masses, one of which is the ordinary mass or gravitoelectric mass, and the other is the gravitomagnetic monopole (GMM). As, the GMM is a topological charge in gravity theory, it is also known as the dual mass, or magnetic mass (Ramaswamy & Sen, 1981; Zimmerman & Shahir, 1989; Shen, 2002). Analogous to the Dirac's

magnetic monopole (Dirac, 1931), 'gravitoelectric charge' or 'mass' can exists when Einstein's general relativity is combined with electromagnetism and GMM is present. Bonnor (1969) and Dowker (1974) interpreted this as a massless rotating rod and a linear source of pure angular momentum. Setting $g^{rr} = 0$, we get the coordinate singularities of this spacetime at $r_{\rm C}^{\rm KTN} = M_{\rm BH} - \sqrt{M_{\rm BH}^2 - a_{\rm k}^2 + n^2}$ (Cauchy horizon) and at $r_{\rm H}^{\rm KTN} = M_{\rm BH} + \sqrt{M_{\rm BH}^2 - a_{\rm k}^2 + n^2}$ (event horizon), where the Killing horizon coincides. This spacetime behaves as BH for $(M_{\rm BH}^2 - a_{\rm k}^2 + n^2) > 0$ or becomes the naked singularity for $(M_{\rm BH}^2 - a_{\rm k}^2 + n^2) < 0$. Another coordinate singularities occur along the symmetry axis $\theta = 0$, and π, where the determinant of the metric vanishes. According to Misner (1963), these singularities (string singularities or Misner string) can be removed by incorporating a periodic identification on the time and azimuthal coordinates. The first coordinate patch covers the northern hemisphere, and the singularity is located along the axis $\theta = \pi$, while the second patch covers the southern hemisphere with the singularity extending along the axis $\theta = 0$. Additionally, Bonnor (1969) elucidated the NUT metric as a spherically symmetric mass along with a semi-infinite massless source of pure angular momentum along the axis of symmetry. The singularity along $\theta = 0$ can be removed by a Cartesian coordinates transformation, whereas $\theta = \pi$ singularity cannot be removed by this transformation. Therefore, the singularity at $\theta = \pi$ is interpreted as a physical singularity, which is a massless source of angular momentum. The curvature singularity occurs at $r = 0$ and $\theta = \arccos(-n/a_{\rm k})$. The ergosurface for KTN BH is situated at $r_{\rm E(\pm)}^{\rm KTN} = M_{\rm BH} \pm \sqrt{M_{\rm BH}^2 - a_{\rm k}^2 \cos^2\theta + n^2}$ (Narzilloev et al., 2023). This relation shows that, in the presence of the NUT parameter, the ergosphere exists without rotation ($a_{\rm k} = 0$), which is absent for Schwarzschild BH. The Kerr BH is asymptotically flat, whereas the KTN BH is not asymptotically flat, it possesses a twisting geometry at infinity due to the presence of the NUT parameter. Moreover, following Chakraborty (2014), we get the value of the ISCO radius around KTN BH by solving the following equation,

$$M_{\rm BH}(r^6 - n^6 + 15n^4r^2 - 15n^2r^4) - 2M_{\rm BH}^2 r(3r^4 - 2n^2r^2 + 3n^4) - 16n^4r^3$$
$$\pm 8a_{\rm k}r^{3/2}\Big[M_{\rm BH}(r^2 - n^2) + 2n^2r\Big]^{3/2} + a_{\rm k}^2\Big[M_{\rm BH}(n^4 + 6n^2r^2 - 3r^4) - 8n^2r^3\Big] = 0. \quad (1.6)$$

1.2 Exotic compact objects

Other than the above mentioned compact objects, there exists another kind of compact objects known as exotic compact objects (ECOs). These theoretically predicted ultra-compact astrophysical objects can mimic the external gravitational field of NSs or BHs, but differ internally. In strong gravity regime, these theoretical equilibrium configurations demand exotic physical phenomena related to various questions such as the nature of dark matter (DM), the formation of singularities, the presence of horizons, possibe quantum effects. Within the GR framework, Buchdahl's theorem sets the maximum compactness of a self-gravitating object, $M_*/\mathscr{R} = 4/9$ (M_* is the mass of compact objects and $\mathscr{R}$ is its radius) (Buchdahl, 1959). In this theory, the radial pressure and energy density are always positive ($P_r \geq 0, \hat{\rho} \geq 0$) and the energy density decreases in the outward direction ($\frac{d\hat{\rho}}{dr} < 0$). On the other hand, ECOs are

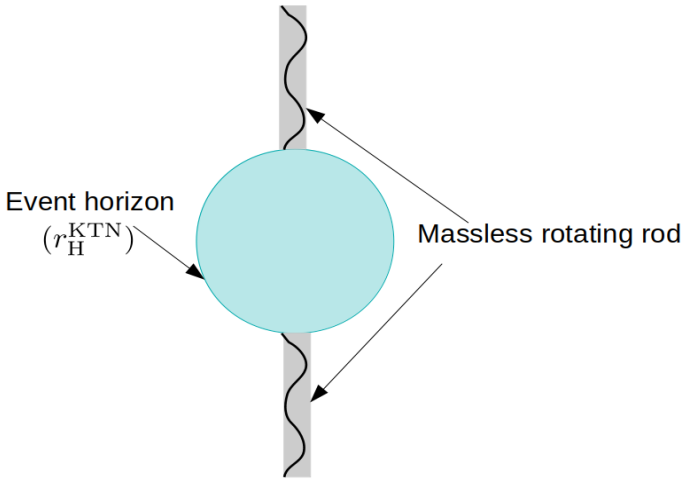

Figure 1.3: A schematic view of a Kerr-Taub-NUT black hole.

those objects that violate the underlying assumptions of Buchdahl's theorem. Below, we summarize some of the prominent ECOs and their key properties.

Boson stars are the descendants of self-gravitating photonic configurations, known as gravitational electromagnetic units (geons) (Wheeler, 1955). These consist of bosons in their ground state that form a self-gravitating macroscopic Bose-Einstein condensate and can be described by a complex or massive scalar field. Moreover, Kaup (1968) and Ruffini & Bonazzola (1969) showed that boson stars are the solitonic solutions of the Einstein-Klein-Gordon system. These regular horizonless objects are stationary and highly compact, massive, and stable due to stronger self-interaction (Schunck & Mielke, 2003). Barceló et al. (2009); Barceló et al. (2016) showed that the semiclassical effects may resist the collapse and produce *dark stars*, which are powered by DM annihilation instead of nuclear fusion. Among various DM candidates, weakly interacting massive particles (WIMPs) are considered the most promising candidate for the heat source, as they can self annihilate inside the star. These dark stars are formed at redshifts $z \sim 10 - 50$ (age of the Universe ~ 200 Myr) in a DM-rich environment. When the dark stars exhaust the DM, they may collapse to a BH (Freese et al., 2016). Therefore, these may be the seeds of the early SMBHs, whereas these may still exist and form at the galactic centers with high DM densities. Another hypothetical cold, dark ECOs are *gravastars* or gravitational vacuum stars (Mazur & Mottola, 2004), which are the solution of Einstein's equations based on Bose-Einstein condensation in gravity. In the interior de-Sitter condensate, pressure is negative to the density ($p = -\rho$), whereas exterior Schwarzschild geometry satisfies $p = \rho = 0$, which are separated by a small finite shell of thickness l of fluid with $p = \rho$. Gravastars possess no singularity and no horizon. Moreover, the rotating axially symmetric and stationary gravastars were introduced by perturbing the nonrotating gravastars (Cardoso et al., 2008; Chirenti & Rezzolla, 2008) and exhibit ergosphere, which helps to trace gravastars by superradiant scattering. Due to repeated scattering, the extracted energy can be encoded in GWs, which may be detected by advanced LIGO or LISA. Ivanenko & Kurdgelaidze (1969) first proposed *quark stars* or *strange stars*, where neutrons could dissolve into quarks under extreme pressure and temperature due to gravitational contraction of the stellar objects (Gell-Mann, 1964; Zweig, 1964). Itoh (1970)

suggested the possibility of the existence of 3-flavor full quark stars (up (u), down (d), and strange quarks (s)). The approximate mass-radius relations of strange stars ($M_* \propto \mathscr{R}^3$) are in contrast with that of NSs ($M_* \propto \mathscr{R}^{-3}$). According to Haensel et al. (1986) and Alcock et al. (1986), the strange stars may have mass $\sim 1 - 2M_\odot$ and radii ~ 10 km. Moreover, bare strange stars (strange stars without crusts) (Xu & Qiao, 1998) may have different spectral features, binding energy and core collapse process during supernova than NSs. *Fuzzballs* are the another ECOs, where the string theory provides the horizon scale microstructure to replace the BH (Mathur, 2005). Each individual microstates are regular and horizonless, which allows a horizon sized structure without gravitational collapse, where quantum tunnelling is possible in huge number of such fuzzball states (Mathur, 2010; Kraus & Mathur, 2015). Consequently, Bacchini et al. (2021) showed that these microstructures capture light rays, which produce chaotic and redshifted trajectories and affects the shadow size and residual glow distinctly from BHs.

In this thesis, we undertake a detailed investigation of accretion flows around wormhole spacetimes, with the aim of understanding how their physical properties are encoded in astrophysical observables. Therefore, we provide the geometrical features and key physical characteristics of wormholes in the subsequent sections.

1.2.1 Wormholes

Wormholes (WHs) are the hypothetical geometric structures that connect two different regions. The spacetime regions are connected via throat, which is a defining property of the WH. The two sides of the throat are defined as Zone-I and Zone-II, which are shown in Fig. 1.4 along with the throat. When the WHs connect our Universe with another Universe, they are called Inter-Universe WHs, whereas the Intra-Universe WHs connect two distant regions of same Universe (Visser, 1995). Historically, the notion of wormhole was first introduced by Flamm in 1916 (Flamm, 1916) and Einstein & Rosen (1935) proposed a bridge-like structure (Einstein-Rosen bridge), which connects two identical spacetimes. Subsequently, Wheeler introduced the idea of 'spacetime foam' (Wheeler, 1955; Fuller & Wheeler, 1962) and Misner & Wheeler (1957) first introduced the term 'wormhole'. The traversable Lorentzian WHs were first introduced by Morris & Thorne (1988). In general relativity, to construct such traversable WHs, one requires exotic matter at least in the neighbourhood of the WH throat. The stress-energy tensors of the exotic matter violate the null, weak, and strong energy conditions (Morris & Thorne, 1988), which are supported by the phantom energy (Lobo, 2005; Cataldo et al., 2009), the cosmological constant (Lemos et al., 2003; Rahaman et al., 2007). On the other hand, in some modified theories of gravity, such as Einstein-Gauss-Bonnet (Mehdizadeh et al., 2015), Born-Infeld gravity (Shaikh, 2018), Einstein-Cartan (Mehdizadeh & Ziaie, 2017), or higher order curvature gravity (Harko et al., 2013), the WH solutions are found to satisfy the energy conditions. In the following part, we highlight only one WH solution.

A. Kerr-like wormhole

Damour & Solodukhin (2007) proposed a WH solution (DSWH), that differs from the Schwarzschild BH by a dimensionless real parameter (β). The DSWH represents a spacetime where a throat connects two asymptotically flat regular symmetric space-

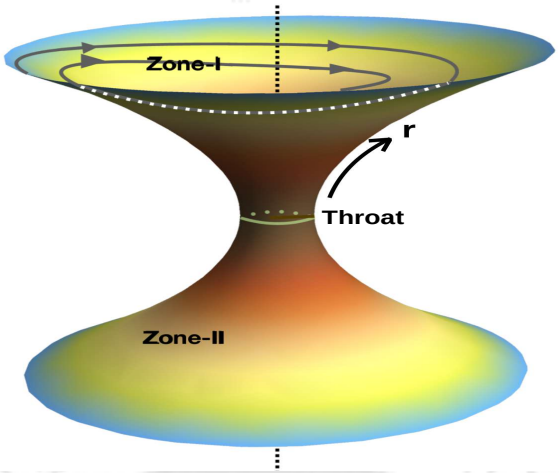

Figure 1.4: Artistic impression of a symmetric WH spacetime that connects Zone-I and Zone-II via a throat (Sen et al., 2024).

times. Extending this idea, the Kerr-like WH or Rotating DSWH (RDSWH) was introduced by Bueno et al. (2018). The spacetime interval of a stationary, axisymmetric, Kerr-like WH spacetime is given by,

$$\begin{aligned} ds^2 =& g_{\mu\nu}dx^\mu dx^\nu \\ =& g_{tt}dt^2 + g_{rr}dr^2 + 2g_{t\phi}dtd\phi + g_{\phi\phi}d\phi^2 + g_{\theta\theta}d\theta^2. \end{aligned} \tag{1.7}$$

Here, the throat radius is denoted by $r_{\rm Th}$, which connects the two sides of this WH. The Z_2 symmetry is imposed on the radial coordinate r and the radial domain is restricted to $r_{\rm Th} \leq |r| \leq \infty$. As, Kerr-like WH is a symmetric WH, we can write the metric components of both sides of the WH throat in Boyer-Lindquist coordinates as,

$$\begin{aligned} g_{tt}|_\pm &= -(1 - \frac{2M_{\rm WH}r}{\Sigma}) \quad , \quad g_{t\phi}|_\pm = -\frac{2M_{\rm WH}a_{\rm k}r\sin^2\theta}{\Sigma} \quad , \\ g_{rr}|_\pm &= \frac{\Sigma}{\Delta} \ , \ g_{\theta\theta}|_\pm = \Sigma \quad , \\ g_{\phi\phi}|_\pm &= (r^2 + a_{\rm k}^2 + \frac{2M_{\rm WH}a_{\rm k}^2 r\sin^2\theta}{\Sigma})\sin^2\theta, \end{aligned} \tag{1.8}$$

with $\Sigma = r^2 + a_{\rm k}^2\cos^2\theta$ and $\Delta = r^2 - 2M_{\rm WH}(1+\beta^2)r + a_{\rm k}^2$. Here, '+' and '−' denote Zone-I and Zone-II, respectively, as shown in Fig. 1.4. In the metric components (see Eq. (1.8)), $M_{\rm WH}$ is the mass of the WH, $a_{\rm k}$ is the spin parameter, and β is the dimensionless parameter, which characterizes the deviation from the Kerr spacetime. For $\beta = 0$, Kerr-like WH reduces to Kerr BH. However, unlike Kerr BH, the Kerr-like WH is not the vacuum solution of the Einstein's equations. The metric components are written using the geometrical unit as $G = c = 1$, and we use the sign convention of the metric as $(-,+,+,+)$. At the throat radius ($r_{\rm Th}$), $g^{rr} = 1/g_{rr} = 0$ and, it is located at $r_{\rm Th} = (1+\beta^2)M_{\rm WH} + \sqrt{(1+\beta^2)^2M_{\rm WH}^2 - a_{\rm k}^2}$. This spacetime contains two commuting Killing vectors $(\eta_t^\mu, \eta_\phi^\mu)$ along (t,ϕ) directions due to its stationary and axisymmetric

nature and the combined Killing vector is $\eta^{\mu} = \eta^{\mu}_{t} + \Omega_{\rm Th}\eta^{\mu}_{\phi}$ with $\Omega_{\rm Th}$ being the angular momentum of the WH at throat. At the throat ($r_{\rm Th}$), $\eta^{\mu}\eta_{\mu} = -ve$, which implies the Killing vector is time-like. Therefore, the time-like trajectory ($\eta^{\mu}\eta_{\mu} = -ve$) at $r > r_{\rm Th}$ remains time-like ($\eta^{\mu}\eta_{\mu} = -ve$) at $r = r_{\rm Th}$. Therefore, the time-like vector remains time-like all throughout the spacetime ($r_{\rm Th} \leq |r| \leq \infty$.) including at the throat ($r_{\rm Th}$). The asymptotic behaviors of energy momentum tensor components at infinity ($r \to \infty$) are obtained as,

$$\lim_{r\to\infty} T_{tt} = \frac{M_{\rm WH}}{r^5}\,, \lim_{r\to\infty} T_{rr} = -\frac{M_{\rm WH}}{r^3}\,, \lim_{r\to\infty} T_{\theta\theta} = \frac{M_{\rm WH}}{r}\,,$$

$$\lim_{r\to\infty} T_{t\phi} = -\frac{M^2_{\rm WH}}{r^4}\,, \lim_{r\to\infty} T_{\phi\phi} = \frac{M_{\rm WH}}{r}\,.$$

On contrary, near the throat radius ($r \to r_{\rm Th}$), these components are calculated as,

$$\lim_{r\to r_{\rm Th}} T_{tt} = \frac{M_{\rm WH}\beta^2}{r^5_{\rm Th}}\,, \lim_{r\to r_{\rm Th}} T_{rr} = -\frac{M_{\rm WH}\beta^2}{r^3_{\rm Th}}\,, \lim_{r\to r_{\rm Th}} T_{\theta\theta} = \frac{M_{\rm WH}\beta^2}{r_{\rm Th}}\,,$$

$$\lim_{r\to r_{\rm Th}} T_{t\phi} = -\frac{M^2_{\rm WH}\beta^2}{r^4_{\rm Th}}\,, \lim_{r\to r_{\rm Th}} T_{\phi\phi} = \frac{M_{\rm WH}\beta^2}{r_{\rm Th}}\,.$$

Therefore, the Kerr-like WH is not the vacuum solution of the Einstein equations. The radial pressure term T_{rr} appears as negative, which indicates a negative tension brane localized around the throat ($r_{\rm Th}$) and regulated by the deformation parameter β. Additionally, the Kerr-like WH is not the result of the cut-and-paste procedure of two identical geometries at $r_{\rm Th}$ instead, the deformation parameter β is introduced such that the spacetime remains regular everywhere, including the throat radius $r_{\rm Th}$. Moreover, The Kretschmann scalar, *i.e.*, $K = R^{\mu\nu\lambda\rho}R_{\mu\nu\lambda\rho}$ is finite at any point of the spacetime including the throat, which indicates that this wormhole does not possess any curvature singularity in the region $r_{\rm Th} \leq |r| \leq \infty$.

1.3 Compact objects in dark matter halo

At large scales, the Standard Model (Peskin & Schroeder, 1995) of particle physics fails in explaining the complete dynamical behavior of our cosmos. One of the most enduring mysteries in modern physics is to know the nature of the invisible matter, namely dark matter (DM). Since DM interacts only via gravity, its fundamental properties remain elusive. Bessel (1844) first proposed the concept of nonluminous matter from positional measurements of Sirius and Procyon. In the case of the Coma Cluster, Zwicky (1933, 2009) studied galaxy velocities using redshift measurements and a significant discrepancy between the visible (luminous) mass and the total gravitational mass was discovered by applying the virial theorem. The measured mass ($\mathscr{M}$) to luminosity (L) ratio ($\mathscr{M}/L$) ~ 400 in the cluster indicated a substantial abundance of 'dunkle Materie' (dark matter) overshadowing the visible matter (Zwicky, 1937). Further observational evidence came from galactic rotation curves (Rubin et al., 1978). Newtonian dynamics predicts the declination in orbital velocity with increasing radius, whereas observations show flat rotation curves far beyond the luminous edge of spiral galaxies (Sofue & Rubin, 2001). The Tully-Fisher relation (Tully & Fisher, 1977) also implies the presence of a vast amount of unseen mass extending beyond the

luminous disk. Moreover, it is now well established that most galaxies host SMBHs at their centers and such BHs are thought to originate from the gravitational collapse of small primordial density fluctuations in the early Universe within cold dark matter (CDM) framework (Volonteri, 2010). In the ΛCDM model, the Universe is composed of roughly 5% baryonic matter, 25% DM, and 70% dark energy (Betoule et al., 2014; Planck Collaboration et al., 2016; Alam et al., 2017; Abbott et al., 2018). Structure formation begins with small fluctuations generated during inflation and grows over time due to gravitational instability. The rapid growth of SMBHs observed at high redshifts can plausibly be explained by a combination of galaxy mergers and the gravitational influence of DM halos in which these systems are embedded (Mayer et al., 2007; Volonteri, 2010; Tulin & Yu, 2018). Furthermore, Cosmic Microwave Background (CMB) observations also indicate the presence of DM (Aghanim et al., 2020). Therefore, DM is not only essential for explaining galactic dynamics and structure formation but also remains a central ingredient to understand the evolution and fate of the Universe. Several experimental and observational missions, such as PAMELA (Payload for Antimatter Matter Exploration and Light-nuclei Astrophysics), Fermi-LAT (Fermi Large Area Telescope) are dedicated to detect DM. The recent breakthrough observations, such as the detection of GWs and the imaging of the BH shadow helps to detect DM indirectly. Various DM density profiles have been proposed to describe their distribution in galaxies and clusters. Some of widely used profiles and their relevance in modelling DM halos are briefly discussed below.

1.3.1 Hernquist profile

An analytic form of the density profile of many elliptical galaxies and bulges was a long-awaited investigation that can closely approximate the Vaucouleurs's $r^{1/4}$ law (de Vaucouleurs, 1948) for the observed luminosity profile. In this direction, Hernquist (1990) showed that DM halos are better described by a logarithmic slope for elliptical galaxies. The corresponding functional form of the density of this Hernquist profile is given by,

$$\rho_{\rm DM}(r) = \frac{M_{\rm halo}}{2\pi}\frac{a_0}{r}\frac{1}{(r+a_0)^3}\ , \tag{1.9}$$

where $M_{\rm halo}$ is the total mass and a_0 is the scale length. The mass inside a_0 is $M_{\rm halo}(a_0) = M_{\rm halo}/4$ and half mass $(M_{\rm halo}/2)$ is contained inside $r = (1+\sqrt{2})a_0$. This distribution function is known analytically for both isotropic and anisotropic velocity dispersions. The flattened rotation curves of globular clusters are well explained by this model formalism (Lynden-Bell, 1962). The fully analytic form of this DM profile helps to initialise N-body simulations of collisionless systems and galaxy mergers (Hernquist, 1993; Baes & Dejonghe, 2002). In BH dynamics, the central cusp of the Hernquist profile provides a realistic background for studying stellar interactions and BH growth.

1.3.2 Navarro-Frenk-White (NFW) profile

It is well known that the formation and evolution of galaxy clusters needs to consider the dynamically dominant DM and the hot X-ray emitting intracluster gas. Therfore, N-body simulations are used to evolve the intracluster medium. To address this, Navarro et al. (1995) carried out a series of N-body simulations to investigate the mass

distribution of DM halos in the non linear regime, where they used a non-radiative model of preheated gas in a CDM dominated Universe. These simulations comprised the realistic cosmological and hydrodynamical conditions for both collisional (gas) and collisionless (DM) components in three dimensions. Therefore, the clusters of varying mass at high resolution using a combined N-body and Smooth Particle Hydrodynamics (SPH) approach were re-simulated, and it as found that the radial profiles of DM distributions do not display uniform density cores but instead steepen gradually with radius. The functional form of the fitted density profile (NFW profile) is given by,

$$\rho_{\rm DM}(r) = \frac{\rho^0_{\rm DM}}{\frac{r}{a_0}\left(1+\frac{r}{a_0}\right)^2}\ , \tag{1.10}$$

where $\rho^0_{\rm DM} = 4\rho_{\rm DM}(a_0)$ is the characteristics density and a_0 is the scale radius of the halo. The logarithmic slope of the density function varies as $\simeq \frac{d\ln\rho_{\rm DM}(r)}{d\ln r}$. The high resolution N-body simulations (Navarro et al., 1997) of DM halos shows that $\rho^0_{\rm DM}$, and a_0 are strongly correlated. Though, the observed rotation curves of dwarf spiral and low surface brightness galaxies (Flores & Primack, 1994; Marchesini et al., 2002) show significantly shallower shape of the density profile at small scales than numerical simulations. To overcome this discrepancy in the CDM scenario, numerous alternative models have been suggested, such as warm (Colín et al., 2000), fluid (Peebles, 2000), fuzzy (Hu et al., 2000), self-interacting DM (Spergel & Steinhardt, 2000), or decaying (Cen, 2001).

1.3.3 Einasto profile

A detailed method for the composite models of galaxies was necessary to fit the observed photometric data and kinematic data of the rotation and velocity dispersion for spiral and elliptical galaxies. The galaxies can be considered as sum of young flat disk, thick disk, core, bulge, and halo and the mass-to-luminosity ratio should be in agreement with models. Keeping this in mind, Einasto (1965) proposed a DM profile, which is a three-dimensional representation of the two-dimensional Sérsic (1963) profile. This model provides an excellent fit with observed data for a wide range of DM halos in the galaxy (Einasto & Kutuzov, 1964; Einasto, 1969). The Einasto profile is characterized by a power-law logarithmic slope $\simeq -\frac{d\ln\rho_{\rm DM}(r)}{d\ln r} \propto r^{1/\hat{n}}$, where $\hat{n}$ is the Einasto index, which is a positive number. By integrating this, the DM density profile is expressed as,

$$\rho_{\rm DM}(r) = \rho^e_{\rm DM}\exp\left\{-d_{\hat{n}}\left[(r/r_e)^{1/\hat{n}}-1\right]\right\}. \tag{1.11}$$

At r_e, the mass density is $\rho^e_{\rm DM}$, and $d_{\hat{n}}$ is a constant that ensures r_e to contain half of the total mass. Later, Navarro et al. (2004) showed that $\hat{n}$ vary between $4.54 \leq \hat{n} \leq 8.33$ for halos ranging from dwarfs to clusters.

N-body simulations further confirmed that the outer regions of galaxies are well explained by $5 \leq \hat{n} \leq 8$ (Dhar & Williams, 2012), while Merritt et al. (2006) found that the Einasto model provides the best fit for $\hat{n} = 6$, $d_{\hat{n}} = 53/3$ based on a set of N-body DM halo simulations. Moreover, the Einasto model successfully explain the brightness of early-type galaxies and spiral galaxies (Graham et al., 2006), rotation curves of spiral galaxies (Chemin et al., 2011), lensing properties (Retana-Montenegro et al., 2012), and SPARC galactic rotation curve data (Acharyya et al., 2024).

1.3.4 Dark matter spike profile

The massive BH at the center of a galaxy can redistribute the DM distributions, which leads to a central cusp or spike by increasing the DM density. Gondolo & Silk (1999) first considered the adiabatical growth of a massive BH in pre-existing DM distribution. The timescale of growth is longer than the orbital timescale of a DM particle, which ensures the adiabatic invariants of the motion to be constant. Sadeghian et al. (2013) did the same calculations with a full relativistic prescription for the adiabatic growth of Schwarzschild BH in a Hernquist DM distribution (Eq. (1.9)). For a marginally bound particle with angular momentum per unit mass $L = 4M_{\rm BH}$, $r = 2r_{\rm Sh}$ is the unstable circular orbit in the Schwarzschild geometry, where $r_{\rm Sh}$ is the Schwarzschild radius. Therefore, a particle with $\mathcal{E} = 1$ and L may be captured by the BH after reaching at $r = 4M_{\rm BH}$, and the density of DM generically vanishes at $r = 2r_{\rm Sh}$, which makes a high density region. Moreover, Speeney et al. (2022, 2024) derived a semi-analytical model for $r \leq a_0$ and $r > a_0$ of a fully relativistic DM spike profile to fit the overdensities in the GW of the binary system, such as,

$$\rho_{\rm DM}(r) = \frac{M_{\rm halo}}{M_{\rm BH}^2} \times \left(\int_{4M_{\rm BH}}^{\tilde{r}_c} 4\pi r^2 \bar{\rho}_{\rm DM}(r) dr \right)^{-1} \bar{\rho}_{\rm DM}(r), \tag{1.12}$$

where,

$$\bar{\rho}_{\rm DM}(r) = \left(1 - \frac{4M_{\rm BH}}{r}\right)^{\alpha} \left(\frac{rM_{\rm BH}}{M_{\rm halo}a_0}\right)^{\beta} \left(1 + \frac{rM_{\rm BH}}{M_{\rm halo}a_0}\right)^{\varsigma}.$$

With $\tilde{r}_c$ is the cut off radius of DM distribution, $\alpha = 2.366$, $\beta = -2.320$, $\varsigma = -1.370$, which are determined by fitting a spike profile with halo mass $M_{\rm halo} = 10^4 M_{\rm BH}$ and $M_{\rm halo}/a_0 = 0.001$ (Speeney et al., 2024). Observationally, the significant dephasing in GW signals due to the dynamical friction (Cardoso et al., 2022a) and the velocity distributions of DM within spikes (Zhang & Tang, 2024) has been reported.

Therefore, based on the above discussions, it is evident that, the DM halos have a significant effect on the spacetime geometry which cannot be neglected.

1.4 Accretion process

Accretion is a process through which matter is accreted around the massive objects, such as WDs, NSs, BHs or ECOs. As matter falls into the compact object, the gravitational potential energy is transformed into thermal energy and radiation. Fig. 1.5 and Fig. 1.6 are the artistic impressions of the accretion in a binary system and active galactic nuclei (AGN), respectively. Though the stars generate energy through nuclear fusion, this is insufficient for luminous objects in the Universe, specifically for AGNs and quasars, to generate the enormous amount of energy. Therefore, accretion is considered as one of the powerful mechanisms responsible for the generation of high-energy radiations. By analyzing the observed high energy radiation, we can probe the nature of the compact objects and the properties of the accreted matter.

When the surrounding material with mass m is accreted onto a compact object with mass M_* and radius $\mathscr{R}$, the released gravitational potential energy is,

$$E_{\rm acc} = \frac{GM_*m}{\mathscr{R}}. \tag{1.13}$$

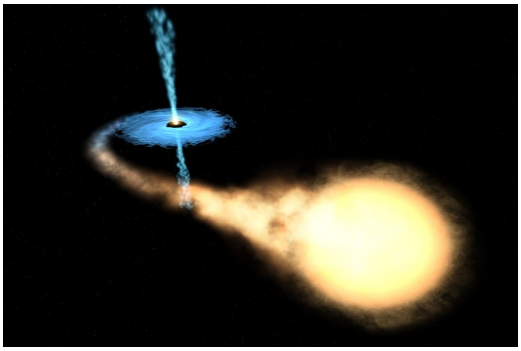

Figure 1.5: Accretion in a binary system. Source: ICRAR.

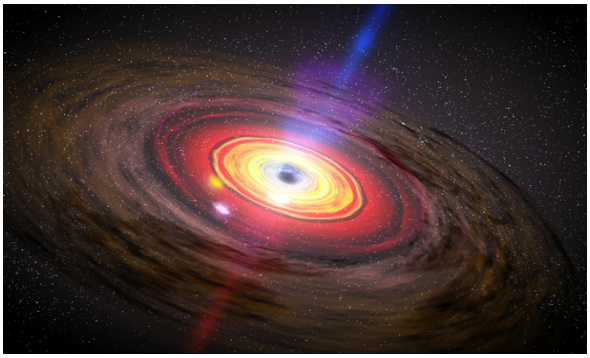

Figure 1.6: Accretion in active galactic nuclei. Source: Sky at Night Magazine.

For instance, if we take a simple non-rotating Schwarzschild BH of $M_{\rm BH} = 10M_{\odot}$, with characteristics radius $r_{\rm Sh} = \frac{2GM_{\rm BH}}{c^2} \simeq 30 \times 10^5$cm, then the energy released per unit accreted mass is $E_{\rm acc} \simeq 4.5 \times 10^{20}$erg g^{-1}. On the other hand, the energy release due to the burning of hydrogen of mass 1 g to convert into helium via nuclear fusion reaction is $E_{\rm nuc} \simeq 5.9 \times 10^{18}$erg g^{-1}. Therefore, it is evident that the energy released due to accretion is higher than the nuclear fusion energy, which also depends on the compactness parameter ($\frac{M_*}{\mathscr{R}}$) of the central object. For highly compact objects, we get higher energy due to the accretion. In addition, for a given $\frac{M_*}{\mathscr{R}}$, the luminosity (energy released per unit time) due to accretion depends on the mass accretion rate ($\dot{M} = \frac{dm}{dt}$) at which the mass is being accreted. The luminosity is expressed as,

$$L = \frac{GM_*\dot{M}}{\mathscr{R}}. \tag{1.14}$$

There is a limiting luminosity, called Eddington luminosity ($L_{\rm Edd}$), which plays an significant role in accretion physics. When the outward radiation pressure force via Coulomb interaction on the electron-proton pair *i.e.*, $F_{\rm rad} = \frac{L\sigma_T}{4\pi cr^2}$ (with L and σ_T being luminosity of the accreting source and the Thomson cross-section) nullify the gravitational force *i.e.*, $F_{\rm grav} = \frac{GM_*(m_p+m_e)}{r^2} \approx \frac{GM_*m_p}{r^2}$, (where, m_p and m_e are the proton and electron mass, respectively), we can define the Eddington luminosity as,

$$L_{\rm Edd} = \frac{4\pi GM_*m_p}{\sigma_T} \approx 1.39 \times 10^{38} \frac{M_*}{M_{\odot}} \text{ erg s}^{-1}. \tag{1.15}$$

The Eddington mass accretion rate ($\dot{M}_{\rm Edd}$) is related to the Eddington luminosity ($L_{\rm Edd}$) as,

$$L_{\rm Edd} = \varrho_e \dot{M}_{\rm Edd} c^2. \tag{1.16}$$

Here, ϱ_e is the efficiency factor, which measures how much the rest mass energy of the accreted material is being converted into the radiation energy. A typical assumption used in accretion physics is that $\varrho_e = 0.1$, *i.e.*, 10% of the rest mass energy is converted into radiation (Yuan & Narayan, 2014), as some of the matter may be swallowed by the compact objects. As a consequence, the Eddington mass accretion rate is obtained as $\dot{M}_{\rm Edd} \simeq 1.4 \times 10^{18} \frac{M_*}{M_{\odot}}$ g s^{-1}. The efficiency factor (ϱ_e) also depends on the properties of the compact objects. During the accretion, the gaseous system consists of free particles such as ions, electrons, and positrons. If the length scale ($\tilde{L}$) of the system is much larger than the mean free path ($\tilde{l}$) , *i.e.*, $\tilde{L} >> \tilde{l}$, it can be treated as a continuous fluid

medium. Therefore, we can define the fluid velocity (v), temperature (T), and density (ρ) to study the dynamics of the accretion by applying the laws of conservation of mass, momentum and energy. With the advent of advanced observational techniques, which include the full range of the electromagnetic spectrum from the radio to X-rays and γ-rays, the theoretical developments to understand the complex physics of accretion around the compact objects have become increasingly important day by day. Therefore, several accretion models have been developed over the years to explain the observed spectral properties (Zeldovich & Sunyaev, 1969; Shakura & Sunyaev, 1973; Shapiro et al., 1976; Sunyaev & Titarchuk, 1980; Fabian et al., 2012; Titarchuk et al., 2025) and timing features (Morgan et al., 1997; Kluzniak & Abramowicz, 2001; Remillard & McClintock, 2006; Pahari et al., 2017; Sreehari et al., 2019; Majumder et al., 2022) of XRBs or AGNs.

In the following sections, we discuss the key theoretical models to understand the underlying physics responsible for the generation of electromagnetic radiation in BH XRBs and AGNs.

1.4.1 Spherical accretion

Hoyle & Lyttleton (1939, 1940, 1941) demonstrated the accretion onto a star passing through an interstellar gas cloud. The gas distribution was considered to be steady, spherical, and pressureless as the generated heat would radiate away rapidly, which makes the temperature of the gas very low. In this framework, the mass accretion rate varies as $dm/dt \propto M_*^2\rho_\infty/v^3$, with M_*, ρ_∞ and v being the star's mass, the density of gas cloud at infinity, and the relative velocity between star and gas, respectively. However, the pressure can not be negligible for real scenarios. After that, Bondi & Hoyle (1944); Bondi (1952) investigated the spherical accretion of a gas cloud, for which the pressure is taken to be proportional to a power of the density of the gas, onto a star of mass M_*. Bondi (1952) modified the mass accretion rate as $dm/dt \propto M_*^2\rho_\infty/C_s^3$, where C_s is the sound speed of the gas, though the angular momentum and magnetic field were neglected here. In this scenario, accretion of the gas starts from a characteristic radius, which is known as the Bondi radius ($r_{\rm B} = \frac{GM_*}{C_s^2}$), where the thermal energy becomes less than the gravitational energy of the gas. In the Bondi flow, the gas's velocity changes its state from subsonic to supersonic as it passes through a sonic point and becomes a transonic flow. Beacuse of radiative inefficiency of this flow, it cannot explain the high energy radiation from AGN or quasars via accretion (Shapiro, 1973; Shapiro & Teukolsky, 1983). However, Bondi's work remains one of the key foundations of accretion theory. Later, the relativistic version of the Bondi flow has been studied by considering two fluids (electrons and ions) accretion flow around Schwarzschild BH (Michel, 1972).

As the accretion occurs either via Roche lobe overflow from binary companions or through tidal disruption of nearby stars, it is obvious that the infalling matter possesses non-zero angular momentum. This angular momentum governs the differential rotation within the accretion flow, which in turn gives rise to viscous forces. Viscosity transports angular momentum in the outward direction, which allows matter to gradually spiral inward around a compact object. As a result, the inflowing material follows a flattened rotating disk. The efficiency of released radiation due to accretion also enhance in presence of magnetic field via Synchrotron radiation along with Bremsstrahlung. Moreover, to explain the X-ray fluxes from the close binary systems

of Scorpius X-1 (Giacconi et al., 1962) and Cyg X-2 (Giacconi et al., 1967), an accretion disk model was proposed by Prendergast & Burbidge (1968). Subsequently, Lynden-Bell (1969) studied the properties of the accretion disk and the emitted spectra in quasars in the presence of the magnetic field. In the next subsection, we discuss the well-known standard disk model, where the matter contains non-zero angular momentum.

1.4.2 Standard disk model

Shakura (1973) analyzed the formation of an accretion disk around a relativistic star in a close binary system, and the well accepted standard disk was proposed by Shakura & Sunyaev (1973) (SS73). According to this model, matter with some angular momentum cannot fall radially onto a compact object. When the centrifugal force due to the angular momentum can balance the gravitational force, the matter starts rotating in circular orbits with Keplerian angular momentum. In this model, the radiative efficiency depends on the density of the matter and its mass accretion rate. Due to high radiative efficiency, the Keplerian disk becomes cool and geometrically thin ($H << r$, where H is the disk height and r is the radial coordinate). Therefore, the Shakura-Sunayev disk is also known as the cool disk. In this model, it is considered that the tangential stress ($T_{r\phi}$) is proportional to the total pressure ($P_{\rm tot}$), (*i.e.*, $T_{r\phi} = \alpha P_{\rm tot}$), which includes both the gas pressure and the radiation pressure and α is a dimensionless viscosity parameter. This provides the α-viscosity prescription, as $\tilde{\nu} = \alpha C_{\rm s} H$, where $\tilde{\nu}$ is the kinematic viscosity, and $C_{\rm s}$ is the sound speed. In the inner region, radiation pressure dominates over the gas pressure, and in the outer region, the disk is mostly gas pressure dominated. The SS73 disk is an optically thick disk and generates the multicolor blackbody spectrum. In this model, the luminosity reaches upto $10^{34} - 10^{36}$ erg s^{-1} for mass accretion rate $\dot{M} \approx 10^{-10} - 10^{-12}\ M_{\odot}$ yr^{-1}. As a result, the maximum surface temperature becomes $\sim 10^5 - 10^6$ K at the inner region of the accretion disk since the temperature varies as $T \sim r^{-3/4}$. After that, the relativistic version of the standard disk model was studied in subsequent works (Novikov & Thorne, 1973; Page & Thorne, 1974; Riffert & Herold, 1995). Since the advection terms are not included in the model, all the heat generated by viscosity is immediately radiated away and thermal equilibrium is created by balancing viscous heating ($Q_{\rm vis}$) and radiative cooling ($Q_{\rm rad}$), *i.e.*, $Q_{\rm vis} = Q_{\rm rad}$. This condition holds only for sufficiently low accretion rates. The inner regions of the SS73 disk are thermally unstable. The linear stability theory for BH accretion in a stationary state is constructed by Shakura & Sunyaev (1976). This SS73 disk terminates at the innermost stable circular orbit ($r_{\rm ISCO}$). Therefore, in the BH case, the flow cannot reach up to the horizon. Though this cool disk model successfully explains the thermal component of the observed spectrum, it fails to explain the non-thermal part. Moreover, observation shows that the BH spectra have a hard power law component, which is resulted from an optically thin plasma with a temperature $\gtrsim 10^9$ K. To address the above mentioned drawbacks of the SS73 model, other disk models were also proposed. Below, we briefly discuss some of those models.

1.4.3 SLE disk model

The observed X-ray spectra of Cygnus X-1 (Cyg X-1) (Agrawal et al., 1972; Tananbaum et al., 1972) suggest that there exist two distinct states. In the 'low state', the luminosity is low $\sim 10^{37}$ erg sec^{-1}, and it is seen in the low energy (< 10 keV) regime as well as in the high energy part (> 10 keV) of the spectrum. In the 'high state', the luminosity in the high energy part appears to remain the same while the luminosity in the low energy part increases by an order of magnitude comparable to that in the high energy part. Shapiro, Lightman and Eardley proposed an accretion disk model (known as the SLE model) around a BH to explain the observed low and hard spectra of Cyg X-1 (Shapiro et al., 1976). For nearly Eddington mass accretion rate ($\dot{M} \sim \dot{M}_{\rm EDD}$), the inner region of the cool disk becomes optically thin, and the corresponding temperature reaches up to $\sim 10^8$ K. Thorne & Price (1975) also demonstrated that, the observed high temperature and high energy can be explained if the inner region consists of high temperature, optically thin region, instead of low temperature optically thick region. Lightman & Eardley (1974) suggested that the secular instability may drive the disk from a cool state ($T \sim 10^6$K) to the hot, two-temperature (T_i denotes the ion temperature and T_e represents the electron temperature) flow in the inner region of the disk. Therefore, with the same boundary conditions for accretion flow with sub-Eddington mass accretion rate ($\dot{M} << \dot{M}_{\rm EDD}$), these two types of solutions coexist. The inner region of this disk is hotter and geometrically thicker than the SS73 disk. Moreover, the inner region of the disk is optically thin and unable to absorb the radiation, which makes it gas pressure dominated. Along with this, the dominant source of opacity is the electron scatterings, therefore, the turbulent viscosity heats most of the ions in the disk, yielding $T_i > T_e$. Another possibility is that, even though electrons and ions are heated equally, the electrons can cool much more efficiently, and due to high gravitational attraction and weak Coulomb interaction, the electrons and ions are unable to reach at thermal equilibrium in low density plasma. Therefore, we get $T_i > T_e$. Since the electron temperature can reach up to $T_e \sim 10^9$ K, and ion temperature becomes $T_i \sim 10^{12}$ K, the high energy (8-500 keV) radiation may be generated by inverse Comptonization of soft X-ray photons from the outer cool disk in the two-temperature inner region. Accordingly, the total luminosity is obtained due to inverse Comptonization by hot electrons and the cooling of electrons. The inner boundary of the cool disk lies at the point where the radiation pressure (p_r) and the gas pressure (p) become equal ($p_r = p$). Similar to the SS73 model, the inner hot region of SLE model also extends up to $r_{\rm ISCO}$.

Though this SLE model was successful in explaining the hard radiation, this model is thermally and viscously unstable. The small perturbations in the temperature increase density and decrease cooling efficiency. As a result, the gas heats rapidly and causes a thermal runaway in the system.

1.4.4 Slim disk model

We have seen that, for thin accretion disk, $\dot{M} < \dot{M}_{\rm Edd}$. Another kind of accretion disk model, which is known as the slim disk model, was presented by Abramowicz et al. (1988), where $\dot{M} \simeq \dot{M}_{\rm Edd}$. Unlike the radiatively efficient models (SS73 and SLE disk models), the radiative cooling becomes inefficient in this slim disk model. As a result, the viscously dissipated heat is being advected with the flow. Due to this advective flux, the instability disappears for a high accretion rate. As the mass

accretion rate increases and temperature of the flow increases due to advection, the initially thin disk ($H << r$) becomes thicker and remains slim ($H < r$) always. As the radiated energy is advected with the flow ,*i.e.*, photon diffusion time scale ($t_{\rm diff}$) > accretion timescale ($t_{\rm acc}$), which in turns makes the disk radiation pressure dominated. In addition to that, because of the high velocity of the flow, the disk becomes sub-Keplerian near the inner edge. It possesses a critical point where the flow velocity becomes nearly equal to the speed of sound. Abramowicz et al. (1988) investigated the slim disk model around a non-rotating BH using Paczyński & Wiita (1980) potential. After that, Lasota (1994) and Abramowicz et al. (1997) derived the equations of a slim accretion disk around a rotating Kerr BH. Watarai et al. (2000), and Mineshige et al. (2000) showed that for the galactic black hole (GBH) candidates, the disk luminosity is around $L_{\rm Edd}$ even if the mass accretion rate exceeds $\dot{M}_{\rm Edd}$. This infers the fact that radiative cooling is not balanced by viscous heating, and as a result, the excess energy is carried by accreting matter. The emitted radiation of these slim disks are multi-colour blackbody characterized by high temperature, $k_BT \sim$ a few keV (k_B being the Boltzmann constant). As $\dot{M}$ increases, the advection inside the disk increases, which affects the temperature profile and the spectra. Furthermore, the X-ray spectral properties and the high luminosity ($L \geq L_{\rm Edd}$) of the ultraluminous X-ray sources (ULX) can be well explained by the slim disk model considering the transonic flow (Watarai et al., 2001; Ghosh & Rana, 2021; Majumder et al., 2023). Ghoreyshi & Shadmehri (2018) also analyzed the stability of the slim disk in presence of a toroidal magnetic field and the radial viscous force via linear perturbation.

1.4.5 Advection dominated accretion flow

Ichimaru (1977) proposed advection dominated accretion flow (ADAF) model where radiative cooling is inefficient and most of the dissipated energy is advected into the BH, which makes it a radiatively inefficient flow. In this model, the two physically distinct spectral states (high and low states) exist for a given mass accretion rate. In addition to the feature of the standard disk model (Shakura & Sunyaev, 1973; Novikov & Thorne, 1973), viscous stresses due to magnetic fields in the differentially rotating plasma and gravitational interactions in the disk are considered. In this model, some portion of the energy is dissipated away via viscous stresses, and the rest of the energy increases the gas temperature. Depending on the initial condition at the disk's outer boundary, the disk becomes optically thin or thick. Therefore, transitions between the cooler and hotter states occur when the density and temperature of the gas near the disk's outer boundary cross critical threshold values. The cooler state is thermally stable, whereas the hotter state is thermally unstable. These transitions are led by the critical accretion rates and magnetic fields, which in turn affect disk luminosity and spectral properties. Within a specific radius, the flow temperature attains a single high temperature irrespective of the outer boundary conditions. This region emits hard X-rays via Comptonization, which can explain the persistent high energy emission observed in Cyg X-1. After that, Narayan & Yi (1994); Abramowicz et al. (1995); Narayan et al. (1997) showed that when the mass accretion rate is very low, the cooling processes become inefficient due to the low density of the accreted gas. As a result, the radiative timescale is much longer than the accretion timescale. Therefore, the energy is advected with the flow and lost into the BH. The advective accretion flow passes through a sonic point before falling supersonically into the BH with a zero

torque condition at the horizon. The ADAF is a poor radiator, and hence the ion temperature can reach $T_i \sim 10^{11-12}$K close to the compact objects. Therefore, for very high temperatures and $(H/r) \sim 1$, the radiative cooling term becomes negligible, and all the viscously generated heat is advected inward. Moreover, when the accreting gas has a very long cooling time scale than the accretion time scale ($t_{\rm cool} >> t_{\rm acc}$) (Narayan & Yi, 1994; Narayan & Yi, 1995b), the subset of the ADAF known as radiatively inefficient accretion flow (RIAF). In advective accretion flow, the temperature and pressure remain very high, which makes the angular velocity sub-Keplerian and radial velocity sufficiently large. As a result, the accretion timescale becomes low. Moreover, due to the weak coupling between electrons and ions via Coulomb interaction in the low density plasma, the flow becomes a two-temperature plasma with $T_e < T_i$ (Narayan & Yi, 1995b). In this model, the Bernoulli parameter is conserved, and the positive value of the Bernoulli parameter suggests that the accreting matter can flow in the outward direction with positive kinetic energy, which implies the possibility of the production of jet (Narayan & Yi, 1994) or outflow in the accreting system. Unlike the SLE model (Shapiro et al., 1976), the ADAF is a thermally stable solution (Narayan & Yi, 1995b; Yamasaki, 1997). After that, Abramowicz et al. (1995); Abramowicz et al. (1996) derived a complete set of equations for ADAF solutions around a rotating BH. For the ADAF flow, if strong convection is present in the high entropy flow, the equatorial inflow and bipolar outflow are found in this convection dominated accretion flow (CDAF) (Stone et al., 1999; Igumenshchev & Abramowicz, 1999; Narayan et al., 2000; Narayan et al., 2012).

1.4.6 Two component advective flow

As discussed in previous sections, numerous accretion models have been developed over the years to explain the spectral properties of compact objects. However, a unified framework that self-consistently accounts all the spectral features remains elusive. Observationally, the X-ray spectra from accreting compact objects generally consist of two parts, a multicolor blackbody emission and a power-law tail. The former is associated with a geometrically thin, optically thick Keplerian disk, while the latter originates from inverse Compton scattering of soft photons by hot electrons in a surrounding hot region, which is commonly referred to as the Compton cloud (Sunyaev & Titarchuk, 1980). The physical origin of this corona is a subject of extensive debate. Early suggestions include a magnetically dominated corona (Galeev et al., 1979) or a thermally driven hot gas corona situated above the disk (Haardt & Maraschi, 1993). Although a high density, high temperature static corona in the inner region of the accretion disk should be self-consistently generated. To account this, Chakrabarti & Titarchuk (1995) proposed a model where low angular momentum flow may be able to form this corona self-consistently. In this model, the accretion disk has two distinct components, Keplerian and sub-Keplerian, which are indicated by the name two component advective flow (TCAF). The accretion flow starts its journey from the outer edge with very negligible speed (subsonic speed), and becomes supersonic due to the high gravitational force close to the BHs. Moreover, the flow experiences a centrifugal barrier because of its angular momentum, and as a result, shock transition happens when the flow makes a sudden jump from supersonic to subsonic state. For the standing shock, at the shock location, the Rankine-Hugoniot shock conditions (Landau & Lifschits, 1975; Fukue, 1987), *i.e*, conservation of mass, momentum and energy flux, must be satisfied. The

shock-induced accretion solutions are thermodynamically preferable than the shock-free solution due to the higher entropy content (Chakrabarti, 1989b). Because of the shock transition, the post-shock region becomes hot and dense, and it behaves as a source of high energy radiation. This is called CENtrifugal pressure supported BOundary Layer (CENBOL) or post-shock corona (PSC). Due to the shock transition, the temperature and density in the post-shock region become higher than in the pre-shock region. Considering this shock transition location (r_s), this TCAF flow can be divided into three parts. An optically thick, geometrically thin and high viscous Keplerian disk is present on the equatorial plane for $r > r_s$, while the optically thin, low viscous sub-Keplerian and geometrically thick disk lies above and below that of the Keplerian disk. Along with this, there is a hot optically slim disk post-shock region for $r < r_s$. This TCAF model requires two accretion rates, one for the Keplerian disk ($\dot{m}_d$) and other for the sub-Keplerian halo ($\dot{m}_h$). The standing shock solutions for inviscid and viscous flows have been studied extensively for non-rotating and rotating BHs (Chakrabarti, 1990a; Chakrabarti, 1996a; Das et al., 2001b). Because of the excess temperature and density, the PSC acts as the source of hot electrons that reprocesses the soft photons from the pre-shock flow via inverse Comptonization and produce high energy radiations (Chakrabarti & Titarchuk, 1995; Mandal & Chakrabarti, 2005). Therefore, the PSC can explain the soft and hard parts of the observed spectra in various AGNs and GBHs (Rees, 1984; Grove et al., 1998; Smith et al., 2001; Melia & Falcke, 2001; Smith et al., 2002; Chakrabarti & Mandal, 2006; Mondal et al., 2014). For a given set of input parameters, the shock may be stable or unstable. The stable shock forms a standing shock, whereas the unstable shocks are oscillatory in nature. Other than spectral properties, the compact objects also exhibit variability in X-ray flux. These features in the power density spectra (PDS) (in the Fourier domain) are known as quasi-periodic oscillations (QPOs). These QPOs are commonly observed in the PDS of GBHs (Morgan et al., 1997; Markwardt et al., 1999; Kluzniak & Abramowicz, 2001; Aschenbach, 2004; Remillard & McClintock, 2006; Sreehari et al., 2019, 2020; Majumder et al., 2022). Molteni et al. (1996) demonstrated that a resonance condition occurs when the infall timescale of the matter within the post-shock region becomes comparable to the cooling timescale. This results in oscillation of the shock front, which modulates the luminosity of the inner accretion region and naturally gives rise to QPOs. This TCAF model also provides a compelling explanation related to the origin of QPOs, and in the subsequent works (Chakrabarti et al., 2004; Nandi et al., 2012; Garain et al., 2014; Molla et al., 2016; Debnath et al., 2016; Debnath, 2024) the shock oscillation frequencies are matched with the observed QPO frequencies, which indicate a key timing signature of the underlying accretion dynamics. Meanwhile, Nandi et al. (2012); Iyer et al. (2015); Nandi et al. (2018) reported that the PSC is possibly responsible for the spectral state transition in galactic XRB sources. The observed jets and outflows are another important feature of various astrophysical accreting systems (Jennison & Das Gupta, 1953; Mirabel & Rodríguez, 1994; Hjellming & Rupen, 1995). Therefore, Chakrabarti (1999a); Das et al. (2001a); Chattopadhyay et al. (2004); Jana et al. (2018); Debnath et al. (2021) studied the thermally driven outflows or radiatively driven jets using the TCAF model to show that the CENBOL is responsible for the production of the jet or outflows.

1.4.7 Shock-induced accretion solution

Although we have already discussed the shock transition and its importance in the TCAF model (see section 1.4.6), it is worth mentioning that the shock transition is very common in an astrophysical context. The shock transition happens in supernova explosions (Colgate, 1973; Weaver et al., 1974; Weaver, 1976; Morag et al., 2024), stellar wind (Anzer et al., 1976; Webb et al., 1985; Ioka et al., 2019; Ito et al., 2025), jets (Falle & Wilson, 1985; Mizuno et al., 2015; Atri et al., 2025) as well as accretion flow (McCrea, 1956; Thorne, 1973; Fukue, 1983). As in this thesis, we focus on the accretion flow and in the following discussion, we elaborate on the shock-induced accretion flow and its astrophysical relevance.

Various analytical studies have investigated the shock transition in hydrodynamical accretion flow. Fukue (1987) provided a full relativistic treatment of the accretion flow around BHs and NSs and pointed out that for the same boundary conditions, the positions of standing shocks in the accretion flow may be multiple due to the rotation and relativistic effects. Later, Yang & Kafatos (1995) investigated isothermal shocks and their stabilities in a fully relativistic regime around BHs and found that only one of the two possible shocks is stable. These shock solutions are also applied to explain the QPO behavior in GBH candidate like Cyg X-1. There are extensive works related to the shock that have been done in hydrodynamical systems around compact objects (Lu et al., 1999; Becker & Kazanas, 2001; Chakrabarti & Das, 2004; Das & Chakrabarti, 2004; Das, 2007; Dihingia et al., 2018; Patra et al., 2022; Singh & Das, 2024, 2025; Kumar et al., 2025). Moreover, shock solutions can also explain the origin of the QPOs in the GBH sources (Dihingia et al., 2019b; Majumder et al., 2023; Patra et al., 2024). After that, Le & Becker (2005); Becker et al. (2008) proposed the energy extracted from the accretion flow via isothermal shocks, which is a potential source for powering relativistic particles in advection dominated accretion flows and may account for the high radio luminosities observed in radio-loud AGNs and GBH candidates. The energy loss has also been modelled as proportional to the temperature jump across the dissipative shock front (Das et al., 2010, 2022). Therefore, the loss of kinetic power can be estimated from this energy loss, which is sufficient to supply the necessary energy budget for the formation of relativistic jets or outflows. Moreover, the formation of Jet/outflow due to shock has been studied in hydrodynamical systems by numerous authors (Chakrabarti, 1999b; Das & Chakrabarti, 1999; Chattopadhyay & Das, 2007; Das & Chakrabarti, 2008; Aktar et al., 2015; Kumar & Chattopadhyay, 2017; Aktar et al., 2017).

Similar to the hydrodynamic scenario, shock formation is also common in the magnetohydrodynamical (MHD) flows. Appl & Camenzind (1988) analyzed the relativistic MHD shock waves in jets and showed that the toroidal component of the magnetic field in the jet will strongly amplify in the shock transition. After that, Chakrabarti (1990b) presented self-consistent formation of the MHD shocks in the conical accretion and wind flows around a compact magnetic star. Later, Takahashi et al. (2002, 2006) extended previous studies for the formation of standing shock in accreting MHD plasma around rotating, stationary and axisymmetric BH magnetosphere and showed that the slow magnetosonic shock becomes strong due to frame dragging effects. As in hydrodynamics, shocked plasma in MHD flows can also power high energy emission. Numerous works have been done to study the properties of shocks in MHD flow (Fukumura, 2005; Das & Chakrabarti, 2007; Sarkar & Das, 2016; Sarkar & Das,

2018; Dihingia et al., 2020c; Mitra & Das, 2024; Jana & Das, 2024; Sarkar et al., 2025; Singh et al., 2025)

Moreover, numerical simulations provide compelling evidence for the shock formation, stability, and their importance in relativistic accretion and outflow scenarios. Nagakura & Yamada (2008); Ryu et al. (2011); Giri & Chakrabarti (2012); Das et al. (2014); Okuda & Das (2015); Lee et al. (2016); Kim et al. (2019); Garain (2025); Dihingia et al. (2025) demonstrated that shocks naturally arise due to centrifugal barriers in the case of relativistic hydrodynamical flows, and lead to compression and heating of the plasma. Similarly, in general relativistic magneto hydrodynamic (GRMHD) simulations, shocks can also form, and the presence of strong magnetic fields significantly affects shock and their properties (Nishikawa et al., 1997; Fukumura et al., 2007; Fragile & Meier, 2009; Dihingia et al., 2025; Meza et al., 2025). All these works showed the importance of the shock solutions in explaining the observational signatures of BHs.

1.5 Magnetized accretion flow

Magnetic fields are ubiquitous in all astrophysical systems. Early studies demonstrated that the dynamics of gas and stars are different, which cannot be explained by considering magnetic force along with the gravitational force (Wentzel, 1963). After that, radio observations (Morris & Berge, 1964) suggest the existence of a large scale magnetic field in the disk of the Galaxy. Parker (1958, 1966) showed that solar wind draws out the magnetic field lines in a nearly radial direction and the field lies mostly within the galactic plane with a strength of $10^{-6} - 10^{-5}$ G. Moreover, Weber & Davis (1967) developed a steady state model for the solar wind considering the effects of pressure gradients, gravitational attraction, and magnetic forces, and showed that magnetic torque has a significant contribution to angular momentum loss.

The magnetic field also plays a critical role in the dynamics and observational characteristics of the accretion flow around compact objects (Pudritz, 1981; Dadhich & Wiita, 1982; Wiita et al., 1983). Magnetic fields in accretion flow may originate from the companion star, the interstellar medium, or may be amplified through dynamo processes inside the disk (Torkelsson & Brandenburg, 1994; Khanna & Camenzind, 1996; Balbus & Hawley, 1998a,b). Through the dynamo process, the small scale turbulence twists, stretches, and folds magnetic field lines, which leads to the organization and amplification of magnetic fields in the accretion disk (Parker, 1955; Moffatt, 1978; Krause & Raedler, 1980; Molchanov et al., 1985). Therefore, the initially homogeneous magnetic fields, which are frozen into the plasma due to ideal magnetohydrodynamic conditions, experience dynamic evolutions as accreted matter spirals inward. Due to frame dragging effects, the magnetic fields become higher around Kerr BHs than the Schwarzschild BHs, which in turn affect the Synchrotron radiation and offer a promising way to distinguish these two BHs (Bisnovatyi-Kogan & Ruzmaikin, 1974, 1976). After that, Shakura & Sunyaev (1973) first conceptualized the Maxwell stresses as α-viscosity prescription, which may dominate angular momentum redistribution within accretion disks. Later, Eardley & Lightman (1975) developed a self-consistent model of magnetic viscosity and Ichimaru (1976) showed the turbulence within the plasma arises due to differential rotation, which dissipates energy via magnetic viscosity. After that, Balbus & Hawley (1991); Hawley & Balbus (1995) connected the turbulent viscosity with magneto rotational instability (MRI),

which arises due to coupling between the magnetic field and differential rotation in the accretion disk. Moreover, Blandford & Znajek (1977) showed that rotating BH can generate relativistic jets via frame dragging effect in the ergosphere, while Blandford & Payne (1982) demonstrated that centrifugally driven outflows can be produced if the poloidal field is inclined by less than 60° to the disk. After that, numerous studies show that magnetic fields may drive jets and outflows in AGNs and XRBs (Miller et al., 2006; Takasao et al., 2022; Jana & Das, 2024). In addition to that, magnetic reconnection contributes to the disk heating (Kawanaka et al., 2005; Machida et al., 2006; Blaes et al., 2007; Ripperda et al., 2020; Camilloni & Rezzolla, 2024; Shen & YuChih, 2025). Global simulations show toroidal fields dominate over poloidal ones inside the disk (Stone & Norman, 1994; Hawley, 2001; Kato et al., 2004; Hirose et al., 2004; McKinney & Gammie, 2004; Begelman & Pringle, 2007; Mishra et al., 2020). Based on these considerations, several attempts were made to study the self-consistent global MHD accretion solutions around BHs (Akizuki & Fukue, 2006; Machida et al., 2006; Begelman & Pringle, 2007; Oda et al., 2007, 2010; Samadi et al., 2014; Sarkar & Das, 2016; Sarkar & Das, 2018). Recently, Mitra et al. (2022) developed a GRMHD formalism to probe steady-state magnetic field configurations around rotating BHs. Furthermore, the Event Horizon Telescope (EHT) collaboration captured the first images of the SMBHs at the center of Messier 87 (M87*) (Collaboration, 2019a) and the Milky Way galaxies (Sagittarius A* or Sgr A*) (Collaboration, 2022a). By performing very long baseline interferometry (VLBI) at a wavelength of 1.3 millimetres, the EHT collaboration observed the Synchrotron emission from near horizon scales. EHT collaboration revealed the asymmetric bright emission ring of M87* with a diameter of $42 \pm 3\mu$as (Collaboration, 2019a,b,c,d,e,f; Collaboration et al., 2021; Akiyama et al., 2021) of mass $\approx 6.5 \times 10^9 M_\odot$. EHT collaboration also captured a bright, thick ring of Sgr A* with a diameter of $51.8 \pm 2.3\mu$as (Collaboration, 2022a,b,c,d,e,f) of mass $\approx 4 \times 10^6 M_\odot$. By comparing the observed polarized image with GRMHD simulations, it has been inferred that the polarization pattern arises due to the ordered magnetic fields of the magnetically arrested disks (MAD) around M87* (Akiyama et al., 2021) and Sgr A* (Akiyama et al., 2024a). The degree and orientation of linear polarization can impose strong constraints on the BH parameters and the magnetic fields of the surrounding medium. Therefore, the polarized Synchrotron emission due to relativistic plasma serves as a powerful tool to shed light on the magnetic field structure as well as accretion dynamics around the BH.

1.6 Tilted accretion disk

The angular momentum of the accretion disk may not always be aligned with the spin of the compact object. When the directions of these two angular momentum are misaligned, a tilted accretion disk forms. Such disks are subject to the relativistic frame dragging effect, which is known as the Lense-Thirring (LT) precession (Lense & Thirring, 1918). Fig. 1.7 illustrates a schematic diagram of a tilted accretion disk around a rotating compact object, where the directions of spin and angular momentum of the disk are misaligned by the tilted angle ($\tilde{\beta}$). The LT precession frequency decreases with the radius and causes differentially precessing rings within the disk, which twist and warp over time. Therefore, for sufficiently large misalignment angle, the disk may undergo tearing (Nixon et al., 2012). The process by which the inner

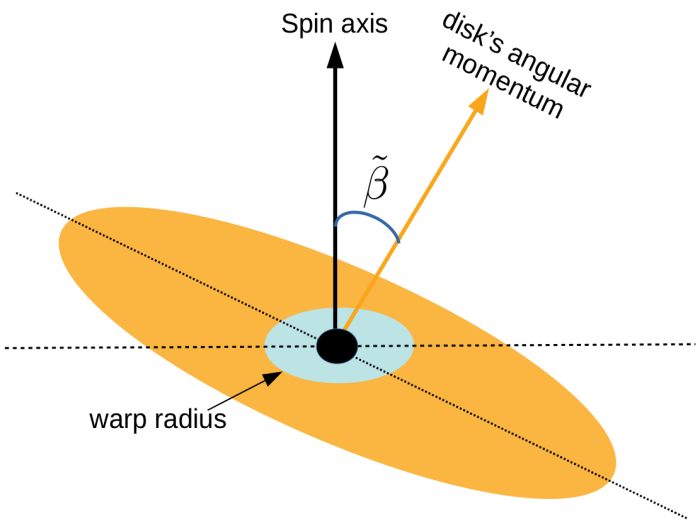

Figure 1.7: A schematic diagram of a tilted accretion disk.

disk becomes aligned with the rotating compact objects is referred to as the Bardeen-Petterson (BP) effect (Bardeen & Petterson, 1975). The BP effect arises due to the competition of the LT precession torque and the viscous torque. Close to the compact objects, the LT torque dominates over the viscous torque, whereas the viscous torque dominates at large distances. Therefore, the inner part aligns along the equatorial plane due to the strong LT effect, whereas the outer part of the disk remains tilted and a twisted transition region forms between the two above mentioned regions. The transition from misaligned to aligned regions occurs via a characteristic BP radius ($r_{\rm BP}$). Bardeen & Petterson (1975) model has been modified by numerous authors to address some inconsistencies (Petterson, 1977a,b; Hatchett et al., 1981; Petterson et al., 1991). After that, Papaloizou & Pringle (1983) first derived the equations for a viscous, tilted accretion disk under external forces by taking into account two kinematic viscosities related to the shear within the plane (ν_1) and perpendicular to the disk (ν_2). Later, Pringle (1992) introduced a generalised formalism of the warped disk equations and Ogilvie (1999) expanded it to the nonlinear regime for any arbitrary warp amplitudes. According to Bardeen & Petterson (1975), the inner disk will be aligned with the equatorial plane while the outer part remains tilted (Pringle, 1992; Scheuer & Feiler, 1996), if the contribution of the inner disk is neglected. On the other hand, Chakraborty & Bhattacharyya (2017); Banerjee et al. (2019a) solved the full warp equation and addressed that the inner disk may be tilted or not for Kerr BH, depending on the spacetime properties. Observational diagnostics such as broad relativistic iron Kα lines and QPOs probe accretion processes in the strong gravity regime. The bound atoms in the disk produce the prominent iron Kα line at ~ 6.4 keV when the emission irradiates the disk. Though, the precessing disk produces a unique characteristic rocking of the iron line (Ingram & Done, 2012b). This precessing disk causes Doppler-shifted iron lines, which appear blue and red while illuminating the approaching and receding sides of the disk, respectively. Moreover, the observed low and high frequency QPOs are often interpreted using the Relativistic Precession Model (RPM) (Stella & Vietri, 1998, 1999; Morsink & Stella, 1999), where small radial and vertical perturbations yield epicyclic frequencies (ν_r, ν_θ). With the help of

Keplerian frequency (ν_ϕ), LT precession frequency ($\nu_{\rm LT} = \nu_\phi - \nu_\theta$) related to the type-C QPO (low frequency QPO) and periastron precession frequency ($\nu_{\rm per} = \nu_\phi - \nu_r$) can be calculated. In this model, the upper and lower high frequency QPOs correspond to ν_ϕ and $\nu_{\rm per}$, respectively. These frequencies depend on the radius of the QPO origin ($r_{\rm QPO}$) and the parameters of compact objects. As a result, RPM model successfully explains the observed QPO frequency for NSs such as GX 17+2 (Stella & Vietri, 1998), XTE J1807-294 (Biemond, 2007), and BHs such as GX 339-4 (Motta et al., 2011), XTE J1550-564 (Ingram & Done, 2012a), GRO J1655-40 (Motta et al., 2014). GRMHD simulations (Dexter & Fragile, 2011) further show that tilted flows naturally produce light curve variability and QPOs via geometric modulations. Jet precession provides another evidence of disk warping and has been observed in sources like GRO J1655-40 (Hjellming & Rupen, 1995), OJ 287 (Britzen et al., 2018), and M87 (Cui et al., 2023). This disk and jet precession in tilted disk are also supported by GRMHD simulations (Liska et al., 2018; Nolting et al., 2023). Furthermore, in AGNs, tilted disks can influence the SMBH spin evolution (Li et al., 2013; Li et al., 2015). Various AGNs such as NGC 4258 and NGC 1068 also show the warped disk structures (Lawrence & Elvis, 2010; Hayasaki et al., 2015) and misaligned jets (Cecil et al., 2000; Raban et al., 2009), which are consistent with the theoretical predictions.

In summary, tilted accretion disks and their associated precession phenomena, which are driven by frame dragging, viscosity, and magnetic torques, play important roles to probe the strong gravity regime.

1.7 Thesis overview

Near the compact objects, the spacetime curvature is very high, and the Newtonian gravity fails to mimic the spacetime geometry. This led to propose effective potentials around compact objects to mimic the relativistic effects in the accretion flow. Paczyński & Wiita (1980) first proposed a pseudo-Newtonian potential around a Schwarzschild BH to study the accretion dynamics (Matsumoto et al., 1984; Lu, 1985; Abramowicz et al., 1988; Chakrabarti, 1989a; Chakrabarti & Das, 2004). Later, Nowak & Wagoner (1991) generalized the approach for weakly magnetized NSs and slowly rotating BHs, while several pseudo-potentials for Kerr spacetimes also proposed. Among them, Chakrabarti & Khanna (1992), Artemova et al. (1996), Peitz & Appl (1997), Semerák & Karas (1999), and Mukhopadhyay (2002) reproduced key relativistic features such as ISCO, disk structure, and orbital dynamics within $\sim 10-20\%$ accuracy. After that, Chakrabarti & Mondal (2006) proposed a pseudo-Kerr potential for the accretion flow onto a Kerr BH within $-1 < a_{\rm k} \leq 0.8$. However, these prescriptions fail for highly spinning BHs with spins ($a_{\rm k} > 0.9$), such as Sgr A* (Akiyama et al., 2024c; Daly et al., 2023), M87* (Collaboration, 2019e; Tamburini et al., 2020), GRO 1915+105 (McClintock et al., 2006; Mills et al., 2021), and Cyg X-1 (Fabian et al., 2012; Zdziarski et al., 2024). To address this, Dihingia et al. (2018) developed an effective potential or the DDMC potential around a general stationary and axisymmetric spacetime, which is applicable for relativistic hydrodynamics onto both non rotating and highly spinning compact objects. Moreover, to describe the relativistic flows around the compact objects, a proper description of the EoS is required to incorporate their proper thermodynamic state. In relativistic hydrodynamics and MHD, the fluid is characterized by relativistic speed ($v \sim c$), very high temperature, where the proper choice of EoS is

necessary. A fluid is thermally relativistic if the thermal (k_BT) is greater than the rest mass energy (mc^2). Therefore, the temperature and fluid compositions determine its thermal state. Moreover, to describe such trans-relativistic fluid, the ideal EoS with a fixed adiabatic index Γ ($= c_p/c_v$, where c_p and c_v are the specific heats at constant pressure and constant volume) is not sufficient (Chandrasekhar, 1939). In an accretion disk, the flow is expected to be in the thermally relativistic domain (*i.e.*, $\Gamma \to 4/3$) at the inner part of the disk, whereas it remains thermally non-relativistic (*i.e.*, $\Gamma \to 5/3$) at a distance far away from the compact objects (Frank et al., 2002). Therefore, relativistic EoS for a single-component fluid (Ryu et al., 2006), and for a multi-component fluid (electrons, positrons, and protons) (Chattopadhyay & Ryu, 2009) was derived to account the thermal state of the accreted matter.

In accretion disks around compact objects, the centrifugal barrier can trigger discontinuous shock transitions if the shock conditions are satisfied. Such shock-induced accretion solutions are thermodynamically favoured due to higher entropy content and can explain the observed high energy radiation, QPOs, jets, and outflows. Therefore, we explore a class of shock-induced accretion solutions around a general class of stationary and axisymmetric vacuum solutions of Einstein's equations, described by the KTN spacetime. Theoretically, the ECOs may also exist along with the compact objects in the Universe. Therefore, BHs are not the only accreting objects, ECOs can also accrete matter from the surrounding medium. In this regard, we study the relativistic accretion flow around Kerr-like WHs using the DDMC potential (Dihingia et al., 2018). Moreover, according to the ΛCDM cosmology, there are roughly 5% visible matter, 25% unseen or dark matter, and 70% dark energy, and the SMBHs may originate from the gravitational collapse of small primordial density perturbations in the highly dense DM region in the early Universe. In addition, it is well known that the SMBHs reside at the center of most galaxies. As the DM doesn't interact electromagnetically, it can influence the baryonic accretion flows near SMBHs gravitationally. Therefore, we comparatively discuss the relativistic accretion flow around a galactic SMBH surrounded by various types of anisotropic CDM halo. Furthermore, very recently, the EHT captured the polarised image of Sgr A* (Collaboration, 2022a,b,c,d,e,f; Akiyama et al., 2024b,d). Combining GRMHD simulations with the ray-tracing method, the analysis favoured a MAD scenario around a spinning black hole with $a_{\rm k} \sim 0.94$ (Collaboration, 2022e). With the help of these simulations, the polarimetric observations gave a constraint on magnetic field strength at different radii, such that, 26^{+3}_{-4} G at 7.3 r_g, 67^{+8}_{-9} G at $4r_g$ and 560^{+80}_{-80} G near the horizon (Akiyama et al., 2024b,d). Motivated by this, we analyze accretion dynamics in Kerr spacetime by solving the ideal GRMHD equations in steady state to reproduce the EHT-constrained magnetic field structure around Sgr A* following Mitra & Das (2024). In all these cases, we use relativistic EoS (Chattopadhyay & Ryu, 2009) for the accreting matter. Interestingly, the orbital plane of infalling matter undergoes LT precession due to frame dragging (Lense & Thirring, 1918) in a tilted or misaligned disk. The inner disk may be tilted or not, depending on the spacetime properties (Chakraborty & Bhattacharyya, 2017; Banerjee et al., 2019a). Moreover, GRO J1655-40 was identified as a candidate, which is better described by KTN spacetime (Chakraborty & Bhattacharyya, 2018), and there is also an indication of a warped disk. Finally, we investigate tilted thin accretion disks around KTN BHs to explore the contribution of both spin ($a_{\rm k}$) and NUT parameter (n) on the orbital plane precession.

In the following sections, we summarize the working chapters of the thesis. Each

Chapter contains the highlighted overviews that contribute to the overall understanding of relativistic accretion flow around compact objects.

1.7.1 Chapter 2

In this Chapter, we present the global solutions of low angular momentum, inviscid, and advective accretion flow around the KTN BH in the presence and absence of shock waves. We obtain these solutions by solving a set of relativistic hydrodynamics equations that govern the relativistic accretion flow in KTN spacetime, which is characterized by the Kerr parameter ($a_{\rm k}$) and NUT parameter (n) along with its mass ($M_{\rm BH}$). For the sake of completeness, we use the relativistic EoS with varying adiabatic index (Γ) to describe the thermodynamic state of the hot accreting matter. Depending upon the input parameters, such as energy ($\mathcal{E}$), angular momentum (λ), $a_{\rm k}$ and n, the flow possesses either single or multiple critical points. During accretion, rotating flow experiences a centrifugal barrier that triggers the discontinuous shock transition when there are multiple critical points and the relativistic Rankine-Hugoniot shock conditions (Landau & Lifschits, 1975; Fukue, 1987) are satisfied. In reality, shock-induced accretion solutions exhibit greater physical viability over shock-free solutions as the former possess high entropy at the inner edge of the disk. Due to the shock compression, the post-shock flow (or PSC) becomes hot and dense, which serves as a source of high energy radiation through the inverse Comptonization after reprocessing the soft photons from the comparatively cooler pre-shock flow. The PSC is characterized by the shock properties, such as shock location (r_s), compression ratio (R), which is defined as the density jump and shock strength (S), which is interpreted as the temperature jump across the shock front. We conduct a detailed analysis of their dependency on $\mathcal{E}$ and λ of the flow as well as black hole parameters ($a_{\rm k}, n$). Through systematic analysis, we identify the effective region of the parameter space in $\lambda - \mathcal{E}$ plane that admits the shock solutions. This implies that shock solutions are not the isolated solutions, and they continue to form for a wide range of flow parameters. Our analysis reveals that $a_{\rm k}$ and n act oppositely to determine the shock properties and shock parameter space. Moreover, we compute the maximum NUT parameter ($n^{\rm max}$) for the shock solutions as a function of $a_{\rm k}$ and it is found that for KTN BH, the shock solutions persist with $a_{\rm k} > 1$ which is absent for Kerr BH $a_{\rm k} < 1$. Finally, we calculate the disk luminosity (L) by incorporating the thermal Bremsstrahlung emission coming from the hot accreting plasma. Our results show that the accretion flows containing shocks exhibit substantially higher luminosity compared to the shock-free solutions, as the shock transition enhances the density and temperature in the post-shock region.

1.7.2 Chapter 3

In this Chapter, we investigate the relativistic, low-angular momentum, inviscid advective accretion flow in a stationary axisymmetric Kerr-like WH spacetime, which is a solution of the Einstein field equations and characterized by the source mass ($M_{\rm WH}$), spin parameter ($a_{\rm k}$), and the dimensionless parameter (β). The WH is characterized by a unique characteristic radius called the throat ($r_{\rm Th}$), which connects the two regions of the same spacetime of two different spacetimes. This WH spacetime is regular for $r_{\rm Th} \leq r \leq \infty$ on both sides of the throat, and the WH is symmetric in nature. Keeping this in mind, we self-consistently solve the set of governing equations describ-

ing the relativistic accretion flow around a Kerr-like WH in the steady state. For the first time, we derive all the possible global transonic accretion solutions around this WH, which includes O-type, A-type, W-type, and I-type solutions. We also find that subsonic flows are also possible in this scenario, along with transonic flows. We study the properties of dynamic and thermodynamic flow variables such as velocity, temperature, pressure, density, and entropy of the accretion flow. This suggests that the transonic flows are more viable than the subsonic flows because of their higher entropy. Furthermore, we examine how the nature of the accretion solutions alters due to a change of the model parameters, namely energy ($\mathcal{E}$), angular momentum (λ), $a_{\rm k}$, and β. After that, we separate the parameter space in $\lambda - \mathcal{E}$ plane based on the nature of the accretion flow and demonstrate the modification of the parameter space by varying $a_{\rm k}$ and β. Moreover, we retrace the parameter space in $a_{\rm k} - \beta$ plane that allows accretion solutions containing multiple critical points. Finally, we calculate the disk luminosity (L) considering free-free emissions and observe the strong dependency of L on $a_{\rm k}$, β, $\mathcal{E}$, and λ. As the WH parameters ($a_{\rm K}$ and β) increase, the luminosity of I-type and O-type solutions also becomes higher. Notably, the I-type solutions always possess higher luminosity than the O-type solutions. Finally, we demonstrate that our model successfully explains the luminosity of the compact X-ray source Cygnus X-3, a mysterious compact X-ray source, during its hypersoft state. Based on this finding, we mention that the present model formalism offers valuable insights for understanding how accretion flows around WH to generate the powerful emissions observed from compact X-ray sources.

1.7.3 Chapter 4

In the previous two Chapters, we have studied the relativistic accretion flow around a bare BH and a WH. We have also discussed previously that the surrounding environment of compact objects is expected to play a crucial role in understanding various astrophysical phenomena around them. Therefore, in this Chapter, we study the relativistic, low angular momentum, inviscid, and advective hot accretion flow onto a galactic SMBH surrounded by CDM halo. We follow the numerical framework to model the spacetime around a static spherically symmetric Schwarzschild BH, which is embedded in various relativistic DM halo distributions. For a comprehensive analysis, we consider different types of DM density distribution (radial distributions), such as Hernquist, NFW, Einasto, and an adiabatically growing DM spike profile from the Hernquist type. We restrict ourselves that the BH mass ($M_{\rm BH}$) is smaller than the mass of the halo ($M_{\rm halo}$) and the characteristic length scale of the halo (a_0) is larger than $M_{\rm halo}$ and $M_{\rm BH}$, *i.e.*, $M_{\rm BH} \leq M_{\rm halo} \leq a_0$. Additionally, the outer edge of the accretion disk ($r_{\rm edge}$) is smaller than a_0 ($r_{\rm edge} \leq a_0$). Therefore, by solving the governing hydrodynamic equations, we study the effect of the DM halo on the solution topologies and properties of the accretion flow in detail. We observe that the presence of a DM halo shifts the critical point location of the transonic flow to smaller radii compared to the bare Schwarzschild BH. After that, we compare the parameter space for multiple critical points in $\mathcal{E} - \lambda$ plane and $M_{\rm halo} - a_0$ plane for all types of DM halo with that of Schwarzschild BH. Finally, we calculate the Bremstrahlung luminosity for the I-type solutions, which provides the highest luminosity compared to the other type solutions. Our results show enhancement of disk luminosity in the presence of DM, depending on the nature and properties (halo mass and compactness) of the DM distribution.

The spectral energy density also shows a significant deviation from that of the vacuum Schwarzschild BH. From our results, it is evident that the dominant contribution to the disk luminosity for compact and massive halos arises from the inner regions of the accretion flow. Consequently, our analysis indicates that luminosity measurements can serve as an effective probe of the underlying DM density spike.

1.7.4 Chapter 5

Till now, we have studied the relativistic hydrodynamic flow around various compact objects and exotic compact objects. The magnetic field is ubiquitous in the astrophysical scenario, and the recent prediction of the magnetic field strength by EHT collaborations motivates us to study the general relativistic magnetohydrodynamic (GRMHD) accretion flow around the Kerr BH. Therefore, in this Chapter, we investigate the properties of steady, advection-dominated accretion flows around a Kerr BH in a GRMHD framework. In this regard, we solve the set of governing equations describing the ideal GRMHD accretion flow in the steady state to provide a comprehensive understanding of the behavior of magnetized plasma in the vicinity of a rotating BH. The accretion solutions are obtained for a set of constant input flow parameters, including energy ($\mathcal{E}$), angular momentum ($\mathcal{L}$), magnetic flux (Φ) and isorotation parameter (I), which uniquely characterize the behavior of magnetized plasma. By systematically varying these parameters, we generate a set of solutions that illuminates the physical environment surrounding the Kerr BH. Utilizing this model framework, we aim to obtain the global GRMHD solutions in the steady state that are consistent with the reported magnetic field strength by the EHT collaboration for Sgr A* within $\pm10\%$ error at $7.3r_{\rm g}$ and $4r_{\rm g}$. We portray one such representative GRMHD accretion solution with its hydrodynamic and magnetohydrodynamic properties. Furthermore, we conduct a systematic investigation across the parameter space spanned by the magnetic flux (Φ) and the angular momentum ($\mathcal{L}$) to evaluate the broader applicability of our findings. This identifies a complete set of global accretion solutions that maintain consistency with the EHT-constrained magnetic field strengths at both radii. These findings indicate that the present study contributes a self-consistent theoretical framework based on GRMHD accretion flows that validates and complements the EHT findings in explaining the dynamics of the magnetized accretion flows around our galaxy's central SMBH.

1.7.5 Chapter 6

In all previous Chapters, we have extensively studied the hydrodynamic and magnetohydrodynamic flow around compact objects, where the direction of the compact objects' spin and the directions of the disk's angular momentum are aligned. However, in the astrophysical scenario, these two directions may be misaligned. Therefore, in the misaligned disk, the orbital plane of the test particle in the accretion disk precesses due to the LT effect. On that account, in this Chapter, we study a tilted, thin inner accretion disk around a slowly spinning KTN BH that contains a small GMM or NUT parameter. In our analysis, we consider the contribution from the inner accretion disk as well as the outer part. By solving the governing equations, we calculate the radial profile of a tilt angle up to the innermost stable circular orbit (ISCO). In the tilted disk, there is always a tug-of-war between the Lense-Thirring torque and the

viscous torque. Therefore, depending on the black hole parameters ($M_{\rm BH}, a_{\rm k}, n$) and the viscosity (ν_2), the disk may be tilted or aligned to the spin of the BH at the inner edge. We show that in the case of the KTN BH, the LT precession does not monotonically increase for lower radial coordinates, unlike a Kerr BH. We also notice that for every combination of $a_{\rm k}, n$ and $M_{\rm BH}(\nu_2)$, there is a specific value of $\nu_2(M_{\rm BH})$, such that the disk will remain misaligned above (below) that value. Therefore, our study of the radial profile of the tilted disk around a KTN BH could be useful in probing the strong gravity regime and could also give indirect evidence for the existence of GMM in nature.

1.7.6 Chapter 7

Following the above discussions, we conclude the thesis with the summary and key findings. Therefore, this Chapter contains the overall conclusion of the thesis. Furthermore, we propose some possible future works based on our present works.

Chapter 2

Properties of shock-induced accretion flow around Kerr-Taub-NUT black hole

The compact objects play a significant role in regulating the accretion around them due to strong gravity. Among them, BHs are the most interesting objects due to the presence of a one way surface called the horizon from where nothing can come out. Therefore, in this strong gravity regime, the relativistic hydrodynamics framework is required, which has been studied quite extensively in the literatures. Moreover, after the recent observations of the shadow of the central compact objects in galaxies by EHT Collaboration (2019a, 2022a), accretion has become a worthwhile direction in probing various gravitational backgrounds (Gyulchev et al., 2020; Gelles et al., 2021; Zeng et al., 2022; Mirzaev et al., 2022; Lin et al., 2022; Liu et al., 2022). As the astrophysical objects are rotating in nature, the Kerr BHs are the most appropriate BH solution around which relativistic hydrodynamic accretion flow has been widely studied (Novikov & Thorne, 1973; Page & Thorne, 1974; Riffert & Herold, 1995; Abramowicz et al., 1997; Dihingia et al., 2018, 2019b). Another bigger class of stationary and axisymmetric vacuum solution of the Einstein field equations is the Kerr-Taub-NUT (KTN) spacetime (Taub, 1951; Misner, 1963; Demianski & Newman, 1966; Misner & Taub, 1969; Bonnor, 1969; Miller, 1973) (see section 1.1.3 for detailed description of KTN BH). This KTN spacetime contains three independent parameters, namely mass ($M_{\rm BH}$), spin ($a_{\rm k}$), and NUT charge or gravitomagnetic monopole (n). Further, depending on the NUT parameter, the KTN spacetime may represent a BH with $a_k > 1$ as opposed to the usual Kerr BHs. The effect of such monopole is already examined in explaining several astrophysical findings, namely the spectra of supernovae, quasars, or AGNs (Lynden-Bell, 1969; Kagramanova et al., 2010), gravitational lens (Nouri-Zonoz & Lynden-Bell, 1997; Lynden-Bell & Nouri-Zonoz, 1998), microlens (Rahvar & Nouri-Zonoz, 2003), and BH shadow (Abdujabbarov et al., 2013). Meanwhile, Dihingia et al. (2020a) came out with an analytic analysis of general rela-

tivistic hydrodynamic flow around this KTN spacetime and discussed a complete set of accretion solutions along with their properties in steady state.

Shock formation is a common phenomenon in nature and frequently arises in accretion flow. It appears as a discontinuous jump in flow velocity, density, pressure and temperature in hydrodynamics (Fukue, 1987; Chakrabarti, 1989c; Abramowicz & Chakrabarti, 1990; Das et al., 2001b) (see section 1.4.6 and 1.4.7 for details). Being hot and dense due to shock compression, the post-shock corona (PSC) provides high energy radiation via inverse Comptonization of soft photons from the pre-shock flow (Chakrabarti & Titarchuk, 1995; Mandal & Chakrabarti, 2005), which explain emission characteristics in AGNs and GBHs, such as spectral state transitions in XRBs (Chakrabarti & Mandal, 2006; Nandi et al., 2012; Iyer et al., 2015; Nandi et al., 2018), outflows/jets (Chakrabarti, 1999b; Das et al., 2001a; Chattopadhyay & Das, 2007; Aktar et al., 2015; Jana & Das, 2024) and observed QPOs in BH sources (Chakrabarti et al., 2004; Nandi et al., 2012; Garain et al., 2014; Molla et al., 2016; Debnath et al., 2016; Dihingia et al., 2019b; Sreehari et al., 2019; Majumder et al., 2022; Patra et al., 2022; Majumder et al., 2023; Debnath, 2024; Patra et al., 2024). However, all these studies were performed around Schwarzschild or Kerr BHs. Being motivated by this, in this Chapter, we aim to explore shock solutions around the more general KTN BH spacetime and for the first time to the best of our knowledge, we portray a complete picture of an important class of accretion solutions. We analyze the global solutions of low angular momentum, inviscid, advective accretion flow around KTN BH in presence and absence of shock waves. While doing so, we solve the full general relativistic hydrodynamic equations in steady state and consider the relativistic EoS to take care of the thermodynamical state of matter (Chattopadhyay & Ryu, 2009). During accretion, rotating flow experiences centrifugal barrier that eventually triggers the discontinuous shock transition provided the relativistic Rankine-Hugoniot shock conditions are satisfied. Thereafter, we examine by the shock properties, namely shock location (r_s), compression ratio (R) and shock strength (S), and their dependencies on the energy ($\mathcal{E}$) and angular momentum (λ) of the flow as well as KTN BH parameters ($a_{\rm k}, n$). We identify that for a wide range of parameter space in the $\lambda - \mathcal{E}$ plane, shock continues to form. Moreover, $a_{\rm k}$ and n act oppositely in determining the shock properties and shock parameter space. Finally, we calculate the disk luminosity (L) considering free-free emissions and observe that accretion flows containing shocks are more luminous compared to the shock-free solutions.

2.1 Assumptions and governing equations

2.1.1 Background geometry

We begin by considering a generic stationary axisymmetric back ground expressed as,

$$\begin{aligned} ds^2 =& g_{\mu\nu} dx^\mu dx^\nu \\ =& g_{tt} dt^2 + g_{rr} dr^2 + 2 g_{t\phi} dt d\phi + g_{\phi\phi} d\phi^2 + g_{\theta\theta} d\theta^2. \end{aligned} \tag{2.1}$$

In terms of Boyer & Lindquist (1967) coordinates , the components of the KTN metric (see section 1.1.3) are given by,

$$g_{tt} = (a_{\rm k}^2 \sin^2\theta - \Delta)/\Sigma, \quad g_{t\phi} = -(A\Delta - a_{\rm k} B \sin^2\theta)/\Sigma,$$
$$g_{rr} = \Sigma/\Delta, \quad g_{\theta\theta} = \Sigma, \quad g_{\phi\phi} = (B^2 \sin^2\theta - A^2\Delta)/\Sigma.$$

Here, $\Delta = r^2 - 2r + a_{\rm k}^2 - n^2$, $\Sigma = (a_{\rm k}\cos\theta + n)^2 + r^2$, $A = a_{\rm k}\sin^2\theta - 2n\cos\theta$, and $B = r^2 + a_{\rm k}^2 + n^2$, where $a_{\rm k}$ and n are the Kerr parameter and NUT parameter, respectively. In this chapter, we use the sign convention as $(-,+,+,+)$ and adopt the unit system $M_{\rm BH} = G = c = 1$, where the length, angular momentum, and time are expressed in terms of r_g $(= GM_{\rm BH}/c^2)$, $r_g c$ and r_g/c, respectively. Setting $g^{rr} = 0$, we obtain the event horizon $(r_{\rm H}^{\rm KTN})$ of the metric and is given by $r_{\rm H}^{\rm KTN} = 1 + \sqrt{1 - a_{\rm k}^2 + n^2}$. Clearly, based on the choice of $a_{\rm k}$ and n, the KTN spacetime yields either BH for $(1 - a_{\rm k}^2 + n^2) > 0$ or naked singularity when $(1 - a_{\rm k}^2 + n^2) < 0$. Needless to mention that KTN spacetime reduces to the usual Kerr spacetime when NUT parameter vanishes $(n = 0)$.

2.1.2 Relativistic hydrodynamics

The relativistic hydrodynamic flow are based on two conservation equations *i.e.*, conservation of energy-momentum $(T^{\mu\nu})$ and conservation of particle number $(j^\mu = \rho u^\mu)$, which are given by,

$$T^{\mu\nu}_{;\nu} = 0 \quad \text{and} \quad j^\mu_{;\mu} = 0. \tag{2.2}$$

Here, non-dissipative energy-momentum tensor is written as,

$$T^{\mu\nu} = (e + p)u^\mu u^\nu + p g^{\mu\nu}. \tag{2.3}$$

In the above expressions, e is the local energy density, p is the pressure, ρ is the mass density, and u^μ is the four velocity of the fluid, where μ, ν run from 0 to 3. We emphasize that the present hydrodynamic analysis is local and confined around the equatorial plane of the KTN space-time within the finite radius. As the KTN spacetime is not asymptotically flat globally, however, it can be regarded as locally flat at spatial infinity (Stelea, 2006; Virmani, 2011). Therefore, the axial singularity mentioned in the section 1.1.3 does not affect this present accretion flow dynamics. We consider a geometrically thin advective accretion flow around a KTN spacetime in the steady state. Due to the axial symmetry of the background, we further assume that the accreting flow remains confined around the disk equatorial plane $(\theta = \frac{\pi}{2})$. At any point on the disk, the time-like four velocity of the flow is symbolized by $u^\mu \equiv (u^t, u^r, 0, u^\phi)$ and $u_\mu u^\mu = -1$. Moreover, the projection operator is defined as, $h^i_\mu = \delta^i_\mu + u^i u_\mu$ and if follows the relation $h^i_\mu u^\mu = 0$ withe i stands for the spatial coordinates only. With the help of projection operator, we can write the relativistic Euler equation as,

$$h^i_\mu T^{\mu\nu}_{;\nu} = (e + p)u^\nu u^i_{;\nu} + (g^{i\nu} + u^i u^\nu)p_{,\nu} = 0. \tag{2.4}$$

Therefore, on the equatorial plane, the radial component of this Euler equation looks like (Dihingia et al., 2020a),

$$u^r u^r_{,r} + \frac{1}{2} g^{rr}\frac{g_{tt,r}}{g_{tt}} + \frac{1}{2}u^r u^r\left(\frac{g_{tt,r}}{g_{tt}} + g^{rr} g_{rr,r}\right)$$
$$+ u^\phi u^t g^{rr}\left(\frac{g_{t\phi}}{g_{tt}} g_{tt,r} - g_{t\phi,r}\right) + \frac{1}{2}u^\phi u^\phi g^{rr}\left(\frac{g_{\phi\phi} g_{tt,r}}{g_{tt}} - g_{\phi\phi,r}\right) + \frac{(g^{rr} + u^r u^r)}{e + p} p_{,r} = 0. \tag{2.5}$$

After that, if we take the projection of energy-momentum conservation equation (Eq. (2.2)) along four-velocity (u^μ), we get energy equation in the following form,

$$u_\mu T^{\mu\nu}_{;\nu} = u^\nu \left[\left(\frac{e+p}{\rho} \right) \rho_{,\nu} - e_{,\nu} \right] = 0. \tag{2.6}$$

Eq. (2.5) can be also written as,

$$v\gamma_v^2 \frac{dv}{dr} + \frac{1}{h\rho}\frac{dp}{dr} + \frac{d\Phi_e^{\rm eff}}{dr} = 0. \tag{2.7}$$

Here, v denotes the radial three-velocity in the comoving frame and is defined as $v^2 = \gamma_\phi^2 v_r^2$, where $\gamma_\phi^2 = 1/(1-v_\phi^2)$, $v_\phi^2 = (u^\phi u_\phi)/(-u^t u_t)$, and $v_r^2 = (u^r u_r)/(-u^t u_t)$. Further, $\gamma_v^2\,[= 1/(1-v^2)]$ is the radial Lorentz factor, $h\,[= (e+p)/\rho]$ is the specific enthalpy. $\Phi_e^{\rm eff}$ represents the effective potential (Dihingia et al., 2020a) at the disk equatorial plane ($\theta = \pi/2$) which is given by,

$$\Phi_e^{\rm eff} = 1 + \frac{1}{2}\ln\left[\frac{(n^2+r^2)\Delta}{(a_{\rm k}^2 - a_{\rm k}\lambda + r^2 + n^2)^2 - (a_{\rm k}-\lambda)^2\Delta} \right], \tag{2.8}$$

where λ ($= -u_\phi/u_t$) is the conserved specific angular momentum of the flow. For a stationary and axisymmetric KTN spacetime, there exists two commutating Killing vector fields, $l_t^\mu \equiv (\partial_t, 0, 0, 0)$ and $l_\phi^\mu \equiv (0, 0, 0, \partial_\phi)$ corresponding to time translation and azimuthal rotation, respectively. The associated two conserved quantities along the direction of the motion are given by,

$$hu_\phi = \mathcal{L}\ \text{(constant)}; \qquad -hu_t = \mathcal{E}\ \text{(constant)}, \tag{2.9}$$

where $\mathcal{E}$ is the Bernoulli constant (equivalently specific energy). By integrating the 2nd part of Eq. (2.2), we get the mass conservation equation as,

$$\dot{M} = -4\pi\rho r u^r H/\eta, \tag{2.10}$$

where $\dot{M}$ refers the mass accretion rate which is treated as global constant. We express mass accretion rate in dimensionless form as $\dot{m} = \dot{M}/\dot{M}_{\rm Edd}$, where $\dot{M}_{\rm Edd}$ ($= 1.44 \times 10^{18} M_{\rm BH}/M_\odot$ gm s^{-1}) is the Eddington accretion rate. In Eq. (2.9), $\eta = r^2/(r^2+n^2)$ and the half thickness (H) of the disk given by (Riffert & Herold, 1995),

$$H = \sqrt{\frac{pr^3}{\rho\mathcal{F}}}; \quad \mathcal{F} = \gamma_\phi^2 \frac{(r^2+a_{\rm k}^2)^2 + 2\Delta a_{\rm k}^2}{(r^2+a_{\rm k}^2)^2 - 2\Delta a_{\rm k}^2}.$$

The entropy generation equation in the radial direction is obtained as,

$$\left(\frac{e+p}{\rho} \right) \frac{d\rho}{dr} - \frac{de}{dr} = 0. \tag{2.11}$$

In order to solve the governing equations (Eqs. (2.7), (2.9), (2.10), and (2.11)), one requires a closure equation in the form of EoS, which describes the relation among the thermodynamical quantities like density (ρ), pressure (p) and local energy density (e). During the course of accretion around the BHs, the accretion flow is expected to be in the thermally relativistic domain (*i.e.*, adiabatic index $\Gamma \to 4/3$) at the inner part of the disc, whereas it remains thermally non-relativistic (*i.e.*, $\Gamma \to 5/3$) at a distance

far away from the BH horizon (Frank et al., 2002). Hence, the EoS with a fixed Γ is inadequate to describe a thermally relativistic flow (Taub, 1948; Ryu et al., 2006) and a relativistic EoS (Chandrasekhar, 1939; Synge, 1957) needs to be employed, where Γ is determined self-consistently based on the thermal properties of the flow. Keeping this in mind, we adopt an EoS for relativistic fluid (Chattopadhyay & Ryu, 2009) which is given by,

$$e = \rho f \left(1 + \frac{m_p}{m_e}\right)^{-1}$$

with

$$f = \left[1 + \Theta\left(\frac{9\Theta + 3}{3\Theta + 2}\right)\right] + \left[\frac{m_p}{m_e} + \Theta\left(\frac{9\Theta m_e + 3m_p}{3\Theta m_e + 2m_p}\right)\right],$$

where Θ $(= k_{\rm B}T/m_e c^2)$ is the dimensionless temperature, m_e is the mass of electron, and m_p is the mass of ion. According to the relativistic EoS, we express the speed of sound as $C_s = \sqrt{2\Gamma\Theta/(f + 2\Theta)}$ (Dihingia et al., 2019a). Following (Chattopadhyay & Ryu, 2009; Dihingia et al., 2020a) and using Eq. (2.10), we calculate the entropy accretion rate as, $\dot{\mathcal{M}} = \exp(k_1)\Theta^{3/2}\,(2 + 3\Theta)^{3/4}\left(3\Theta + \frac{2m_p}{m_e}\right)^{3/4} u^r r H/\eta$, where $k_1 = [f - (1 + m_p/m_e)]\,/2\Theta$.

We simplify Eqs. (2.7), (2.9), (2.10), and (2.11) and after some simple algebra, we obtain the wind equation as,

$$\frac{dv}{dr} = \frac{\mathcal{N}}{\mathcal{D}}, \tag{2.12}$$

where, $\mathcal{N}$ and $\mathcal{D}$ are respectively given by,

$$\mathcal{N} = \frac{C_s^2}{\Gamma + 1}\left[\frac{1}{\Delta}\frac{d\Delta}{dr} - \frac{1}{\eta}\frac{d\eta}{dr} + \frac{3}{r} - \frac{1}{\mathcal{F}}\frac{d\mathcal{F}}{dr}\right] - \frac{d\Phi_e^{\rm eff}}{dr}, \tag{2.12a}$$

$$\mathcal{D} = \gamma_v^2\left[v - \frac{2C_s^2}{v(\Gamma + 1)}\right], \tag{2.12b}$$

Subsequently, usingEqs. (2.7), (2.10), and (2.11) and employing the definition of sound speed, we calculate the differential form of the temperature as,

$$\frac{d\Theta}{dr} = -\frac{\Theta}{2N + 1}\left[\frac{\gamma_v^2}{2v}\frac{dv}{dr} + \frac{1}{\Delta}\frac{d\Delta}{dr} - \frac{1}{\eta}\frac{d\eta}{dr} + \frac{3}{r} - \frac{1}{\mathcal{F}}\frac{d\mathcal{F}}{dr}\right], \tag{2.13}$$

where, $N\,[= (1/2)(df/d\Theta)]$ denotes the polytropic index of the flow and it is related to the adiabatic index as $\Gamma = (1 + N)/N$.

2.2 Critical point and transonic solutions

In an accretion process, gravity pulls matter towards the center of the gravitating object from the surrounding medium. In reality, inflowing matter starts its journey far away from the BH with negligible radial velocity and enters into the BH with velocity comparable to the speed of light just to satisfy the inner boundary conditions imposed by the event horizon. Because of this, the accretion around BHs bears an unique property that inevitably leads the flow to suffer smooth transition from subsonic to supersonic at the critical point before crossing the BH horizon. Interestingly,

depending on the flow parameters, namely energy and angular momentum, the flow may contain multiple critical points and thus is potentially viable to harbour shock waves as indicated in the Introduction. Before embarking on discussing shocks which is the main topic of the paper, let us briefly describe about the critical point, where both numerator and denominator of Eq. (2.12) simultaneously vanish as $\mathcal{N} = \mathcal{D} = 0$. Setting $\mathcal{D} = 0$ in Eq. (2.12b), the radial flow velocity (v_c) at the critical point (r_c) is expressed as,

$$v_c = \sqrt{\frac{2}{\Gamma_c + 1}} C_{sc}, \tag{2.14}$$

with equating $\mathcal{N} = 0$ in Eq. (2.12a), we get the expression for the sound speed as,

$$C_{sc}^2 = \frac{\Gamma_c + 1}{4} \left(\frac{d\Phi_e^{\rm eff}}{dr}\right)_c \left[\frac{1}{\Delta}\frac{d\Delta}{dr} + \frac{1}{\eta}\frac{d\eta}{dr} + \frac{3}{r} - \frac{1}{\mathcal{F}}\frac{d\mathcal{F}}{dr}\right]_c^{-1} \tag{2.15}$$

In the Eqs. (2.14), (2.15), subscript 'c' refers the flow variables measured at r_c. Since the flow remains smooth along the streamline including the critical points (r_c), the radial velocity gradient (dv/dr) must be real and finite everywhere. Hence, we apply l'Hôpital's rule to evaluate radial velocity gradient at r_c, and it generically possesses two types: $(dv/dr)_c < 0$ leads to the accretion solution while $(dv/dr)_c > 0$ yields winds. In the present work, we focus only on the accretion solutions keeping winds aside as they are of our particular interest. Depending upon the mathematical nature of $(dv/dr)_c$, critical points are classified in three categories. When $(dv/dr)_c$ assumes values which are real and of opposite sign, the critical point is called as saddle type. If $(dv/dr)_c$ are real and of same sign, it is called nodal type, and when $(dv/dr)_c$ are imaginary, it is called spiral type critical point. In the astrophysical context, saddle type critical points are of specially importance as the inflowing matter can only pass through them before entering into the black hole.

In Fig. 2.1, we show the variation of the flow energy ($\mathcal{E}$) as a function of the critical points (r_c) for different values of $a_{\rm k}$ (upper panel) and n (lower panel). In the figure, we choose $\lambda = 2.04$, and solid (black), dotted (red) and dashed (blue) curves represent the saddle, nodal and spiral type critical points, respectively. In the upper panel, we fix $n = 0.2$ and vary $a_{\rm k}$ as 0.9, 0.95 and 1.0 which are marked. We find that for a given $a_{\rm k}$, when r_c is increased, the nature of the critical points is systematically altered following the sequence as saddle — nodal — spiral —nodal— saddle — nodal. Moreover, we find that the range of multiple saddle type critical point locations required for shock transition increases as $a_{\rm k}$ is increased. We also find that there exists an upper limit of the location of the saddle type critical points for a relativistic flow accreting onto a KTN BH. Similarly, in the lower panel, we choose $a_{\rm k} = 0.95$, and vary NUT parameter as $n = 0.1$, 0.2 and 0.3. Here, we observe that the role played by n is characteristically opposite of $a_{\rm k}$ in deciding the properties of the critical points, however, the effect of one can not be completely negated by other due to the fact that KTN spacetime non-linearly depends on them.

In reality, depending on the input parameters $(\mathcal{E}, \lambda, a_{\rm k}, n)$, accretion flow may contain maximum of three critical points outside the horizon (Chakrabarti, 1989c; Das et al., 2001b). Among them, the inner critical points ($r_{\rm in}$) and the outer critical points ($r_{\rm out}$) generally form close to the horizon and far away from the horizon, whereas the middle critical points ($r_{\rm mid}$) form in between $r_{\rm in}$ and $r_{\rm out}$ (Das et al., 2001b). Considering this, we present the change of critical point characteristics due to the variation of the input parameters in Table 2.1.

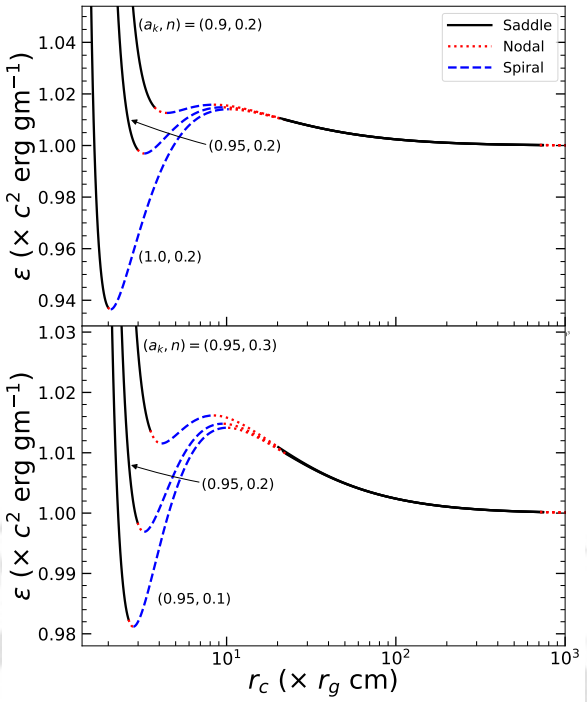

Figure 2.1: Plot of energy ($\mathcal{E}$) as a function of critical points (r_c) for angular momentum $\lambda = 2.04$. In upper panel, NUT parameter $n = 0.2$ and Kerr parameters are varied as $a_k = 0.9$, 0.95 and 1.0, while in the lower panel, $a_{\rm k}$ is kept fixed as 0.95, and n is varied as 0.1, 0.2 and 0.3, respectively. In both panels, solid (black), dotted (red) and dashed (blue) curves represent the saddle, nodal and spiral type critical points and $a_{\rm k}$ and n values are marked. See text for details.

Input Parameters				Critical Points		
λ	$a_{\rm k}$	$\mathcal{E}$	n		Location	Type
(cr_g)		(c^2)			(r_g)	
2.04	0.95	1.0180	0.3	$r_{\rm in}$	3.336	Saddle
				$r_{\rm mid}$	–	–
				$r_{\rm out}$	–	–
2.04	0.95	1.0150	0.3	$r_{\rm in}$	3.539	Saddle
				$r_{\rm mid}$	5.972	Spiral
				$r_{\rm out}$	11.915	Nodal
2.04	0.95	1.0130	0.3	$r_{\rm in}$	3.825	Nodal
				$r_{\rm mid}$	4.792	Spiral
				$r_{\rm out}$	15.667	Nodal
2.04	0.95	1.0100	0.3	$r_{\rm in}$	–	–
				$r_{\rm mid}$	–	–
				$r_{\rm out}$	22.763	Saddle
2.04	0.95	1.0001	0.3	$r_{\rm in}$	–	–
				$r_{\rm mid}$	–	–
				$r_{\rm out}$	1022.410	Nodal
2.04	0.95	1.0050	0.2	$r_{\rm in}$	2.741	Saddle
				$r_{\rm mid}$	4.596	Spiral
				$r_{\rm out}$	49.189	Saddle
2.04	0.95	0.9999	0.2	$r_{\rm in}$	2.934	Saddle
				$r_{\rm mid}$	3.832	Spiral
				$r_{\rm out}$	–	–
2.04	0.95	0.9990	0.2	$r_{\rm in}$	2.996	Nodal
				$r_{\rm mid}$	3.688	Spiral
				$r_{\rm out}$	–	–

Table 2.1: Critical point locations and their natures obtained for various sets of input parameters (see Fig. 2.1). See text for details.

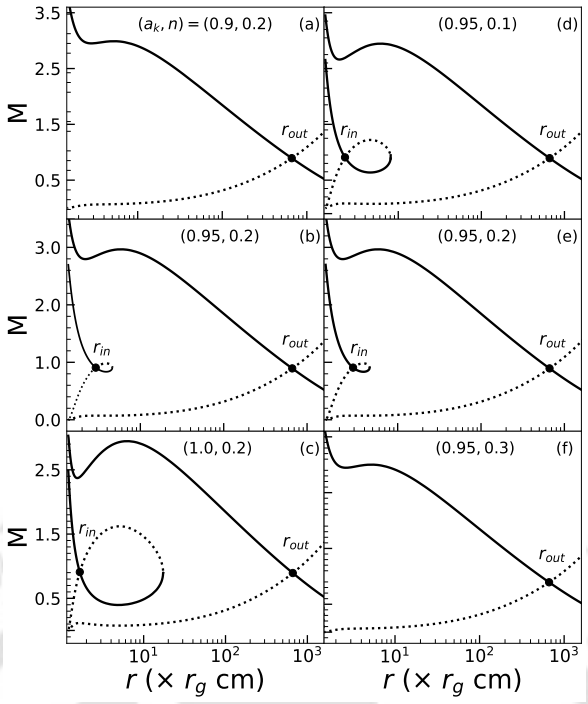

Figure 2.2: Variation of Mach no ($M = v/C_s$) with the radial coordinate (r) for energy $\mathcal{E}$ = 1.0002 and angular momentum λ = 2.04. In the left panel, Kerr parameter is varied as a_k = 0.9 (top), 0.95 (middle) and 1.0 (bottom) keeping NUT parameter fixed as n = 0.2. Similarly, in the right panels, Mach number is plotted for n = 0.1 (top), 0.2 (middle) and 0.3 (bottom), where a_k = 0.95. The solid and dotted curves denote the accretion and wind solutions, respectively and filled circles refer the critical points. See text for details.

In order to understand the behavior of the flow containing saddle type critical points, in Fig. 2.2, we provide representative plots of Mach number ($M = v/C_s$) as a function of radial co-ordinate (r) for $\mathcal{E} = 1.0002$ and $\lambda = 2.04$. In the left panels, we investigate the effect of Kerr parameter (a_k) on the transonic solutions, whereas in the right panels, the role of NUT parameter (n) is examined. As mentioned earlier, we are interested to study the accretion solutions only, however, in each panel, we depict both accretion (solid curve) and its corresponding wind branch (doted) for the purpose of completeness. In Fig. 2.2a, we choose $(a_{\rm k}, n) = (0.9, 0.2)$ and flow contains only outer critical points at $r_{\rm out} = 663.348$ and it successfully connects the BH event horizon ($r_{\rm H}^{\rm KTN}$) with the outer edge of the disk ($r_{\rm edge} = 2000$). Here, filled circle denotes the critical point location. As Kerr parameter is increased keeping remaining parameters unchanged as $(a_{\rm k}, n) = (0.95, 0.2)$, the inner critical point emerges (see Fig. 2.2b) at $r_{\rm in} = 2.917$. Interestingly, solution passing through $r_{\rm in} = 2.917$ fails to connect the event horizon with $r_{\rm edge}$. With further increase of Kerr parameter as $(a_{\rm k}, n) = (1.0, 0.2)$, inner critical point solution extends up to ~ 1.660 (see Fig. 2.2c). The solution of such kind is potentially promising as it can join with another solution possessing $r_{\rm out}$ via discontinuous shock transition and ultimately provides a complete global accretion solutions connecting $r_{\rm H}^{\rm KTN}$ and $r_{\rm edge}$. We discuss the shock-induced global accretion solutions in the subsequent sections. In the right panels of Fig. 2.2(d)-2.2(f), examples of accretion solutions corresponding to three different NUT parameters $n = 0.1, 0.2, 0.3$ (marked in the figure) are presented, where $a_k = 0.95$ is kept fixed. We observe that NUT parameter (n) responds in the opposite manner on the nature of the flow portrait as the multiple saddle type critical points gradually disappear with the increase of n for flows with fixed $a_{\rm k}$ values. Similar to the right panel, here also the solid and dotted curves denote accretion and wind solutions, respectively and the critical points are represented by filled circles.

2.3 Accretion flow possessing shock

As already mentioned that accreting matter around the BH may contain multiple saddle type critical points depending on the flow parameters. In such cases, flow can not pass through both critical points simultaneously, unless a discontinuous transition of the flow variables happens at some radius in between the critical points. In reality, rotating accretion flow from the outer edge of the disk ($r_{\rm edge}$) starts accreting towards the BH with negligible subsonic radial velocity and gradually gains its radial velocity as it proceeds towards the black hole. At $r_{\rm out}$, flow becomes transonic and continues to proceed further supersonically. Meanwhile, flow starts experiencing centrifugal repulsion that eventually slows down the inflowing matter causing its accumulation in the vicinity of the BH and a centrifugal barrier is developed. The accumulation of matter does not continue indefinitely as the centrifugal barrier triggers the discontinuous transitions of the flow variables in the form of shock wave. Across the shock front, supersonic flow jumps into the subsonic branch and flow become compressed. Because of this, kinetic energy of pre-shock flow is converted into the thermal energy resulting the PSC. Usually, PSC acts as the source of hot and dense electrons where soft photons from the cooled pre-shock flow are intercepted and further reprocessed via inverse Comptonizationt to produce high energy radiations. After the shock transition, subsonic flow eventually picks up its radial velocity as it moves further inwards

and again becomes supersonic after passing through $r_{\rm in}$ before crossing the black hole horizon. In order to execute such shock transition, accretion flow must satisfy the relativistic shock conditions (Taub, 1948), which are given by,

$$[\rho u^r] = 0; \quad \Big[(e+p)u^t u^r\Big] = 0; \quad [(e+p)u^r u^r + pg^{rr}] = 0, \tag{2.16}$$

where the quantities within the square bracket refer the differences of their values across the shock front. We utilize Eq. (2.16) to calculate the location of the shock transition (r_s).

2.3.1 Typical global accretion solutions with shock

In Fig. 2.3, we present a typical example of the shock-induced global accretion solution, where the variation of (a) Mach number (M), (b) entropy accretion rate ($\dot{\mathcal{M}}$), (c) density (ρ), (d) temperature (T), and (e) surface density (Σ) are plotted as function of radial coordinate. Here, we choose the flow parameters as $(\mathcal{E}, \lambda) = (1.005, 2.1)$, and KTN BH parameters as $(a_{\rm k}, n) = (1.1, 0.5)$. In the figure, subsonic flow starts accreting from $r_{\rm edge}$ and becomes supersonic after crossing $r_{\rm out} = 49.6575$ (see Fig. 2.3a). Subsequently, supersonic flow satisfies the relativistic shock conditions (equation 11) at $r_s = 8.0599$ and joins with the subsonic branch that eventually passes through the inner critical point at $r_{\rm in} = 2.1968$ before falling in to the KTN black hole. In the figure, arrows indicate the overall direction of the flow motion towards the black hole where vertical arrow denotes the location of the shock transition. Indeed, after crossing $r_{\rm out}$, accretion flow has the possibility to enter into the black hole supersonically as depicted by the dashed curve (red). However, since entropy ($\dot{\mathcal{M}}$) associated with the post-shock flow is higher than the pre-shock flow (see Fig. 2.3b), the second law of thermodynamics affirms that the shock solution is preferred over the shock-free solution (Becker & Kazanas, 2001). In Fig. 2.3c, we demonstrate the density profile (ρ) corresponding to the shocked accretion solution presented in Fig. 2.3a. We observe that ρ increases immediately after the shock transition. This happens as radial velocity v drops down to subsonic value at PSC and inward mass flux remains conserved across the shock front (see Eq. (2.10). We further display the temperature profile of the accretion flow in Fig. 2.3d. As expected, most of the kinetic energy of the pre-shock matter is converted into the thermal energy across the shock front that eventually causes the heating of PSC. Because of this, the rise of post-shock temperature profile is clearly seen. In Fig. 2.3e, we show the profile of surface density ($\Sigma = \rho H$) (Frank et al., 2002), where Σ assumes higher values at PCS due to the density compression across the shock front. Such a distinct feature of PSC is naturally favourable to contain the swarm of hot electrons that can inverse Comptonize the soft photons coming from the outer region of the disk to produce high energy radiations commonly observed in GBH sources. Accordingly, the shocked accretion solutions emerge as a promising candidate in explaining the observational signatures of black holes (Chakrabarti & Titarchuk, 1995; Mandal & Chakrabarti, 2005; Nandi et al., 2012; Das et al., 2021).

2.3.2 Shock properties

In order to study the accretion disk structure around KTN BH, one requires overall four parameters in the present formalism. Among them, two are conserved quantities

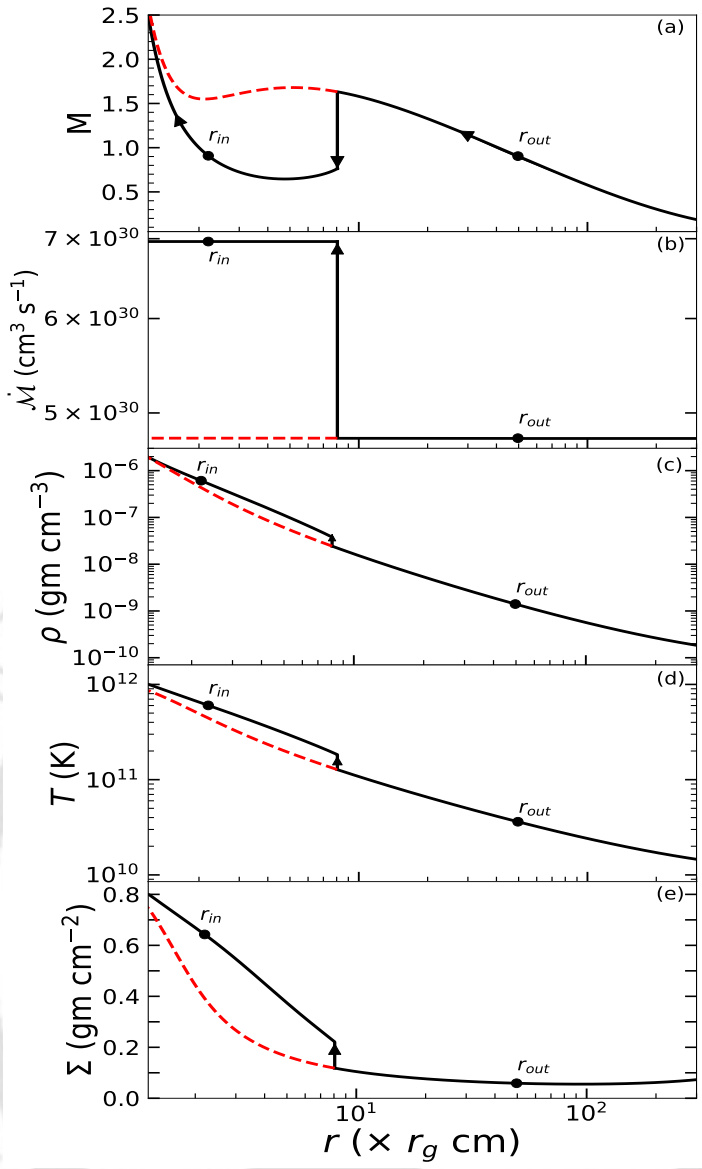

Figure 2.3: Variation of (a) Mach number ($M = v/C_s$), (b) entropy accretion rate ($\dot{\mathcal{M}}$), (c) density (ρ), (d) temperature (T), and (e) surface density (Σ) as function of radial coordinate (r). Results are obtained for $(\mathcal{E}, \lambda, a_{\rm k}, n) = (1.005, 2.1, 1.1, 0.5)$, where solid (black) and dashed (red) curves represent shocked and shock free solutions. In each panel, filled circles denote the critical points ($r_{\rm in}$ and $r_{\rm out}$) and vertical arrow indicates the location of the shock transition. See text for details.

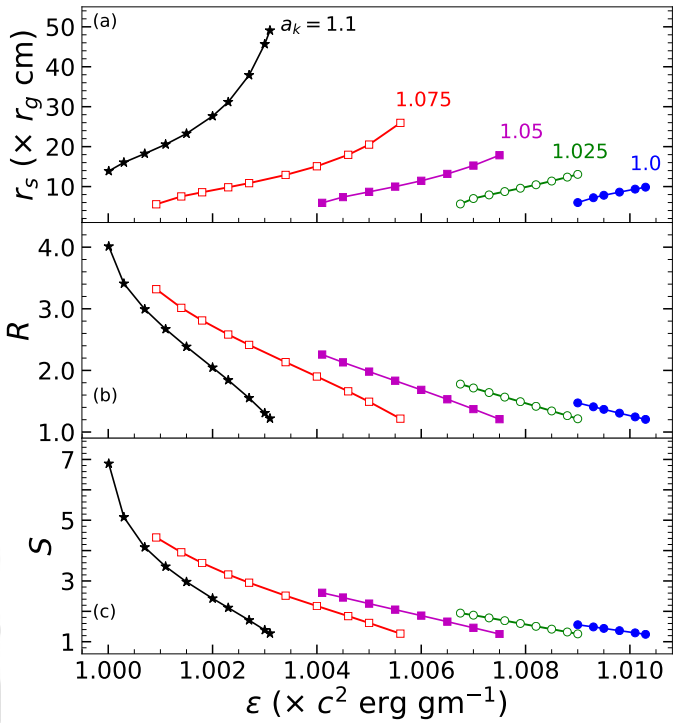

Figure 2.4: Variation of (a) shock location (r_s), (b) compression ratio (R), and (c) shock strength (S) as a function of specific energy ($\mathcal{E}$). Here, we vary Kerr parameter (a_k) from 1.00 to 1.10 with an interval $\Delta a_{\rm k} = 0.025$ from the right most curve to the left most curve. Here, we choose $\lambda = 2.2$ and $n = 0.5$. See text for details.

associated with the flow, namely $\mathcal{E}$ and λ, and the remaining two are a_k and n that describe the KTN BH. As already pointed out in section 2.3.1, when shock conditions are satisfied, shock-induced global accretion solutions are favoured over shock free solution. Therefore, in this section, we intend to examine the various shock properties, namely shock location (r_s), compression ratio (R), and shock strength (S).

Fig. 2.4a shows the variation of shock location (r_s) as a function of specific energy ($\mathcal{E}$) for different values of Kerr parameter ($a_{\rm k}$). Here, we choose $\lambda = 2.2$ and $n = 0.5$. The results plotted with filled circles (blue), open circles (green), filled squares (magenta), open squares (red), and asterisks (black) are for black hole spin starting from $a_{\rm k} = 1.0$ with increment $\Delta a_{\rm k} = 0.025$, respectively. We find that for a given $a_{\rm k}$, shock conditions are satisfied for a minimum energy ($\mathcal{E}_{\rm min}$), and shock continues to form at larger radii as $\mathcal{E}$ is increased until it ceases to exist beyond $\mathcal{E}_{\rm max}$. This clearly indicates that for a given set of $(a_{\rm k}, \lambda, n)$, there exist a range of energy $\mathcal{E}_{\rm min} < \mathcal{E} < \mathcal{E}_{\rm max}$ that yields global accretion solutions possessing standing shock. We also find that for a given $\mathcal{E}$, shock forms at smaller radii for BHs with smaller $a_{\rm k}$. Since the flow is compressed across the shock transition (see Fig. 2.3) and the emergent radiations from the disk strongly depends on the density (Chakrabarti & Titarchuk, 1995; Mandal & Chakrabarti, 2005), it is useful to compute the compression ratio (R), which is defined as the ratio of the vertical averaged post-shock density (Σ_+) to the pre-shock density (Σ_-). In Fig. 2.4b, we present the variation of R as function of $\mathcal{E}$ for the same set of flow parameters as in Fig. 2.4a. For a given set of $(a_{\rm k}, \lambda, n)$, R monotonically decreases with the increase of $\mathcal{E}$. This happens because the size of PSC increases with $\mathcal{E}$ that weakens the density compression across the shock front. A cut off is observed

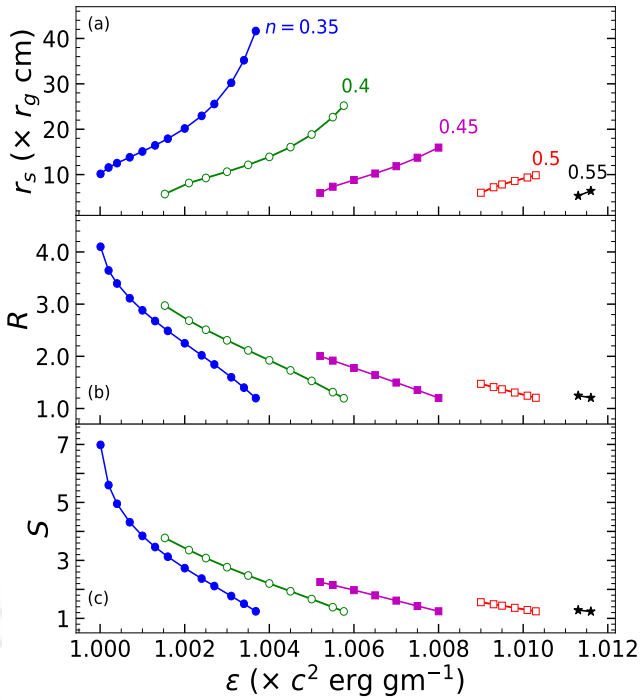

Figure 2.5: Variation of (a) shock location (r_s), (b) compression ration (R), and (c) shock strength (S) as a function of specific energy ($\mathcal{E}$). Here, we vary NUT Parameter (n) from 0.35 to 0.55, with an interval $\Delta n = 0.05$ from the left most curve to the right most curve. We choose $\lambda = 2.2$ and $a_{\rm k} = 1.0$. See text for details.

when shock disappears. We further emphasize that one would obtain both strong shock ($R \sim 4$) and weak shock ($R \to 1$) by suitably tuning the input parameters. We continue the study of shock properties by introducing another quantity called shock strength (S) which is defined as the ratio of the pre-shock Mach number (M_-) to the post-shock Mach number (M_+). In reality, S determines the temperature jump across the shock front. In 2.4c, we depict the variation of S as function of $\mathcal{E}$ for the same set of flow parameters as in Fig. 2.4a. We find that for a given set of $(a_{\rm k}, \lambda, n)$, S is stronger when $\mathcal{E}$ is small and it gradually becomes weak as $\mathcal{E}$ is increased till shock continues to exist.

In reality, since PSC is the source of hot electrons by nature, it reprocesses the soft photons via inverse Comptonization to produce high energy radiations. In addition, R and S collectively regulate the efficiency of the inverse Comptonization process (Chakrabarti & Titarchuk, 1995). Therefore, the spectral properties of the central source are expected to be strongly dependent on these observables. Accordingly, by tuning the model parameters, namely $\mathcal{E}$, λ, $a_{\rm k}$ and n, it is possible to account the various spectral states commonly observed in black hole XRB sources (Nandi et al., 2012, 2018).

In Fig. 2.5, we present the variation of shock location (r_s), compression ratio (R), and shock strength (S) as a function of specific energy ($\mathcal{E}$). Here, we keep angular momentum and spin of the BH fixed as $\lambda = 2.2$, and $a_{\rm k} = 1.0$. The results plotted using filled circles (blue), open circles (green), filled squares (magenta), open squares (red), and asterisks (black) are for $n = 0.35, 0.40, 0.45, 0.50$ and 0.55, respectively. We observe that the role of n in regulating the shock transition is entirely opposite to that

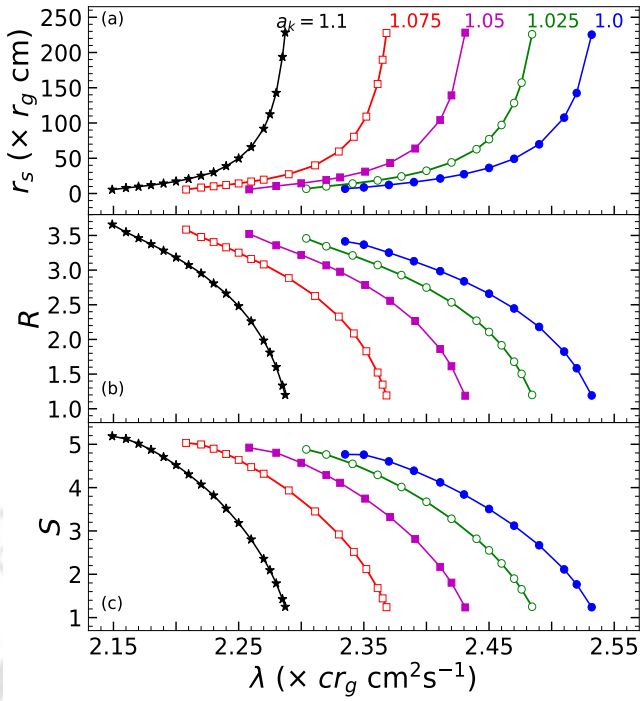

Figure 2.6: Variation of (a) shock location (r_s), (b) compression ratio (R), and (c) shock strength (S) as a function of specific angular momentum (λ). Here, we vary Kerr parameter (a_k) from 1.0 to 1.10, with an interval $\Delta a_k = 0.025$ from the right most curve to the left most curve. The specific energy $\mathcal{E} = 1.0005$ and NUT parameter $n = 0.5$. See text for details.

of the BH spin ($a_{\rm k}$) (see Fig. 2.4). Similar behaviours are seen for R and S as well. What is more is that for a given set of ($a_{\rm k}, \lambda$), shock-induced global accretion solutions are seen to exist for a wide range of NUT parameter (n).

We continue the investigation of the shock properties and examine the role of angular momentum (λ) in regulating the shock dynamics. Towards this, we fix energy and NUT parameter as $\mathcal{E} = 1.0005$ and $n = 0.5$, and depict r_s, R and S as function of λ for different $a_{\rm k}$ values in Fig 2.6a-c. Here, filled circles (blue), open circles (green), filled squares (magenta), open squares (red), and asterisks (black) denote the results obtained for $a_{\rm k}$ = 1.00, 1.025, 1.05, 1.075, and 1.10, respectively. For a given $a_{\rm k}$, the shock forms further out for flows possessing higher λ. In reality, larger λ causes enhanced centrifugal pressure that pushes the shock front outwards. In contrary, we find that shocks form for a particular range of $a_{\rm k}$, and for a given λ, the shock location decreases with the decrease of $a_{\rm k}$. Moreover, we observe that shock exists around BH with higher $a_{\rm k}$, when the flow angular momentum is relatively lower and vice versa. This happens due to the spin-orbit coupling embedded within the space-time geometry where the marginally stable angular momentum is seen to decrease with the increase of $a_{\rm k}$ (Das & Chakrabarti, 2008). Consequently, the range of λ for shock is also decreased with the increase of $a_{\rm k}$. Next, in Fig. 2.6b, we present the variation of compression ratio R which are seen to decrease with λ for black hole with identical spin value $a_{\rm k}$. In Fig. 2.6c, we plot the variation of the shock strength S with λ, where similar variation is observed as in Fig. 2.6b.

Fig. 2.7 illustrates the plot of (a) r_s, (b) R, and (c) S with λ for flows having different NUT parameter (n). Here, the remaining input parameters are chosen as

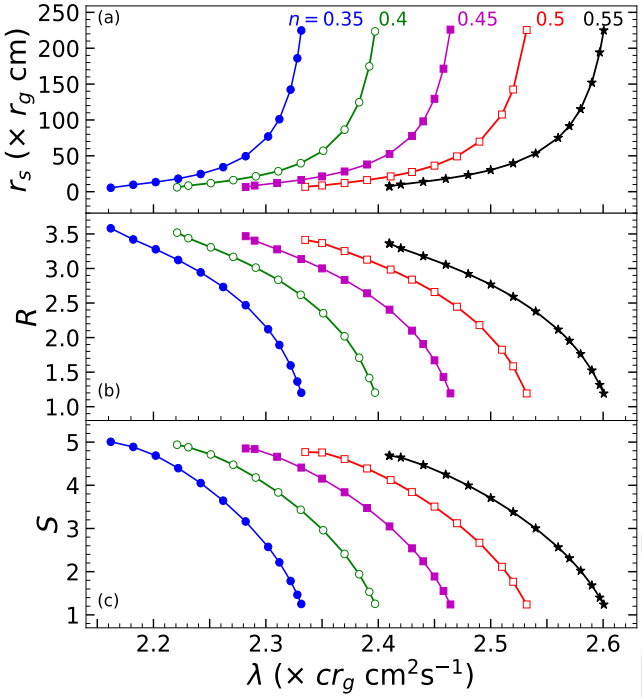

Figure 2.7: Variation of (a) shock location (r_s), (b) compression ration (R), and (c) shock strength (S) as a function of specific angular momentum (λ). Here, we vary NUT Parameter (n) from 0.35 to 0.55, with an interval $\Delta n = 0.05$ from the left most curve to the right most curve. We set $\mathcal{E} = 1.0005$ and $a_k = 1.0$. See text for details.

$\mathcal{E} = 1.0005$ and $a_{\rm k} = 1.00$. In each panel, filled circles (blue), open circles (green), filled squares (magenta), open squares (red), and asterisks (black) denote the results corresponding to $n = 0.35, 0.40, 0.45, 0.50$ and 0.55, respectively. Figure clearly indicates that shock solutions persist for a wide range of n. We find that r_s, R and S vary with λ very similarly as in Fig. 2.6, however, as expected, the effect of n on these observables is seen to be opposite of $a_{\rm k}$.

Next, we examine how r_s, R and S vary with $a_{\rm k}$, when energy and angular momentum of the flow are kept fixed as $\mathcal{E} = 1.0005$ and $\lambda = 2.2$. The obtained results are shown in Fig. 2.8, where each curve differs by $\Delta n = 0.05$ starting form the left most curve (filled circles, blue) with $n = 0.4$. For a given set of $(\mathcal{E}, \lambda, n)$, r_s increases with $a_{\rm k}$, whereas both R and S decreases, as expected. We find that for a fixed $a_{\rm k}$, shocks form at smaller radii as n is increased. It is evident from the figure that there exist a range $a_{\rm k}$ that admits shock solutions around KTN black hole and the said range explicitly depends on the other input parameters $(\mathcal{E}, \lambda, n)$.

In Fig. 2.9, we show the variation of r_s, R and S with the NUT parameter (n) for rotating flows with $\mathcal{E} = 1.0005$ and $\lambda = 2.2$. Here, filled circles (blue), open circles (green), filled squares (magenta), open squares (red), filled asterisks (black), and open asterisks (cyan) represent the result for $a_{\rm k} = 0.9$, 0.92, 0.94, 0.96, 0.98 and 1.0, respectively. We observe that for a fixed $(\mathcal{E}, \lambda, a_{\rm k})$, r_s in general decreases with n, and this eventually causes the increase of both R and S as well. It may be noted that accretion flow continues to experience shock transition around KTN BH even for relatively high n values. Evidently, when $a_{\rm k}$ is increased, the upper limit of NUT parameter ($n^{\rm max}$) for shock also increased. We quantify the correlation between $a_{\rm k}$

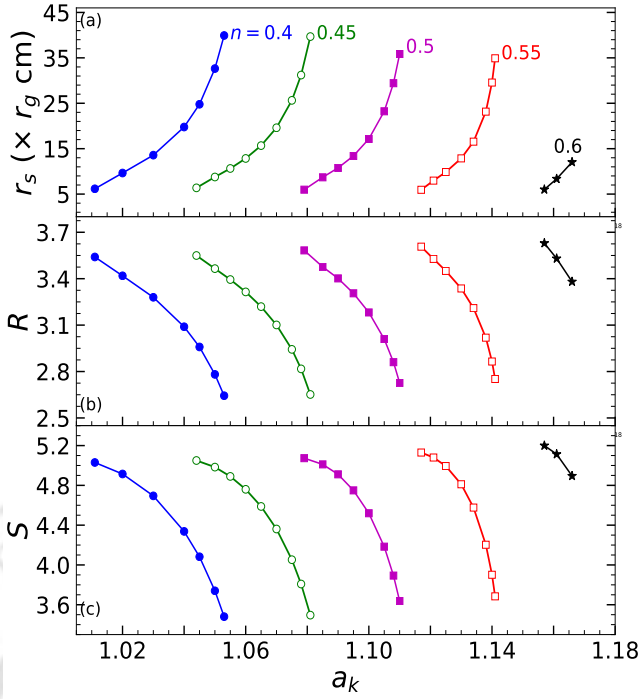

Figure 2.8: Plot of (a) r_s, (b) R, and (c) S as a function of $a_{\rm k}$ for flows with $\mathcal{E} = 1.0005$ and $\lambda = 2.2$. In each panel, filled circles (blue), open circles (green), filled squares (magenta), open squares (red), and asterisks (black) joined using solid curves denote results obtained for $n = 0.4, 0.45, 0.5, 0.55$, and 0.6, respectively. See text for details.

and $n^{\rm max}$ keeping energy of the flow fixed as $\mathcal{E} = 1.0005$ and depict the obtained results in Fig. 2.10. Filled circles joined using solid curves in black, magenta, blue and green denote the results corresponding to $\lambda = 2.1$, 2.2, 2.3, and 2.4, respectively. It is apparent from the figure that for lower $a_{\rm k}$, $n^{\rm max}$ initially increases sharply and thereafter, it tends to sluggish at higher $a_{\rm k}$, in general.

2.4 Parameter space for shock

In this section, we study the parameter space spanned by angular momentum (λ) and energy ($\mathcal{E}$) that admits shock-induced global accretion solutions around KTN BH. In the upper panel of Fig. 2.11, we depict the modification of the parameter space for different $a_{\rm k}$, where NUT parameter is kept fixed as $n = 0.5$. The effective region bounded by the solid (red), dotted (black) and dashed (green) curves are for $a_{\rm k} = 0.9$, 1.0 and 1.1, respectively. Clearly, lower $a_{\rm k}$ renders shock formation for relatively large λ values. This findings are evident as the weakly rotating KTN black hole effectively diminishes the influence of the flow angular momentum due to the inherent spin-orbit coupling present within the space-time geometry describing the accreting system (Das & Chakrabarti, 2008). Similarly, in the lower panel of Fig. 2.11, we identify the effective domain of the parameter space for different NUT parameters n keeping the black hole spin fixed as $a_{\rm k} = 1.1$. The regions enclosed by the solid (red), dotted (black) and dashed (green) curves are obtained for $n = 0.5$, 0.8 and 1.1, respectively. We observe that the parameter space for shock gradually reduces and shifted towards the higher λ and lower $\mathcal{E}$ domain as n is increased. Overall, it is indeed evident that $a_{\rm k}$ induces

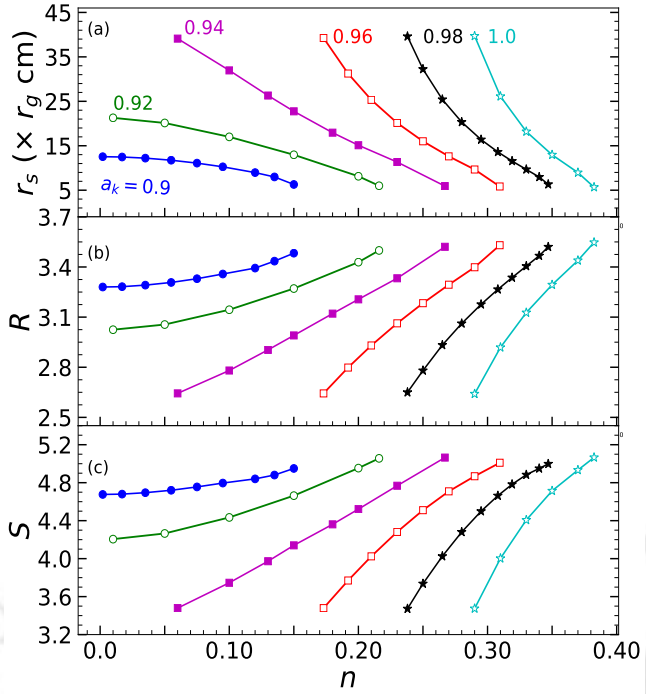

Figure 2.9: Plot of (a) r_s, (b) R, and (c) S as a function of n for flows with $\mathcal{E} = 1.0005$ and $\lambda = 2.2$. In each panel, filled circles (blue), open circles (green), filled squares (magenta), open squares (red), filled asterisks (black), and open asterisks (cyan) joined using solid curves represent results for $a_{\rm k} = 0.9, 0.92, 0.94, 0.96, 0.98$ and 1.0, respectively. See text for details.

effects opposite to n in deciding the shock parameter space around KTN black holes.

2.5 Radiative emissions in KTN spacetime

During the course of the accretion, the density (ρ) and temperature (T) of the infalling matter are increased as flow proceeds towards the BH. This usually happens due to the overall geometrical compression experienced by a convergent flow. In addition, when the flow variables undergoes discontinuous transition, both density and temperature are enhanced further at the post-shock region due to shock compression. Because of these, the flow emits high energy radiations as the relevant radiative cooling mechanisms directly depend on ρ and T (Das, 2007; Dihingia et al., 2020c). As the accretion flow contains both species, namely electrons and ions, the free-free emission seems to be potentially viable. Hence, we consider Bremsstrahlung radiation as an active radiative mechanism present inside the disk and calculate the total luminosity (L) as,

$$L = 2\int_0^{\infty}\int_{r_{\rm H}^{\rm KTN}}^{r_{\rm edge}}\int_0^{2\pi}(r+\eta^2/r)H\epsilon(\nu_e)d\nu_o dr d\phi. \tag{2.17}$$

Here, $\epsilon(\nu)$ is the Bremsstrahlung emission rate per unit volume per unit time per unit frequency (Vietri, 2008) and is given by,

$$\epsilon(\nu) = \frac{32\pi\tilde{e}^6}{3m_e c^3}\left(\frac{2\pi}{3k_B m_e T_e}\right)^{1/2} Z_i^2 n_e n_i g_{br} e^{-(h\nu/k_B T_e)}, \tag{2.18}$$

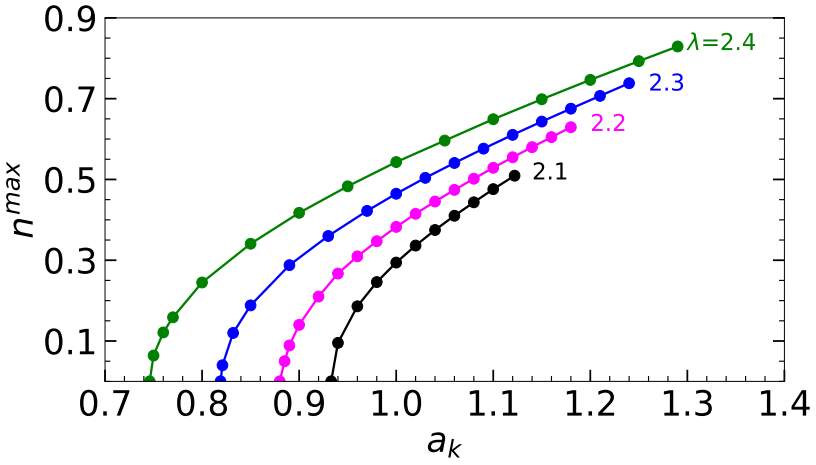

Figure 2.10: Variation of the maximum value of NUT-parameter ($n^{\rm max}$) as a function of Kerr parameter (a_k) that admit shocks. Here, the flow energy is kept fixed as $\mathcal{E} = 1.0005$. Filled circles connected using solid curves in black, magenta, blue and green represent results for $\lambda = 2.1, 2.2, 2.3$, and 2.4, respectively. See text for details.

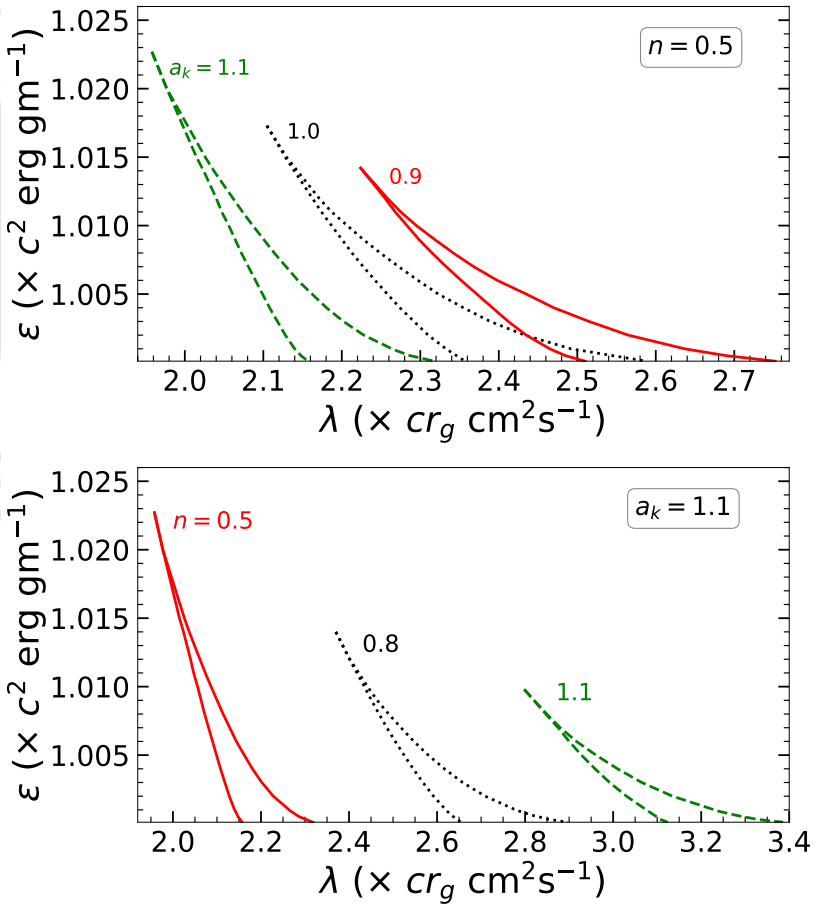

Figure 2.11: Modifications of the parameter space for shock in $\lambda - \mathcal{E}$ plane. In the upper panel, NUT parameter is set as $n = 0.5$ and the effective area bounded by red, black and green curves denote results for $a_{\rm k} = 0.9, 1.0$, and 1.1, respectively. In the bottom panel, Kerr parameter is chosen as $a_{\rm k} = 1.1$ and the region separated using red, black and green boundaries are obtained for $n = 0.5, 0.8$, and 1.1, respectively. See text for details.

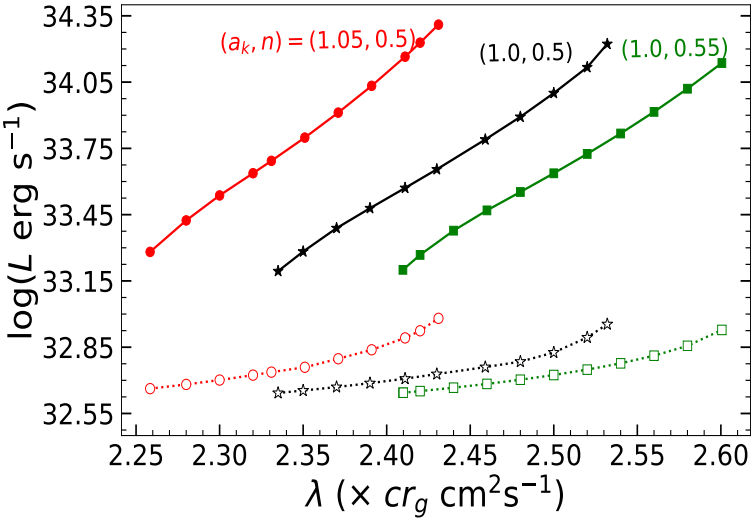

Figure 2.12: Variation of disk luminosity (L) as a function of λ for flows of energy $\mathcal{E} = 1.005$. Results depicted using filled circles, filled asterisks and filled squares are obtained for shocked accretion solutions, whereas open circles, open asterisks and open squares are for shock free solutions. Different points joined using red, black, and green solid curves are for $(a_{\rm k}, n) = (1.05, 0.5)$, $(1.00, 0.5)$, and $(1.00, 0.55)$, respectively. Here, we set $\dot{m} = 0.1$ and $M_{\rm BH} = 10 M_{\odot}$. See text for details.

where m_e and $\tilde{e}$ are mass and charge of the electron, k_B is the Boltzmann constant, h is the Planck's constant, ν is the frequency, Z_i is the charge of ion, and g_{br} is the Gaunt factor (Karzas & Latter, 1961) assumed as unity in this work. We estimate the electron temperature as $T_e = \sqrt{(m_e/m_p)}T$ (Chattopadhyay & Chakrabarti, 2002), where m_p is the ion mass and T refers the flow temperature. The emitted frequency is obtained as $\nu_e = (1+z)\nu_o$, where ν_o is the observed frequency and z denotes the red-shift factor. Following the approach of (Luminet, 1979; Dihingia et al., 2020b), we determine z considering fixed inclination angle $\theta_0 = \pi/4$ for the KTN BH while calculating the disk luminosity (see also Appendix-A). In this work, we choose $r_{\rm edge} = 1500$, and $M_{\rm BH} = 10 M_{\odot}$ all throughout unless stated otherwise.

In Fig. 2.12, we present the variation of luminosity (L) with flow angular momentum λ for various combination of $(a_{\rm k}, n)$, which are marked. Here, we choose $\mathcal{E} = 1.005$, and rate $\dot{m} = 0.1$. Filled points joined using solid curve denote the results corresponding to the shocked accretion solutions, whereas open points joined by the dotted curve are for shock free solutions (see Fig. 2.3). In the figure, it is evident that the disk luminosity for shocked accretion solutions always remains higher compared to the shock free solutions. Following this, we argue that the accretion solutions containing shock waves are potentially preferred in examining the energetics of the KTN BH sources. We also find that for a given set of $(a_{\rm k}, n)$, L increases with λ when flows harbor shocks, however, such increase is merely noticeable for flows having no shocks. In reality, for a given set of $(\mathcal{E}, a_{\rm k}, n)$, the shock radius (equivalently the size of the PSC) increases with λ (see Fig. 2.6 and 2.7) and therefore, density and temperature profiles continue to remain higher within the PSC that eventually increase the disk luminosity.

2.6 Chapter conclusions

In this Chapter, we examine the structure of relativistic advective accretion flow around KTN BH that possess shock waves. During the course of accretion, inflowing matter experiences the centrifugal repulsion that eventually triggered the shock transition. The dynamical shocked accretion solution overall includes the explicit dependence on energy ($\mathcal{E}$) and angular momentum (λ) of the flow as well as Kerr parameter ($a_{\rm k}$) and NUT parameter (n) of black hole. As part of the formalism, we adopt the relativistic EoS that satisfactorily describes the thermodynamical state of the accreting matter. The obtained results are summarized as follows.

We find that accretion flow around KTN BH possesses either single or multiple critical points depending on the input parameters. We further observe that the nature of the flow solution alters as the spin parameter ($a_{\rm k}$) and NUT parameter (n) are varied (see Figs. 2.1-2.2). When multiple critical points exist, accretion flow experiences discontinuous transition of the flow variables in the form of shock wave, provided relativistic shock conditions are satisfied (see Fig. 2.3). We calculate the accretion solution containing shock waves and examine the shock properties, *i.e.*, shock location (r_s), compression ratio (R), and shock strength (S) in terms of the input parameters (Figs. 2.4-2.9).

Moreover, We notice that shock-induced global accretion solutions are not the isolated solutions, instead they exist for a wide range of the input parameters. We identify the effective domain of the parameter space in $\lambda-\mathcal{E}$ plane, that admits shocked accretion solutions. Further, we examine the modification of the parameter space due to the variation of $(a_{\rm k}, n)$ and find that $a_{\rm k}$ and n act oppositely in deciding the shock parameter space (see Fig. 2.11). Then, We compute the maximum NUT parameter ($n^{\rm max}$) for shock as a function of $a_{\rm k}$, and find that shock solutions continue to exist for KTN BH with $a_{\rm k} > 1$ as opposed to the Kerr BHs having $a_{\rm k} < 1$ (see Fig. 2.10).

Finally, we calculate the disk luminosity (L) corresponding to the Bremsstrahlung processes. We observe that L is always higher for flows possessing shock waves compared to the shock free solutions (see Fig. 2.11).

Needless to mention that the present formalism is developed based on some simplifying assumptions. We neglect viscosity and radiative cooling mechanisms, namely Synchrotron and Compton cooling processes, although they are expected to play viable role in regulating the disk dynamics. In addition, we ignore the magnetic fields as well. However the basic conclusion of this work will not alter at least qualitatively upon involving all these physical processes.

Indian Institute of Technology Guwahati

Chapter 3

Investigation of relativistic hot accretion flow around Kerr-like wormhole

In the standard general relativistic framework, a massive compact object at the center of the accreting system plays a central role in the accretion process. In this direction, most of the studies have been done considering the compact objects to be a BH (Pringle & Rees, 1972; Shakura & Sunyaev, 1973; Novikov & Thorne, 1973). However, from the observational point of view, it is not confirmed that the central gravitating object is the BH, it may be any consistent solution of general relativity or other gravity theory, that seems to mimic the BH spacetime in the asymptotic region. Meanwhile, recent observations of BH shadows by the EHT Collaboration (2019a, 2022a) have opened up the possibility of detecting the direct signature of strong gravity. In recent years, the study of compact objects within the framework of general relativity has gained immense interest, particularly through accretion dynamics. It is worth mentioning that BHs need not be the only accreting objects in the universe, instead there may be other categories of hypothetical exotic compact objects (ECOs) (see section 1.2 for detailed discussions on ECOs), which can not be ruled out by theory to date. Meanwhile, numerous attempts along this line were carried out adopting various gravity theories, such as higher dimensional braneworld gravity (Pun et al., 2008; Heydari-Fard, 2010), Chern-Simons modified gravity (Harko et al., 2010), Hořava gravity (Lü et al., 2009), more exotic boson stars (Torres, 2002; Guzmán, 2006), wormholes (Harko et al., 2009b), gravastars (Harko et al., 2009a), quark stars (Kovács et al., 2009).

Indeed, rotating Damour Solodukhin wormhole (RDSWH) (Bueno et al., 2018) is another solution of Einstein's field equations, which differs from the Kerr BH by a dimensionless parameter β. Therefore, it has been an active area of research to distinguish the RDSWHs from Kerr BHs by means of various diagnostics, such as echoes (Bueno et al., 2018), shadows (Amir et al., 2019; Kasuya & Kobayashi, 2021), and accretion disk properties (Karimov et al., 2019). However, a complete hydrody-

namical analysis of the accretion process is still pending in the RDWH background. This motivates us to investigate the hydrodynamic properties of accretion flow around Kerr-like WH in full general relativistic framework.

Therefore, in this Chapter, we study relativistic, low angular momentum, inviscid advective accretion flows around a stationary, axisymmetric Kerr-like WH in steady state conditions. Using the relativistic EoS, we self-consistently solve the governing equations and, for the first time, we obtain all possible classes of global accretion solutions, including transonic and subsonic flows. We analyze their dynamical and thermodynamical properties as functions of flow properties, namely energy ($\mathcal{E}$), angular momentum (λ), and WH properties ($a_{\rm k}$, β). Furthermore, we classify the nature of the solutions by mapping the parameter space in the λ–$\mathcal{E}$ and $a_{\rm k}-\beta$ plane to identify distinct regions of different flow topologies. Finally, we calculate the disk luminosity (L) considering free-free emissions for transonic solutions, as these solutions are astrophysically relevant. Furthermore, we discuss the implications of our model formalism in the context of astrophysical applications.

3.1 Background geometry

In order to start with, we consider a stationary, axisymmetric, Kerr-like WH spacetime (Bueno et al., 2018), where the spacetime interval is expressed as,

$$\begin{aligned} ds^2 =& g_{\mu\nu}dx^\mu dx^\nu \\ =& g_{tt}dt^2 + g_{rr}dr^2 + 2g_{t\phi}dtd\phi + g_{\phi\phi}d\phi^2 + g_{\theta\theta}d\theta^2. \end{aligned} \tag{3.1}$$

Here, the coordinate r globally defines the WH spacetime (see section 1.2.1 for detailed properties) and varies in the range $r_{\rm Th} \leq |r| \leq \infty$, where $r_{\rm Th}$ denotes throat radius. In both cases, the wormhole spacetime is globally static, and the time-like Killing vector remains time-like everywhere. On the contrary, in the black hole scenario, time-like spacetime becomes space-like beyond the horizon. The metric components in both sides of the WH throat are obtained in terms of Boyer & Lindquist (1967) coordinates, which are given by,

$$\begin{aligned} g_{tt}|_\pm &= -(1-\frac{2r}{\Sigma}) \;\; ; \quad g_{t\phi}|_\pm = -\frac{2a_{\rm k}r\sin^2\theta}{\Sigma} \; ; \\ g_{rr}|_\pm &= \frac{\Sigma}{\Delta} \; ; \; g_{\theta\theta}|_\pm = \Sigma; \\ g_{\phi\phi}|_\pm &= (r^2 + a_{\rm k}^2 + \frac{2a_{\rm k}^2 r\sin^2\theta}{\Sigma})\sin^2\theta, \end{aligned}$$

where, $\Sigma = r^2 + a_{\rm k}^2\cos^2\theta$, $\Delta = r^2 - 2r(1+\beta^2) + a_{\rm k}^2$, $a_{\rm k}$ is the spin parameter (equivalently Kerr parameter), and β is the dimensionless parameter. In these analysis, we follow the sign convention as $(-,+,+,+)$ and adopt a unit system $M_{\rm WH} = G = c = 1$, where $M_{\rm WH}$ denotes the WH mass. In this unit system, length, time, and angular momentum are expressed in units of $GM_{\rm WH}/c^2$, $GM_{\rm WH}/c^3$, and $GM_{\rm WH}/c$, respectively. Here, we refer '+' to Zone-I and '−' to Zone-II as illustrated in Fig. 1.4. For a limiting value $\beta = 0$, the Kerr-like WH turns out to be a Kerr BH.

The property of a stationary axisymmetric spacetime is the existence of two commuting killing vectors along (t, ϕ) directions. The other two components (r, θ) are mutually orthogonal to each other. The throat radius for thiw Wh is located at

$r_{\rm Th} = (1+\beta^2)^2 + \sqrt{(1+\beta^2)^2 - a_{\rm k}^2}$. In this Chapter, we consider traversable WH, where, depending on the appropriate boundary conditions, accreting matter from one Zone can smoothly pass to the other Zone via throat. Hence, in order to study the properties of accretion flow, we analyze the governing equations for both sides (Zone-I and Zone-II) of the throat.

3.2 Assumptions and governing equations

We consider a low angular momentum, steady, inviscid, axisymmetric, advective accretion flow around a WH. In addition, the flow is assumed to remain confined at the equatorial plane of the central object and flow does not suffer energy dissipation due to various physical processes, namely viscosity, radiative cooling and magnetic fields.

In the general relativistic hydrodynamic framework, the energy-momentum tensor and four current are given by,

$$T^{\mu\nu} = (e+p)u^\mu u^\nu + pg^{\mu\nu} \quad \text{and} \quad j^\mu = \rho u^\mu, \tag{3.2}$$

where e, p, ρ, and u^μ denote the total energy density, pressure, mass density and four velocities of the perfect fluid, respectively and the spacetime indices μ and ν run from 0 to 3.

The hydrodynamical accretion flow is governed by conservation of energy-momentum and mass flux equations, which are given by,

$$T^{\mu\nu}_{;\nu} = 0 \quad \text{and} \quad (\rho u^\nu)_{;\nu} = 0. \tag{3.3}$$

Here, the time-like velocity field obeys the condition $u_\mu u^\mu = -1$. We use the projection operator defined as $h^i_\mu = \delta^i_\mu + u^i u^\mu$ to take the projection of the conservation equation on the spatial hypersurface and obtain the Euler equation as,

$$h^i_\mu T^{\mu\nu}_{;\nu} = (e+p)u^\nu u^i_{;\nu} + (g^{i\nu} + u^i u^\nu)p_{,\nu} = 0. \tag{3.4}$$

Note that the projection operator also satisfies the condition $h^i_\mu u^\mu = 0$ which ensures that the projection operator and the four velocity remain orthogonal to each other. Further, we project the conservation equation along u^μ and obtain the first law of thermodynamics as,

$$u_\mu T^{\mu\nu}_{;\nu} = u^\nu \left[\left(\frac{e+p}{\rho} \right) \rho_{,\nu} - e_{,\nu} \right] = 0. \tag{3.5}$$

In this work, we assume the flow to remain confined around the disk equatorial plane and hence, we choose $\theta = \pi/2$ which leads to $u^\theta = 0$. Further, following (Lu, 1985), we define the three radial velocity of the fluid in the co-rotating frame as $v^2 = \gamma_\phi^2 v_r^2$, where $\gamma_\phi^2 = 1/(1-v_\phi^2)$, $v_\phi^2 = (u^\phi u_\phi)/(-u^t u_t)$, and $v_r^2 = (u^r u_r)/(-u^t u_t)$, respectively. The radial Lorentz factor $\gamma_v^2 = 1/(1-v^2)$ and the total bulk Lorentz factor is $\gamma = \gamma_\phi \gamma_v \gamma_\theta$. With the above definitions of velocities, we obtain the radial component of the momentum equation from Eq. (3.4) for $i = r$ as,

$$v\gamma_v^2 \frac{dv}{dr} + \frac{1}{h\rho}\frac{dp}{dr} + \frac{d\Phi_{\rm e}^{\rm eff}}{dr} = 0, \tag{3.6}$$

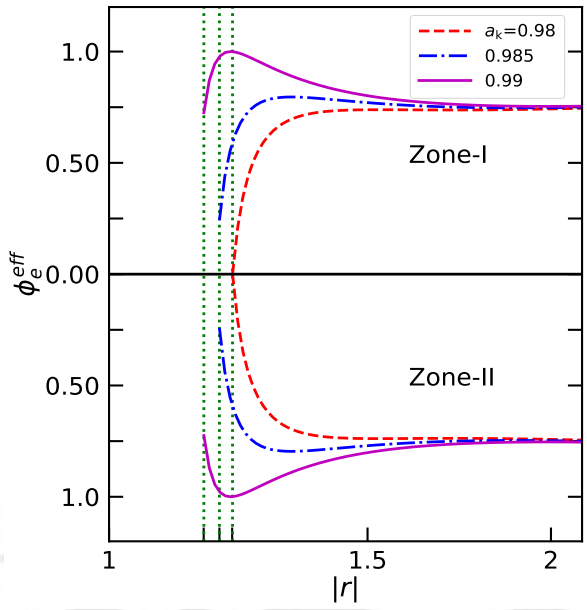

Figure 3.1: Variation of effective potential ($\Phi_{\rm e}^{\rm eff}$) as function radial coordinate ($|r|$; modulus is used for the simultaneous representation of Zone-I and Zone-II) for angular momentum $\lambda = 2.20$. Dashed (red), dot-dashed (blue) and solid (magenta) curves denote results corresponding to $a_{\rm k} = 0.98$, 0.985, and 0.99, respectively, and dotted (green) vertical lines indicate the respective throat radius as $r_{\rm Th} = 1.2137$, 1.1890, and 1.1603. See the text for the details.

where $h\,[= (e+p)/\rho]$ is the specific enthalpy, $\Phi_{\rm e}^{\rm eff}$ refers the effective potential (Dihingia et al., 2018) at the disk equatorial plane and is given by,

$$\Phi_{\rm e}^{\rm eff} = 1 + \frac{1}{2}\ln\left[\frac{r(a_{\rm k}^2 + r(r-2))}{a_{\rm k}^2(r+2) - 4a_{\rm k}\lambda + r^3 - \lambda^2(r-2)}\right]. \tag{3.7}$$

Needless to mention that the overall characteristics of the accretion flow crucially depend on the nature of the gravitational potential outside WH under consideration. Hence, we examine the effective potential ($\Phi_{\rm e}^{\rm eff}$) in Fig. 3.1, where the variation of $\Phi_{\rm e}^{\rm eff}$ with radial coordinate (r) is illustrated for a fixed angular momentum $\lambda = 2.20$. In the figure, the obtained results are plotted with dashed (red), dot-dotted (blue) and solid (magenta) curves for $a_{\rm k} = 0.98$, 0.985, and 0.99, respectively. The dotted (green) vertical lines denote the throat radius ($r_{\rm Th}$) of WH that solely depends on both $a_{\rm k}$ and β, respectively. Here, we choose $\beta = 0.05$ and find $r_{\rm Th} = 1.2137$, 1.1890, and 1.1603 for the chosen spin parameters ($a_{\rm k}$) in increasing order. Note that the horizontal solid (back) line separates Zone-I from Zone-II on both sides of the WH throat. Figure evidently indicates that the potential is symmetric in both sides (Zone-I and Zone-II) of WH throat. Using Eq. (3.5), we obtain the entropy generation equation along the radial direction as,

$$\left(\frac{e+p}{\rho}\right)\frac{d\rho}{dr} - \frac{de}{dr} = 0. \tag{3.8}$$

The stationary and axisymmetric spacetime under consideration is associated with two Killing vectors due to its symmetries. This yields two conserved quantities, which are given by,

$$-hu_t = \mathcal{E} \quad ; \quad hu_\phi = \mathcal{L}, \tag{3.9}$$

where, $\mathcal{E}$ is the Bernoulli constant (equivalently specific energy) and $\mathcal{L}$ is the bulk angular momentum per unit mass of the flow. We express the specific angular momentum of the flow as $\lambda = \mathcal{L}/\mathcal{E} = -u_\phi/u_t$, which is also a conserved quantity for an inviscid accretion flow. We integrate Eq. (3.3) to obtain another constant of motion in the form of mass accretion rate ($\dot{M}$) and is given by,

$$\dot{M} = -4\pi r \rho u^r H. \tag{3.10}$$

In this work, we express the mass accretion rate in dimensional form as $\dot{m} = \dot{M}/\dot{M}_{\rm Edd}$, where $\dot{M}_{\rm Edd}$ ($= 1.44 \times 10^{18}(M_{\rm WH}/M_\odot)$ gm s^{-1}) is the Eddington accretion rate, $M_\odot$ being the solar mass. In Eq. (3.10), H refers the local half-thickness of the accretion disk. Following (Riffert & Herold, 1995; Peitz & Appl, 1997), we compute H assuming the flow to maintain hydrostatic equilibrium in the vertical direction, and is given by

$$H = \sqrt{\frac{pr^3}{\rho F}}; \quad F = \frac{1}{1-\lambda\Omega} \times \frac{(r^2+a_{\rm k}^2)^2 + 2\Delta a_{\rm k}^2}{(r^2+a_{\rm k}^2)^2 - 2\Delta a_{\rm k}^2}, \tag{3.11}$$

where Ω [$= (2a_{\rm k}+\lambda(r-2))/(a_{\rm k}^2(r+2)-2a_{\rm k}\lambda+r^3)$] is the angular velocity of the accreting matter. We close the Eqs. (3.3) and (3.10) adopting the relativistic EoS (Chattopadhyay & Ryu, 2009) that relates local energy density (e), pressure (p) and mass density (ρ) as,

$$e = \frac{\rho f}{\tau}, \quad p = \frac{2\rho\Theta}{\tau}, \tag{3.12}$$

with $\tau = 1 + m_p/m_e$ and

$$f = \left[1 + \Theta\left(\frac{9\Theta+3}{3\Theta+2}\right)\right] + \left[\frac{m_p}{m_e} + \Theta\left(\frac{9\Theta m_e + 3m_p}{3\Theta m_e + 2m_p}\right)\right],$$

where m_p and m_e denote the masses of ion and electron, respectively, and Θ ($= k_{\rm B}T/m_e c^2$) is the dimensionless temperature. In accordance with relativistic EoS, the speed of sound is expressed as $C_s = \sqrt{2\Gamma\Theta/(f+2\Theta)}$, where Γ [$= (1+N)/N$] refers the adiabatic index and N [$= (1/2)(df/d\Theta)$] is the polytropic index of the flow, respectively (Dihingia et al., 2019a). Using Eq. (3.8), we estimate the measure of entropy by calculating the entropy accretion rate ($\dot{\mathcal{M}}$) (Chattopadhyay & Ryu, 2009; Dihingia et al., 2020a), which is given by,

$$\dot{\mathcal{M}} = \exp(k_1)\Theta^{3/2}(2+3\Theta)^{3/4}\left(3\Theta + \frac{2m_p}{m_e}\right)^{3/4} u^r r H, \tag{3.13}$$

where $k_1 = [f - (1 + m_p/m_e)]/2\Theta$. Note that for a non-dissipative flow characterized with a given set of energy ($\mathcal{E}$) and angular momentum (λ), $\dot{\mathcal{M}}$ remains conserved all throughout the disk.

We simplify Eqs. (3.6), (3.8), (3.9), (3.10) and (5.11) and obtain the wind equation as,

$$\frac{dv}{dr} = \frac{\mathcal{N}}{\mathcal{D}}, \tag{3.14}$$

where the numerator ($\mathcal{N}$) is given by,

$$\mathcal{N} = \frac{2C_s^2}{\Gamma+1}\left(\frac{1}{2\Delta}\frac{d\Delta}{dr} + \frac{3}{2r} - \frac{1}{2F}\frac{dF}{dr}\right) - \frac{d\Phi_{\rm e}^{\rm eff}}{dr}, \tag{3.15}$$

and the denominator ($\mathcal{D}$) is given by,

$$\mathcal{D} = \gamma_v^2 \left(v - \frac{2C_s^2}{v(\Gamma + 1)} \right). \tag{3.16}$$

Further, using Eqs. (3.10), (3.11) and (3.14), we calculate the radial gradient of the dimensionless temperature as,

$$\frac{d\Theta}{dr} = \frac{-2\Theta}{2N+1} \left[\frac{1}{2\Delta}\frac{d\Delta}{dr} + \frac{3}{2r} + \frac{\gamma_v^2}{v}\frac{dv}{dr} - \frac{1}{2F}\frac{dF}{dr} \right]. \tag{3.17}$$

3.3 Solution methodology

During the course of accretion around WH, rotating flow from the outer edge ($r_{\rm edge}$) of the disk in Zone-I (Zone-II) starts accreting subsonically ($v < C_s$). Because of the strong gravity of WH, inward moving flow gradually gains its radial velocity and depending of the input parameters, namely $\mathcal{E}$, λ, $a_{\rm k}$ and β, flow may become super-sonic after crossing the critical point ($r_{\rm c}$; flow of this kind is called transonic flow) or remain subsonic all throughout before approaching to the WH throat ($r_{\rm Th}$). Thereafter, flow is diverted to Zone-II (Zone-I) with identical velocity (v), temperature (Θ) and accretion rate ($\dot{M}$) at $r_{\rm Th}$ of Zone-I (Zone-II), and continues to proceed away from the WH till $r_{\rm edge}$. It is noteworthy that a transonic (subsonic) flow in Zone-I remains transonic (subsonic) in Zone-II, and vice versa.

3.3.1 Transonic accretion solutions

In general, the accretion flow around WH remains smooth everywhere ($r_{\rm Th} \leq r \leq r_{\rm edge}$), and hence, the flow radial velocity gradient (dv/dr) must be real and finite along the flow streamline. However, Eq. (3.16) clearly indicates that the denominator ($\mathcal{D}$) may vanish at some points. If so, numerator ($\mathcal{N}$) also vanishes there. Such a special point, where $\mathcal{N} = \mathcal{D} = 0$, is called as critical points ($r_{\rm c}$). Setting the condition $\mathcal{D} = 0$, we obtain the radial velocity ($v_{\rm c}$) of the flow at the critical point ($r_{\rm c}$) as,

$$v_{\rm c} = \sqrt{\frac{2}{\Gamma_{\rm c} + 1}} C_{\rm sc}. \tag{3.18}$$

Similarly, the condition $\mathcal{N} = 0$ yields the sound speed ($C_{\rm sc}$) at $r_{\rm c}$ as,

$$C_{\rm sc}^2 = \frac{\Gamma_{\rm c} + 1}{4} \left(\frac{d\Phi_{\rm e}^{\rm eff}}{dr} \right)_{\rm c} \left(\frac{1}{2\Delta}\frac{d\Delta}{dr} + \frac{3}{2r} - \frac{1}{2F}\frac{dF}{dr} \right)_{\rm c}^{-1}. \tag{3.19}$$

In Eqs. (3.18) and (3.19), quantities with subscript 'c' are evaluated at the critical point ($r_{\rm c}$).

As the radial velocity gradient (dv/dr) takes 0/0 form at r_c, we apply L'Hôpital's rule to evaluate $(dv/dr)_{\rm c}$ at $r_{\rm c}$. For a given set of input parameters ($\mathcal{E}$, λ, $a_{\rm k}$ and β), $(dv/dr)_{\rm c}$ yields two values. When both $(dv/dr)_{\rm c}$ are real and of opposite sign, the critical point is called as saddle type, whereas nodal type critical point is obtained if $(dv/dr)_{\rm c}$ are real and of the same sign. For spiral type critical point, $(dv/dr)_{\rm c}$ are imaginary. Needless to mention that saddle type critical points are stable, whereas

both nodal and spiral types critical points are unstable (Kato et al., 1993). Hence, saddle type critical points are specially relevant in the astrophysical context as transonic accretion solution can only pass through them. Now onwards, we refer saddle type critical points as critical points only unless stated otherwise. Furthermore, depending on the input parameters, flow may possess more than one critical points. When critical point forms close to throat, it is called as inner critical point ($r_{\rm in}$) and when it forms far away from the throat is referred as outer critical point ($r_{\rm out}$).

In order to obtain the self-consistent transonic solution around WH, we simultaneously solve Eq. (3.14) and Eq. (3.17) for a given set of input parameters ($\mathcal{E}$, λ, $a_{\rm k}$, β) in Zone-I (Zone-II). In doing so, we first integrate Eq. (3.14) and Eq. (3.17) starting from the critical point ($r_{\rm c}$) up to the outer edge of the disk ($r_{\rm edge}$) and then from $r_{\rm c}$ to $r_{\rm Th}$. Finally, we join these two segments of the solution to obtain the global transonic solution in Zone-I (Zone-II). It is worth mentioning that for a traversable WH, an accretion solution in Zone-I appears to be analogous in Zone-II.

3.3.2 Subsonic accretion solutions

Unlike transonic solution, subsonic solution does not pass through the critical point and hence, to obtain such solution uniquely, we require entropy accretion rate ($\dot{\mathcal{M}}$) as additional parameter along with the other input parameters. Therefore, for a set of input parameters ($\mathcal{E}$, λ, $a_{\rm k}$, β, and $\dot{\mathcal{M}}$), we integrate Eq. (3.14) and Eq. (3.17) starting from the outer edge of the disk ($r_{\rm edge}$) up to $r_{\rm Th}$. To start the integration, we tune the flow radial velocity ($v_{\rm edge}$) at $r_{\rm edge}$ to calculate $\Theta_{\rm edge}$ using Eq. (3.13), that renders smooth subsonic solution in the range $r_{\rm Th} \leq r \leq r_{\rm edge}$ in Zone-I (Zone-II). Note that for a given set of ($\mathcal{E}$, λ, $a_{\rm k}$, β), one can obtain a set of subsonic solutions around WH for different $\dot{\mathcal{M}}$ values.

3.4 Results

In this section, we present the results obtained form our model formalism that include the global solutions, parameter space and the emission properties of the accretion flow around WH.

3.4.1 Global transonic solutions

In Fig. 3.2, we present a typical global transonic accretion solution where Mach number ($M = v/C_s$) of the flow is plotted as function of the radial coordinate (r). Here, we choose $a_{\rm k} = 0.99$, and $\beta = 0.05$, and the solutions are computed for flows of energy $\mathcal{E} = 1.02$ and angular momentum $\lambda = 1.90$. For the chosen set of input parameters, we find that in Zone-I (upper panel), flow starts accreting subsonically from the outer edge of the disk ($r_{\rm edge}$) and gains radial velocity as it moves inward due the strong attraction of WH gravity. Eventually, flow changes its sonic state to become supersonic at the inner critical point at $r_{\rm in} = 1.7160$ and continues to accrete until it reaches the WH throat at $r_{\rm Th} = 1.1603$. In the figure, we present the accretion solution using the solid (blue) curve. The corresponding wind solution (from $r_{\rm Th}$ to $r_{\rm edge}$) is also depicted as shown by the dashed (red) curve. For the purpose of completeness, we present the flow solutions for Zone-II in the lower panel which is the mirror image of the flow solutions presented in the Zone-I. Now onwards, to avoid repetitions, we

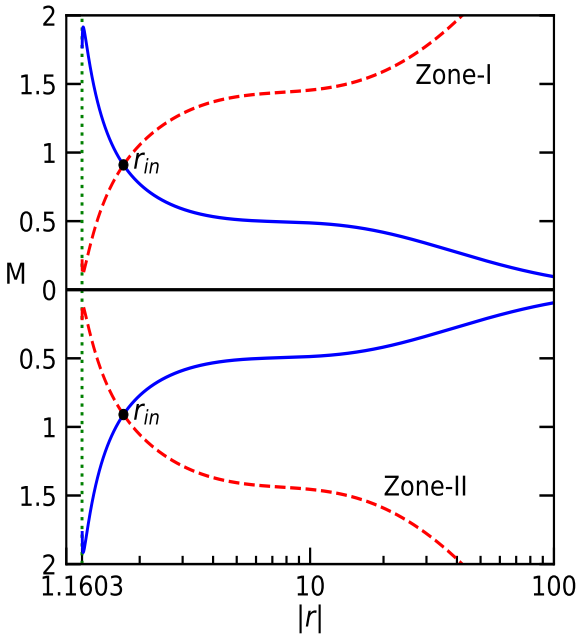

Figure 3.2: Variation of Mach no ($M = v/C_s$) as function of the modulus of radial coordinate ($|r|$) around WH. Here, we choose $\mathcal{E} = 1.02$, $\lambda = 1.90$, $a_{\rm k} = 0.99$, and $\beta = 0.05$, respectively. Solid (blue) and dashed (red) curves represent solutions corresponding to accretion and winds. Filled circles (black) refer to the inner critical points ($r_{\rm in}$) and dotted vertical line (green) denotes throat radius of WH. See the text for the details.

shall exclusively present the flow solutions in Zone-I only, unless stated otherwise. In Fig. 3.3, we display the variation of other flow variables with the radial coordinate (r) corresponding to the accretion solution presented in Fig. 3.2. In Fig. 3.3a, we depict the profile of density (ρ) variation for convergent accretion flow and observe that ρ increases as the flow moves towards WH. We put effort to represent the density profile using a power-law and the best fit is obtained as $\rho \propto r^{-(n+2/5)}$, where $n \sim 1$. This finding is consistent with the results reported in (Narayan & Yi, 1995a; Frank et al., 2002). Next, we show the radial profile of pressure (p) and temperature (T) of the flow in Fig. 3.3b-c, and attain the optimal power-law fit as $p \propto r^{-(n+1)}$ and $T \propto r^{-(n-1/3)}$, respectively. It is noteworthy that we observe poor fitting of the flow variables at the inner part of the disk close to WH. This possibly happens due to that fact that the simple power-law fit fails to capture the complex nature of the flow characteristics in the vicinity of the WH.

3.4.2 Classification of global transonic solutions

Indeed, the nature of the transonic accretion solutions depends on the energy ($\mathcal{E}$) and angular momentum (λ) of the flow around WH. Towards this, in Fig. 3.4a, we separate the effective domain of the parameter space in $\lambda - \mathcal{E}$ plane according to the nature of the transonic accretion solutions around WH. Here, we choose $a_{\rm k} = 0.99$ and $\beta = 0.05$, and identify four distinct regions in the parameter space that provide O-type, A-type, W-type and I-type transonic accretion solutions. For the purpose of representation, we depict the typical examples of transonic accretion solutions from these four regions in panels (b-e) of Fig. 3.4, where M is plotted as function of

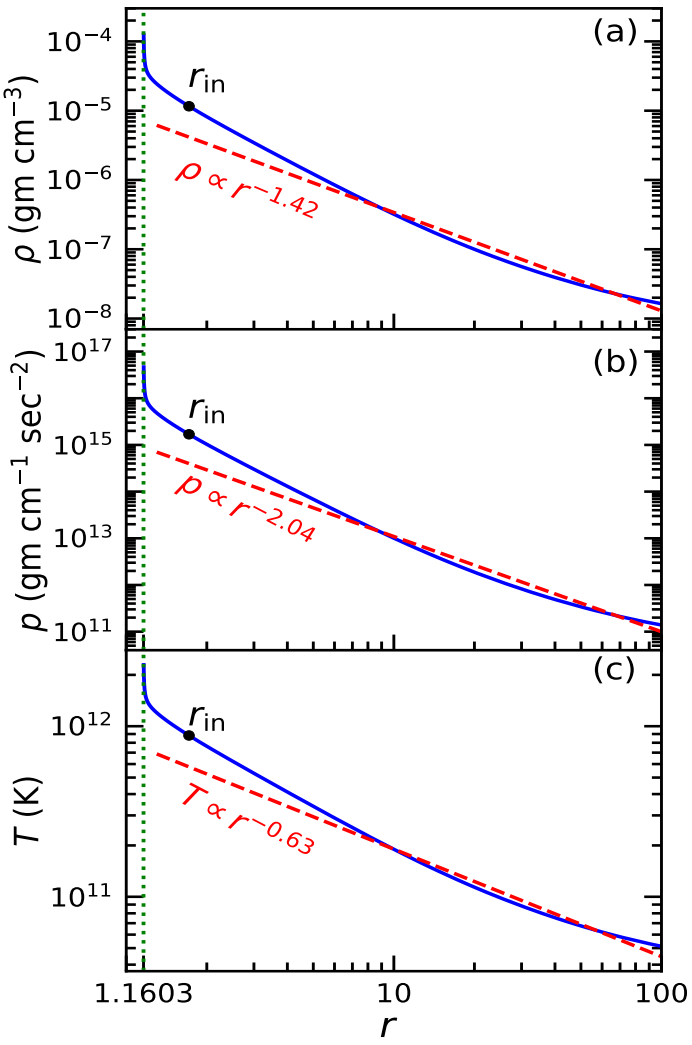

Figure 3.3: Variation of (a) density (ρ), (b) pressure (p), and (c) temperature (T) of the accretion flow as function of radial coordinate (r). Here. model parameters are chosen same as in Fig. 3.2. In each panel, dashed (red) curve represents the best fit power-law profile of the flow variables and filled circle (black) denotes the critical point $r_{\rm in} = 1.7160$. The vertical dotted lines (green) denote throat radius $r_{\rm Th} = 1.1603$. See the text for the details.

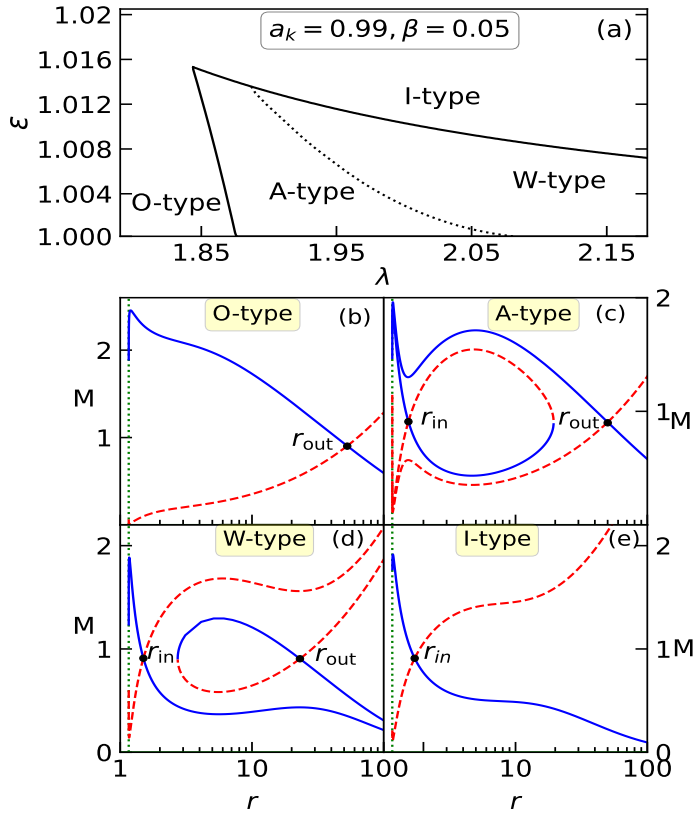

Figure 3.4: Sub-division of parameter space in $\lambda - \mathcal{E}$ plane according to the nature of the flow solutions around WH (panel a). Here, we choose $a_{\rm k} = 0.99$ and $\beta = 0.05$. Four distinct regions marked as O-type, A-type, W-type and I-type are identified and typical flow solutions (M vs. r) from these regions are depicted in panels (b-e), where solid (blue) and dashed (red) curves denote accretion and winds. Filled circles (black) refer critical points ($r_{\rm in}$ and/or $r_{\rm out}$) and vertical dotted lines (green) denote throat radius $r_{\rm Th} = 1.1603$. See the text for the details.

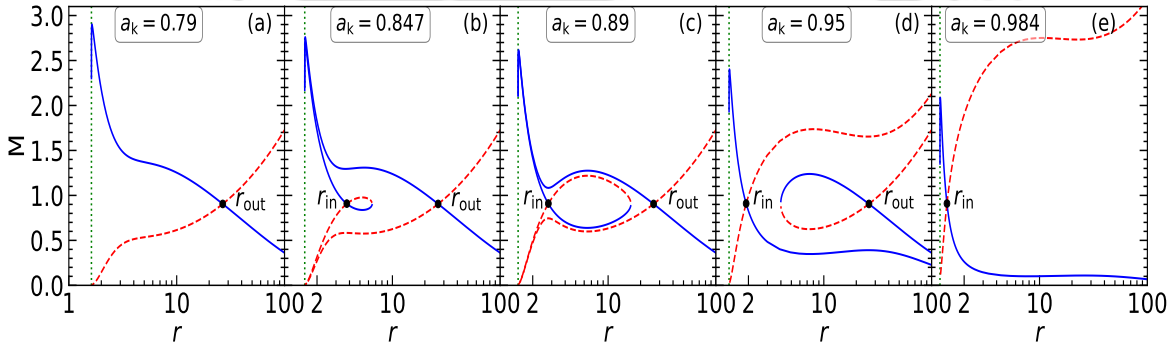

Figure 3.5: Modification of transonic accretion solutions (M vs r) with the increase of $a_{\rm k}$ as marked in each panel. Here, we fix the model parameters as $\mathcal{E} = 1.0084$, $\lambda = 2.1$, and $\beta = 0.05$, respectively. Solid (blue) curves denote accretion solutions, whereas dashed (red) curves are for winds. Filled circles refer critical points ($r_{\rm in}$ and/or $r_{\rm out}$). Dotted vertical line denotes the throat radius as (a) $r_{\rm Th} = 1.6196$, (b) $r_{\rm Th} = 1.5387$, (c) $r_{\rm Th} = 1.4639$, (d) $r_{\rm Th} = 1.3226$ and (e) $r_{\rm Th} = 1.1942$. See the text for the details.

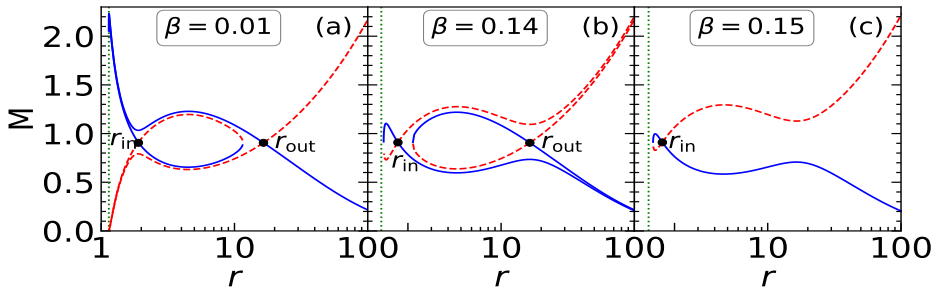

Figure 3.6: Same as Fig. 3.5, but for different β as marked in each panel. Here, we fix the model parameters as $\mathcal{E} = 1.0137$, $\lambda = 1.881$, and $a_{\rm k} = 0.99$, respectively. Dotted vertical line denotes the throat radius as (a) $r_{\rm Th} = 1.1418$, (b) $r_{\rm Th} = 1.2634$ and (c) $r_{\rm Th} = 1.2782$, respectively. See the text for the details.

r. These solutions are obtained for different sets of $(\lambda, \mathcal{E})$ chosen from the marked regions of the $\lambda - \mathcal{E}$ parameter space. In each panels, solid (blue) and dashed (red) curves represent flow solutions corresponding to accretion and wind, and filled circles denote the critical points ($r_{\rm in}$ and/or $r_{\rm out}$). In panel (b), we present the O-type solution which are obtained for $(\lambda, \mathcal{E}) = (1.70, 1.005)$ and the solution possesses outer critical point at $r_{\rm out} = 52.8253$ before advancing towards the WH throat ($r_{\rm Th}$). We calculate A-type solution for $(\lambda, \mathcal{E}) = (1.95, 1.005)$ and the obtained results are shown in panel (c). The solution of this kind contains both inner and outer critical points, and we find $r_{\rm in} = 1.5384$ and $r_{\rm out} = 50.0378$. The entropy accretion rate at $r_{\rm in}$ and $r_{\rm out}$ are computed as $\dot{\mathcal{M}}(r_{\rm in}) \equiv \dot{\mathcal{M}}_{\rm in} = 8.66 \times 10^7$ and $\dot{\mathcal{M}}(r_{\rm out}) \equiv \dot{\mathcal{M}}_{\rm out} = 7.337 \times 10^7$, respectively. Note that accretion solution passing through $r_{\rm out}$ successfully connects the outer edge of the disk ($r_{\rm edge}$) and the WH throat ($r_{\rm Th}$), where solution containing $r_{\rm in}$ fails to do so. Next, we obtain W-type solution for $(\lambda, \mathcal{E}) = (1.96, 1.01)$ that yields $r_{\rm in} = 1.4995$ and $r_{\rm out} = 23.1166$ (see panel (d)). We find that for W-type solutions, entropy accretion rate at $r_{\rm out}$ is higher than the entropy accretion rate at $r_{\rm in}$ as $\dot{\mathcal{M}}_{\rm out} = 11.474 \times 10^7$ and $\dot{\mathcal{M}}_{\rm in} = 8.2 \times 10^7$. We also notice that accretion solution possessing $r_{\rm out}$ can not extend up to the WH throat ($r_{\rm Th}$), however, it seamlessly connects $r_{\rm edge}$ and $r_{\rm Th}$ while passing through $r_{\rm in}$. Finally, the results corresponding to I-type solution is shown in panel (e) which possesses only inner critical point ($r_{\rm in}$), and results are obtained for $(\lambda, \mathcal{E}) = (1.9, 1.02)$ with $r_{\rm in} = 1.7160$.

3.4.3 Modification of global transonic solutions

It is intriguing to examine the role of $a_{\rm k}$ in deciding the nature of the accretion solution around WH. In order for that we fix the model parameters as $\mathcal{E} = 1.0084$, $\lambda = 2.1$, and $\beta = 0.05$ and calculate the flow solutions by tuning $a_{\rm k}$. The obtained results are depicted in Fig. 3.5, where solid curve denotes accretion solution and dashed curve is for wind. In panel (a), we obtain O-type solution for $a_{\rm k} = 0.79$ having outer critical point at $r_{\rm out} = 26.7261$ and throat radius at $r_{\rm Th} = 1.619$. When $a_{\rm k}$ is increased as 0.847, we find that inner critical point appears at $r_{\rm in} = 3.7780$ along with the outer critical point at $r_{\rm out} = 26.5471$, as shown in panel (b). For $a_{\rm k} = 0.89$, flow continue to possess multiple critical points at $r_{\rm in} = 2.7921$ and $r_{\rm out} = 26.4077$ (see panel c) and the overall character of the solution remains qualitatively same as in panel (b). As mentioned earlier that for accretion solutions of this kind, $\dot{\mathcal{M}}_{\rm in} > \dot{\mathcal{M}}_{\rm out}$. When $a_{\rm k}$ is

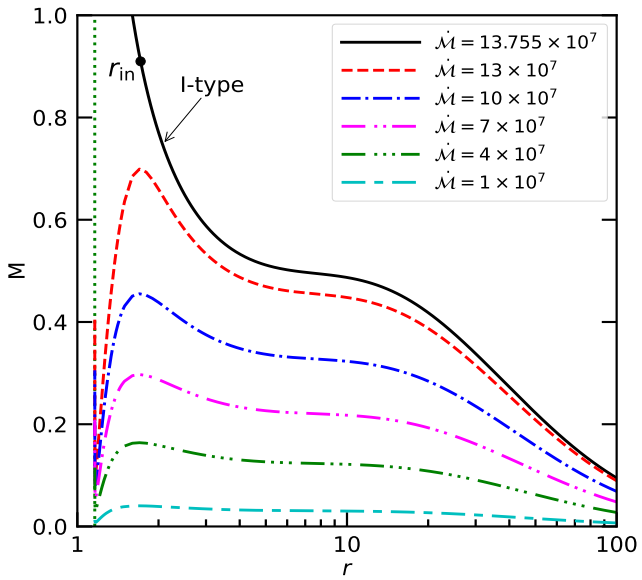

Figure 3.7: Variation of Mach number (M) as a function of radial coordinate (r) for subsonic solutions associated with I-type transonic accretion solution. Here, we choose the model parameters as $\mathcal{E} = 1.02$, $\lambda = 1.90$, $a_{\rm k} = 0.99$ and $\beta = 0.05$. Dashed (red), dot-dashed (blue), dot-dot-dashed (magenta), dot-dot-dot-dashed (green) and small-big-dashed (cyan) curves are for $\dot{\mathcal{M}} = 13 \times 10^7$, 10×10^7, 7×10^7, 4×10^7, and 1×10^7, respectively. Solid (black) curve refers the I-type transonic accretion solution (see Fig. 3.4e) possessing entropy accretion rate as $\dot{\mathcal{M}} = 13.755 \times 10^7$. Dotted vertical line denotes the throat radius $r_{\rm Th} = 1.1603$. See the text for the details.

increased further as 0.95, the character of the solution alters, although it continues to possess multiple critical points at $r_{\rm in} = 1.9050$ and $r_{\rm out} = 26.2056$ (see panel d). For accretion solutions similar to this, we obtain $\dot{\mathcal{M}}_{\rm out} > \dot{\mathcal{M}}_{\rm in}$. Beyond a critical limit, such as $a_{\rm k} = 0.984$, we notice that the outer critical point disappears and the flow solution passed through the inner critical point only at $r_{\rm in} = 1.3860$, as depicted in panel (e).

For the purpose of completeness, we examine the effect of β in deriving the flow solutions. Towards this, we choose the model parameters as $\mathcal{E} = 1.0137$, $\lambda = 1.881$ and $a_{\rm k} = 0.99$, and vary β to compute the solutions. In Fig. 3.6, we present the obtained results where β is increased in succession. We observe that $\beta = 0.01$ provides A-type solution possessing multiple critical points at $r_{\rm in} = 1.9016$ and $r_{\rm out} = 16.5016$, as shown in Fig. 3.6a. As β is increased to 0.14, the nature of the accretion solution alters to W-type with $r_{\rm in} = 1.6829$ and $r_{\rm out} = 16.4300$ (see Fig. 3.6b). For $\beta = 0.15$, the outer critical point disappears and we obtain solution containing only inner critical point at $r_{\rm in} = 1.6202$.

3.4.4 Subsonic accretion solutions

As already mentioned, besides the transonic solutions, subsonic solutions are also exist around WH. Accordingly, we examine the nature of the subsonic solutions for flows with fixed model parameter $(\mathcal{E}, \lambda, a_{\rm k}, \beta)$. For this, we begin with a reference I-type transonic accretion solution obtained for $\mathcal{E} = 1.02$, $\lambda = 1.90$, $a_{\rm k} = 0.99$ and $\beta = 0.05$ (see Fig. 3.4e). The entropy accretion rate for this solution is computed as

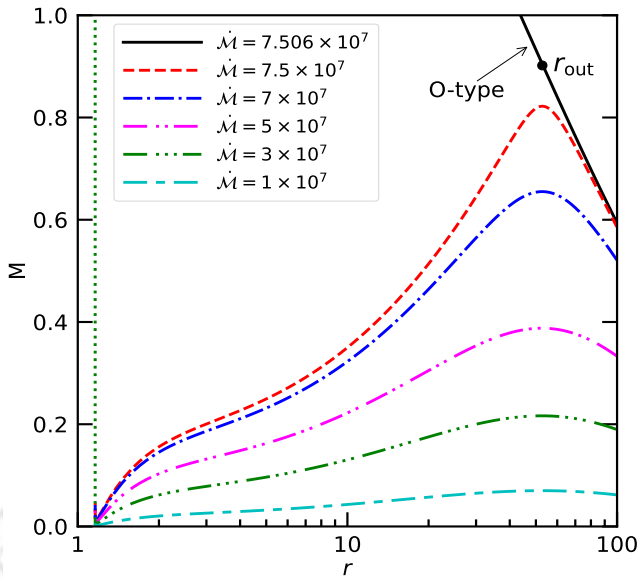

Figure 3.8: Same as Fig. 3.7, but for subsonic solution associated with O-type transonic accretion solution (see Fig. 3.4b). Here, we choose $\mathcal{E} = 1.70$, $\lambda = 1.005$, $a_{\rm k} = 0.99$ and $\beta = 0.05$. Dashed (red), dot-dashed (blue), dot-dot-dashed (magenta), dot-dot-dot-dashed (green) and small-big-dashed (cyan) curves are for $\dot{\mathcal{M}} = 7.5 \times 10^7$, 7×10^7, 5×10^7, 3×10^7, and 1×10^7, respectively. Solid (black) curve refers the O-type transonic accretion solution with $\dot{\mathcal{M}} = 7.505 \times 10^7$. Dotted vertical line denotes the throat radius $r_{\rm Th} = 1.1603$. See the text for the details.

$\dot{\mathcal{M}} = 13.755 \times 10^7$. Now, we follow the method described in section 3.3.2 to calculate the subsonic accretion solution around WH by decreasing $\dot{\mathcal{M}}$ while keeping all the remaining model parameters unchanged. The obtained results are depicted in Fig. 3.7, where the results presented with dashed (red), dot-dashed (blue), dot-dot-dashed (magenta), dot-dot-dot-dashed (green) and small-big-dashed (cyan) curves are obtained for $\dot{\mathcal{M}} = 13 \times 10^7$, 10×10^7, 7×10^7, 4×10^7, and 1×10^7, respectively. Interestingly, we observe that for a given set of model parameters $(\mathcal{E}, \lambda, a_{\rm k}, \beta)$, $\dot{\mathcal{M}}$ always remains lower for subsonic solutions compared to the transonic solution (solid curve in black), which predominantly indicates that transonic solutions are thermodynamically preferred over the subsonic solutions because of their high entropy content. Further, in Fig. 3.8, we present the subsonic solution associated with the O-type transonic accretion solution. Here, the results are obtained by varying the entropy accretion rate as $\dot{\mathcal{M}} = 7.5 \times 10^7$, 7×10^7, 5×10^7, 3×10^7, and 1×10^7, keeping other model parameters fixed as $\mathcal{E} = 1.70$, $\lambda = 1.005$, $a_{\rm k} = 0.99$ and $\beta = 0.05$. As in Fig. 3.7, here also we observe that $\dot{\mathcal{M}}$ is lower for subsonic solutions compared to the transonic accretion solution (solid curve in black) suggesting that transonic accretion solution are preferred over the subsonic solutions.

3.4.5 Modification of parameter space for multiple critical points

It is noteworthy that depending on the model parameters, transonic flow possesses either single or multiple critical points. Following this, we identify the ranges of λ and $\mathcal{E}$ that render multiple critical points while keeping $a_{\rm k}$ and β fixed (see Fig. 3.4).

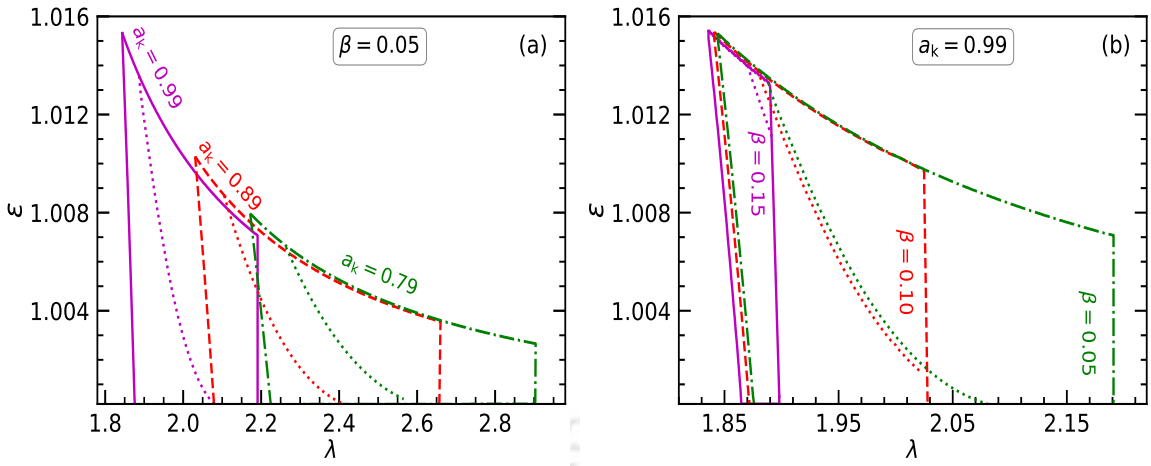

Figure 3.9: Parameter space for multiple critical points in $\lambda - \mathcal{E}$ plane for different (a) $a_{\rm k}$ and (b) β values. In panel (a), we choose $\beta = 0.05$ and the regions bounded with solid (magenta), dashed (red) and dot-dashed (green) curves are obtained for $a_{\rm k} = 0.99$, 0.89 and 0.79, respectively. Similarly, in panel (b), we fix $a_{\rm k} = 0.99$, and solid (magenta), dashed (red) and dot-dashed (green) curves separate the region for $\beta = 0.15$, 0.10 and 0.05, respectively. Dotted curve separates the A-type and W-type solutions in each parameter space. See the text for the details.

However, it is useful to examine the modification of $\lambda - \mathcal{E}$ parameter space due to the change of $a_{\rm k}$ and β values. Towards this, in Fig. 3.9a, we present how the effective domain of the parameter space alters due to the increase of $a_{\rm k}$ for a fixed β value as 0.05. Regions bounded with solid (magenta), dashed (red) and dot-dashed (green) curves are obtained for $a_{\rm k} = 0.99$, 0.89 and 0.79, respectively. Each parameter space is further subdivided using dotted curve that separates A-type solutions (left side) from the W-type solutions (right side). We also observe that flow continues to possess multiple critical points for higher $a_{\rm k}$, provided λ is relatively lower. This is expected because of the fact that the marginally stable angular momentum generally decreases with the increase of $a_{\rm k}$ due to the spin-orbit coupling embedded in the spacetime (Das & Chakrabarti, 2008). Similarly, in Fig. 3.9b, we present the variation of the parameter space for different β. Here, we fix $a_{\rm k} = 0.99$, and boundaries drawn with dot-dashed (green), dashed (red) and solid (magenta) curves separate the regions for $\beta = 0.05$, 0.10 and 0.15, respectively. We observe that for a fixed $a_{\rm k}$, the effective domain of the parameter space is shrunk with the increase of deformation parameter β.

Moreover, it is compelling to analyze the range of β that renders multiple critical points as well. In doing so, for the purpose of representation, we fix the energy of the flow as $\mathcal{E} = 1.004$, and freely vary angular momentum (λ) to find its minimum value ($\lambda_{\rm min}$) yielding multiple critical points for $\beta \geq 0$ and $0 \leq a_{\rm k} < 1$. Here, we focus on $\lambda_{\rm min}$ as it coarsely interprets the limiting value describing the quasi-radial nature of the flow containing multiple critical points. The obtained results are plotted in Fig. 3.10, where two-dimensional projection of the three-dimensional plot spanned with $a_{\rm k}$, β and $\lambda_{\rm min}$. In the figure, vertical colorbar denotes the range as $1.8 \leq \lambda_{\rm min} \leq 2.65$. Figure evidently indicates that the range of β is decreased with the increase of $a_{\rm k}$, and $\lambda_{\rm min}$ anti-correlates with $a_{\rm k}$.

Next, we put effort to calculate the upper limit of angular momentum ($\lambda_{\rm max}$) that

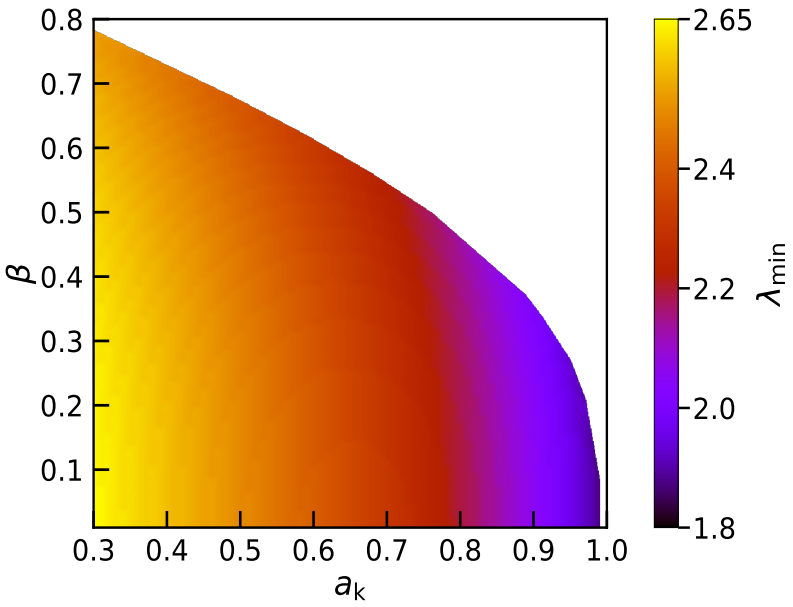

Figure 3.10: Two-dimensional projection of the three-dimensional plot of a_k, β and λ_{min} for solutions containing multiple critical points. Here, we choose energy $\mathcal{E} = 1.004$. The colorbar represents the range of minimum angular momentum (λ_{min}). See the text for the details.

renders multiple critical points. The obtained results are presented in Fig. 3.11, where we illustrate the variation of λ_{max} as function of β for different a_k values. Open circles, squares and asterisks joined with solid lines denote the results obtained for $a_k = 0.0$, 0.5 and 0.99, respectively. Here, energy of the flow is varied freely. We observe that for a fixed a_k, λ_{max} monotonically decreases with the increase of β, and as a_k is increased, the allowed range of β for multiple critical points decreases. We also notice that for a given β, when a_k is higher, λ_{max} becomes lower and vice versa.

3.5 Radiative emission properties

In this section, we examine the disk luminosity (L) focusing on free-free emission as it is regarded as one of the relevant radiative mechanism active inside the convergent single temperature accretion flow (Sarkar & Das, 2016; Okuda et al., 2019, and references therein). Accordingly, we calculate L as,

$$L = 2\int_0^{\infty}\int_{r_{\rm Th}}^{r_{\rm edge}}\int_0^{2\pi}(Hr)\epsilon(\nu_e)d\nu_o dr d\phi. \tag{3.20}$$

Here, $\epsilon(\nu)$ denotes the Bremsstrahlung emissivity at frequency ν and is given by (Vietri, 2008),

$$\epsilon(\nu) = \frac{32\pi\tilde{e}^6}{3m_e c^3}\left(\frac{2\pi}{3k_B m_e T_e}\right)^{1/2} Z_i^2 n_e n_i e^{-h\nu/k_B T_e} g_{br}, \tag{3.21}$$

where m_e and e are mass and charge of the electron, k_B is the Boltzmann constant, h is the Planck's constant, ν is the frequency, Z_i is the ion charge, and g_{br} is the Gaunt factor (Karzas & Latter, 1961) assumed to be unity. In this work, we consider single temperature flow and following (Chattopadhyay & Chakrabarti, 2002), we estimate electron temperature as $T_e = \sqrt{(m_e/m_p)}T$, where T denotes the flow temperature and

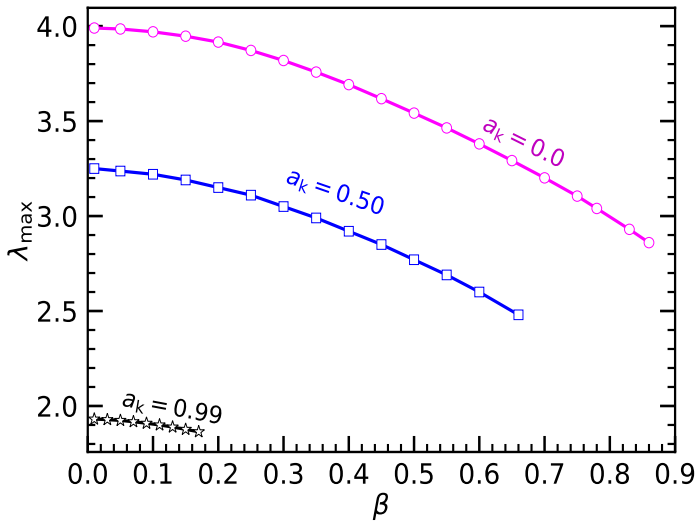

Figure 3.11: Variation of $\lambda_{\rm max}$ with β for three different values of $a_{\rm k}$ yielding solutions possessing multiple critical points. Open circles, squares and asterisks joined with solid lines represent results corresponding to $a_{\rm k} = 0.0, 0.50$, and 0.99, respectively. See the text for the details.

m_i is the ion mass. The emitted frequency (ν_e) is related to the observed frequency (ν_o) as $\nu_e = (1+z)\nu_o$, where z denotes the red-shift factor. Following (Luminet, 1979), we determine z considering fixed inclination angle $\theta_0 = \pi/4$ for Kerr-like WH. In addition, we choose $M_{\rm WH} = 10M_\odot$ and $\dot{m} = 0.1$ while computing disk luminosity.

We present the obtained results in Fig. 3.12, where the variation of disk luminosity (L) with β for different $a_{\rm k}$ is depicted. The results corresponding to I-type and O-type solutions are presented in panel (a) and (b). In both panels, open circles, squares and asterisks joined with solid lines denote results for $a_{\rm k} = 0.99$, 0.94 and 0.89, respectively. We find that for a fixed $a_{\rm k}$, L increases with the increase of β. Similarly, when β is kept fixed, L is seen to increase for higher $a_{\rm k}$. Overall, we observe that for a fixed set of $(a_{\rm k}, \beta)$, I-type solutions yields higher disk luminosity compared to the same obtained from O-type solutions. This happens because I-type solutions exhibit higher density profile compared to the O-type solutions as I-type flow remains subsonic in the range $r_{\rm in} < r \leq r_{\rm edge}$.

We also put effort to explain the luminosity of a compact object Cygnus X-3, using our model formalism. Indeed, the nature of the compact object in Cygnus X-3, whether it is a BH or a NS, remains an open question till date (Pahari et al., 2017, and references therein). Earlier, Szostek et al. (2008) investigated the X-ray and radio states of Cygnus X-3 and found that the correlation between radio and X-ray emissions closely resembles the features generally observed in BH binaries (such as GRS 1915+105, XTE J1550-564), yet differs significantly from those seen in neutron star binaries. In a subsequent effort, Zdziarski et al. (2013) examined the nature of the central source in Cygnus X-3 and indicated that central source possibly be a BH of mass $2.4^{+2.1}_{-1.1}M_\odot$ based on radio, infrared and X-ray data. However, the possibility of neutron star was not ruled out. Very recently, the Imaging X-ray Polarimetry Explorer (IXPE) has revealed Cyguns X-3 as a hidden Galactic ultra-luminous X-ray (ULX) source (Yang et al., 2023; Veledina et al., 2023). All these studies evidently indicate that the nature of the central source in Cygnus X-3 remains unclear and

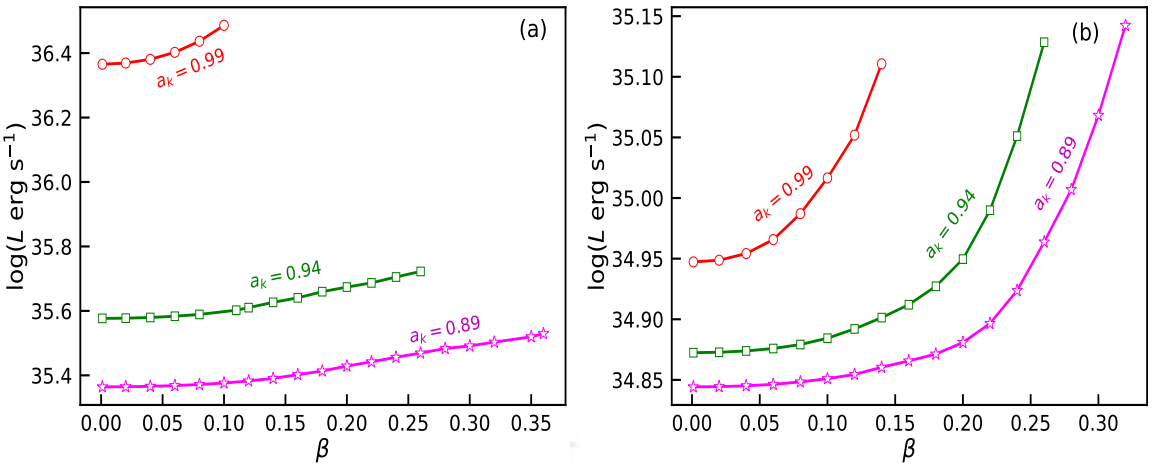

Figure 3.12: Variation of disk luminosity (L) as function of β for different $a_{\rm k}$. In panel (a), results corresponding to I-type accretion solutions are depicted for flow with $\mathcal{E} = 1.02$ and $\lambda = 1.90$. Open circles, squares and asterisks joined with solid lines are for $a_{\rm k} = 0.99$, 0.94, and 0.89, respectively. In panel (b), results same as panel (a) are shown, but for O-type accretion solutions, where $\mathcal{E} = 1.004$ and $\lambda = 1.85$ are chosen. See the text for the details.

inconclusive. Keeping this in mind, in the present analysis, we attempted to explain the disk luminosity of Cygnus X-3 during its hypersoft state considering the source as a rotating Kerr-like WH. Cygnus X-3 displays intense luminosity, predominantly in X-ray wavelengths. This sustained brightness, amidst its erratic behavior, hints at underlying mechanisms continuously fueling its emissions. Moreover, Cygnus X-3 exhibits a unique hypersoft state characterized by its bolometric X-ray flux reaching peak values in the range $2-8\times10^{-8}$ erg cm^{-2} s^{-1} (Hjalmarsdotter et al., 2008; Koljonen et al., 2018). Adopting the source distance of 7.4 kpc (McCollough et al., 2016), the source luminosity is estimated as $L_S \sim 1 - 5 \times 10^{38}$ erg s^{-1} (Zdziarski et al., 2012). In order to explain L_S, we compute the 'model predicted' disk luminosity (L) arising from free-free emission for transonic accretion solutions around WH. In doing so, we use the source mass as $M_{\rm WH} = 2.4 M_\odot$ (Zdziarski et al., 2013), and for the purpose of representation, we consider typical accretion rate $\dot{m} = 0.1$, source spin $a_{\rm k} = 0.99$ and $\beta = 0.001$. The obtained results are presented in Fig. 3.13, where we illustrate the two-dimensional projection of the three-dimensional plot of λ, $\mathcal{E}$ and log (L erg s^{-1}). In the figure, the vertical colorbar denotes the disk luminosity in the range $35 \leq$ log (L erg s^{-1}) ≤ 39. In the figure, we identify a region bounded with dotted curves that yields the luminosity $1 \times 10^{38} \lesssim L \lesssim 5 \times 10^{38}$ erg s^{-1}. These findings evidently indicate that our analysis in turn renders the representative values of the luminosity (L_S) of Cygnus X-3. Moreover, we argue that present model formalism seems to be potentially promising in explaining the luminosity of compact X-ray sources.

3.6 Chapter conclusions

In this Chapter, we study the low angular momentum, inviscid, advective accretion flow around a stationary axisymmetric Kerr-like WH spacetime. The Kerr-like WH is characterized by the spin parameter ($a_{\rm k}$) and dimensionless parameter (β) along with its mass ($M_{\rm WH}$). In doing so, we examine the steady state accretion solutions

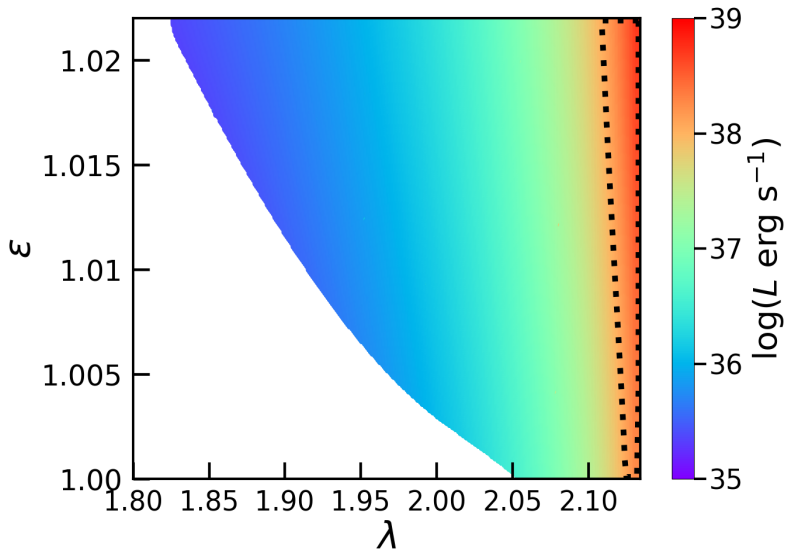

Figure 3.13: Two-dimensional projection of the three-dimensional plot of $\mathcal{E}$, λ and $\log(L$ erg $s^{-1})$ for transonic flow due to free-free emission. The colorbar denotes the range of luminosity values. The region enclosed by the dotted curve yields disk luminosity consistent with the observed luminosity of Cygnus X−3 during its hypersoft state. See the text for the details.

which are obtained by solving the governing equations describing the accretion flow confined around the disk equatorial plane. Further, we investigate the role of $a_{\rm k}$ and β in regulating the accretion dynamics. With this, we summarize our key findings in the below.

We calculate the transonic accretion solution (I-type) that passes through the inner critical point $r_{\rm in}$ around WH (see Fig. 3.2). We find that the radial profile of the flow variables corresponding to this solution, such as density (ρ), pressure (p) and temperature (T) follow power-law distributions as $\rho \propto r^{-(n+2/5)}$, $p \propto r^{-(n+1)}$ and $T \propto r^{-(n-1/3)}$ with $n \sim 1$ inside the disk (see Fig. 3.3). However, solution deviates from self-similarity close to $r_{\rm Th}$ mainly due to the non-linearity present in the WH spacetime. Further, for the first time to the best of our knowledge, we obtain the complete set of transonic accretion solutions (O-type, A-type, W-type and I-type) around WHs by tuning the model parameters, namely energy ($\mathcal{E}$), angular momentum (λ), spin parameter ($a_{\rm k}$), and dimensionless parameter (β). We find that a given type of accretion solutions are not isolated solutions as these solutions continue to exist for wide range of model parameters. We also separate the domains of the parameter space in $\lambda - \mathcal{E}$ plane according to the nature of the accretion solutions (see Fig. 3.4). Furthermore, we investigate the impact of $a_{\rm k}$ (β) values in altering the parameter space for multiple critical points. Our findings reveal that when $a_{\rm k}$ (β) is increased keeping β ($a_{\rm k}$) fixed, the parameter space shifts towards the higher energy and lower angular momentum domain (see Fig. 3.9).

Then, we examine the role of $a_{\rm k}$ and β in obtaining the transonic accretion solutions. We observe that for fixed $\mathcal{E}$, λ, and β ($a_{\rm k}$), accretion solution alters its character as $a_{\rm k}$ (β) is increased (see Fig. 3.5 and Fig. 3.6). This findings evidently indicate that both $a_{\rm k}$ and β play pivotal role in deciding the nature of the transonic accretion solutions around WH. We further emphasize that subsonic accretion solutions are also possible

around WH (see Fig. 3.7 and Fig. 3.8). However, for fixed $\mathcal{E}$, λ, $a_{\rm k}$ and β, these solutions possess lower entropy content compared to the transonic solutions. Hence, we argue that transonic solutions around WH are thermodynamically preferred over the subsonic solutions.

Finally, we compute the disk luminosity (L) considering Bremsstrahlung emission and observe strong dependency of L on both $a_{\rm k}$ and β. It becomes evident that for a fixed β ($a_{\rm k}$), increasing $a_{\rm k}$ (β) leads to higher L for both I-type and O-type transonic accretion solutions. In addition, we note that I-type solutions yield higher L compared to O-type solutions (see Fig. 3.12). Finally, we indicate that our model successfully elucidates the luminosity of compact X-ray source Cygnus X-3 during its hypersoft state. Based on this finding, we mention that the present model formalism offers the valuable insights of the accretion flow dynamics around WH that could drive the energetic emissions observed from enigmatic compact X-ray sources. Although, we neglect the effect of viscosity, magnetic fields, which are ubiquitous in astrophysical scenario.

Chapter 4

Impact of generic dark matter halo on relativistic accretion flow around galactic black holes

It is well known that almost all galaxies host supermassive black holes (SMBHs) ($M_{\rm BH} \sim 10^6 - 10^{10} M_\odot$) (Richstone et al., 1998; Kormendy & Ho, 2013) at their center including the Milky Way (Sgr. A) (Ghez et al., 2008; Genzel et al., 2010; Collaboration, 2022a). The current theoretical models on the formation of SMBHs fail to explain the distribution of the BH mass, as most of the SMBHs are found at high redshifts (Kormendy & Ho, 2013). Although galaxy mergers in the early universe may lead to a possible explanation for the rapid growth rate of the SMBHs, it requires the presence of DM (Volonteri & Rees, 2005; Sanders, 2008; Skordis & Zlosnik, 2021; McGaugh et al., 2024). There are also various observational evidences such as galaxy velocities (Zwicky, 1933), galactic rotation curves (Rubin et al., 1978), cosmic microwave background (CMB) observations (Aghanim et al., 2020) supports the existence of DM (see section 1.3). Therefore, the strong gravity of SMBHs can redistribute the DM distributions near the galactic center, which results a density spike outside the event horizon. At low redshift, SMBHs primarily grow via the process of accretion of luminous matter, and their mass gradually increases. As a result, the accretion rate influences AGN properties, that may shape the host galaxy's growth (Bower et al., 2006; Morganti, 2017; Harrison, 2017). Furthermore, the environmental dependence of AGN activities can provide powerful constraints on evolutionary scenarios of SMBH fueling and feedback (Powell et al., 2022).

Since the spacetime geometry strongly governs the dynamics of accretion flow around compact objects, one must accurately model the modification of the spacetime geometry due to the relativistic distribution of the DM particles around the SMBHs at the galactic center. In this direction, Natarajan (2002) first modelled the

galactic DM density profile from observations and simulations. Later, Cardoso et al. (2022a); Cardoso et al. (2022b) derived an exact analytical solution for SMBHs minimally coupled to the anisotropic DM fluid using the Einstein Cluster model (Geralico et al., 2012; Einstein, 1939) within GR using a Hernquist-type distribution (Hernquist, 1990). Going beyond the Hernquist-type DM distribution, a fully numeric pipeline was developed by Figueiredo et al. (2023) and Speeney et al. (2024) to treat generic density distributions around spherically symmetric galactic SMBHs. After that, numerous works have also been done on the influence of DM halos on different spacetime properties and phenomenology (Retana-Montenegro et al., 2012; Jusufi et al., 2020; Stuchlík & Vrba, 2021; Liu et al., 2022; Singha & Biswas, 2024; Chen et al., 2024; Faraji & Rosa, 2024; Patra & Majhi, 2025; Ranjbar et al., 2025).

In Chapter 2 and Chapter 3, we have studied the relativistic accretion flow around bare BHs and a WHs. It is timely to study the effect of DM halos on the accretion around BHs, as the surrounding environment is expected to play a crucial role in understanding various astrophysical phenomena around them. Therefore, in the present Chapter, we study relativistic, low angular momentum, inviscid, and advective hot accretion flow onto a galactic supermassive BH dressed with different relativistic density distributions of cold DM halo, namely Hernquist (see subsection 1.3.1), Navarro-Frenk-White (NFW) (see subsection 1.3.2), and Einasto (see subsection 1.3.3), along with a fully relativistic model of the DM spike based on Hernquist-type distribution (see subsection 1.3.4) following the numerical framework developed by Figueiredo et al. (2023) to model the spacetime geometry around a Schwarzschild BH (see section 1.1.3 for detailed description of this spacetime). All DM profiles are characterized by the halo mass ($M_{\rm halo}$) and a characterized length scale (a_0). Focusing on different relativistic DM distributions with an inner density spike, we analyze the effect of the DM halo on the topology and properties of the accretion flow. As from the previous chapters, we knew that the I-type solution provides the highest luminosity compared to the other types of solutions, we calculate the Bremstrahlung luminosity for these types of solutions. Our results indicate that the change in geometry due to the feedback from the relativistic distribution of DM halo causes a significant change in the effective gravitational potential, which leads to deviation in the topology and properties of the accretion flow. The quantitative deviation of the flow properties and luminosity from that of the vacuum Schwarzschild BH depends on the exact nature of the halo density profile (and the DM spike model). This results in substantial differences in the spectral energy density and the bolometric luminosity, particularly for highly compact halos with large halo mass.

4.1 Background geometry and density profiles

This section briefly reviews the formalism to construct an asymptotically flat, static, spherically symmetric BH solution embedded in a DM halo with different density distributions.

4.1.1 Background geometry

We model the spacetime geometry of a BH by the line element,

$$ds^2 = -\tilde{f}(r)dt^2 + \frac{dr^2}{1-\frac{2\tilde{m}(r)}{r}} + r^2 d\Omega^2 \ , \tag{4.1}$$

where $d\Omega^2$ represents the metric on a unit two-sphere. Throughout this chapter, we use geometric units ($G = c = 1$) unless stated otherwise.

Following some previous papers (Cardoso et al., 2022a; Figueiredo et al., 2023; Speeney et al., 2024; Chakraborty et al., 2024; Pezzella et al., 2024), we employ a generalized Einstein cluster formalism (Einstein, 1939; Geralico et al., 2012). Einstein cluster is a collection of collisionless particles in all possible circular geodesics. The average stress energy tensor is given by,

$$\langle T^{\mu\nu} \rangle = \frac{n}{\tilde{m}_p} \langle P^\mu P^\nu \rangle \ ,$$

where n is the proper number density of particles with rest mass $\tilde{m}_p$ and P^μ is the four-momentum satisfying the geodesic equation. The averaging $\langle \ldots \rangle$ is done over all trajectories with all the directions and phases passing through a spatial point where the energy-momentum tensor of the orbiting particles is computed. This averaging ensures that the system remains static and spherically symmetric. The number density, $n(r)$, on a given shell is independent of that in the other shells. This construction is equivalent to an anisotropic material with only tangential pressure P_t and zero radial pressure. Thus, we assume the metric in Eq. (4.1) to be a solution of the Einstein's equations,

$$G_{\mu\nu} = 8\pi T^{\rm env}_{\mu\nu}, \tag{4.2}$$

where

$$(T^\mu_\nu)^{\rm env} = {\rm diag}(-\rho_{\rm DM}(r), 0, P_t(r), P_t(r)) \ , \tag{4.3}$$

is the anisotropic stress-energy tensor encoding the properties of the environment in terms of the density $\rho_{\rm DM}(r)$ and the tangential pressure $P_t(r)$ of the matter distribution. The zero radial pressure of the distribution is also indicative of the negligible DM accretion rate within the timescale of baryonic accretion. For a given density profile, the continuity equation determines the mass profile as,

$$\tilde{m}'(r) = 4\pi r^2 \rho_{\rm DM}(r) \ , \tag{4.4}$$

whereas the metric function $\tilde{f}(r)$ and the tangential pressure $P_t(r)$ are determined by the rr component of the field Eq. (4.2) and the Bianchi identities, respectively,

$$\frac{\tilde{f}'(r)}{\tilde{f}(r)} = \frac{2\tilde{m}(r)/r}{r - 2\tilde{m}(r)} \ , \tag{4.5}$$

$$P_t(r) = \frac{\tilde{m}(r)/2}{r - 2\tilde{m}(r)} \rho_{\rm DM}(r) \ . \tag{4.6}$$

The metric functions $\tilde{f}(r)$ and $\tilde{m}(r)$ completely specify the geodesic structure of the spacetime.

The stationarity and spherical symmetry of the metric (Eq. (4.1)) implies the existence of a timelike and a spacelike Killing vector associated with the conserved quantities, the specific energy and the specific angular momentum at infinity. The radius of the innermost stable circular orbit for massive particles is given by the roots of the equation,

$$r^2\tilde{m}'(r) + r\tilde{m}(r) - 6\tilde{m}^2(r) = 0 \ , \tag{4.7}$$

with the associated angular frequency,

$$\Omega_{\rm ISCO} = \left[\frac{\tilde{f}(r)\tilde{m}(r)}{r^2(r-2\tilde{m}(r))}\right]_{r=r_{\rm ISCO}} \ . \tag{4.8}$$

The radius of the lightring (unstable null circular geodesic) is determined by the roots of the equation, $r = 3\tilde{m}(r)$, with the associated angular frequency

$$\Omega_{\rm LR} = \frac{\sqrt{\tilde{f}(r_{\rm LR})}}{r_{\rm LR}} \ . \tag{4.9}$$

To evaluate the metric functions $\tilde{f}(r)$ and $\tilde{m}(r)$, we follow the numerical procedure outlined in Speeney et al. (2024) motivated by the solutions obtained in Konoplya & Zhidenko (2022); Shen et al. (2024); Maeda et al. (2025). We start with a specific choice of the DM density profile $\rho_{\rm DM}(r)$ (as outlined in section 4.1.2) and numerically integrate Eq. (4.4) from $r = 2M_{\rm BH}$ to $r_\infty = 10^{16}M_{\rm BH}$ (corresponding to our numerical infinity) to determine $\tilde{m}(r)$. We then use $\tilde{m}(r)$ in Eq. (4.5) to evaluate $\tilde{f}(r)$ by integrating backwards from r_∞ with the boundary conditions,

$$\tilde{m}_{r_\infty} = M_{\rm BH} + M_{\rm halo} \ , \tag{4.10}$$

$$\tilde{f}(r_\infty) = 1 - \frac{2\tilde{m}(r_\infty)}{r} \ , \tag{4.11}$$

where $M_{\rm halo}$ is the total mass of the DM environment surrounding the BH. Note that by construction, the event horizon is $r_{\rm H} = 2M_{\rm BH}$. The obtained metric functions can then be used in Eq. (4.6) to determine the tangential pressure. Similarly, the location and angular momentum at the ISCO and lightring can also be determined explicitly, using Eqs. (4.7), (4.8), (4.9), respectively.

4.1.2 Environmental density profiles

Since we are interested in studying the effect of collisionless CDM distribution on the accretion onto the central BH, we consider two of the most widely studied CDM density profiles, the Hernquist profiles (Hernquist, 1990) and the NFW distributions (Navarro et al., 1995; Navarro et al., 1996). Whereas the Hernquist profile is mostly used to model the Sérsic profile observed in bulges and elliptic galaxies, the NFW profile is mainly used for galaxies with the largest content of DM (Kormendy & Ho, 2013). Both these profiles can be parametrically described as (Taylor & Silk, 2003),

$$\rho_{\rm DM}(r) = \rho^0_{\rm DM}(r/a_0)^{-\varsigma}\left[1 + (r/a_0)^\alpha\right]^{(\varsigma-\beta)/\alpha} \ , \tag{4.12}$$

where $\rho^0_{\rm DM} = 2^{(\beta-\varsigma)/\alpha}\rho_{\rm DM}(a_0)$ is a scale factor with a_0 being the scale radius of the halo. The parameters β and ς respectively govern the dependence of the profile at

large and small radii, whereas α determines the sharpness of the change of the profile slope at a_0 (Taylor & Silk, 2003). The Hernquist and NFW density profiles correspond to the parameter set $(\alpha, \beta, \varsigma) = (1, 4, 1)$ and $(\alpha, \beta, \varsigma) = (1, 3, 1)$, respectively. Since the total mass of the NFW profile is logarithmically divergent, we use a cutoff radius $\tilde{r}_c$ for the dark matter distribution, such that $M_{\rm halo}(r > \tilde{r}_c) = 0$. Henceforth, for the NFW density profile, we will use two values of the cutoff radius: (a) $\tilde{r}_c = 5a_0$ (referred to as NFW), (b)$\tilde{r}_c = a_0$ (referred to as NFW1) . We also use a third-density profile named, Einasto (1969) profile, that provides an excellent fit to a wide range of DM halos as per recent N-body CDM simulations. The Einasto profile is given by,

$$\rho_{\rm DM}(r) = \rho^e_{\rm DM} \exp\left\{-d_{\hat{n}}\left[(r/r_e)^{1/\hat{n}} - 1\right]\right\} , \tag{4.13}$$

where r_e denotes the radius of the sphere containing half of the total mass, and $\rho^e_{\rm DM}$ is the mass density at $r = r_e$ with $\hat{n} = 6$ and $d_{\hat{n}} = 53/3$ (Graham et al., 2006; Prada et al., 2006). Throughout the work, we set $r_e = a_0$ for brevity.

Due to the adiabatic accretion growth of a seed nonrotating BH sitting at the core, the DM distribution is expected to develop an overdensity with a sharp cutoff close to the horizon at $r = 4M_{\rm BH}$ (Gondolo & Silk, 1999; Sadeghian et al., 2013). Following Speeney et al. (2024), we model the overdensity in two different ways:

1. We multiply the DM density profile with the cut-off factor $(1 - 4M_{\rm BH}/r)$. The choice of the cutoff factor ensures that the dominant energy condition is satisfied (Datta, 2024; Speeney et al., 2024) in the region, $2M_{\rm BH} < r < 4M_{\rm BH}$.

2. We consider a fully relativistic DM spike model introduced in Speeney et al. (2022). We concentrate on the Hernquist subclass of the DM spike i.e., we consider the adiabatic growth of the DM spike starting from a Hernquist distribution given by Speeney et al. (2024),

$$\begin{aligned}\rho_{\rm DM}(r) =& \bar{\rho}_{\rm DM}(r)\frac{M_{\rm halo}}{M^2_{\rm BH}} \\ &\times \left(\int_{4M_{\rm BH}}^{r_c} 4\pi r^2 \bar{\rho}_{\rm DM}(r) dr\right)^{-1} ,\end{aligned} \tag{4.14}$$

with

$$\begin{aligned}\bar{\rho}_{\rm DM}(r) =& \left(1 - \frac{4M_{\rm BH}}{r}\right)^{\alpha}\left(\frac{rM_{\rm BH}}{M_{\rm halo}a_0}\right)^{\beta} \\ &\times \left(1 + \frac{rM_{\rm BH}}{M_{\rm halo}a_0}\right)^{\varsigma} ,\end{aligned} \tag{4.15}$$

where $\alpha = 2.366$, $\beta = -2.320$ and $\varsigma = -1.370$. The functional dependence of $\bar{\rho}_{\rm DM}(r)$ on a_0 and $M_{\rm halo}$ was determined empirically by studying the behaviour of an ensemble of DM profiles computed numerically for selected values of $M_{\rm halo}$ and a_0 (Sadeghian et al., 2013). The numerical values of α, β and ς were then determined by fitting with a numerical spike with $M_{\rm halo} = 10^4 M_{\rm BH}$ and $M_{\rm halo}/a_0 = 0.001$.

Fig. 4.1 shows the representative plots of different DM distributions for different values of the halo mass and scale radius. We note that the Hernquist and the NFW profiles behave almost similarly, with the Hernquist density being greater than the

NFW density at a fixed radius. The NFW distribution terminated at a_0 (NFW1) has a higher density than the one terminated at $5a_0$ since the total halo mass remains constant. For the halo-compactness ($M_{\rm halo}/a_0$) considered in fig. 4.1, the Hernquist type spike profile has the highest density of DM close to the BH, however for more compact halos, the situation is reversed (Speeney et al., 2024).

In the subsequent sections, we study the accretion flow of the baryonic matter onto the galactic BH dressed with a dark matter halo. We again stress that the DM influences the accretion flow of the baryonic matter by modifying spacetime geometry. Since there are multiple length scales involved in the problem, we maintain a strict separation of the length scales, $M_{\rm BH} \leq M_{\rm halo} \leq a_0$ and $r_{\rm edge} \leq a_0$, where $r_{\rm edge}$ is the outer edge of the accretion disk. Note that in all the cases, we treat $M_{\rm halo}$ and a_0 as free model parameters for a qualitative analysis.

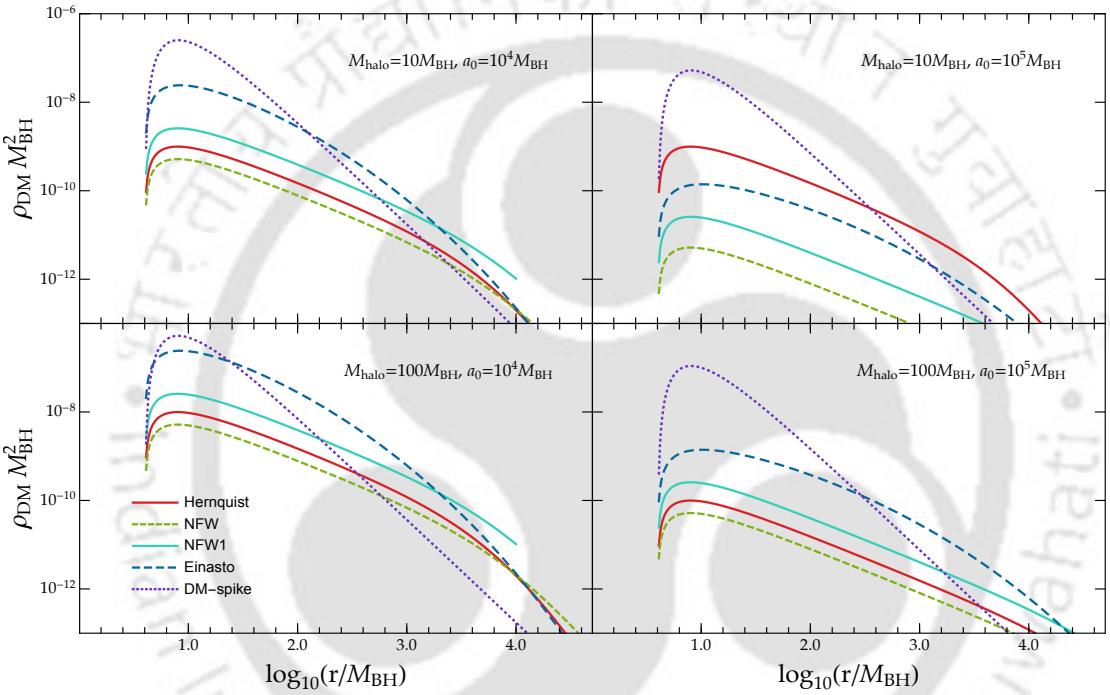

Figure 4.1: Halo density profiles for different values of the $M_{\rm halo}$ and a_0. For the NFW profile, two values of the truncation radius have been used, $\tilde{r}_c = 5a_0$ (NFW) and $\tilde{r}_c = a_0$ (NFW1). The DM spike profile is of the Hernquist subclass. See the text for details.

4.2 Assumptions and model equations

In this section, we present the basic equations governing the advection dominated, steady, inviscid, hot accretion flow of non-magnetic and optically thin plasma (Yuan & Narayan, 2014) onto the central BH. The spherical symmetry of the background geometry (Eq. (4.1)) allows us to consider a planar accretion flow (for brevity we choose to be the equatorial plane). The energy-momentum tensor and the four-current of the fluid is given by,

$$T^{\mu\nu} = (e+p)u^\mu u^\nu + pg^{\mu\nu} \quad \text{and} \quad j^\mu = \rho u^\mu \tag{4.16}$$

where e, p, ρ, and u^μ are the local energy density, pressure, mass density and four-velocity of the fluid element, respectively, with $u^\mu u_\mu = -1$. The conservation of the

energy-momentum tensor and the mass-flux provide the relativistic hydrodynamical equations that completely determine the accretion flow. These are given by,

$$T^{\mu\nu}_{;\nu} = 0, \quad \text{and} \quad j^{\nu}_{;\nu} = 0. \tag{4.17}$$

Using the projection tensor, $h_{\mu\nu} = g_{\mu\nu} + u_\mu u_\nu$, projecting the conservation equation onto the hypersurface orthogonal to the flow velocity, we get the relativistic Euler equation as,

$$h^{\alpha}_{\mu} T^{\mu\nu}_{;\nu} = (e+p)u^\nu u^\alpha_{;\nu} + (g^{\alpha\nu} + u^\alpha u^\nu)\, p_{,\nu} = 0. \tag{4.18}$$

Similarly, the component of the conservation equation along the flow velocity yields the energy equation,

$$u_\mu T^{\mu\nu}_{;\nu} = u^\mu \left[\left(\frac{e+p}{\rho} \right) \rho_{;\mu} + e_{;\mu} \right] = 0. \tag{4.19}$$

Since the temperature of the accretion flow close to the BH is of the order $\sim 10^{10} - 10^{11}$K, the accretion flow is thermally relativistic. Thus, we use the relativistic EoS (Chattopadhyay & Ryu, 2009) with variable adiabatic index to relate the density and pressure of the flow,

$$e = \frac{\rho}{\tau} f, \quad p = \frac{2\rho\Theta}{\tau}, \tag{4.20}$$

with, $\tau = 1 + m_p/m_e$ and

$$\begin{aligned} f = &\left[1 + \Theta \left(\frac{9\Theta + 3}{3\Theta + 2} \right) \right] \\ &+ \left[\frac{m_p}{m_e} + \Theta \left(\frac{9\Theta m_e + 3m_p}{3\Theta m_e + 2m_p} \right) \right], \end{aligned} \tag{4.21}$$

where m_e and m_p are the masses of electron and ion, respectively, and Θ $(= k_B T/m_e c^2)$ is the dimensionless temperature. In the above equation and all subsequent calculations, we implicitly assume the number density of the electrons and ions to be the same. Using the relativistic EoS in eq. (4.20), we express the associated sound-speed as $C_s = \sqrt{2\Gamma\Theta/(f + 2\Theta)}$, where Γ $(= (1+N)/N)$ is the adiabatic index with $N = (1/2)(df/d\Theta)$ being the polytropic index of the flow. Since the accretion flow is assumed to be confined in the equatorial plane ($\theta = \pi/2, u^\theta = 0$), we write the radial component of the relativistic Euler equation as,

$$v\gamma_v^2 \frac{dv}{dr} + \frac{1}{h\rho}\frac{dp}{dr} + \frac{d\Phi_e^{\text{eff}}}{dr} = 0, \tag{4.22}$$

where $\gamma_v = 1/\sqrt{1 - v^2}$ is the Lorentz factor associated with the fluid three velocities in the corotating frame, $v = \gamma_\phi v_r = \sqrt{u^r u_r / \left[u^t u_t (\lambda^2 \tilde{f}(r)/r^2 - 1) \right]}$. The quantity h $(= (e+p)/\rho)$ is the specific enthalpy and Φ_e^{eff} is the effective potential (Dihingia et al., 2018) given by,

$$\Phi_e^{\text{eff}} = 1 - \frac{1}{2} \ln \left(\frac{1}{\tilde{f}(r)} - \frac{\lambda^2}{r^2} \right), \tag{4.23}$$

As evident from Eq. (4.23), the effective potential depends on the spacetime geometry and the specific angular momentum of the flow.

The symmetry of the background spacetime allows us to consider stationary and axisymmetric accretion flow. Thus, we define the specific energy ($\mathcal{E}$) and the conserved angular momentum ($\mathcal{L}$) associated with the timelike and spacelike Killing vectors (∂_t) and (∂_ϕ) respectively as,

$$-hu_t = \mathcal{E}, \quad \text{and} \quad hu_\phi = \mathcal{L}\ . \tag{4.24}$$

We also define the specific angular momentum as $\lambda = \mathcal{L}/\mathcal{E}$, which is conserved along the flow streamline.

The effect of the DM density profile on the effective potential is shown in Fig. (4.2). We observe that compared to the vacuum Schwarzschild BH, the presence of the DM

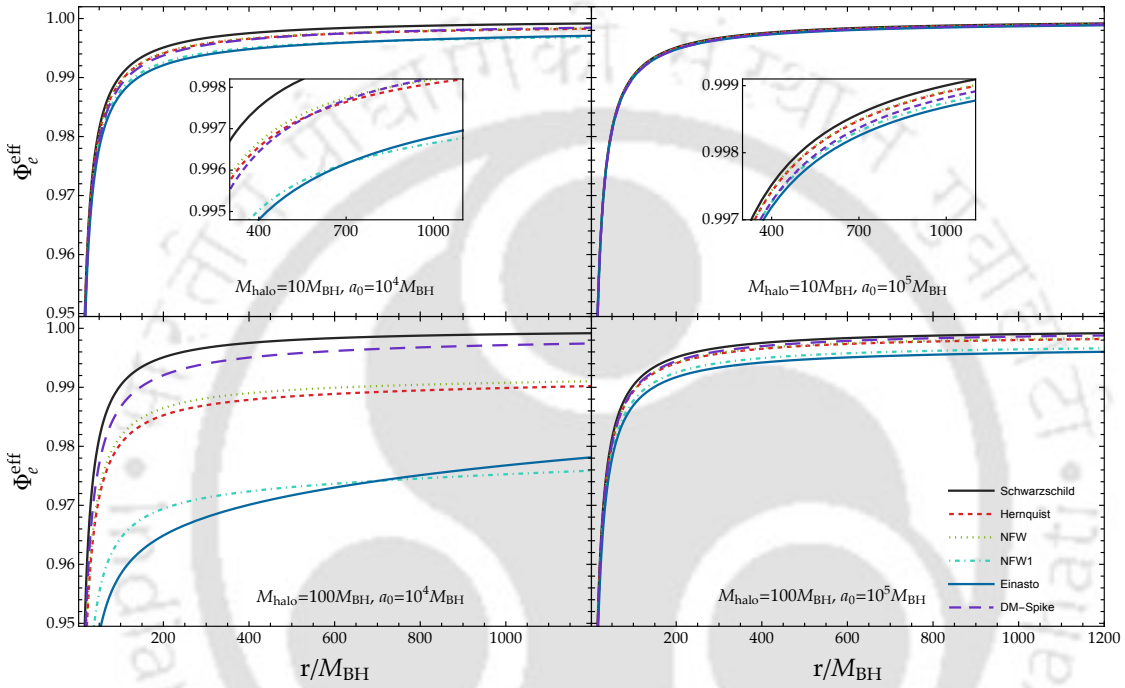

Figure 4.2: Variation of the effective potential ($\Phi_e^{\rm eff}$) as a function of the radial coordinate r in the unit of the BH mass for different DM halo density profiles. Here, we choose $\lambda = 3$. See the text for details.

halo lowers the effective potential at any given radius. Thus, a flow with lower specific energy can overcome the potential barrier. For a fixed total halo mass as a_0 increases (DM distribution gets more dilute), $\Phi_e^{\rm eff}$ approaches the Schwarzschild limit for all DM distributions. Again, for a given a_0, as the halo mass increases, the deviation of the effective potential of each of the DM distributions from the Schwarzschild value increases. However, for a fixed compactness, ($\Psi = M_{\rm halo}/a_0$), the higher the halo mass, the lower the effective potential. Though the effective potential for the different DM distributions follows a similar trend, they differ largely among themselves. We observe that close to the central BH, the Einasto profile gives rise to the smallest effective potential. Far away from the central BH the effective potential for the NFW1 profile is usually the smallest. The effective potential for Hernquist-type DM spike (HQ-type DM spike) distribution strongly depends on the halo mass as shown in Appendix-B.2.

The radial component of the entropy-generation equation (Eq. (4.19)) gives

$$\left(\frac{e+p}{\rho}\right)\frac{d\rho}{dr} - \frac{de}{dr} = 0. \tag{4.25}$$

The integrated form of the continuity equation (Eq. 4.16) gives the conserved mass accretion rate of the flow as,

$$\dot{M} = 4\pi r \rho v \gamma_v H \sqrt{\tilde{f}(r)}, \tag{4.26}$$

where $H = \sqrt{pr\left(r^2 - \lambda^2 \tilde{f}(r)\right)/\rho}$ is the local half-thickness of the disk. We define the entropy accretion rate of the flow as (Chattopadhyay & Kumar, 2016; Kumar & Chattopadhyay, 2017),

$$\dot{\mathcal{M}} = \frac{\dot{M}}{4\pi\mathcal{K}} = \frac{\rho}{\mathcal{K}} v \gamma_v H r \sqrt{\tilde{f}(r)}, \tag{4.27}$$

where the density is obtained by integrating Eq. (4.25) using Eqs. (4.20), (4.21),

$$\begin{aligned} \rho =& \mathcal{K} \exp\left(\frac{f-\tau}{2\Theta}\right) \Theta^{3/2} (3\Theta + 2)^{3/4} \\ & \times (3\Theta + 2m_p/m_e)^{3/4} \ , \end{aligned} \tag{4.28}$$

$\mathcal{K}$ being the constant of integration. Since we have considered an adiabatic accretion flow, the entropy accretion rate $\dot{\mathcal{M}}$ remains constant throughout the flow streamline. Furthermore, using Eqs. (4.25), (4.26), we express the dimensionless temperature gradient as,

$$\begin{aligned} \frac{d\Theta}{dr} =& -\frac{2\Theta}{2N+1} \\ & \times \left[\frac{1}{r}\left(\frac{5}{2} + \frac{\lambda^2}{r^2-\lambda^2}\right) + \frac{\gamma_v^2}{v}\frac{dv}{dr} + \frac{\tilde{f}'(r)}{2\tilde{f}(r)}\right]. \end{aligned} \tag{4.29}$$

Using Eqs. (4.22), (4.29), we obtain the wind equation in terms of the sound speed as,

$$\frac{dv}{dr} = \frac{\mathcal{N}}{\mathcal{D}}, \tag{4.30}$$

where,

$$\mathcal{N} = \frac{2C_s^2}{\Gamma+1}\left[\frac{1}{r}\left(\frac{5}{2} + \frac{\lambda^2}{r^2-\lambda^2}\right) + \frac{\tilde{f}'(r)}{2\tilde{f}(r)}\right] - \frac{d\Phi_e^{\rm eff}}{dr}, \tag{4.31}$$

$$\mathcal{D} = \gamma_v^2\left(v - \frac{2C_s^2}{v(\Gamma+1)}\right). \tag{4.32}$$

4.3 Critical point analysis and global accretion solution

The accretion flow starts subsonically from the outer edge of the accretion disk ($v < C_s$) and continues smoothly along a streamline with the infall velocity approaching the speed of light as it reaches the event horizon. Thus, during the course of accretion the flow turns supersonic at a critical radius r_c depending on the background geometry, the specific angular momentum and energy of the flow. Hence, the accretion flow is transonic in nature. At the critical radius, both $\mathcal{D}$ and $\mathcal{N}$ in Eq. (4.30) must vanish

identically to maintain the smoothness of the accretion flow. Setting the critical point conditions $\mathcal{D} = \mathcal{N} = 0$, we get,

$$v_c^2 = \frac{2C_{sc}^2}{\Gamma_c + 1}, \tag{4.33}$$

$$C_{sc}^2 = \frac{\Gamma_c + 1}{2}\left(\frac{d\Phi_e^{\rm eff}}{dr}\right)_c \times \left[\frac{1}{r_c}\left(\frac{5}{2} + \frac{\lambda^2}{r_c^2 - \lambda^2}\right) + \frac{\tilde{f}'(r_c)}{2\tilde{f}(r_c)}\right]^{-1}, \tag{4.34}$$

where the subscript c denotes the corresponding quantity being evaluated at the critical point $r = r_c$. Since dv/dr takes "0/0" form at the critical point, we use the L'Hôspital's rule to calculate the radial velocity gradient of the flow, $(dv/dr)_{r_c}$. At a critical point, if both values of $\left(\frac{dv}{dr}\right)_{r_c}$ are real and of opposite sign, the critical point is referred to as saddle type, whereas if they are of the same sign, the critical point is referred to as nodal type. In case, the radial velocity gradient at a critical point becomes imaginary, the corresponding critical point is referred to as spiral type. Henceforth, we only consider saddle-type critical points since they are stable against small-amplitude perturbations (Kato et al., 1993). If a saddle-type critical point develops close to the event horizon, it is referred to as the inner critical point ($r_{\rm in}$), whereas if it develops away from the event horizon, it is referred to as the outer critical point ($r_{\rm out}$).

Using the flow velocity (v_c) and temperature ($\Theta_{\rm c}$) evaluated at the critical point as initial conditions, we integrate Eqs. (4.29), (4.30) from the critical point to the outer edge ($r_{\rm edge}$) and again from the critical point to the horizon ($r_{\rm h}$). Finally, we combine both these segments to get the global transonic accretion solution. If the accretion flow contains only an inner critical point ($r_{\rm in}$), the corresponding flow topology is referred to as I-type, whereas if the flow contains only an outer critical point ($r_{\rm out}$), it is called O-type. Depending on the background geometry and flow parameters, the accretion flow may as well contain both the inner and outer critical points simultaneously. In such cases, if the entropy accretion rate at $r_{\rm in}$ is greater than that at $r_{\rm out}$ ($\dot{\mathcal{M}}_{\rm in} > \dot{\mathcal{M}}_{\rm out}$), the flow is referred to as A-type, whereas for the reversed case, when $\dot{\mathcal{M}}_{\rm in} < \dot{\mathcal{M}}_{\rm out}$, the flow is called W-type (Chakrabarti, 1989c; Chakrabarti, 1996b). We represent all these types of solutions in section 4.3.2. For an A-type solution, the flow coming from the outer edge ($r_{\rm edge}$), connects the horizon ($r_{\rm Sh}$) only through the outer critical point ($r_{\rm out}$). On the other hand, for a W-type solution, the accretion flow passing through $r_{\rm in}$ only connects the outer edge ($r_{\rm edge}$) and horizon ($r_{\rm Sh}$).

4.3.1 Critical point analysis

We analyze the dependency of the critical points on flow properties *i.e.*, energy ($\mathcal{E}$) and angular momentum (λ) in the absence and presence of various dark matter distribution ($M_{\rm halo} = 10M_{\rm BH}, a_0 = 10^5 M_{\rm BH}$). In Fig. 4.3, the surface plot represents the nature of the critical points with $\mathcal{E}$ and λ. Critical points r_c are plotted along the x-axis in the logarithmic scale, λ is plotted along the z-axis. The yellow, grey, and green colours denote the saddle, nodal, and spiral-type critical points. The range of critical points is not the same for all DM distributions and exhibits notable deviations from the Schwarzschild case for the HQ-type DM spike. A common feature is that there is an upper and lower limit of energy and angular momentum, beyond which the

multiple saddle-type critical points cease to exist. This happens due to the choice of the relativistic equation of state and is in agreement with the findings of previous studies (Dihingia et al., 2020b). As we increase the angular momentum, the likelihood of forming outer critical points is reduced. Under such conditions, the flow enters the BH only through the inner critical points. Accretion flow with lower specific angular momentum passes through the outer critical points only. As these solutions are adiabatic in nature, the entropy accretion rate is constant throughout the journey from the outer edge to the horizon, passing through a critical point. To analyse the

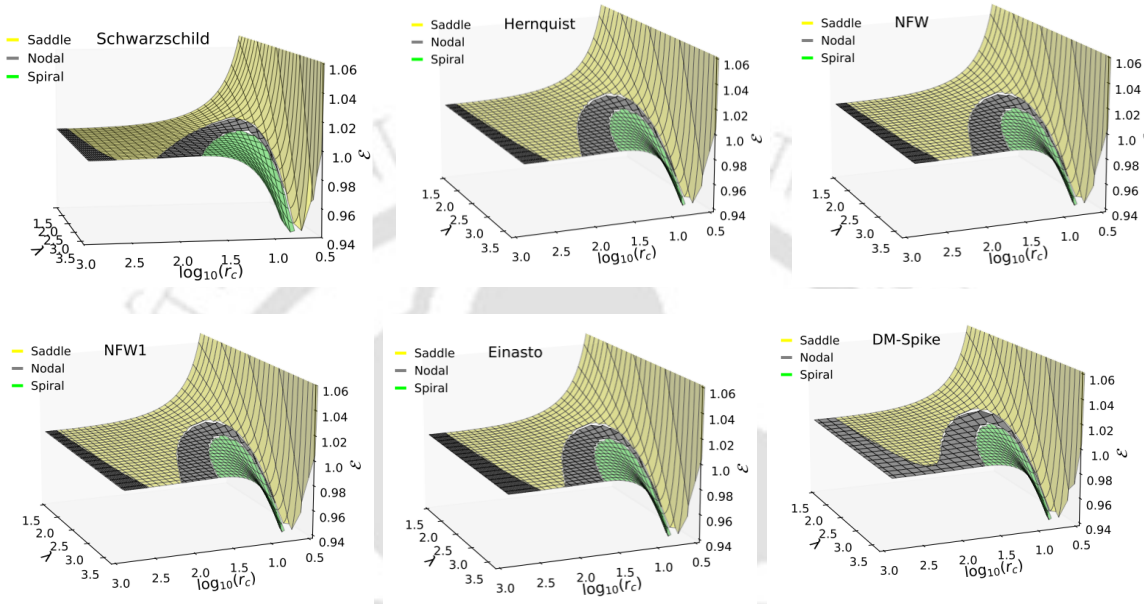

Figure 4.3: Variation of specific energy ($\mathcal{E}_c$) measured at a critical point (r_c) with specific angular momentum (λ_c) for different DM density profiles with fixed $M_{\rm halo} = 10M_{\rm BH}$ and $a_0 = 10^5 M_{\rm BH}$. The top left plot corresponds to that of a Schwarzschild BH. The yellow, grey, and green points represent the saddle, nodal, and spiral-type critical points. See the text for details.

effect of $M_{\rm halo}$ and a_0, we refer the reader to section 4.4, where we focus on the portion of the $M_{\rm halo} - a_0$ parameter space for which both the inner and outer critical point exists.

4.3.2 Global accretion solution

In this section, we analyze of the variation of flow topologies due to the presence of DM halo. Table 4.1 summarizes the variation of the flow topologies with specific angular momentum (λ) for $\mathcal{E} = 1.0015$, $M_{\rm halo} = 10M_{\rm BH}$, and $a_0 = 10^5 M_{\rm BH}$ for different types of DM distribution and equal mass Schwarzschild BH. For simplicity, in Fig. 4.4, we depict the flow topologies around a vacuum Schwarzschild BH and that around a galactic BH of the same mass immersed in an Einasto-type DM halo for the parameters mentioned above. We observe that for the chosen specific flow energy, the specific angular momentum range for the I-type solution for Schwarzschild BH falls within the λ range of the I-type solutions for all DM profiles. From Fig. 4.4, we note that the presence of the Einasto-type DM halo changes the flow topology from O-type to A-type for $\lambda = 2.875$ and A-type to W-type for $\lambda = 3.1$. Increasing the angular

momentum as $\lambda = 3.36$, the topology of the solution changes from W-type to I-type in the presence of the Einasto-type DM distribution. Thus, changing the DM distribution can, in general, change the topology of the accretion flow depending on the choice of the DM and flow parameters. To elucidate this point further, in the following sections, we study the DM and flow parameter space for the existence of multiple saddle-type critical points.

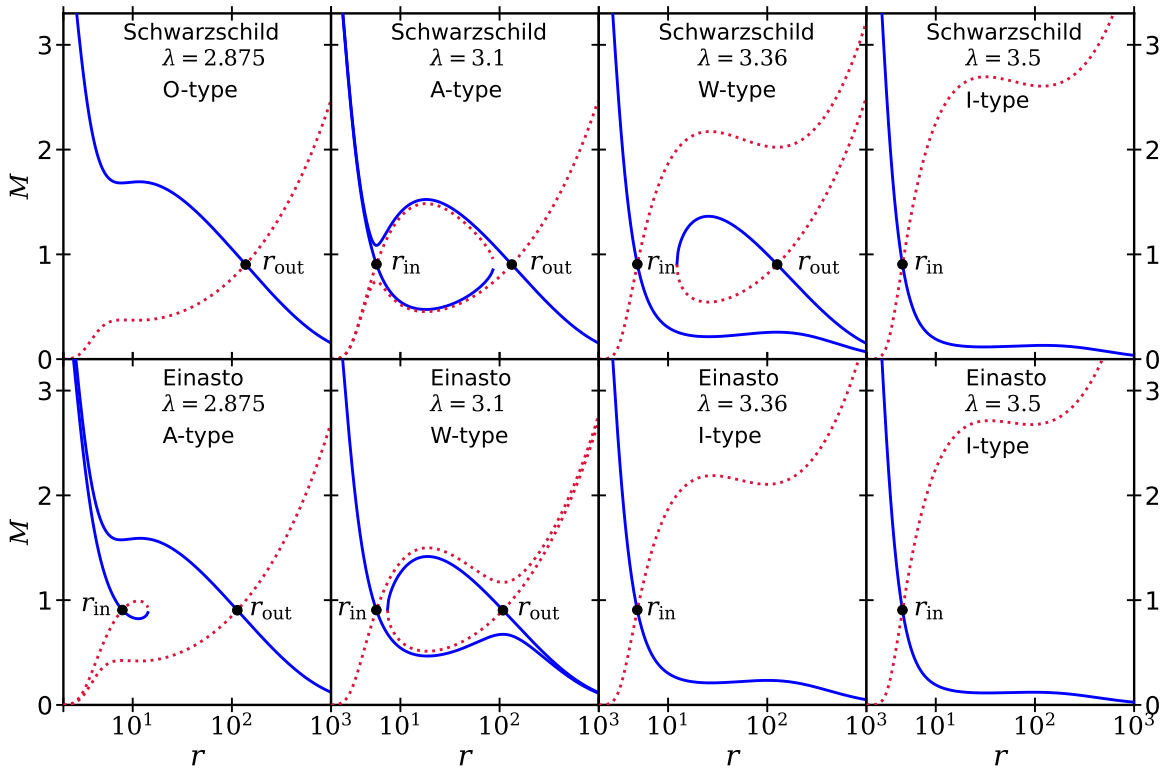

Figure 4.4: Accretion flow topologies around a galactic BH surrounded by an Einasto type DM distribution (bottom row), compared to an equal mass Schwarzschild BH (top row) with same flow parameters. Here, we choose $M_{\rm halo} = 10M_{\rm BH}$, $a_0 = 10^5 M_{\rm BH}$, $\mathcal{E} = 1.0015$. See the text for details.

4.4 Parameter space for multiple critical points

As discussed earlier, the occurrence of multiple (saddle-type) critical points happens only for a specific range of the flow parameters and DM parameters. In this section, fixing the DM parameters, we first scan the $\mathcal{E} - \lambda$ plane for multiple saddle type critical points (Fig. 4.5), then fixing the flow parameters, we repeat the analysis in the $a_0 - M_{\rm halo}$ plane (Fig. 4.6). Even within the portion of the parameter space allowing multiple (saddle-type) critical points, the topology of the accretion flow can be different. Though the entropy accretion rate ($\dot{\mathcal{M}}$) remains constant along the flow streamline, $\dot{\mathcal{M}}$ is different for the inner and outer critical points. Thus, we differentiate the accretion flow based on the solution topologies and the entropy accretion rates. In Fig. 4.5, we show the $\mathcal{E} - \lambda$ parameter space for multiple saddle-type critical points for galactic BHs with different dark matter profiles. In each panel, we portray the corresponding parameter space for a Schwarzschild BH

(black dotted line) of the same mass for comparison. The bounded regions with green (solid), blue (dash-dotted), and magenta (dashed) lines stand for three sets of DM parameters $(M_{\rm halo}, a_0) = \{(10M_{\rm BH}, 10^4 M_{\rm BH}), (10M_{\rm BH}, 10^5 M_{\rm BH}), (10^2 M_{\rm BH}, 10^4 M_{\rm BH})\}$, respectively. On the top and left of the boundary of the existence of multiple saddle critical points, the flow topologies are I-type and O-type, respectively. Contrary to the Hernquist, NFW and NFW1 profiles, the accretion flow does not possess multiple saddle type critical points for the HQ-type DM spike distribution with $(M_{\rm halo}, a_0)$=$(10M_{\rm BH}, 10^4 M_{\rm BH})$, whereas, for the Einasto type DM distribution the same is also true for $(M_{\rm halo}, a_0 = 10^2 M_{\rm BH}, 10^5 M_{\rm BH})$. In Fig. 4.5, we observe that compared to a vacuum Schwarzschild BH, the presence of DM halo shifts the allowed region of the parameter space for multiple (saddle) critical points to lower specific energies and smaller specific angular momenta. In cases of Hernquist, NFW, and NFW1 profiles, we observe that for a given halo-compactness ($\Psi = M_{\rm halo}/a_0$), increasing the halo mass shifts the upper bound of the specific energy slightly towards higher specific angular momentum. In all cases, we observe that for a fixed halo mass, increasing the halo compactness (lowering a_0) shrinks the allowed region of the parameter space, which also shifts towards lower specific angular momenta and lower specific energy of the flow. Although the admissible regions of the parameter space for the Hernquist and NFW distributions are almost similar, they are considerably different for the NFW1, Einasto and HQ-type DM spike profiles. The maximum values of λ for all the cases considered in Fig. 4.5 are set by the minimum value of the Keplerian angular momentum (i.e., λ at the marginally stable orbit, See Appendix-B.1 for details) for the corresponding DM distributions. In each panel, the shaded regions of the allowed parameter space correspond to the W-type solution, whereas the unshaded regions represent the A-type solution. Note that, for the NFW1 profile with $\Psi = 0.001$, there exists a small portion of the $\mathcal{E} - \lambda$ parameter space, where only A-type solutions exist.

Fig. 4.6 illustrates the admissible region for multiple critical points in $a_0 - M_{\rm halo}$ parameter space, corresponding to various sets of flow parameters, namely $(\mathcal{E}, \lambda) = \{(1.0009,3.0), (1.0009,3.5), (1.0022,3.0)\}$. The magenta (solid), blue (dashed) and green (dash-dotted) lines represent the lower boundary for the admissible portion of the $a_0 - M_{\rm halo}$ plane. We observe that for a fixed set of flow parameters, the allowed region of the $a_0 - M_{\rm halo}$ parameter space may contain either A type, W type or both types of accretion flow. For $\mathcal{E} = 1.0022$ and $\lambda = 3.0$, the magenta (dotted) line marks the upper bound of the W-type solutions (and lower bound of A-type solutions) for the NFW, NFW1 and Einasto DM distributions. The other solution topologies are marked in the figures respectively.

4.5 Solution properties

In this section, we study how the presence of different DM halo distributions affects the properties of the accretion flow onto the central BH. Following the I-type accretion solution[1], in Fig. 4.7, we show a representative plot of the flow properties for different halo mass and scale radius for fixed $\mathcal{E}$ (= 1.001) and λ (= 3.674). In the first two columns in Fig. 4.7, the halo compactness (Ψ) increases from 10^{-4} to 10^{-2} for a fixed $M_{\rm halo} = 10^2 M_{\rm BH}$), whereas in the third column, $M_{\rm halo}$ is increased to $10^{10} M_{\rm BH}$ keeping the halo compactness fixed at $\Psi = 0.01$. The first to fifth rows in each column

[1]For other types of solutions, the similar variations also exist.

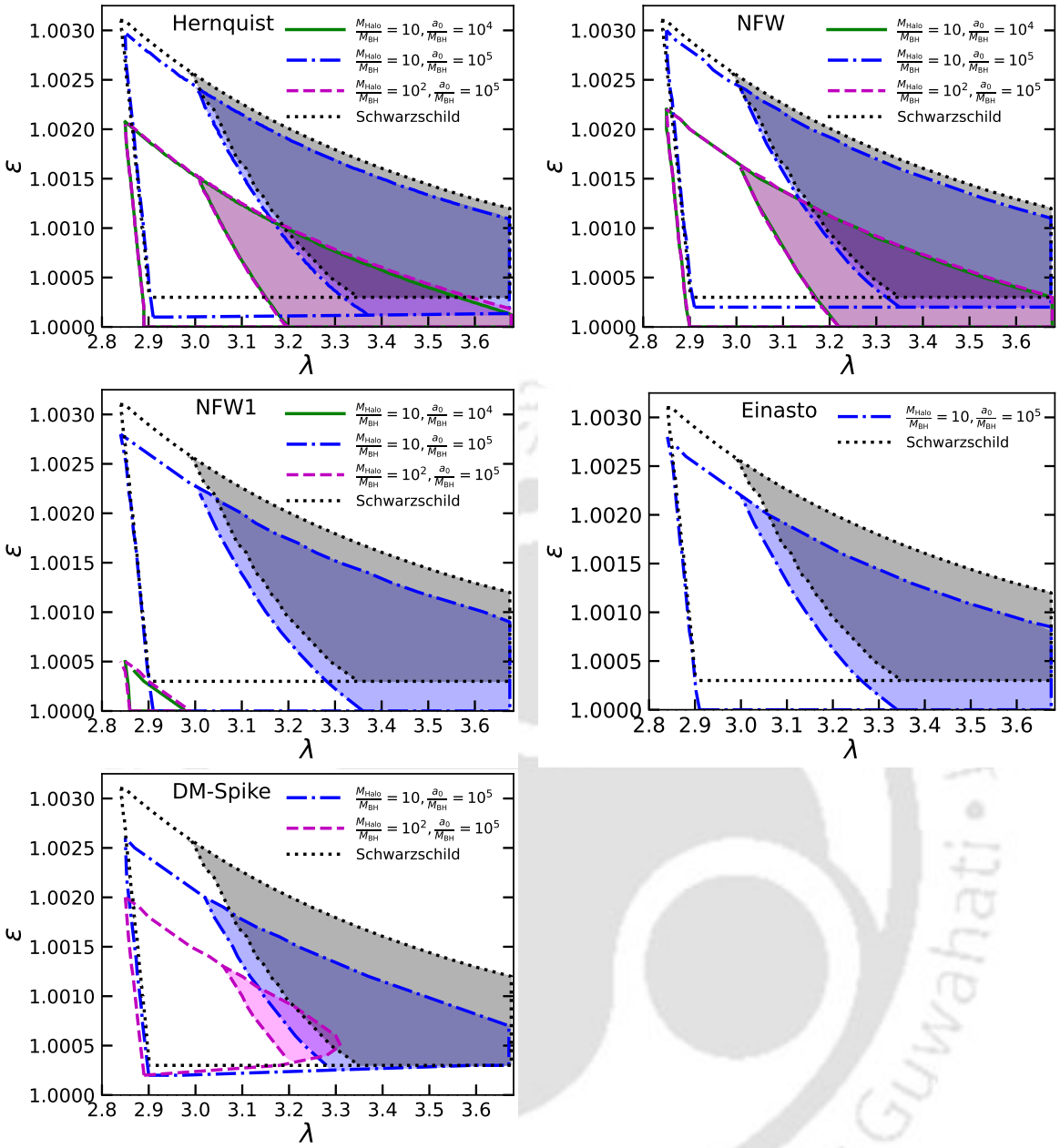

Figure 4.5: parameter space in $\mathcal{E} - \lambda$ plane for different DM profiles. Here, we take three different $(M_{\rm halo} - a_0)$ sets. The boundary region represents the parameter space in the $\mathcal{E} - \lambda$ plane for multiple saddle-type critical points. In all the figures, the black dotted line corresponds to a vacuum Schwarzschild BH with the same mass. The middle lines $(\dot{\mathcal{M}}_{\rm in} = \dot{\mathcal{M}}_{\rm out})$ in each plot divide the A-type and W-type solutions. See the text for details.

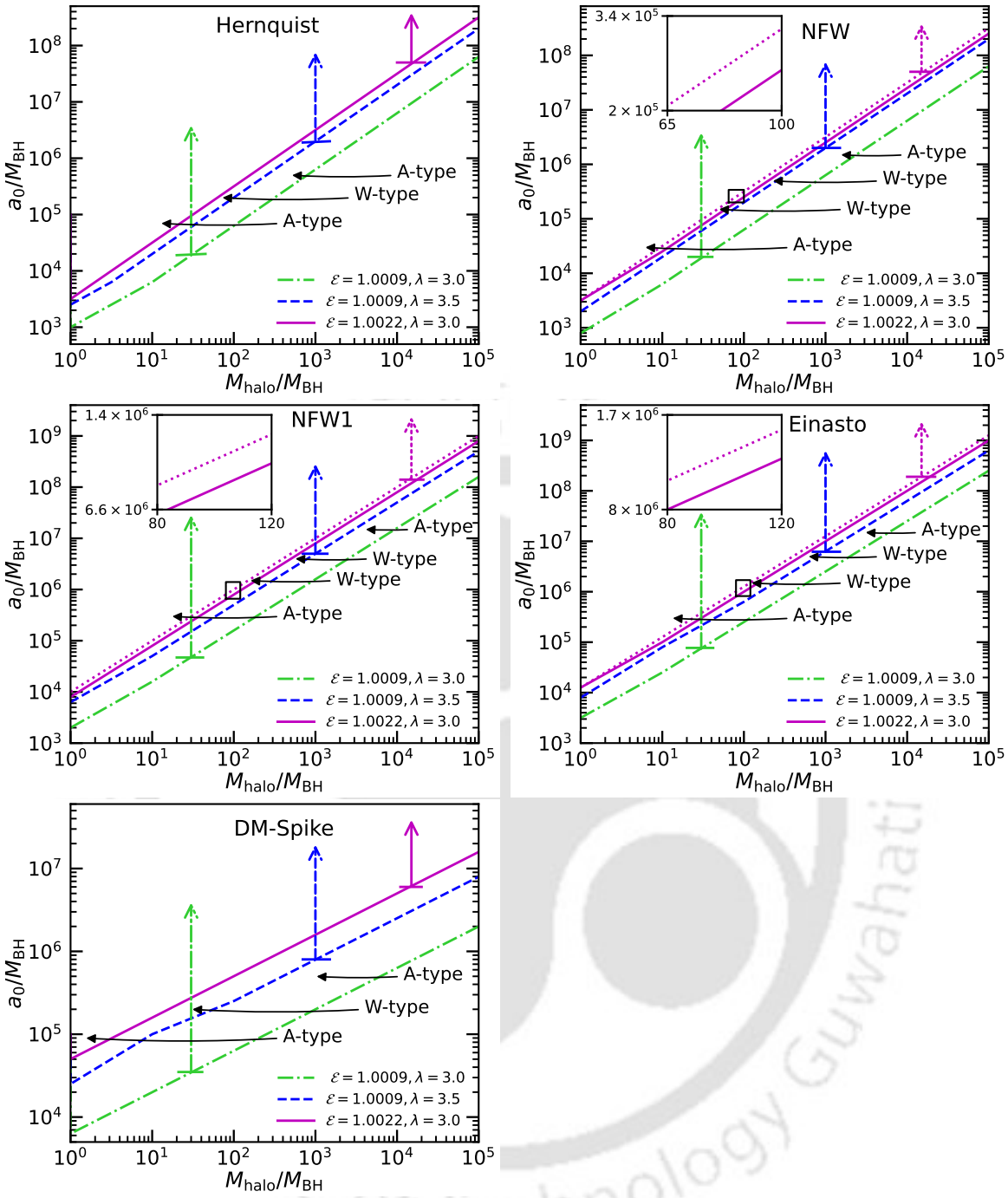

Figure 4.6: Parameter space in $a_0 - M_{\rm halo}$ plane for different DM profiles. Here we take three different $(\mathcal{E}, \lambda)$ combinations. In all the figures, we show the lower boundary of the allowed region of parameter space for multiple saddle-type critical points. See the text for details.

	λ/λ_K(O-type)	λ/λ_K(A-type)	λ/λ_K(W-type)	λ/λ_K(I-type)
Schwarzschild	<0.78	0.78–0.85	0.85–0.94	>0.94
Hernquist	<0.78	0.87–0.84	0.84–0.92	>0.92
NFW	<0.78	0.78–0.85	0.85–0.93	>0.93
NFW1	<0.78	0.78–0.84	0.84–0.90	>0.90
Einasto	<0.78	0.78–0.84	0.84–0.89	>0.89
DM - Spike	<0.78	0.78–0.84	0.84–0.87	>0.87

Table 4.1: Table showing the specific angular momenta range for different accretion flow topologies around a galactic BH with different types of DM distributions with $M_{\rm halo} = 10M_{\rm BH}$, $a_0 = 10^5 M_{\rm BH}$ and $\mathcal{E} = 1.0015$. The maximum value of λ for each profile is fixed by the corresponding Keplerian angular momentum λ_K, where, $\lambda_K^{\rm Sch} = 3.67424$, $\lambda_K^{\rm HQ} = 3.67460$, $\lambda_K^{\rm NFW} = 3.6756$, $\lambda_K^{\rm NFW1} = 3.67519$, $\lambda_K^{\rm Ein} = 3.67549$ and $\lambda_K^{\rm DM-Spk} = 3.67625$. See text for details.

represents the Mach number ($M = v/c_s$), temperature (T), density (ρ), aspect ratio (H/r), and optical depth ($\tau_{\rm eff}$), respectively. For comparison in each panel, we also plot the corresponding flow property around a vacuum Schwarzschild BH. We observe that the presence of DM halo shifts the critical point to smaller radii and decreases the flow velocity (as well as Mach number) close to the BH, in general. As the mass accretion rate of the flow is assumed to remain constant throughout, the local mass density varies inversely with the flow velocity (see Eq. (4.26)). So, when the flow velocity (as well as Mach number) is lower than the Schwarzschild BH, the density becomes higher and vice versa. The constant specific energy of the accretion flow with reduced flow velocity results in increased thermal energy of the accreting fluid. This raises the local temperature resulting in an increased thermal pressure, which puffs up the disk, making it quasi-spherical. Thus, at a fixed radius the flow with higher temperature has a higher aspect ratio (H/r).

Our analysis assumes the accretion disk to be optically thin. To ascertain that the accretion disk continues to remain optically thin, we explicitly calculate the optical depth ($\tilde{\tau}$) of the accretion disk. In fact, the optical thinness of the accretion disk is necessary for the emitted Bremsstrahlung radiation to be observable. Opacity to Bremsstrahlung radiation primarily occurs due to multiple coherent Thompson scattering of the emitted photon by the free electrons in the plasma as well as the free-free absorption in the fully ionized plasma. The opacity coefficient of Thompson Scattering is taken as $\kappa_{\rm s} = 0.4{\rm cm}^2{\rm gm}^{-1}$. We evaluate the Rosseland mean opacity coefficient for free-free emission as (Maoz, 2016),

$$\begin{aligned} k_{\rm R}^{\rm ff} =& 0.64 \times 10^{23} \rho T_e^{-7/2} \\ & \times (1 + 4.4 \times 10^{-10} T_e) \bar{g}_{\rm ff} \ {\rm cm}^2{\rm gm}^{-1}, \end{aligned} \tag{4.35}$$

where $\bar{g}_{\rm ff}$ is the frequency-averaged Gaunt factor of g_{br}. Considering the half-thickness (H) of the disk as the typical associated length scale, we evaluate the effective optical depth as,

$$\tau_{\rm eff} = \sqrt{\tau_a \left(\tau_a + \tau_s\right)} \ , \tag{4.36}$$

where $\tau_a = k_{\rm s}\rho H$ is the optical depth due to Thompson scattering and $\tau_a = k_{\rm R}^{\rm ff}\rho H$ is the absorption optical depth. We note from Eqs. (4.35), (4.36) that the optical depth depends on the local flow temperature, density and disk height. Since the presence of DM halo changes each of these flow properties, the exact deviation of the local optical depth is the result of an interplay between them. However, we note from Fig. 4.7 that the presence of DM halo does not make the accretion disk optically thick. The disk is particularly optically thinner close to the inner edge from where maximum emission occurs (see section 4.6 for details).

Comparing the first and second columns, we note that increasing the halo compactness increases the deviation from the Schwarzschild BH with the Einasto profile showing the maximum variation. Apart from the HQ-type DM spike profile, increasing the halo mass also increases the deviation of the flow properties from those of the Schwarzschild BH. In the case of HQ-type DM spike distribution, the density profile has a strong nonlinear dependence on the halo mass. For this particular case, it is observed that for small $M_{\rm halo}$ the DM density at a fixed radius decreases with the halo mass, however for large $M_{\rm halo}$, the behaviour is reversed. This change in the halo density with $M_{\rm halo}$ strongly influences the background geometry, which in turn affects the effective potential, causing the flow properties to behave nonlinearly with the halo mass (see Appendix-B.2 for details on HQ-type DM spike profile).

4.6 Radiative emission properties

In this section, we study the emission of the thermal Bremsstrahlung (free-free) radiation from the accretion disk. Bremsstrahlung emission is the radiation emitted from an accelerating electron as it passes through the field of a heavy ion. However, in the case of hot accretion flow, the flow is thermally relativistic ($k_B T_e > m_e c^2$), making the electron-electron emission more significant. Thus, following Novikov & Thorne (1973), we incorporate the relativistic effect and electron-electron emission in addition to the standard electron-ion emission channel to obtain an approximate expression for Bremsstrahlung emissivity at a frequency ν as,

$$\begin{aligned}\varepsilon_\nu =& \frac{32\pi\tilde{e}^6}{3m_e c^3}\sqrt{\frac{2\pi}{3m_e k_B}} n_e n_i z^2 T_e^{-1/2} \\ & \times (1 + 4.4\times 10^{-10} T_e) e^{-h\nu/k_B T_e} g_{br},\end{aligned} \tag{4.37}$$

where h is the Planck constant, k_B is the Boltzmann constant, n_i is the ion-number density, and $\tilde{e}$, m_e, n_e, and T_e are the charge, mass, number density and temperature of electrons, respectively. The factor g_{br} is the thermally averaged Gaunt factor that incorporates the quantum-mechanical corrections and is taken to be 1.2 (Yarza et al., 2020). Here, we consider the plasma to be hydrogenic and the electron number density to be equal to the ion number density ($n_e = n_i$). Furthermore, since the electrons are much lighter than the ions, the electron temperature must be lower than the ion temperature, which, in turn, is approximately equal to the flow temperature T. Thus, we approximate the electron temperature as $T_e \approx T/10$ throughout the accretion disk for simplicity (Yarza et al., 2020). The strong gravitation potential of the central BH implies that the emitted radiation is red-shifted as it travels towards an asymptotic observer. The rotation of the accretion disk also induces a Doppler shift of the emitted radiation. Thus, ignoring any light-bending effects, the frequency

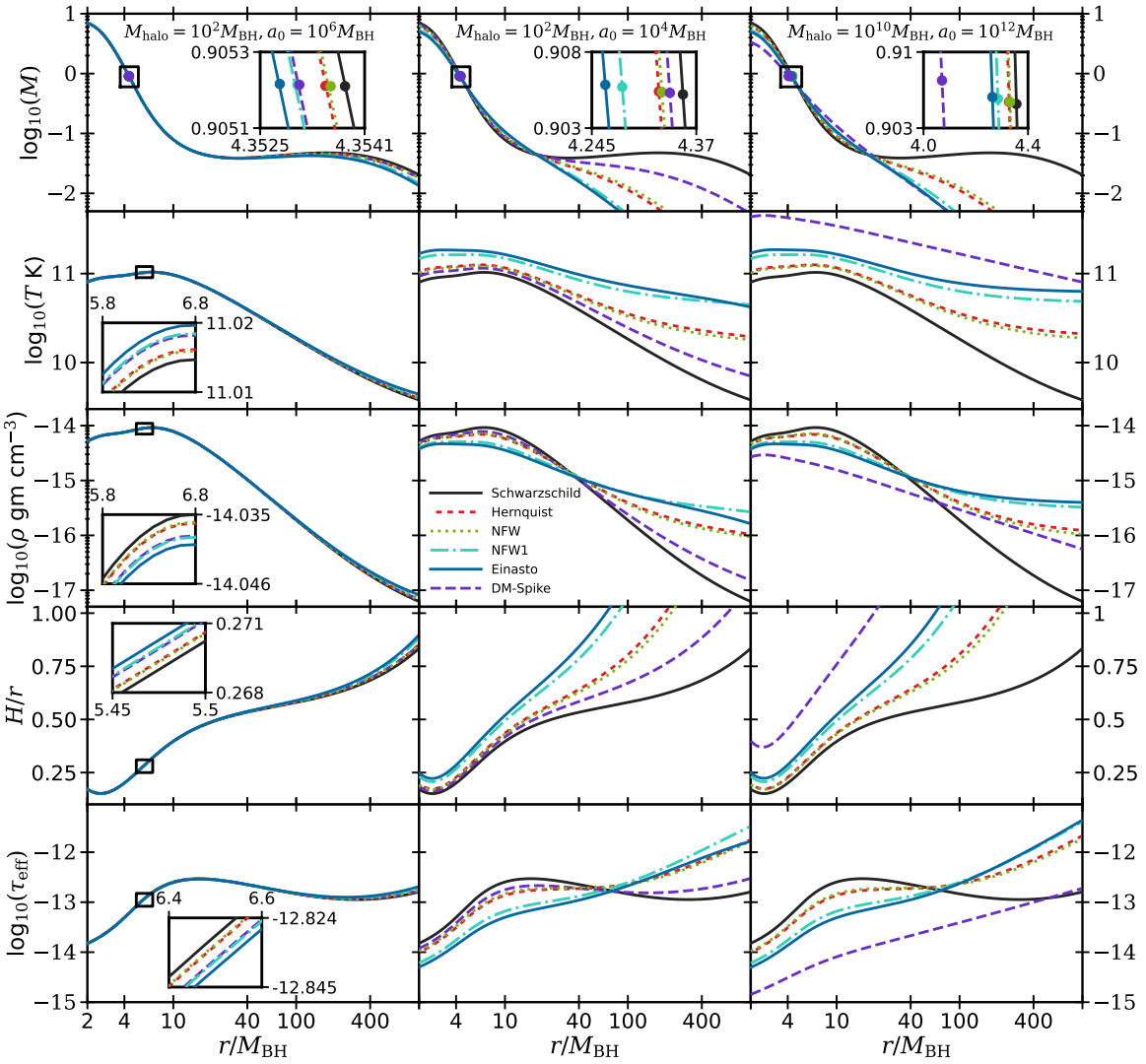

Figure 4.7: Variation of flow variables of I-type accretion flow with radial coordinate (r) for different compactness and halo mass with $\mathcal{E} = 1.001$ and $\lambda = 3.674$. In the first column, we consider $M_{\rm halo} = 10^2 M_{\rm BH}$ and $a_0 = 10^6 M_{\rm BH}$. In the second and third columns, plots are for ($M_{\rm halo}$, a_0)= ($10^2 M_{\rm BH}, 10^4 M_{\rm BH}$) and ($10^{10} M_{\rm BH}, 10^{12} M_{\rm BH}$), respectively. See the text for details.

of the emitted radiation is related to the observed frequency at asymptotic infinity as (Luminet, 1979),

$$\nu_e = \nu_o(1+z) = \nu_o u^t \left(1 + \frac{e\lambda\tilde{f}(r)}{r^2 c}\sin\theta_0 \sin\phi\right), \tag{4.38}$$

where z is the redshift factor, and θ_0 is the inclination angle of the accretion disk, which we consider to be $\pi/4$ for galactic BHs. Taking all these into account, we write the monochromatic disk luminosity for an asymptotic observer as,

$$\begin{aligned} L_{\nu_0} =& 2\int_{r_{\rm Sh}}^{r_{\rm edge}}\int_0^{2\pi} \varepsilon_{\nu_e} H r \, dr d\phi, \\ =& A\int_{r_{\rm Sh}}^{r_{\rm edge}}\int_0^{2\pi} \left[\rho^2 (T/10)^{-1/2} \times (1 + 4.4\times 10^{-11} T) e^{-10(1+z)h\nu_o/k_B T} H r \, dr d\phi\right], \end{aligned} \tag{4.39}$$

where $A = 4.875\times 10^{10} g_{br}$ erg s^{-1}Hz^{-1}, $r_{\rm H}$ and $r_{\rm edge}$ are the inner and outer edges of the accretion disk, respectively. For our analysis, we take $r_{\rm edge} = \min(1000M_{\rm BH}, r_0)$, where r_0 is such that $H/r_0 \sim 1$. This choice of $r_{\rm edge}$ is essential to ensure that our analysis respects the assumptions in section 4.2. To analyse the radiative properties of the galactic BHs, we assume the mass of the central supermassive BH as $M_{\rm BH} = 5\times 10^8 M_\odot$ (Boshkayev et al., 2020; Wu & Liu, 2004) and mass accretion rate of $\dot{M} = 0.01\dot{M}_{\rm EDD}$, where $\dot{M}_{\rm EDD} = 1.4\times 10^{18}\,(M_{\rm BH}/M_\odot)$ gm s^{-1} is the Eddington mass accretion rate.

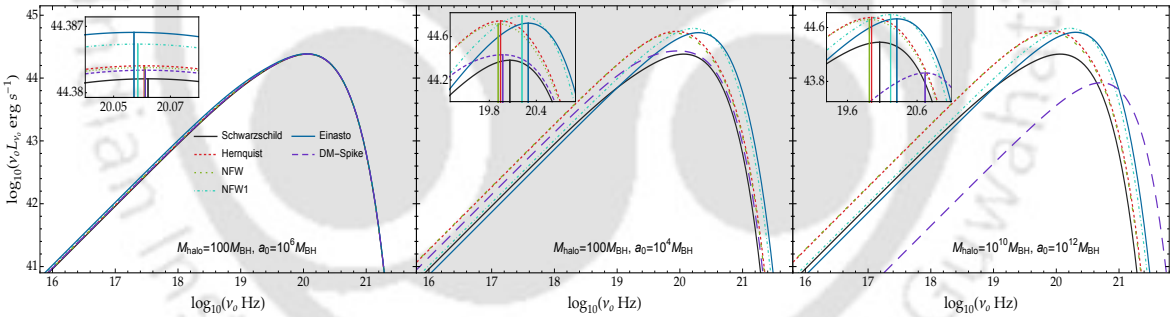

Figure 4.8: Plot of the spectral energy distribution (top row) for different DM distributions for different values of the halo mass and scale radius: $M_{\rm halo} = 100M_{\rm BH}, a_0 = 10^6 M_{\rm BH}$ (left), $M_{\rm halo} = 100M_{\rm BH}, a_0 = 10^4 M_{\rm BH}$ (middle), $M_{\rm halo} = 10^{10}M_{\rm BH}, a_0 = 10^{12}M_{\rm BH}$ (right). Halo compactness ($M_{\rm halo}/a_0$) changes from 10^{-4} (left panel) to 10^{-2} (middle panel) for a fixed halo mass, whereas it is kept fixed at 0.01 for right panel ($M_{\rm halo} = 10^{10}M_{\rm BH}$) with $M_{\rm BH} = 5\times 10^8 M_\odot$. The solid black curve in each plot shows the SED for a Schwarzschild BH of the same mass. The insets show the location of the peak of the SEDs in each case. The flow parameters are $\lambda = 3.674$ and $\mathcal{E} = 1.001$. See the text for details.

In Fig. 4.8, we show the spectral energy distribution (SED) of galactic BHs for the different DM distributions with varying halo mass and compactness, ($M_{\rm halo}/M_{\rm BH}$, Ψ)={(100, 10^{-4}), (100, 0.01), (10^{10}, 0.01) }. We choose the specific energy and angular momentum of the flow as $\mathcal{E} = 1.001$ and $\lambda = 3.674$. We choose $\lambda < \lambda_{\rm K}^{\rm Sch}$ to ensure the flow remains sub-keplerian all throughout, where $\lambda_{\rm K}^{\rm Sch}$ is the Keplerian angular momentum for Schwarzschild BH (see Appendis-B.1 for details). We observe that the presence of DM causes significant deviation of the SEDs from that of a vacuum

Schwarzschild BH of the same mass. The SED also shows a sharp cutoff at $\nu \approx 10^{21} - 10^{22}$ Hz, which is governed by the electron temperature at the inner edge of the accretion disk. The presence of a DM halo increases the cutoff frequency from that of the vacuum Schwarzschild BH. Although qualitatively similar, the SEDs for a given DM distribution show significant quantitative variation with the halo mass and compactness. For the low compactness of the DM halo, the spectral energy distribution at high frequency is almost similar to that of the vacuum Schwarzschild BH, whereas the deviation from Schwarzschild BH is relatively large in the low frequencies. On the other hand, for very high compactness, SED shows an even stronger deviation from the vacuum Schwarzshild BH. For a given halo mass, as the halo gets more and more compact, the spectral luminosity increases both in the high and low-frequency regimes. The peak luminosity is also higher for more compact halos and occurs at a relatively lower frequency (except for the Einasto and NFW1 distribution, where it shifts to a higher frequency). The location of the peak of SED corresponds to the frequency and, hence, the energy of the electrons that provide the maximum contribution to the emitted radiation. The cutoff frequency is also higher for more compact halos, which is again an artefact of the higher flow temperature for more compact halos. Though the changes in the SED with halo mass for a given halo compactness are even smaller, we observe the following general trend. The peak luminosity of the Hernquist, NFW, NFW1 and Einasto profiles slightly increases with the halo mass (left to right in Fig. 4.8) and shifts towards a higher frequency. However, for the HQ-type DM spike profile, the peak spectral luminosity decreases and shifts towards higher frequency as the halo mass is increased. For Hernquist and NFW profiles, the spectral luminosity increases with the halo mass in both low and high-frequency ranges. For NFW1, Einasto and HQ-type DM spike distributions, though the spectral luminosity at high frequencies increases with the halo mass, the behaviour is reversed at low frequencies. The cutoff frequency stays unaffected by the change in halo mass for a given halo compactness except for the HQ-type DM spike distribution, where it increases with the halo mass. Integrating the spectral luminosity over all frequencies, we get the bolometric disk luminosity as,

$$L = \int_0^\infty L_{\nu_o} d\nu_o. \tag{4.40}$$

Fig. 4.9 shows the variation of the bolometric luminosity with the halo compactness and halo mass for a given value of the flow energy[2] and angular momentum. For constant halo mass, as the halo compactness increases, the luminosity for each DM distribution increases from the Schwarzschild value reaching a maximum and then decreasing sharply. The compactness at which the maximum bolometric luminosity is obtained is different for different DM distributions. The maximum value of the luminosity for the Hernquist, NFW, NFW1 and Einasto profiles is almost the same; however, for the DM spike profile, the maximum attained luminosity is substantially smaller. In Fig. 4.9, we observe that for constant halo mass, as the halo compactness increases, the maximum bolometric luminosity for the Einasto distribution is obtained, followed by the NFW1, Hernquist, NFW and the HQ-type DM spike distributions. As discussed in section 4.5, when the compactness of the DM halo increases, the critical

[2]As the $\mathcal{E}$ is increased keeping a constant λ (=3.674), the difference with the Schwarzschild Bh's bolometric luminosity starts decreasing. At the value of the specific energy at which the Schwarzschild BH's bolometric luminosity is maximum, all the DM distributions show a reduced bolometric luminosity.

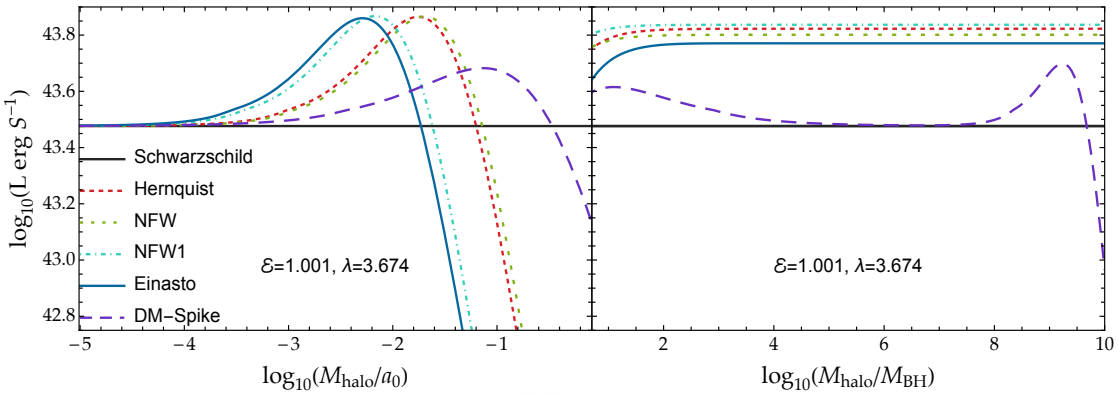

Figure 4.9: Right: Plot of bolometric luminosity for different dark matter profiles with halo compactness, $M_{\rm halo}/a_0$ for $M_{\rm halo} = 100M_{\rm BH}$ for $\mathcal{E} = 1.001$ and $\lambda = 3.674$. Left: Plot of the luminosity for different dark matter profiles with $M_{\rm halo}$ for $M_{\rm halo}/a_0 = 0.01$ for the same values of energy and specific angular momentum of the flow. See the text for details.

point shifts to smaller radii and the temperature of the accretion flow also increases, which in turn increases the luminosity. However, the increasing temperature also puffs up the accretion disk. Since our analysis is valid when the aspect ratio is less than unity ($H/r \leq 1$), the effective portion of the accretion disk contributing to the luminosity reduces, decreasing the luminosity at high compactness.

On the contrary, for fixed compactness, the bolometric luminosity increases with the halo mass, but it soon saturates with the NFW1 profile, giving the maximum luminosity followed by the Hernquist, NFW, Einasto and HQ-type DM spike distributions. The variation of the bolometric luminosity for the HQ-type DM spike distribution with the halo mass shows a rather curious behaviour when compared to other profiles (see the right panel of Fig. 4.9). For sufficiently high halo mass, the bolometric luminosity of the HQ-type DM spike distribution is less than that of a vacuum Schwarzschild BH of the same mass. This initial variation of the bolometric luminosity with the halo mass for a HQ-type DM spike distribution of constant compactness (~ 0.01) is related to the variation of the halo density profile and the associated change in geometry and properties of the accretion flow with the halo mass as discussed in section 4.5 and Appendix-B.2. At a high enough halo mass, the relative disk height attains unity at a much smaller radius, reducing the luminosity even below the Schwarzschild limit.

In Fig. 4.10, we plot the maximum luminosity of the galactic BH with different DM profiles for a constant halo mass of $100M_{\rm BH}$ and halo compactness 0.01 with $M_{\rm BH} = 5\times10^8\ M_\odot$. In the plot, we vary the specific flow energy while maintaining the specific angular momentum of the flow slightly less than the Keplerian angular momentum in each case. We observe that the maximum bolometric luminosity is obtained for the NFW1 distribution, followed by the Einasto, Hernquist and NFW distributions. The maximum luminosity in each of these cases is higher than the maximum bolometric luminosity of a vacuum Schwarzschild BH. However, the bolometric luminosity of the HQ-type DM spike distribution around an equal mass BH with the same set of halo parameters show a significantly lower luminosity. This low luminosity is a manifestation of the fact that at the chosen compactness and halo mass, the critical radius r_0 is very small (see Fig. 4.7).

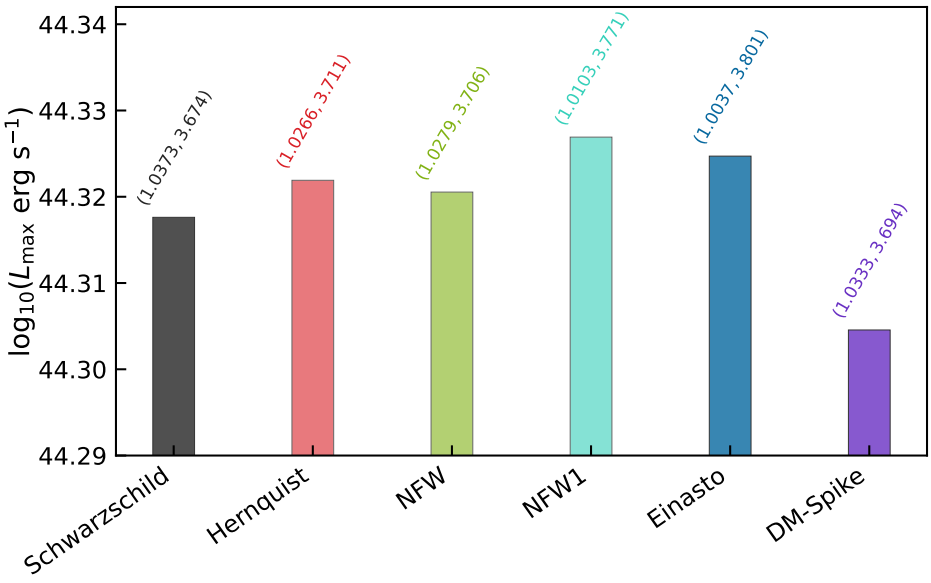

Figure 4.10: Maximum bolometric luminosity for different dark matter profiles. Here, we choose $M_{\rm halo} = 10^2 M_{\rm BH}$ and $a_0 = 10^4 M_{\rm BH}$. See the text for details.

4.7 Chapter conclusions

In this chapter, we study the advection dominated transonic hot accretion flow of an inviscid relativistic fluid onto a galactic SMBH described by the metric (Eq. (4.1)). We model the geometry of the galactic BH as a spherically symmetric central Schwarzschild BH immersed in a DM halo with radial density distributions. We represent the DM halo as an ideal gas composed of cold collisionless DM particles. In the absence of hierarchical mergers (Merritt et al., 2002), our assumptions imply a seed BH at the centre of a galaxy, dressed with the relativistic distribution of DM (Sadeghian et al., 2013) and a density spike in the inner region (Ullio et al., 2001; Merritt, 2004; Gnedin & Primack, 2004; Bertone & Merritt, 2005; Vasiliev, 2007; Shapiro & Shelton, 2016). Following Speeney et al. (2024), we have modelled this DM density spike in two different ways: (i) Hernquist, NFW, and Einasto distributions, truncated at $r = 4M_{\rm BH}$ (ensuring that all energy conditions are obeyed) and (ii) a fully relativistic HQ-type DM spike model where we assume the HQ-type DM spike grows adiabatically from an initial Hernquist type distribution. We explicitly assume the central BH to grow adiabatically, with the accretion rate of the DM particles being negligible Fig. 4.1. This leads to the anisotropic nature (zero radial pressure) of the DM distributions, a key ingredient in the entire analysis.

We maintain a strict hierarchy of the different length scales involved in the problem, $M_{\rm BH} \leq M_{\rm halo} \leq a_0$ and $r_{\rm edge} \leq a_0$, $r_{\rm edge}$ being the outer edge of the accretion disk. Although the presence of the DM halo does not change the location of the event horizon ($r_{\rm Sh} = 2M_{\rm BH}$), it greatly modifies the geometry of the surrounding spacetime (including the location of the lightrings and ISCO). This change in geometry, in turn, reduces the effective gravitational potential experienced by an infalling fluid element Fig. 4.2. The Keplerian angular momentum also shows a significant deviation from that of Schwarzschild BH, allowing flow with higher specific angular momenta to reach the event horizon (Fig. B.1). We observe that in all the cases, the presence of DM halo shifts the critical points to smaller radii, affecting the solution topologies

(Fig. 4.4, 4.5, 4.6). The primary observable in our study is the luminosity of the emitted Bremsstrahlung radiation. Since the bolometric luminosity for I-type accretion flow is known to be the highest, we chose the flow parameters such that the flow passes only through the inner saddle type critical point.

In Fig. 4.7, we observe that the gravitational effect of the DM halo weakens the inflow of the accreting fluid resulting in reduced flow velocity. The gravitational effect of the DM halo also increases the local flow temperature compared to that of a Schwarzschild BH. Since the mass accretion rate is assumed to remain constant throughout the accretion flow, the local mass density of the accreting fluid is always inversely proportional to the local velocity of the flow. Again, since the specific energy of the flow remains constant, the lower flow velocity implies a lower kinetic energy and higher thermal energy of the accreting fluid, resulting in an increased local temperature (particularly, close to the inner edge of the disk). The increase in local flow temperature results in an increased thermal pressure, which increases the relative disk height, making the accretion disk quasi-spherical. Though the optical depth (τ) of the disk still remains small, the increased disk height reduces the effective portion of the disk, contributing to the disk luminosity. This is more prominent for highly compact halos with a higher halo mass. The SED also shows a significant deviation from that of the vacuum Schwarzschild BH (Fig. 4.8). Since the dominant contribution to the luminosity for I-type accretion comes from the inner portion of the accretion disk, where deviation from the vacuum Schwarzschild geometry is strongly governed by the presence and nature of DM spike (overdensity), the variation in luminosity for the same set of halo and flow parameters indeed encode information about the nature of the density spike. The variations of the luminosity of the emitted radiation and properties of the accretion flow increase with the mass and compactness of the DM halo (Fig. 4.9). However, in the case of the HQ-type DM spike distribution, the nonlinear dependence of the density profile on the halo mass changes the flow properties significantly with the halo mass (see Appendix-B.2 for details).

Our results indicate that SMBHs in distant galaxies can, in fact, be less massive than expected if the DM contributions are considered. Since there exist tight correlations between the mass of the SMBHs and the properties of the host galaxies (such as the bulge mass (Magorrian et al., 1998; Marconi & Hunt, 2003) and velocity dispersion (Tremaine et al., 2002; Marconi & Hunt, 2003)) leading to coevolution of the SMBHs and the host galaxies our results suggest modifications in our understanding of galactic evolution (Kormendy & Ho, 2013).

Indeed, the presence of DM and the nature of its distribution around the SMBH strongly influences the geometry of the surrounding spacetime. However, the variation of bolometric luminosity may not be significant to infer the exact nature of the DM spike close to the BH. Thus, further research is required on more accurate modelling of the DM density spike around the SMBH and its correlation with a more realistic accretion model. In this regard, we must also emphasize the limitations of our accretion model. As a first step to address this complicated problem involving multiple length and time scales, we assume the accretion flow to be governed by ideal fluid dynamics, free of any dissipation mechanism. This results in a constant angular momentum of the fluid throughout the accretion flow. Incorporating dissipation mechanisms, such as radiative cooling of the disk and thermal conduction, will result in regulating the disk temperature and, hence, the disk height influencing the spectral emission properties. Furthermore, throughout our analysis, we assume the electron and ion temperatures

to be related by a simple scaling factor. We also assume the absence of long-range magnetic field.

Chapter 5

Exploring GRMHD accretion flow around Sgr A* with EHT constrained data

In all the previous Chapters (Chapters 2-4), we have studied the relativistic hydrodynamic flow around various compact and exotic compact objects. We also had a detailed discussion on how the accretion solutions and the corresponding observables are affected due to the presence of a DM halo around SMBHs. Another inherent feature is the presence of a magnetic field in astrophysical environments (see section 1.3), and it is evident from the most striking observational signatures of BH shadow of central SMBHs of M87 galaxy and Sagittarius A, which originates from the surrounding accretion disk of infalling, hot, magnetized matter.

The EHT collaboration observed the first polarimetric images of the SMBH at the center of the M87 galaxy, marking a major milestone in BH astrophysics (Collaboration, 2019a,b,c,d,e,f). Soon after, the EHT collaboration successfully captured the image of Sagittarius A* (Sgr A*) at the center of the Milky Way galaxy (Collaboration, 2022a,b,c,d,e,f; Akiyama et al., 2024b,d). Imaging and modelling analyses reveal that the image of Sgr A* is dominated by a bright, thick ring with a diameter of 51.8 ± 2.3 μas. To interpret the asymmetric ring, the EHT collaboration employed general relativistic magnetohydrodynamic (GRMHD) simulations along with general relativistic ray-tracing techniques. These simulations explored both Standard and Normal Evolution (SANE) and Magnetically Arrested Disk (MAD) scenarios across a range of BH spins. The observational data, particularly the resolved polarized structure, favoured the MAD framework with a spin parameter of $a_{\rm k} \sim 0.94$, suggesting a magnetically dominated accretion environment (Collaboration, 2022e). This asymmetry in the ring structure is well explained by strong gravitational lensing of Synchrotron radiation emitted by hot plasma near the event horizon, offering compelling evidence for the presence of a Kerr BH with mass $\sim 4\times10^6\ M_\odot$. The polarimetric measurements provided further constraints on the accretion flow properties, including the BH spin,

the mass accretion rate, the electron-to-ion temperature ratio, and the inclination angle of the observer relative to the angular momentum axis of the flow (Collaboration, 2022e; Akiyama et al., 2024b,d). Importantly, the magnetic field configuration near the event horizon was characterized using these data, revealing field strengths of 26^{+3}_{-4} G at 7.3 r_g, 67^{+8}_{-9} G at 4 r_g, and 560^{+80}_{-80} G in the vicinity of the event horizon. These measurements, along with signatures of flare related structural variability, evidently infer the critical role of magnetic fields in the dynamics of the near horizon region. Simulations based on the MAD scenario have successfully reproduced similar polarimetric features (Narayan et al., 2021; Palumbo et al., 2023), which demonstrates the dynamic role of strong magnetic fields in shaping the observed emissions from SMBHs.

Motivated by these groundbreaking observations, our goal is to investigate the accretion dynamics around a Kerr BH by solving the ideal GRMHD equations (Mitra & Das, 2024), constrained by the magnetic field strengths at various radii as reported by the EHT for Sgr A*. By solving the full set of GRMHD equations, we study low angular momentum, advective magnetized flows around a Kerr BH in the steady state. Our model framework focuses on key flow parameters, namely energy ($\mathcal{E}$), angular momentum ($\mathcal{L}$), magnetic flux (Φ), and isorotation parameter (I) (McKinney & Gammie, 2004), to construct self-consistent GRMHD accretion solutions. We also incorporate a relativistic EoS to accurately describe the thermodynamic properties of the inflowing plasma (Chattopadhyay & Ryu, 2009). Using this approach, we investigate whether the inferred magnetic field strengths reported by the EHT collaboration for Sgr A* at various radii can be reproduced. We find that, for a broad range of parameter values, our model successfully reproduces the EHT inferred magnetic field strengths with an accuracy of approximately 10%, which offers a self-consistent framework for interpreting valuable insights into the structure and magnetized properties of near horizon accretion flows.

5.1 GRMHD framework and model assumptions

We examine the accretion flow around a Kerr BH in the GRMHD framework. The line element for a stationary, axisymmetric spacetime is expressed as,

$$\begin{aligned} ds^2 =& g_{\mu\nu} dx^\mu dx^\nu \\ =& g_{tt} dt^2 + g_{rr} dr^2 + 2 g_{t\phi} dt d\phi + g_{\phi\phi} d\phi^2 + g_{\theta\theta} d\theta^2. \end{aligned} \tag{5.1}$$

In terms of Boyer & Lindquist (1967) coordinates, the components of the Kerr metric (see section 1.1.3 for detailed properties of Kerr BH) are given by,

$$\begin{aligned} g_{tt} &= (a_{\rm k}^2 \sin^2\theta - \Delta)/\Sigma, \quad ; \quad g_{rr} = \Sigma/\Delta \quad ; \quad g_{\theta\theta} = \Sigma, \\ g_{t\phi} &= (A\Delta - a_{\rm k} B \sin^2\theta)/\Sigma \quad ; \quad g_{\phi\phi} = (B^2 \sin^2\theta - A^2\Delta)/\Sigma; \end{aligned}$$

where $A = a_{\rm k} \sin^2\theta$, $\Sigma = a_{\rm k}^2 \cos\theta^2 + r^2$, $B = r^2 + a_{\rm k}^2$, and $\Delta = (r - r_{\rm H})(r - r_{\rm C})$. Here, $r_{\rm H}$ $(= 1 + \sqrt{1 - a_{\rm k}^2})$ is the event horizon, $r_{\rm C}$ $(= 1 - \sqrt{1 - a_{\rm k}^2})$ is the Cauchy horizon, and $a_{\rm k}$ is the Kerr parameter. In our analysis, we use $(-,+,+,+)$ sign convention and adopt a unit system as $M_{\rm BH} = G = c = 1$. In this unit system, length, angular momentum, and energy are expressed in terms of r_g $(= GM_{\rm BH}/c^2)$, $r_g c$ and c^2, respectively. We constrain our whole analysis on the equatorial plane of the disk considering $\theta = \pi/2$.

5.1.1 Governing Equations

We use fundamental principles to obtain the GRMHD equations that describe a relativistic, magnetized, advective accretion flow around a rotating BH in the steady state. These equations are derived from the conservation laws, *i.e.*, the conservation of mass, conservation of energy-momentum, and homogeneous Faraday's law in the presence of strong gravitational fields (Anile, 1989; De Villiers et al., 2003; Gammie et al., 2003; McKinney & Gammie, 2004), which are as follows:

$$\nabla_\mu \left(\rho u^\mu\right) = 0;\ \nabla_\mu T^{\mu\nu} = 0;\ \nabla_\mu {}^*F^{\mu\nu} = 0. \tag{5.2}$$

Here, ρ is the mass density and u^μ is the four-velocity of matter. $T^{\mu\nu}$ is the energy-momentum tensor that describes the matter distributions. ${}^*F^{\mu\nu} = \frac{1}{2}(-g)^{-1/2}\eta^{\mu\nu\delta\kappa}F_{\delta\kappa}$ is the Hodge dual of the Faraday electromagnetic tensor $F^{\mu\nu}$ and $\eta^{\mu\nu\delta\kappa}$ is the Levi-Civita symbol. Considering the fluid and Maxwell part, the total energy-momentum tensor is given by,

$$T^{\mu\nu} = (e+p)u^\mu u^\nu + pg^{\mu\nu} + F^\mu_{\ \lambda}F^{\nu\lambda} - \frac{1}{4}F^2 g^{\mu\nu}, \tag{5.3}$$

where e is the local energy density, p is the gas pressure of the flow, and $F^2 = F_{\mu\nu}F^{\mu\nu}$. We consider perfectly conducting fluid (ideal MHD condition) (Baumgarte & Shapiro, 2003; McKinney & Gammie, 2004), where the electric field in the rest frame of fluid is zero, which implies $e^\mu = F^{\mu\nu}u_\nu = 0$. In this frame, the magnetic field is written as $b^\mu = {}^*F^{\mu\nu}u_\nu$, where $u_\mu b^\mu = 0$. Finally, we write the electromagnetic tensor as $F^{\mu\nu} = -(-g)^{-1/2}\eta^{\mu\nu\lambda\delta}u_\lambda b_\delta$. Using the aforementioned relations, we get the energy-momentum tensor as,

$$T^{\mu\nu} = \rho h_{\rm tot}u^\mu u^\nu + p_{\rm tot}g^{\mu\nu} - b^\mu b^\nu, \tag{5.4}$$

where $h_{\rm tot}$ $(= h + \frac{B^2}{\rho})$ is the total specific enthalpy of the fluid, and $h = (e+p)/\rho$. The total pressure is $p_{\rm tot} = p + p_{\rm mag}$ with $p_{\rm mag} = B^2/2$ and $B^2 = b_\mu b^\mu$. We define plasma-β as the ratio of gas pressure to magnetic pressure ($\beta = p/p_{\rm mag}$) that measures the magnetic activity inside the disk.

5.1.2 Conserved quantities

Using Eq. (5.2), we get the conserved mass accretion rate along the radial direction as,

$$\dot{M} = -4\pi\rho v\gamma_v H\sqrt{\Delta} = \text{Constant}, \tag{5.5}$$

where $\dot{M}$ refers the mass accretion rate, and H denotes the local half-thickness (Riffert & Herold, 1995) of the disk, which is given by,

$$H^2 = \frac{pr^3}{\rho\mathcal{F}},\quad \mathcal{F} = \gamma_\phi^2\frac{(r^2+a_k^2)^2 + 2\Delta a_k^2}{(r^2+a_k^2)^2 - 2\Delta a_k^2}.$$

Here, v is the radial three-velocity in the corotating frame and is defined as $v^2 = \gamma_\phi^2 v_r^2$ with $\gamma_\phi^2 = 1/(1-v_\phi^2)$, $v_\phi^2 = (u^\phi u_\phi)/(-u^t u_t)$, and $v_r^2 = (u^r u_r)/(-u^t u_t)$. The radial Lorentz factor is $\gamma_v = 1/(1-v^2)^{1/2}$ and $\Omega = u^\phi/u^t = (g^{t\phi} - \lambda g^{\phi\phi})/(g^{tt} - \lambda g^{t\phi})$ is the angular velocity of the fluid.

The Kerr spacetime possesses two commuting Killing vectors associated with time (ξ^t) and azimuthal coordinate (ξ^ϕ). Using $\nabla_\mu(T^{\mu\nu}\xi_\nu) = 0$, we derive two conserved quantities along t and ϕ directions. Along the radial direction, we get,

$$\frac{-\sqrt{-g}\;\; T^r_t}{\sqrt{-g}\rho u^r} = -h_{\rm tot}u_t + \frac{1}{\rho u^r}b^r\left(g_{tt}b^t + g_{t\phi}b^\phi\right) = \mathcal{E}, \tag{5.6}$$

and

$$\frac{\sqrt{-g}\;\; T^r_\phi}{\sqrt{-g}\rho u^r} = h_{\rm tot}u_\phi - \frac{1}{\rho u^r}b^r\left(g_{\phi\phi}b^\phi + g_{t\phi}b^t\right) = \mathcal{L}, \tag{5.7}$$

where $\mathcal{E}$ and $\mathcal{L}$ are the conserved energy and angular momentum, respectively. The time component of the source-free Maxwell equation (Eq. (5.2)) implies,

$$-\sqrt{-g}\;{}^*F^{rt} = \sqrt{-g}(u^tb^r - u^rb^t) = \Phi, \tag{5.8}$$

and ϕ component of the equation (Eq. 5.2) gives us the relativistic isorotation equation (McKinney & Gammie, 2004) as,

$$\sqrt{-g}\;{}^*F^{r\phi} = \sqrt{-g}(u^rb^\phi - u^\phi b^r) = I. \tag{5.9}$$

Here, Φ and I are the magnetic flux and isorotation parameter, respectively, that remain constant all throughout along the flow streamline within the disk.

Next, we project the energy-momentum conservation equation (Eq. (5.2)) along the three spatial directions using the projection operator $h^i_\mu = \delta^i_\mu + u^iu_\mu$, where $i = 1, 2, 3$ and $\mu, \nu = 0, 1, 2, 3$. This yields the component form of the Navier–Stokes equations. The r-component of the Navier-Stokes equation, equivalently the radial momentum equation, is given by,

$$h^r_\mu\nabla_\nu T^{\mu\nu} = 0. \tag{5.10}$$

It is worth mentioning that in the vicinity of the black hole, the accretion flow is inherently relativistic due to its bulk velocity and thermal energy, whereas at sufficiently large radii, the flow is essentially non-relativistic. This implies that as matter accretes inward, it undergoes a natural transition from the non-relativistic to the relativistic regime. Describing such trans-relativistic flows requires a relativistically consistent equation of state (EoS), since formulations based on a fixed adiabatic index Γ are inadequate for capturing the thermodynamic behavior across these regimes. Therefore, to close the system of governing equations, we employ the relativistic EoS, where the adiabatic index (Γ) depends on the temperature (T) and the fluid composition, as the ideal EoS with constant Γ unable to describe the proper nature of the fluid. Following Chattopadhyay & Ryu (2009), the local energy density (e), gas pressure (p) and mass density (ρ) are related as,

$$e = \frac{\rho f}{\tau}, \quad p = \frac{2\rho\Theta}{\tau}, \tag{5.11}$$

where

$$f = (2-\zeta)\left[1 + \Theta\left(\frac{9\Theta+3}{3\Theta+2}\right)\right] + \zeta\left[\frac{m_p}{m_e} + \Theta\left(\frac{9\Theta m_e + 3m_p}{3\Theta m_e + 2m_p}\right)\right],$$

with $\tau = 1 + (m_p/m_e)$, $\zeta = n_p/n_e$, and dimensionless temperature $\Theta = k_{\rm B}T/m_ec^2$. Here, m_p and m_e denote the masses of the ion and electron, respectively, while n_i and

n_e represent their corresponding number densities. In this study, we consider $\zeta = 1$ for simplicity. The polytropic index (N) and the specific heat ratio (Γ) are given by $N = \frac{1}{2}\frac{df}{d\Theta}$ and $\Gamma = 1 + \frac{1}{N}$. It is noteworthy that the characteristic wave speeds in magnetized flows correspond to the Alfvén and magnetosonic waves. Accordingly, we define the Alfvén speed as $C_a^2 = B^2/(\rho h_{\rm tot})$ and the fast magnetosonic speed as $C_{\rm f}^2 = C_s^2 + C_a^2 - C_s^2 C_a^2$ (see Gammie et al., 2003), where the relativistic sound speed is expressed as $C_s^2 = \Gamma p/\rho h$ and the magnetosonic Mach number is given by $M = v/C_{\rm f}$.

Next, using the condition $b^\mu u_\mu = 0$, we determine the components of the magnetic field as follows:

$$\begin{aligned} b^\phi &= \frac{\frac{I}{\sqrt{-g}} + \frac{\Omega\Phi}{\sqrt{-g}(1-v_r^2)}}{\frac{v\gamma_v}{\sqrt{g_{rr}}}\left(1 - \frac{\lambda\Omega}{1-v_r^2}\right)}, \\ b^r &= \frac{\frac{\Phi}{\sqrt{-g}} + \lambda b^\phi \frac{v\gamma_v}{\sqrt{g_{rr}}}}{\left(\gamma_\phi\gamma_v\sqrt{\frac{-1}{g_{tt}+g_{t\phi}\Omega}}\right)(1-v_r^2)}, \\ b^t &= -b^r \frac{v\sqrt{g_{tt}+g_{t\phi}\Omega}}{\gamma_\phi\sqrt{-g_{rr}}} + \lambda b^\phi. \end{aligned} \tag{5.12}$$

With this, the total strength of the magnetic field is obtained as,

$$B = \left(g_{rr}(b^r)^2 + g_{tt}(b^t)^2 + g_{\phi\phi}(b^\phi)^2 + 2g_{t\phi}b^t b^\phi\right)^{\frac{1}{2}}. \tag{5.13}$$

5.1.3 Critical points analysis and transonic solutions

The derivatives of the energy conservation equation (Eq. (5.6)) and angular momentum conservation equation (Eq. (5.7)) yield,

$$\frac{d\mathcal{E}}{dr} = \mathcal{E}_r + \mathcal{E}_v\frac{dv}{dr} + \mathcal{E}_\Theta\frac{d\Theta}{dr} + \mathcal{E}_\lambda\frac{d\lambda}{dr} = 0, \tag{5.14}$$

$$\frac{d\mathcal{L}}{dr} = \mathcal{L}_r + \mathcal{L}_v\frac{dv}{dr} + \mathcal{L}_\Theta\frac{d\Theta}{dr} + \mathcal{L}_\lambda\frac{d\lambda}{dr} = 0. \tag{5.15}$$

Furthermore, we rewrite the radial momentum equation (Eq. (5.10)) as,

$$\mathcal{R}_r + \mathcal{R}_v\frac{dv}{dr} + \mathcal{R}_\Theta\frac{d\Theta}{dr} + \mathcal{R}_\lambda\frac{d\lambda}{dr} = 0. \tag{5.16}$$

All coefficients in Eqs. (5.14)-(5.16), namely $\mathcal{E}_j$, $\mathcal{L}_j$, and $\mathcal{R}_j$ (with $j = r, v, \Theta, \lambda$), are provided explicitly in the Appendix-C. Combining Eqs. (5.14)-(5.16), we obtain the wind equation of the GRMHD flow as,

$$\frac{dv}{dr} = \frac{-(\mathcal{R}_r + \mathcal{R}_\Theta\Theta_r + \mathcal{R}_\lambda\lambda_r)}{(\mathcal{R}_v + \mathcal{R}_\Theta\Theta_v + \mathcal{R}_\lambda\lambda_v)} = \frac{\mathcal{N}(r, v, \Theta, \lambda)}{\mathcal{D}(r, v, \Theta, \lambda)}, \tag{5.17}$$

where

$$\begin{aligned} \Theta_r &= (\mathcal{E}_\lambda\mathcal{L}_r - \mathcal{E}_r\mathcal{L}_\lambda)/(\mathcal{E}_\Theta\mathcal{L}_\lambda - \mathcal{E}_\lambda\mathcal{L}_\Theta), \\ \Theta_v &= (\mathcal{E}_\lambda\mathcal{L}_v - \mathcal{E}_v\mathcal{L}_\lambda)/(\mathcal{E}_\Theta\mathcal{L}_\lambda - \mathcal{E}_\lambda\mathcal{L}_\Theta), \\ \lambda_r &= (\mathcal{E}_\Theta\mathcal{L}_r - \mathcal{E}_r\mathcal{L}_\Theta)/(\mathcal{E}_\lambda\mathcal{L}_\Theta - \mathcal{E}_\Theta\mathcal{L}_\lambda), \\ \lambda_v &= (\mathcal{E}_\Theta\mathcal{L}_v - \mathcal{E}_v\mathcal{L}_\Theta)/(\mathcal{E}_\lambda\mathcal{L}_\Theta - \mathcal{E}_\Theta\mathcal{L}_\lambda), \end{aligned}$$

and $\mathcal{N}(r, v, \Theta, \lambda)$ is the numerator and $\mathcal{D}(r, v, \Theta, \lambda)$ is the denominator, respectively. Furthermore, the gradient temperature and angular momentum are expressed in terms of dv/dr as,

$$\frac{d\Theta}{dr} = \Theta_r + \Theta_v \frac{dv}{dr}, \tag{5.18}$$

and

$$\frac{d\lambda}{dr} = \lambda_r + \lambda_v \frac{dv}{dr}, \tag{5.19}$$

In the presence of magnetic fields, we simultaneously solve Eqs. (5.17)-(5.19) for a set of model parameters $(\mathcal{E}, \mathcal{L}, \Phi, I)$ to obtain the GRMHD accretion flow solutions around a Kerr BH of spin $a_{\rm k}$.

The BH accretion process initiates from the distant outskirts of the accretion disk, where gravitational influence begins to dominate the dynamics of the inflowing matter. At the outer edge of the accretion disk ($r_{\rm edge}$), the accreting plasma exhibits negligible radial motion ($v << 1$) and remains subsonic, setting the stage for a transonic transition as it spirals inward toward the event horizon. As the flow spirals inward, the immense gravitational pull of the BH accelerates the material, causing the radial velocity to rise rapidly. Near the event horizon ($r_{\rm H}$), the inflow velocity asymptotically approaches the speed of light ($v \sim 1$), satisfying the inner boundary conditions. The gravitational attraction of the BH causes the inflowing matter to undergo a transonic transition, changing from subsonic to supersonic flow. This transition necessitates that the flow passes smoothly through a critical point (r_c) on its way to the event horizon. At the critical point, the denominator ($\mathcal{D}$) of Eq. (5.17) becomes zero. Since the accretion flow remains smooth and continuous outside the event horizon, the numerator ($\mathcal{N}$) must also vanish at r_c to maintain regularity. As a result, Eq. (5.17) takes the indeterminate form $\frac{dv}{dr}\Big|_{r_c} = \frac{\mathcal{N}}{\mathcal{D}}\Big|_{r_c} = \frac{0}{0}$. To resolve this, we apply l'Hôpital's rule to evaluate the velocity gradient at the critical point at r_c. In this study, we focus on accretion solution that possesses critical point where $\frac{dv}{dr}|_{r_c}$ owns two real values with opposite signs (Kato et al., 1993; Chakrabarti & Das, 2004). It is worth mentioning that such solutions have been demonstrated to be stable under perturbations (Kato et al., 1993). Among the two real values, the negative value of $\frac{dv}{dr}|_{r_c}$ corresponds to the accretion solution, while the positive value corresponds to the winds (Das, 2007; Sarkar & Das, 2016). In the present work, we focus exclusively on accretion solutions.

Depending on the input parameters, the accretion flow may contain single or multiple critical points. A critical point located near the horizon is termed the inner critical point ($r_{\rm in}$), while one formed far away from the horizon is called the outer critical point ($r_{\rm out}$) (Chakrabarti & Das, 2004; Das, 2007). By choosing the set of input parameters ($\mathcal{E}$, $\mathcal{L}$, Φ, I, $a_{\rm k}$, and $\dot{M}$), we simultaneously solve $\mathcal{N} = 0$ and $\mathcal{D} = 0$ along with Eq. (5.6) and Eq. (5.7) to compute the flow variables, such as radial velocity ($v_{\rm c}$), temperature ($\Theta_{\rm c}$), and angular momentum ($\lambda_{\rm c}$) at $r_{\rm c}$. Using these flow variable, we integrate Eqs. (5.17)-(5.19) outward from $r_{\rm c}$ to the outer edge ($r_{\rm edge}$) and inward to the BH horizon ($r_{\rm H}$). Combining these two branches yields a global accretion solution for the GRMHD flow around rotating BH (Mitra et al., 2022; Mitra & Das, 2024).

The formalism developed in this study to obtain global GRMHD accretion solutions serves as a robust framework to investigate the magnetic environment of Sgr A*. As the SMBH at the center of our galaxy, Sgr A* exhibits low-luminosity accretion,

where magnetic fields are expected to play a pivotal role in shaping the structure and dynamics of the accretion flow. By adopting suitable input parameters consistent with observational constraints for Sgr A*, the present model framework allows for a self-consistent analysis of the flow structure, including the profiles of Mach number (M), velocity (v), density (ρ), temperature (T), magnetic field (B) and plasma-β. This, in turn, can provide valuable insights into the physical conditions prevailing in the vicinity of the event horizon and contribute to the theoretical interpretation of high-resolution observations, such as those conducted by the Event Horizon Telescope (EHT) collaboration (Akiyama et al., 2024b,d).

5.2 Results and astrophysical implications

In this section, we explore the astrophysical relevance of our model solutions, with a particular focus on the compact, luminous source Sgr A*. This SMBH, located at the center of the Milky Way, is a prominent emitter of radio waves (Balick & Brown, 1974; Ekers et al., 1975). Owing to its distinctive characteristics, Sgr A* serves as a natural laboratory for testing the predictions of general relativity. Long-term observational campaigns, encompassing precise measurements of its proper motion and the orbital dynamics of nearby stars, have confirmed Sgr A* as a highly compact mass concentration situated approximately $D \sim 8$ kpc from Earth (Do et al., 2019; Abuter et al., 2019). Furthermore, direct imaging of the central source and its immediate environment by EHT, a global array of eight radio telescopes spanning six geographic locations, has produced an image consistent with the shadow of an accreting Kerr BH with a mass of $M_{\rm BH} \sim 4\times10^6 M_\odot$ (Collaboration, 2022a). Complementary observations by the Chandra X-ray Observatory, which detect Bremsstrahlung emission near the gas capture radius, estimate the accretion rate at large radii ($\sim 10^5 r_{\rm Sh}$, where $r_{\rm Sh}$ is the Schwarzschild radius) to be in the range of $10^{-6} - 10^{-5} M_\odot {\rm yr}^{-1}$ (Quataert, 2002). In contrast, Faraday rotation measurements of polarized millimeter-wavelength emission near the event horizon suggest a much lower accretion rate, approximately $10^{-9} - 10^{-7} M_\odot {\rm yr}^{-1}$ (Bower et al., 2003; Marrone et al., 2006).

The EHT collaboration investigated MAD models with spin parameters $a_{\rm k} = -0.94, -0.5, 0, 0.5$, and 0.94, and constrained the mass accretion rate to lie within the range $10^{-9} - 10^{-8} M_\odot {\rm yr}^{-1}$, accompanied by an outflow power of approximately 10^{38} erg s^{-1}. Sgr A* exhibits broadband emission extending from radio to hard X-ray wavelengths. Comparative analysis of EHT observations and numerical simulations suggests that the mass accretion rate is of the order of $\sim 10^{-8} M_\odot {\rm yr}^{-1}$, with a bolometric luminosity not exceeding 10^{36} erg s^{-1} (Collaboration, 2022e). These findings collectively indicate that Sgr A* hosts a radiatively inefficient accretion flow, classifying it as a low-luminosity SMBH. Remarkably, EHT imaging reveals a bright, thick emission ring with an angular diameter of 51.8 ± 2.3 μas (Collaboration, 2022a). Furthermore, leveraging polarized intensity maps and GRMHD simulations, the EHT collaboration has constrained the radial profile of the magnetic field strength in the vicinity of the event horizon (Akiyama et al., 2024b,d). Specifically, the mass-weighted average magnetic field strength is found to be 26^{+3}_{-4} G at $7.3 r_g$, increasing to 67^{+8}_{-9} G at $4 r_g$, and reaching 560^{+80}_{-80} G near the event horizon. These results are most consistent with MAD models featuring a high spin value of $a_{\rm k} \sim 0.94$, and serve as essential observational benchmarks for validating theoretical models of BHs and their surrounding

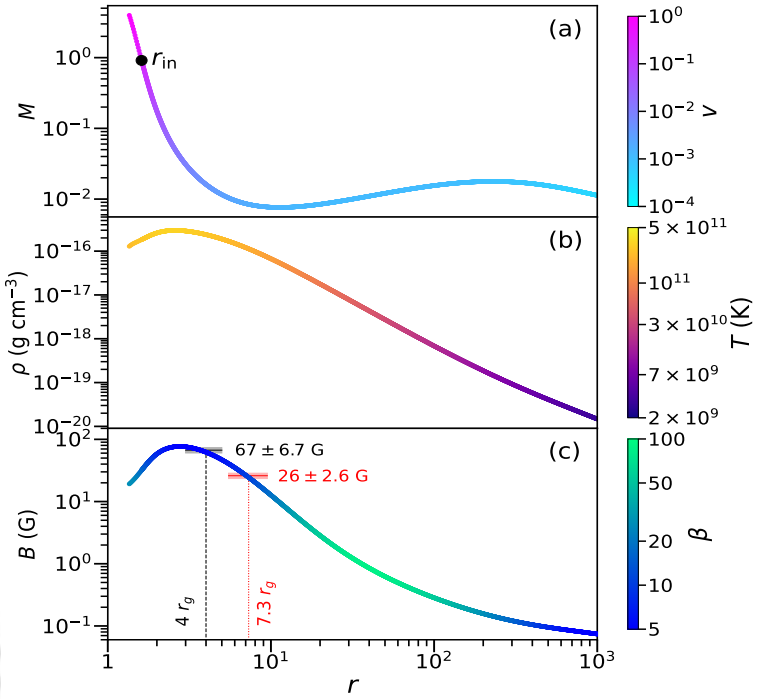

Figure 5.1: Example of a global GRMHD accretion solution around a Kerr BH that accounts the EHT inferred magnetic fields at 7.3 $r_{\rm g}$ and 4 $r_{\rm g}$. In panel (a), variation of Mach number (M) is depicted with radial coordinate (r), where color denotes the flow velocity (v). Filled circle in black denotes the inner critical point ($r_{\rm in}$). Panel (b) shows the radial variation of density (ρ), whereas temperature (T) is shown using color. Panel (c) illustrates the magnetic field (B) variation with r, while plasma-β is plotted using color. Thick grey and red horizontal lines denote the magnetic field strengths of 67 ± 6.7 G and 26 ± 2.6 G, respectively that intersect GRMHD accretion solution at 4 $r_{\rm g}$ and 7.3 $r_{\rm g}$. See the text for details.

magnetized accretion flows.

We therefore aim to investigate the viability of our magnetized accretion solutions, discussed earlier, in light of the recent observational constraints reported by the EHT collaboration (Akiyama et al., 2024d). For this purpose, we adopt two key inputs from their analysis, namely the mass accretion rate and the radial profile of the magnetic field strength. In addition, we consider a BH mass of $M_{\rm BH} = 4{\times}10^6 M_\odot$ (Do et al., 2019; Abuter et al., 2019) and a spin parameter $a_{\rm k} = 0.94$ (Akiyama et al., 2024d), consistent with values reported in the literature. Guided by these, we explore the properties of the corresponding global GRMHD accretion solutions. We depict a representative solution along with its hydrodynamic and magnetic properties in Fig. 5.1. This solution is selected such that the magnetic field strength remains within ±10% of the EHT reported best-fit values at $7.3r_{\rm g}$ and $4r_{\rm g}$. Here, we choose the following model input parameters as $\mathcal{E} = 1.001$, $\mathcal{L} = 2.4$, $\Phi = 10.5 \times 10^{-13}$, $I = 5 \times 10^{-15}$, and a mass accretion rate of $\dot{M} = 10^{-8} M_\odot {\rm yr}^{-1}$.

In Fig. 5.1a, we display the radial variation of the Mach number (M), where the color bar indicates the corresponding fluid velocity (v). The transition from subsonic to supersonic flow, via the inner critical point located at $r_{\rm in} = 1.612r_g$ (marked with filled black circle), is clearly evident. The flow velocity at $r_{\rm in}$ is $v(r_{\rm in}) = 0.235$ and the corresponding fast magnetosonic speed at $r_{\rm in}$ is $C_{\rm f}(r_{\rm in}) = 0.255$. Fig. 5.1b illustrates

the variation of density (ρ) as a function of radial distance (r), with the color bar representing the temperature of fluid (T). As the accreting matter approaches the event horizon, both the density and temperature increase significantly relative to their values at the outer edge ($r_{\rm edge} = 10^3 r_g$). The temperature of the accreting plasma exceeds 10^{11} K in the innermost regions of the disk, indicative of a geometrically thick, optically thin, and radiatively inefficient hot accretion flow (Narayan & Yi, 1994; Yuan et al., 2003). Such extreme thermal conditions are characteristic of low-luminosity accretion systems and are consistent with the physical properties expected near the event horizon of Sgr A* (Genzel et al., 2010; Collaboration, 2022a). The lower panel (Fig. 5.1c) presents the variation of the total magnetic field strength (B) as the accretion flow progresses inward toward the horizon. The associated color bar represents the plasma-β parameter, which quantifies the ratio of gas pressure to magnetic pressure, thereby offering insights into the relative dominance of magnetic pressure over thermal pressure in different regions of the flow (Mitra et al., 2022). Overplotted on this panel are two horizontal shaded bands in red and grey that correspond to the mean magnetic field strengths of 26 G and 67 G, respectively, each with 10% uncertainty, as inferred from the EHT observations. The intersections of these shaded regions with our model GRMHD accretion solution occur at radial distances of approximately $7.3r_{\rm g}$ and $4r_{\rm g}$ that demonstrate the consistency of our model formalism with the findings from EHT collaboration (Akiyama et al., 2024d) reported for Sgr A*. Note that as matter approaches the BH horizon, its velocity rises sharply (see panel (a)) due to strong gravity, leading to decreases in density and temperature in order to conserve the mass accretion rate (see Eq. (5.5)). In an ideal MHD flow with frozen-in magnetic fields, this drop in density with decreasing radius results in a corresponding reduction in magnetic field strength. Furthermore, we assess the state of the magnetized accretion flow by computing the magnetic flux threading the inner region near the BH using $\int_0^{2\pi} \sqrt{-g}(u^t b^r - u^r b^t) d\phi \sim 1.36 \times 10^{25}\,{\rm G\,cm^2}$. This flux remains well below the threshold for a MAD estimated as $\sim 3.8 \times 10^{27}\,{\rm G\,cm^2}$ for Sgr A* (Yuan & Narayan, 2014).

We emphasize that Fig. 5.1 presents only one representative example among many possible global GRMHD accretion solutions that are consistent with the magnetic field strengths observed by the EHT near Sgr A* at specific radii. To systematically identify the full range of such GRMHD accretion solutions, we explore the parameter space in the $\mathcal{L}-\Phi$ plane, which reveals a substantial domain supporting magnetic field strengths that match the EHT-inferred values within observational uncertainties. In doing so, we fix the BH mass $M_{\rm BH} = 4 \times 10^6 M_\odot$ and the mass accretion rate $\dot{M} = 10^{-8} M_\odot {\rm yr}^{-1}$, as indicated by EHT observations. Furthermore, we choose $\mathcal{E} = 1.001$, $I = 5 \times 10^{-15}$ and $a_{\rm k} = 0.94$, as the model parameters. The resulting parameter space is illustrated in Fig. 5.2, where we identify effective domains in the $\mathcal{L} - \Phi$ plane that result in magnetic field strengths within $\pm 10\%$ error of the EHT-reported mean values at $4r_{\rm g}$ and $7.3r_{\rm g}$ (Akiyama et al., 2024d). In the figure, the region shaded in cyan corresponds to GRMHD accretion solutions that yield $B = 67 \pm 6.7$G at $4r_{\rm g}$, while the magenta shaded region includes those solutions consistent with $B = 26 \pm 2.6$G at $7.3r_{\rm g}$. It is important to emphasize that the overlapping region (appeared as violet) in Fig. 5.2 represents the subset of GRMHD accretion solutions that simultaneously satisfy both magnetic field constraints inferred from the EHT observations, namely, the magnetic field strengths of $B = 26 \pm 2.6$ G at $7.3r_{\rm g}$ and $B = 67 \pm 6.7$ G at $4r_{\rm g}$. The inset panels provide the magnified views of these overlapping regions. This convergence

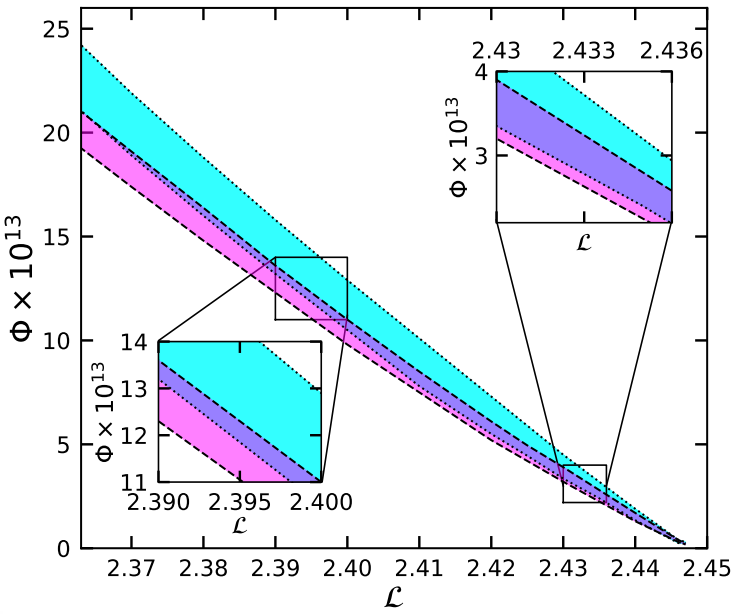

Figure 5.2: Effective domain of the parameter space in $\mathcal{L}-\Phi$ plane corresponding to GRMHD accretion solutions that reproduce EHT inferred magnetic field strength. The region shaded with cyan admits accretion solutions yielding magnetic field strength of 67 ± 6.7 G at $7.3r_g$, while magenta shaded region corresponds to solutions matching 26 ± 2.6 G at $4r_{\rm g}$. Overlapping region (appeared as violet) provides accretion solutions that simultaneously satisfy magnetic fields constraints at both radii. See the text for details.

of observational consistency at two distinct radii makes these solutions particularly significant, as they offer a self-consistent framework for describing the magnetized accretion environment around Sgr A*. Therefore, the GRMHD solutions corresponding to this overlapping parameter space are well-suited to interpret and reproduce the magnetic field structure reported by the EHT collaboration (Akiyama et al., 2024d) for the Galactic Center SMBH Sgr A*.

5.3 Chapter conclusions

In this study, we investigate the properties of the magnetized accretion flows around a spinning BH by solving the GRMHD equations within a simplified 1.5-dimensional disk geometry under steady state conditions. Our motivation stems from recent observations of Sgr A* by EHT (Collaboration, 2022a,b,c,d,e,f; Akiyama et al., 2024b,d), which offer crucial constraints on the magnetic field distribution in the immediate vicinity of the BH. According to the EHT collaboration, the magnetic field strength near Sgr A* is estimated to be 26^{+3}_{-4}G at $7.3r_{\rm g}$ and 67^{+8}_{-9}G at $4r_{\rm g}$, assuming a Kerr BH with mass $M_{\rm BH} = 4 \times 10^6 M_\odot$, mass accretion rate $\dot{M} = 10^{-8} M_\odot$ yr^{-1}, and spin parameter $a_{\rm k} = 0.94$.

Upon imposing these key constraints, we obtain global GRMHD accretion solutions that are consistent with the reported field strengths within $\pm 10\%$ error at $7.3r_{\rm g}$ and $4r_{\rm g}$. One such representative solution is presented that captures the detailed characteristics of the GRMHD accretion flow, including the radial profiles of Mach number (M), radial velocity (v), density (ρ), temperature (T), magnetic field strength (B), and the

plasma-β parameter (see Fig. 5.1).

To assess the generality of our findings, we systematically explore the parameter space spanned by the magnetic flux (Φ) and the angular momentum ($\mathcal{L}$), identifying the global accretion solutions that remain consistent with the EHT-inferred magnetic field strengths at both radii. This analysis reveals that a family of solutions can simultaneously account for the magnetic field values at $7.3r_{\rm g}$ and $4r_{\rm g}$ as reported by the EHT, suggesting that the magnetized accretion flow around Sgr A* can be well described by GRMHD models within a constrained but physically realistic range of parameters (see Fig. 5.2). With this, we indicate that the present study provides a self-consistent theoretical framework based on GRMHD accretion flows that supports and complements the EHT findings in explaining the magnetized accretion flows around Sgr A*.

At the end, we mention that the present study involves several simplifying assumptions. The accretion flow is modelled in a 1.5-dimensional geometry, confined near the disk equatorial plane, and the polar magnetic field component (b^θ) is neglected, although it is important for launching winds, jets, and outflows. Radiative cooling is ignored, and the flow is treated as a single-temperature fluid, neglecting the two-temperature nature of ions and electrons. The analysis is also restricted to the ideal MHD limit, omitting resistive or dissipative effects.

Indian Institute of Technology Guwahati

Chapter 6

Properties of the tilted thin accretion disk around Kerr-Taub-NUT black hole

In the preceding Chapters, we have focused on hydrodynamic and magnetohydrodynamic accretion flows around compact objects, where the spin axis of the compact object is aligned with the angular momentum axis of the disk. In realistic astrophysical environments, such alignment is not always possible, which results in a misaligned disk structure. Therefore, the Lense-Thirring (LT) effect causes the orbital plane of a test particle to precess around a rotating central object (Lense & Thirring, 1918) in a tilted disk (see section 1.6 for detailed description). This effect does not occur in the non-rotating Schwarzschild spacetime, which apparently indicates that the LT effect arises due to the rotation of the spacetime. If one goes deeper, one can discover that the 'rotation' is not the fundamental entity responsible for the orbital plane precession. It turns out that the orbital plane precession can arise in any stationary spacetime (Chakraborty & Majumdar, 2014) which violates the time reflection ($t \to -t$) symmetry but preserves the time translation ($t \to t+k$, where k is a constant) symmetry (Wald, 1984). The presence of spin parameter or Kerr parameter ($a_{\rm k}$) is responsible to make the Kerr spacetime stationary. If the Schwarzschild spacetime contains the NUT parameter/gravitomagnetic monopole (GMM) (Newman et al., 1963), it is called as the Taub-NUT spacetime, which is stationary but spherically symmetric (Misner, 1963). In principle, the stationary nature of the Taub-NUT spacetime allows us to observe the orbital plane precession (Chakraborty & Bhattacharyya, 2018). Thus, it is evident that the orbital plane not only precesses in the stationary and axisymmetric spacetime, but it can also precess if either of them does not hold. NUT parameter gives a 'rotational sense' (Chakraborty & Majumdar, 2014) in this spacetime, as it violates the time reflection symmetry. Now, if a Kerr spacetime contains the NUT parameter, it is called as the KTN spacetime (see the interpretation of NUT parameter in section 1.1.3). According to Bardeen & Petterson (1975), the inner region of a tilted

accretion disk will be in the equatorial plane around a spinning BH (see section 1.6). After that, many authors did the analysis of tilted disk (Papaloizou & Pringle, 1983; Pringle, 1992; Scheuer & Feiler, 1996; Ogilvie, 1999) without taking the contribution from the inner accretion disk. Chakraborty & Bhattacharyya (2017) shows that the inner disk may not be aligned at all for certain reasonable ranges of parameter values of spacetime and flow variables. Observationally, the signature of warped accretion disk was found around the BHs H1743-322 (Ingram et al., 2016) and GRO J1655-40 (Martin et al., 2008). Along with this, the existence of GMM was reported by Chakraborty & Bhattacharyya (2018); Chakraborty & Bhattacharyya (2019) in the astrophysical collapsed object GRO J1655-40, primordial BHs (Chakraborty & Bhattacharyya, 2022) and M87* (Ghasemi-Nodehi et al., 2021). Flattening out of the galaxy rotation curves may be a manifestation of the presence of n, without the need for DM particles (Govaerts, 2023; Ruggiero, 2024). Thus, one should probe the inner accretion disk around a KTN BH and find how the inner accretion disk structure is affected due to the presence of both the Kerr parameter and GMM.

Motivated by these, in this Chapter, we study a tilted thin inner accretion disk around a slowly-spinning KTN BH that contains a small NUT parameter. Taking into account the contribution from the inner accretion disk around the KTN BH, we calculate the radial profile of a tilt angle. Depending on the numerical values of the viscosity of the accreting material and Kerr parameter, we show that the GMM tends the angular momentum of the disk to align along the BH's spin axis, or to make it more tilted. Our solution for the radial profile of the tilted disk around a KTN BH could be useful to probe the strong gravity regime and could also give indirect evidence for the existence of GMM in nature.

6.1 Lense-Thirring precession in Kerr-Taub-NUT spacetime

The KTN metric is expressed here in Schwarzschild-like coordinates $(t,\ R,\ \theta,\ \phi)$ in the geometrized unit $(G = c = 1)$ (Miller, 1973; Chakraborty & Bhattacharyya, 2018),

$$ds^2 = -\frac{\Delta}{\Sigma}(dt - Ad\phi)^2 + \frac{\Sigma}{\Delta}dr^2 + \Sigma d\theta^2 + \frac{1}{\Sigma}\sin^2\theta(a_{\rm k}dt - Bd\phi)^2, \tag{6.1}$$

where

$$\Delta = r^2 - 2M_{\rm BH}r + a_{\rm k}^2 - n^2, \quad \Sigma = r^2 + (n + a_{\rm k}\cos\theta)^2,$$
$$A = a_{\rm k}\sin^2\theta - 2n\cos\theta, \quad B = r^2 + a_{\rm k}^2 + n^2.$$

with $M_{\rm BH}$ is the mass of the BH, $a_{\rm k}$ is the Kerr parameter and n is the NUT parameter. The outer horizon is located at $r_{\rm H}^{\rm KTN} = M_{\rm BH} + \sqrt{M_{\rm BH}^2 + n^2 - a_{\rm k}^2}$.

The exact LT precession frequency ($\Omega_{\rm LT}^{\rm KTN}$) for the prograde orbits at $\theta \to \pi/2$ in the KTN spacetime is derived as (Chakraborty & Bhattacharyya, 2018),

$$\Omega_{\rm LT}^{\rm KTN} = \frac{m^{1/2}}{r^{1/2}\ (r^2+n^2) + a_{\rm k}\ m^{1/2}}\left[1 - \frac{1}{m^{1/2}\ (r^2+n^2)} \times \left[+2n^2r(3r^4 - 2n^2r^2 + 3n^4)\right.\right.$$
$$M_{\rm BH}(r^6 - n^6 + 15n^4r^2 - 15n^2r^4) - 4a_{\rm k}r^{1/2}m^{1/2}(n^2 + M_{\rm BH}r)(n^2 + r^2)$$
$$\left.\left.+16M_{\rm BH}^2n^2r^3 - a_{\rm k}^2\left\{M_{\rm BH}(n^4 + 6n^2r^2 - 3r^4) - 8n^2r^3\right\}\right]^{1/2}\right], \tag{6.2}$$

where $m = M_{\rm BH}\ (r^2 - n^2) + 2\ n^2 r$. For $n \to 0$, Eq. (6.2) reduces to LT precession frequency for Kerr BH as,

$$\Omega_{\rm LT} = \frac{M_{\rm BH}^{1/2}}{\left(r^{3/2} + a_{\rm k} M_{\rm BH}^{1/2}\right)} \times \left[1 - \left(1 - \frac{4a_{\rm k} M_{\rm BH}^{1/2}}{r^{3/2}} + \frac{3a_{\rm k}^2}{r^2}\right)^{1/2}\right], \tag{6.3}$$

which is well-known expression of the orbital plane precession frequency ($\Omega_{\rm LT}$) in the Kerr spacetime.

In this work, we study the tilted thin accretion disk around a KTN BH of mass $M_{\rm BH}$ neglecting the higher order terms related to $a_{\rm k}/r$ and n/r. Thus, let us first write down the expression of $\Omega_{\rm LT}^{\rm KTN}$ (Eq. (6.2)) upto the second order of $a_*(\equiv a_{\rm k}/M_{\rm BH})$ and $n_*(\equiv n/M_{\rm BH})$, *i.e.*,

$$\Omega_{\rm p} \equiv \Omega_{\rm LT}^{\rm KTN} \approx \frac{2a_* M_{\rm BH}^2}{r^3} - \frac{3a_*^2 M_{\rm BH}^{5/2}}{2r^{7/2}} - \frac{2n_*^2 M_{\rm BH}^{3/2}}{r^{5/2}} \times (1 - 2M_{\rm BH}/r)^2 + \mathcal{O}(a_*^3, n_*^3). \tag{6.4}$$

The reason for considering upto the second order of both the parameters in Eq. (6.4) is that the lowest order of NUT parameter appears in the metric (Eq. (6.1)), and thereby in the LT precession frequency expression (Eq. (6.2)) is in the second order. Thus, in order to observe the effect of GMM in our study, it is necessary to take into account up to the second order of n_*. It is also evident from Eq. (6.4) that no linear order term of n_* appears in the expression of $\Omega_{\rm p}$. To compensate n_*^2 in Eq. (6.4), we consider upto the second order term of Kerr parameter (i.e., a_*^2). The first term of Eq. (6.4) represents the LT precession frequency for the Kerr BH (Caproni et al., 2006; Fragile et al., 2007; Fragile & Anninos, 2005; Martin et al., 2008; Nelson & Papaloizou, 2000; Natarajan & Armitage, 1999; Banerjee et al., 2019b; Li et al., 2015; Li et al., 2013). The second term of Eq. (6.4) represents the precession due to the quadrupole moment of the Kerr BH (Bardeen & Petterson, 1975). This second term is negligible compared to the first term and might be less important at the large distance (i.e., $r >> M_{\rm BH}$) as it varies $\sim a_*^2/r^{7/2}$. On the other hand, the third term which corresponds to the LT precession due to the NUT parameter/GMM, dominates over the second term as it varies $\sim n_*^2/r^{5/2}$. Note that, the modulus of third term can even dominate over the first term of Eq. (6.4) depending on the numerical values of a_*, n_* and r. This indicates that $\Omega_{\rm p}$ vanishes at a particular orbit of radius $r = \tilde{r}_0$, and the negative LT precession arises for $r > \tilde{r}_0$. The negative LT precession in the KTN BH arises due to the sole effect of NUT charge (Chakraborty & Bhattacharyya, 2018), and it represents the orbital plane precession in the opposite direction (Chakraborty et al., 2017). This peculiar behavior of the LT precession does not arise in case of the Kerr BH where it follows the inverse cube law of distance ($\Omega_{\rm LT} \sim 2a_* M_{\rm BH}^2/r^3$). [1] In case of the KTN BH, it is evident from Eq. (6.4) that $\Omega_{\rm p}$ does not follow the same law for all combinations of (a_*, n_*), and it can even vanish at $\tilde{r}_0$. The exact expression of $\tilde{r}_0$ can be obtained from Eq. (6.4) by setting $\Omega_{\rm p} = 0$ at $r = \tilde{r}_0$. However, the approximate form of $\tilde{r}_0$ can be expressed as,

$$\tilde{r}_0 \approx \frac{M_{\rm BH}}{4n_*^4}\left(2a_*^2 - 3a_*^2 n_*^2 + 16n_*^4 + 2a_*\sqrt{a_*^2 - 3a_*^2 n_*^2 + 16n_*^4}\right) \tag{6.5}$$

[1] The negative LT precession arises in the Kerr naked singularity for the range $r_{\rm ISCO}^{\rm Kerr} \leq r < 0.5625 a_*^2 M_{\rm BH}$ (Chakraborty et al., 2017). Thus, the value of $\tilde{r}_0$ in the Kerr spacetime is $\tilde{r}_0^{\rm Kerr} = 0.5625 a_*^2 M_{\rm BH}$. For the Kerr naked singularity, the negative LT precession arises in the orbit(s) of inner disk, whereas it arises in the outer portion ($r > \tilde{r}_0$) of the disk for the KTN BH.

by neglecting $\sim n_*^2 M_{\rm BH}^{7/2}/r^{9/2}$ from the last term of Eq. (6.4) and solve it. Note that the exact numerical value of $\tilde{r}_0$ is very close to the approximate value obtained from Eq. (6.5), if $\tilde{r}_0$ really occurs close to the order of $\sim M$. In most of the cases, the value of $\tilde{r}_0$ is sufficiently greater than $M_{\rm BH}$. Thus, $\tilde{r}_0$ gives correct values in those cases[2].

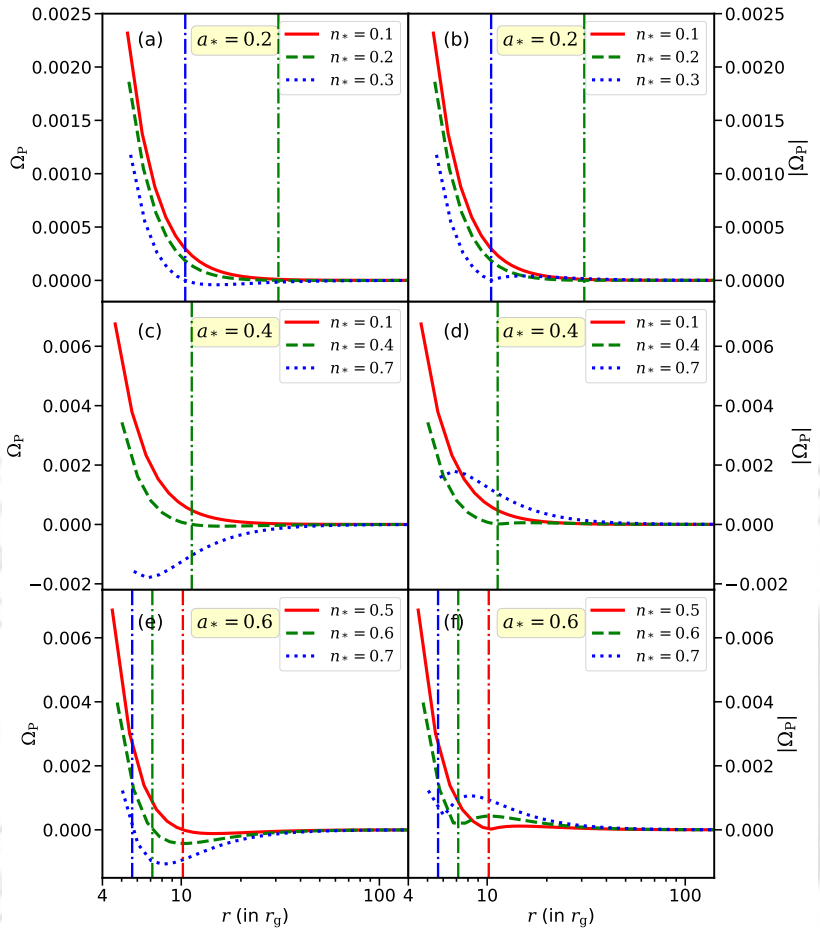

Figure 6.1: Variation of $\Omega_{\rm p}$ (left panel) and $|\Omega_{\rm p}|$ (right panel) with radial distance (r) for three different values of n_* with $a_* = 0.2$ (Panels (a) and (b)), $a_* = 0.4$ (Panels (c) and (d)), and $a_* = 0.6$ (Panels (e) and (f)). All the corresponding $\tilde{r}_0$ are represented in the figure by the dot-dashed lines with respective colors of each set of (a_*, n_*). The values of $\tilde{r}_0$ for solid red curves for Panels (a)-(d) are greater than the value considered in this figure along the X-axes, and hence the corresponding dot-dashed red lines are not seen for those said panels. On the other hand, as $\tilde{r}_0 < r_{\rm ISCO}$, the blue dot-dashed line is not shown in Panels (c)-(d). Note that $\Omega_{\rm p}$ and $|\Omega_{\rm p}|$ tend to zero for $r \to \infty$, as expected. See the text for details.

In accordance with Eq. (6.4), the LT effect for a KTN BH exhibits dominance either by the Kerr parameter (a_*) or the NUT parameter/GMM (n_*) at any given radial coordinate, as there is a competition between these parameters at r. To investigate the characteristic behaviors of $\Omega_{\rm p}$ and $|\Omega_{\rm p}|$, we explore three distinct sets of Kerr parameters (a_*) in Fig. 6.1, each followed by three different values of the NUT parameter (n_*). This will help us for the comprehensive understanding of the influence of these parameters on the LT frequency and tilted angle of the KTN BH at a later stage. It is

[2]The exact value of $\tilde{r}_0$ is not important in this paper. We introduce this only to show how the tilting of the disk depends on the behavior of LT effect.

useful to note here that all the curves of Fig. 6.1 are started from their respective innermost stable circular orbits (ISCOs). The numerical value of the ISCO for a specific combination of (a_*, n_*) can be obtained by solving the following ISCO equation for prograde orbit (Chakraborty & Bhattacharyya, 2018; Chakraborty & Bhattacharyya, 2019)

$$\begin{aligned} & M_{\rm BH}(r^6 - n^6 + 15n^4r^2 - 15n^2r^4) - 2M_{\rm BH}^2 r(3r^4 - 2n^2r^2 + 3n^4) - 16n^4r^3 \\ + \quad & 8ar^{3/2}m^{3/2} + a_{\rm k}^2\left\{M_{\rm BH}(n^4 + 6n^2r^2 - 3r^4) - 8n^2r^3\right\} = 0. \end{aligned} \tag{6.6}$$

However, as the LT torque mainly depends on the value of $\Omega_{\rm p}$, we present the corresponding analyses in Fig. 6.1. In Panels (a) and (b) of Fig. 6.1, we examine the variations of $\Omega_{\rm p}$ and $|\Omega_{\rm p}|$, where the Kerr parameter is set to $a_* = 0.2$ with NUT parameter values as $n_* = 0.1$ (red solid line), $n_* = 0.2$ (green dashed line), and $n_* = 0.3$ (blue dotted line). The values of $\tilde{r}_0$ for $(a_*, n_*) = (0.2, 0.1), (0.2, 0.2)$, and $(0.2, 0.3)$ are $402r_g, 31r_g$, and $10.5r_g$, respectively, where r_g $(\equiv GM_{\rm BH}/c^2)$ is the gravitational radius. Similarly, Panels (c) and (d) of Fig. 6.1 show the same variations with $a_* = 0.4$, paired with $n_* = 0.1$ (red solid line), $n_* = 0.4$ (green dashed line), and $n_* = 0.7$ (blue dotted line). The values of $\tilde{r}_0$ for $(a_*, n_*) = (0.4, 0.1), (0.4, 0.4)$, and $(0.4, 0.7)$ are $1583r_g, 11.3r_g$, and $4.7r_g$, respectively. Panels (e) and (f) of Fig. 6.1 are illustrated for $a_* = 0.6$, along with $n_* = 0.5$ (red solid line), $n_* = 0.6$ (green dashed line), and $n_* = 0.7$ (blue dotted line). The values of $\tilde{r}_0$ for $(a_*, n_*) = (0.6, 0.5), (0.6, 0.6)$, and $(0.6, 0.7)$ are $10.2r_g, 7.1r_g$, and $5.7r_g$, respectively. Note that all the corresponding $\tilde{r}_0$ are represented in Fig. 6.1 by the dot-dashed lines with the respective color of each set of (a_*, n_*). As the X-axis in each panel of Fig. 6.1 is considered up to $\sim 100r_g$, one cannot see those $\tilde{r}_0$ which occur at $\tilde{r}_0 > 100r_g$. For example, the dot-dashed red lines are not seen in Panels (a)-(d) of Fig. 6.1. For $(a_*, n_*) = (0.4, 0.7)$, $\tilde{r}_0$ $(= 4.7r_g)$ occurs inside the ISCO radius $(r_{\rm ISCO} = 5.8r_g)$, i.e., $\tilde{r}_0 < r_{\rm ISCO}$. Thus, the blue dot-dashed line is not shown in Panels (c)-(d), as it is not feasible. For this particular case, $\Omega_{\rm p}$ always has a negative value for $r \geq r_{\rm ISCO}$. These six plots in Fig. 6.1 provide a clear depiction of the interplay between GMM and the Kerr parameter on the value of $\Omega_{\rm p}$. The behavior of all the curves of $|\Omega_{\rm p}(r)|$ look almost similar. If the value of r decreases from the outer orbit to the ISCO, $|\Omega_{\rm p}(r)|$ first increases, attains a peak, then decreases to zero, and increases again depending on the location of the ISCO. Comparing three sets of figures, we infer that, $\Omega_{\rm p}$ or $|\Omega_{\rm p}|$ do not follow the same pattern. They depend on the combinations of a_* and n_*. Thus, the behavior of the tilted angle of the accretion disk is subject to dependencies on the values of a_* and n_* along with the other parameters, which we discuss as we proceed.

6.2 Formalism: tilted and warped disk equation

In our investigation, we focus on a spinning KTN BH characterized by a small NUT parameter/GMM at its core. This scenario assumes a Keplerian disk configuration with an aspect ratio $H/r \ll 1$, where H represents the disk thickness and r signifies the radial distance from the BH. Notably, the BH's spin axis aligns with the z axis and the accretion disk exhibits a tilt concerning the BH's spin axis. The disk consists of the circular rings with width Δr and surface density $\Sigma(r, t)$. The angular momentum per unit surface area on each annulus of the disk is defined as, $\mathbf{L}(r, t) = \Sigma r^2 \Omega(r)\mathbf{l}(r, t)$, where $\mathbf{l}$ is the unit tilt vector directed normal to the plane of the disk and $\Omega(r)$ is

the Keplerian angular speed. We adopt the assumption of a small tilt angle following Scheuer & Feiler (1996), implying that $\mathbf{l}$ can be approximated as $(l_x, l_y, 1)$. Moreover, we consider the accretion disk to be sufficiently viscous, satisfying the condition $\alpha > H/r$ (where, α is the Shakura–Sunyaev parameter). In this viscous regime, warping is transported diffusively in the disk (Papaloizou & Pringle, 1983). In the opposite regime, i.e., $\alpha < H/r$, which is not considered in this work, the warping disturbances propagate in a wave-like manner (Ivanov & Illarionov, 1997; Lubow et al., 2002). In the latter case, people have also been very interested in the radial tilt oscillations which could be developed in the inner disk around a Kerr BH (Ivanov & Illarionov, 1997; Demianski & Ivanov, 1997; Lubow et al., 2002).

In this paper, our focus lies in investigating the effect of both the viscous and LT torques within the disk in a steady state. Thus, following Pringle's Pringle (1992) equation with LT precession, one can rewrite the basic tilted/warped disk equation (Scheuer & Feiler, 1996) as,

$$\frac{1}{r}\frac{\partial}{\partial r}\left[\left(\frac{3r}{\mathscr{L}}\frac{\partial}{\partial r}\left(\nu_1\mathscr{L}\right)-\frac{3}{2}\nu_1\right)\mathbf{L}+\frac{1}{2}\nu_2 r\mathscr{L}\frac{\partial \mathbf{l}}{\partial r}\right]+\left(\mathbf{\Omega}_{\rm p}\times\mathbf{L}\right)=0, \tag{6.7}$$

where $\mathscr{L}=|\mathbf{L}|$. In the context of accretion disk dynamics, ν_1 of Eq. (6.7) represents the viscosity associated with the azimuthal shear, pertaining to the (r,ϕ) component of shear, while ν_2 denotes the viscosity linked with the vertical shear, corresponding to the (r,z) component of shear (Papaloizou & Pringle, 1983). The ratio ν_2/ν_1, termed as viscous anisotropy, holds significance in this context and can be associated with α for small amplitude warps, as evidenced in prior investigations (Ogilvie, 1999). Note that this is not done according to the method described in (Martin et al., 2008), where ν_1 and ν_2 were considered as a function of r. In this paper, we assume both of these viscosities are independent of the radial distance following (Scheuer & Feiler, 1996; Chakraborty & Bhattacharyya, 2017). The ratio of ν_2 and ν_1 is expressed as (Ogilvie, 1999)

$$\frac{\nu_2}{\nu_1}=\frac{1}{2\alpha^2}.\frac{4(1+7\alpha^2)}{4+\alpha^2}. \tag{6.8}$$

To account for the relativistic effects induced by the presence of a KTN BH, we extend Eq. (6.7) to incorporate the external torque arising from the LT precession. The external torque ($\boldsymbol{\tau}$) in Eq. (6.7) due to the LT precession is given by,

$$\boldsymbol{\tau}=\mathbf{\Omega}_{\rm p}\times\mathbf{L}, \tag{6.9}$$

where $\Omega_{\rm p}$ in the cgs unit is written as (see Eq. (6.4)),

$$\Omega_{\rm p} \;=\; \frac{c}{r}\left(\frac{2a_* r_g^2}{r^2}-\frac{3a_*^2 r_g^{5/2}}{2r^{5/2}}-\frac{2n_*^2 r_g^{3/2}}{r^{3/2}}(1-2r_g/r)^2\right). \tag{6.10}$$

Taking the scalar product of $\mathbf{l}$ (Scheuer & Feiler, 1996) with Eq. (6.7), we get

$$\frac{1}{r}\frac{\partial}{\partial r}\left[r\frac{\partial}{\partial r}\left(\nu_1\mathscr{L}\right)-\frac{1}{2}\nu_1\mathscr{L}\right]=0, \tag{6.11}$$

under the small tilt angle approximation (we have ignored the term $|\partial\mathbf{l}/\partial r|^2$). Solving the above equation, one obtains (Scheuer & Feiler, 1996),

$$\mathscr{L}(r)=C_2 r^{1/2}-2C_1, \tag{6.12}$$

where C_1 and C_2 are the integration constants. They are obtained as $C_2 = \sqrt{GM_{\rm BH}}\Sigma_\infty$ and $C_1 = \frac{1}{2}\sqrt{GM\tilde{r}_{\rm in}}\,(\Sigma_\infty - \Sigma_{\rm in})$ (Chakraborty & Bhattacharyya, 2017), where $\Sigma \to \Sigma_\infty$ at $r \to \infty$ and $\Sigma \to \Sigma_{\rm in}$ at $r \to r_{\rm ISCO}$. Here, $\tilde{r}_{\rm in}$ corresponds to the inner edge radius of the disk, that is, in fact, the ISCO radius ($\tilde{r}_{\rm in} \equiv r_{\rm ISCO}$) for a KTN BH. Note that one can obtain $r_{\rm ISCO}$ by solving Eq. (6.6). Finally, substituting the above expressions for C_1 and C_2 into Eq. (6.12), we obtain the expression for $\mathscr{L}(r)$ in steady state as,

$$\mathscr{L}(r) = \sqrt{GM}\left[r^{1/2}\Sigma_\infty + r_{\rm in}^{1/2}\,(\Sigma_{\rm in} - \Sigma_\infty)\right]. \tag{6.13}$$

The steady state distribution of the surface density can similarly be obtained from Eq. (6.13) as

$$\Sigma(r) = \Sigma_\infty + (\tilde{r}_{\rm in}/r)^{\frac{1}{2}}\,(\Sigma_{\rm in} - \Sigma_\infty)\,. \tag{6.14}$$

Now, substituting $L(r)$ in Eq. (6.7) we obtain,

$$\frac{1}{r}\frac{\partial}{\partial r}\left[3\nu_1 C_1 \mathbf{l} + \frac{1}{2}\nu_2 r\mathscr{L}\frac{\partial \mathbf{l}}{\partial r}\right] + (\mathbf{\Omega}_{\rm p} \times \mathbf{L}) = 0. \tag{6.15}$$

Equation (6.15) can be decomposed into x and y components (i.e., l_x and l_y) of the tilt vector ($\mathbf{l}$) as

$$\frac{\partial}{\partial r}\left(3\nu_1 C_1 l_x + \frac{1}{2}\nu_2 r\mathscr{L}\frac{\partial l_x}{\partial r}\right) = \omega_{\rm p}\mathscr{L} l_y, \tag{6.16}$$

and

$$\frac{\partial}{\partial r}\left(3\nu_1 C_1 l_y + \frac{1}{2}\nu_2 r\mathscr{L}\frac{\partial l_y}{\partial r}\right) = -\omega_{\rm p}\mathscr{L} l_x, \tag{6.17}$$

where $\boldsymbol{\omega}_{\rm p} \times \mathbf{l} = (-\omega_{\rm p} l_y, \omega_{\rm p} l_x, 0)$ and $\omega_{\rm p} = c\left(\frac{2a_* r_g^2}{r^2} - \frac{3a_*^2 r_g^{5/2}}{2r^{5/2}} - \frac{2n_*^2 r_g^{3/2}}{r^{3/2}}(1 - 2r_g/r)^2\right)$. Combining Eqs. (6.16) and (6.17), we obtain

$$\frac{\partial}{\partial r}\left(3\nu_1 C_1 W + \frac{1}{2}\nu_2 r\mathscr{L}\frac{\partial W}{\partial r}\right) = -i\omega_{\rm p}\mathscr{L} W, \tag{6.18}$$

where we define $W = l_x + i l_y = \tilde{\beta}e^{i\gamma}$ with $\tilde{\beta} = \sqrt{l_x^2 + l_y^2}$ is the tilt angle and $\gamma = \tan^{-1}(l_y/l_x)$ is the twist angle. Eqs. (6.16) and (6.17) refer the evolution and characteristics of the warped disk around a KTN BH in the steady state.

Here, we use the dimensionless form of some parameters for our convenience in the mathematical calculations. For instance, the dimensionless form for $\mathscr{L}$ (Banerjee et al., 2019b) is given by $\mathscr{L} \to \mathscr{L}/C_1 = (C\sqrt{r} - 2)$, where $C = \frac{2z_{\rm in}}{z_{\rm in}-1}\frac{1}{\sqrt{\tilde{r}_{\rm in}}}$ and $z_{\rm in} = 1 + \frac{2C_1}{\mathscr{L}(\tilde{r}_{\rm in})} = \frac{\Sigma_\infty}{\Sigma_{\rm in}}$ (Banerjee et al., 2019b). We make r dimensionless by replacing $r \to \frac{r}{r_g}$, $\xi \to \frac{cr_g}{\nu_2}$ and $\tilde{\eta} \to \frac{6\nu_1}{\nu_2}$. Using the above-mentioned scheme and by following Banerjee et al. (2019b), we obtain the dimensionless form of Eqs. (6.16) and (6.17) as,

$$r\frac{\partial^2 l_x}{\partial r^2} + \left[(\tilde{\eta}+1)\frac{C_1}{\mathscr{L}} + 3/2\right]\frac{\partial l_x}{\partial r} = 2\xi\overline{\omega} l_y, \tag{6.19}$$

and

$$r\frac{\partial^2 l_y}{\partial r^2} + \left[(\tilde{\eta}+1)\frac{C_1}{\mathscr{L}} + 3/2\right]\frac{\partial l_y}{\partial r} = -2\xi\overline{\omega} l_x. \tag{6.20}$$

where,

$$\overline{\omega} = \left(\frac{2a_*}{r^2} - \frac{3a_*^2}{2r^{5/2}} - \frac{2n_*^2}{r^{3/2}}(1 - 2/r)^2\right). \tag{6.21}$$

Now, to see the behavior of the tilted accretion disk, we have to solve the eqs. (6.19) and (6.20) numerically with proper boundary conditions. We solve these equations as a boundary value problem. For this case, we fix the boundary at $r_{\rm edge}$ as an outer edge of the accretion disk and $\tilde{r}_{\rm in}$ as the inner edge of the disk. Thereafter, we also fix the tilted and twisted angle at the outer and inner edge. For a set of fixed parameters (*i.e.*, a_*, n_*, $M_{\rm BH}$, ν_2 and $\tilde{\eta}$) we solve these above-mentioned equations bounded by $r_{\rm edge}$ and $\tilde{r}_{\rm in}$ and see the behaviour of $\tilde{\beta}$ with radial coordinate (r). To solve the before-mentioned warped disk equations (Eqs. (6.19) and (6.20)), we need four boundary conditions, which are taken as Banerjee et al. (2019b)

$$l_x(\tilde{r}_{\rm in}) = \tilde{\beta}_i \cos(\gamma_i),\ l_y(\tilde{r}_{\rm in}) = \tilde{\beta}_i \sin(\gamma_i), \tag{6.22}$$

and,

$$l_x(r_{\rm edge}) = \tilde{\beta}_f,\ l_y(r_{\rm edge}) = 0. \tag{6.23}$$

We define several key parameters: γ_i, $\tilde{\beta}_i$, and $\tilde{\beta}_f$, representing the twist angle at $\tilde{r}_{\rm in}$, tilt angle at $\tilde{r}_{\rm in}$, and tilt angle at r_f of the disk, respectively. At the outer edge of the disk, we assume the twist angle to be zero since the effect of LT precession is negligible there (Banerjee et al., 2019b). Consequently, l_y can be assumed to be zero at the outer edge. Note that Chakraborty & Bhattacharyya (2017) focused on the disk inner edge tilt, and thus assumed the inner edge twist to be zero. Here, we retain the disk inner edge twist term to make our solutions more general following Banerjee et al. (2019b). However, choosing different numerical value for γ_i, the tilt profile does not show any significant differences qualitatively and quantitatively. The inner edge of the disk ($\tilde{r}_{\rm in}$) is considered here as the ISCO radius ($r_{\rm ISCO}$) for a prograde disk. We have shown the nature of a tilted disk considering non-zero tilt angle ($\tilde{\beta}_i \neq 0$) and zero tilt angle ($\tilde{\beta}_i = 0$) at $r_{\rm ISCO}$.

6.3 Results and discussion

In this section, we investigate the behavior of the tilt angle radial profile ($\tilde{\beta}(r)$) as a function of the parameters a_*, n_*, $\tilde{\beta}_i$, ν_2, and $\tilde{\eta}$ in detail. In case of the Kerr BH, it was earlier shown (Banerjee et al., 2019b) that the interplay between the LT torque (controlled by $M, a_*, \tilde{\beta}_i$) and viscous torque (controlled by ν_2) in the plane of the disk decides the radial profile of $\tilde{\beta}$. In case of the KTN BH, the LT torque is additionally controlled by n_* as well. In section 6.1, we have shown that the LT effect (Eq. 6.4) can decrease or increase or even vanish at a particular orbit ($\tilde{r}_0$) depending on the values of a_* and n_*. The similar effect does not arise for the Kerr BH. In case of the KTN BH, although there is certainly an interplay between the LT torque and viscous torque, one cannot neglect another interplay between a_* and n_* inside the LT torque. Due to the interplay between three primary parameters (a_*, n_* and ν_2), some peculiar effect will appear around $\tilde{r}_0$ (not exactly at $\tilde{r}_0$), which we discuss as we proceed.

6.3.1 Parameter values

In order to discuss the behavior of $\tilde{\beta}(r)$, we need to choose suitable numerical values for the different parameters relevant to the astrophysical scenario. As we are mainly interested in the Galactic accreting BHs, we choose $M_{\rm BH} \sim 5 - 25 M_\odot$ (where $M_\odot$ is

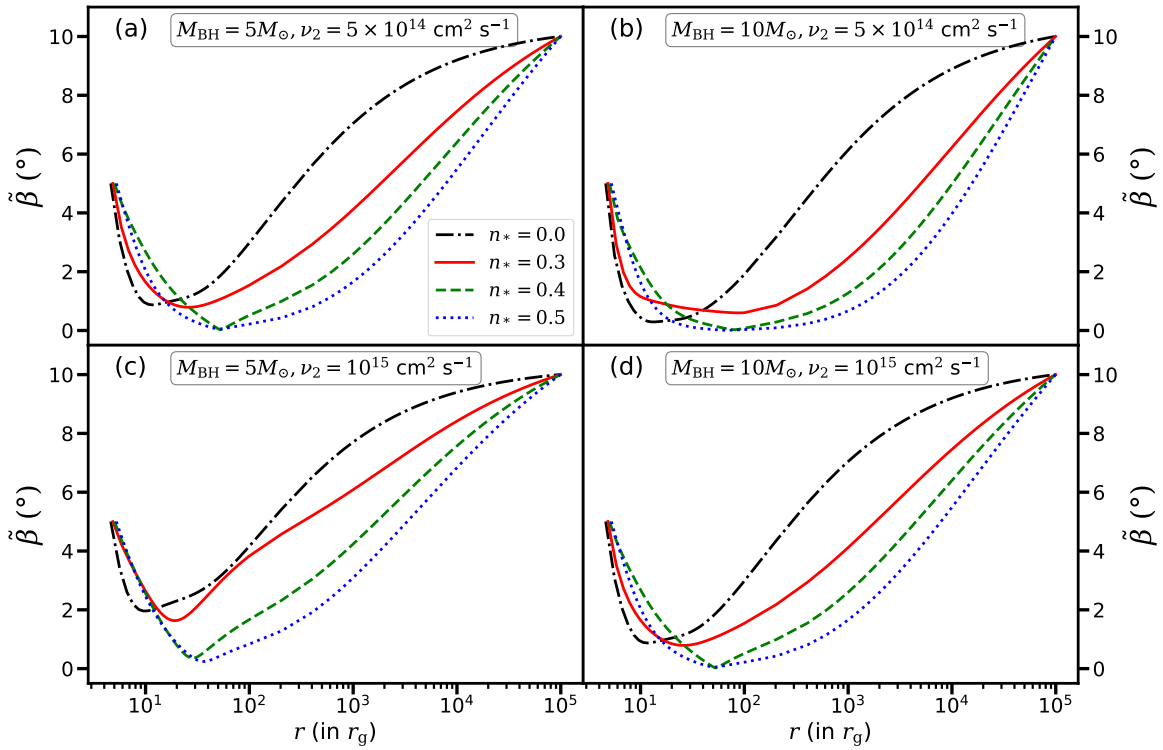

Figure 6.2: Variation of tilt angle ($\tilde{\beta}$) with radial distance (r) for four different values of n_* with a fixed value of $a_* = 0.4, \tilde{\beta}_i = 5°, \tilde{\eta} = 0.25$ and $z_{\rm in} = 0.75$. The value of $M_{\rm BH}$ (ν_2) is fixed in the plots of 1st/2nd column (row) with different values of ν_2 ($M_{\rm BH}$) as mentioned in the inset. All the curves are started from $\tilde{r}_{\rm in} \equiv r_{\rm ISCO}(a_*, n_*)$ which are calculated using Eq. (6.6). See the text for details.

the solar mass) for most of the cases. The value of ν_2 is considered as $10^{14} - 10^{15}$ cm^2 s^{-1} (Frank et al., 2002). $\tilde{\eta}$ is chosen as $\tilde{\eta} = 0.25$ which translates $\alpha = 0.156$ (King et al., 2007). We consider $z_{\rm in} = 0.75$, as in our formalism $\Sigma_{\rm in} > \Sigma_\infty$. The inner edge twist and outer edge tilt to $\sim 5°$ and $\sim 10°$, respectively, throughout the paper following Banerjee et al. (2019b). We consider $\tilde{\beta}_i$ as a free parameter (Chakraborty & Bhattacharyya, 2022), and use the range $0° - 10°$ for the purpose of demonstration. Note that we consider only the case of prograde rotation ($a_* > 0$) in this paper, and the numerical values of a_* and n_* are considered upto 0.7 (Natarajan & Armitage, 1999; Nelson & Papaloizou, 2000; Fragile & Anninos, 2005; Caproni et al., 2006; Fragile et al., 2007; Martin et al., 2008; Li et al., 2013; Li et al., 2015; Banerjee et al., 2019b).

6.3.2 Numerically computed radial profiles of the disk tilt angle

Fig. 6.2 is plotted for $a_* = 0.4$ with the four different values of n_* : $n_* = 0.0$ (black dot-dashed solid line), $n_* = 0.3$ (red solid line), $n_* = 0.4$ (green dashed line), and $n_* = 0.5$ (blue dotted line). The values of $\tilde{r}_0$ are $\sim 24.5r_g, 11.3r_g$ and $7.3r_g$ for the combinations of $(a_*, n_*) \equiv (0.4, 0.3), (0.4, 0.4)$ and $(0.4, 0.5)$, respectively. $\tilde{r}_0$ is not feasible for the combinations of $(a_*, n_*) \equiv (0.4, 0.0)$ which means Ω_p cannot be zero in between $r_{\rm edge}$ and $r_{\rm ISCO}$. However, when transitioning from the left to right $\Big[(a \to b), (c \to d)\Big]$, we maintain a constant value for ν_2 while varying $M_{\rm BH}$ from $5M_\odot$ to $10M_\odot$. Comparing

panels (a) and (b), or, panels (c) and (d), one can see that the transition point of disk misalignment moves to the larger r, as the mass increases. This is because, when the mass of the BH increases, the LT torque increases, and the disk tries to align from a larger radius. Conversely, moving from the upper to the lower arrangement $\Big[(a \to c), (b \to d)\Big]$, we keep the mass $M_{\rm BH}$ fixed and adjust the viscosity parameter ν_2 from 5×10^{14} cm^2 s^{-1} to 10^{15} cm^2 s^{-1}, with all other parameters held constant. Comparing panels (a) and (c), or, panels (b) and (d), one can see that the transition point of disk misalignment moves to the smaller r, as the viscosity increases. As in panel (c), we increase viscosity more than in panel (a), keeping all other parameters fixed, the viscous torque increases, which is held out the disk against being aligned.

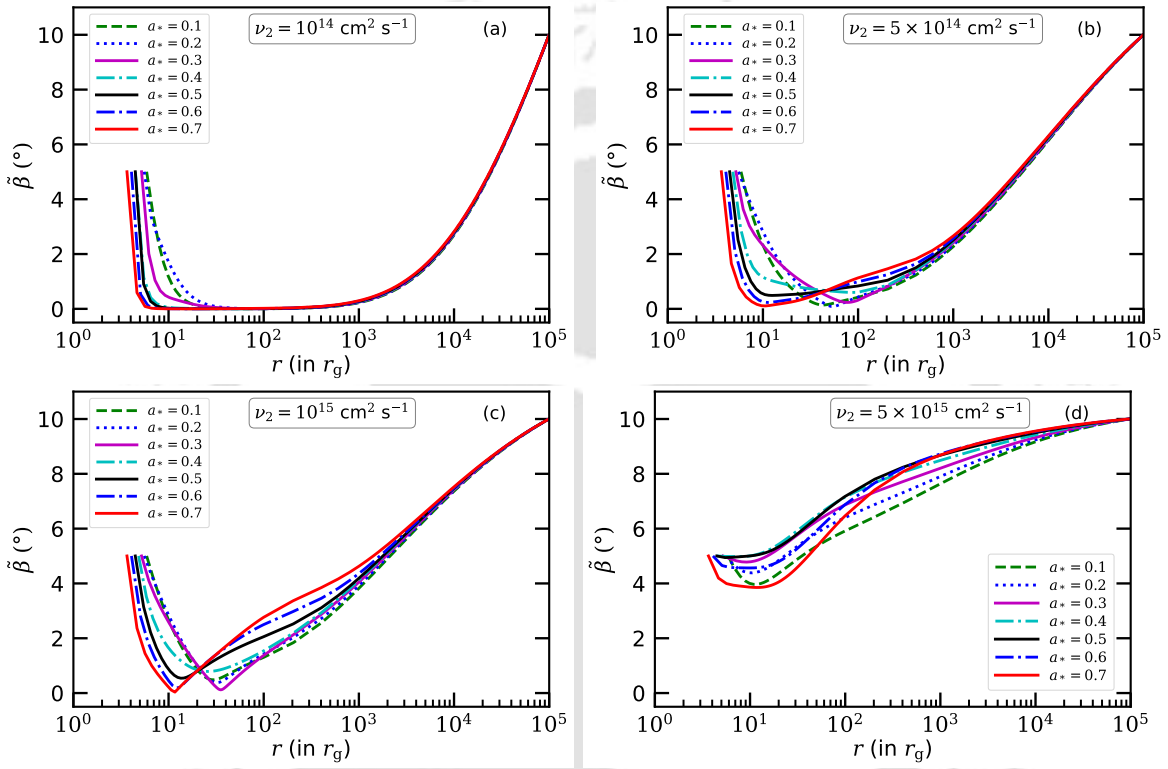

Figure 6.3: Variation of $\tilde{\beta}$ with r for the different values of a_* with a fixed value of $M_{\rm BH} = 10M_\odot, \tilde{\beta}_i = 5°, n_* = 0.3, \tilde{\eta} = 0.25$ and $z_{\rm in} = 0.75$. The value of ν_2 changes in the plots as mentioned in the inset. All the curves are started from $\tilde{r}_{\rm in} \equiv r_{\rm ISCO}(a_*, n_*)$ which are calculated using Eq. (6.6). See the text for details.

Fig. 6.3 illustrates the variation of $\tilde{\beta}$ with respect to the radial coordinate for different values of ν_2. The upper-left figure corresponds to $\nu_2 = 10^{14}$ cm^2 s^{-1}, the upper-right figure to $\nu_2 = 5 \times 10^{14}$ cm^2 s^{-1}, the lower-left figure to $\nu_2 = 10^{15}$ cm^2 s^{-1}, and the lower-right figure to $\nu_2 = 5 \times 10^{15}$ cm^2 s^{-1}. The various curves within each figure represent different values of the Kerr parameter (a_*), ranging from 0.0 to 0.8 with an interval of $\Delta a_* = 0.1$. It is notable that higher values of a_* tend to align the angular momentum of the disk along the BH's spin axis, resulting in smaller values of $\tilde{\beta}$. Observing the plots, it becomes evident that as the value of ν_2 increases, the viscous torque begins to dominate over the LT torque for a fixed set of (a_*, n_*). The competition between viscous and LT torques plays a crucial role in determining the orientation of the accretion disk, with higher values of ν_2 exerting a greater influence on the disk's inclination relative to the BH's spin axis.

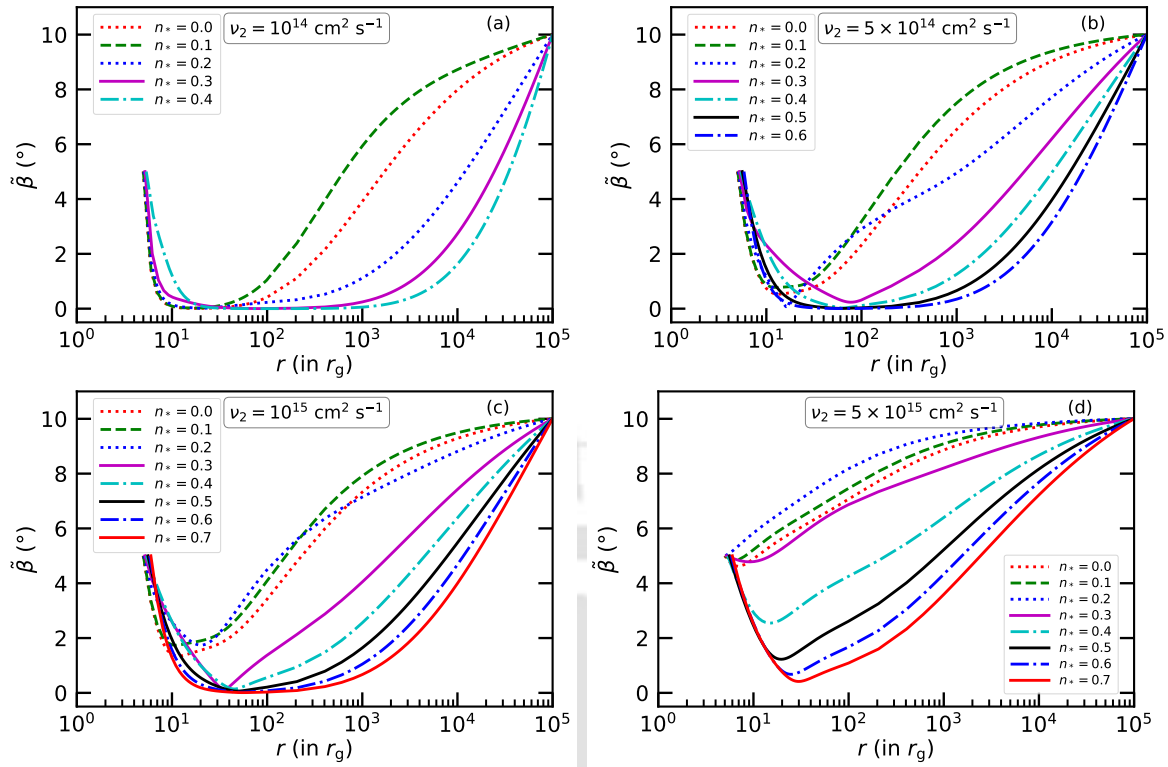

Figure 6.4: Variation of $\tilde{\beta}$ with r for different values of n_* with a fixed $a_* = 0.3$, $M_{\rm BH} = 10M_\odot$, $\tilde{\eta} = 0.25$, $\tilde{\beta}_i = 5°$ and $z_{\rm in} = 0.75$. The value of ν_2 changes in the different panels as mentioned in the inset. See the text for details.

Fig. 6.4 depicts the variation of the tilt angle ($\tilde{\beta}$) with radial distance (r) for different values of ν_2 but similar to Fig. 6.3. The various curves in each panel represent different values of n_*, ranging from 0.0 to higher values with an interval of $\Delta n_* = 0.1$ with a fixed value of $M_{\rm BH} = 10M_\odot$ and $a_* = 0.3$. For $\nu_2 = 10^{14}$ cm^2 s^{-1}, the disk remains mostly aligned along the equatorial plane for any values of n_*. For $\nu_2 = 5\times10^{14}$ cm^2 s^{-1}, the disk tends to align along the equatorial plane for $n_* > 0.4$. For $\nu_2 = 10^{15}$ cm^2 s^{-1}, the disk aligns beyond $n_* > 0.5$, while for $\nu_2 = 5 \times 10^{15}$ cm^2 s^{-1}, the disk remains mostly tilted for any values of n_*. Here also, as the value ν_2 increases, the viscous torque starts to dominate over the LT torque for a fixed set of (a_*, n_*). In all the panels of Fig. 6.4, the solid magenta curve shows the tilt profile for $a_* = n_*$. Remarkably, the curves for $n_* < a_*$ are located at the upper portion of the xy plane, whereas the curves are located at the lower portion of the same plane for $n_* > a_*$, in the case of larger r. This indicates that the LT torque becomes stronger for the higher value of n_* in that range of r. This does not only help to align the disk in the equatorial plane, but the alignment of the disk is also extended to the outer portion of the disk significantly. This could be clear by comparing the first and last terms of Eq. (6.4), as it varies $\sim a_*/r^3$ and $\sim n_*^2/r^{5/2}$ respectively. However, the above mentioned trend is not necessarily true at the lower r near the inner boundary, as the dominant LT torque term switches from being the a_* term to the n_* term at $\tilde{r}_0$. Note that although the switching of LT torque occurs at $\tilde{r}_0$, the switching of the curves does not occur exactly at $\tilde{r}_0$. This is because $\Omega_{\rm p}$ is a function of a_* and n_*. On the other hand, $\tilde{\beta}(r)$ is not only a function a_* and n_*, but it is also largely dependent on ν_2 and some other parameters, e.g., $M_{\rm BH}$, $\alpha, z_{\rm in}$, etc. Thus, the nature of $\Omega_{\rm p}$ and $\tilde{\beta}$ do not

change in a similar manner always. Due to the same reason, the cross-over of $\tilde{\beta}$ curves does not occur exactly at $\tilde{r}_0$. In the absence of n_* (red dotted curve), the disk might be aligned in the equatorial plane for small viscosity (see panel (a)), but it is not aligned for the comparatively higher viscosity (see panels (b)-(d)). It is evident from panels (a)-(d) that there is a tendency of the alignment of disk in the equatorial plane for the higher values of n_*. It indicates that the higher values of n_* play a significant role in the alignment, compared to a_*. It is because the last term ($\sim n_*^2/r^{5/2}$) of Eq. (6.4) dominates over the first and second terms of the same equation. It is interesting to see the behavior of the dotted blue curves in panels (b) and (c) of Fig. 6.4. As the difference between the value of a_* (e.g., $a_* = 0.3$) and n_* (e.g., $n_* = 0.2$) is small (~ 0.1), the overall LT torque remains small for $r < 100r_g$ and $r < 300r_g$ for panels (b) and (c), respectively. Note that $\tilde{r}_0$ occurs at $\tilde{r}_0 \sim 60r_g$ for $(a_*, n_*) = (0.3, 0.2)$. Thus, the viscous torque dominates over the LT torque and the disk tends to be more tilted compared to the dashed green and dotted red curves around $\tilde{r}_0$. On the other hand, the LT torque due to n_* starts to dominate over the LT torque due to a_* for the larger r, and, hence, the overall torque dominates over the viscous torque. Thus, the disk tries to be aligned and, thereby, the dotted blue curves bent and cross the dashed green and dotted red curves at larger r in panels (b) and (c). The dotted blue curve in panel (d) indicates that the viscous torque dominates over the overall LT torque in almost the whole range of r. Thus, one cannot see the tendency of disk alignment.

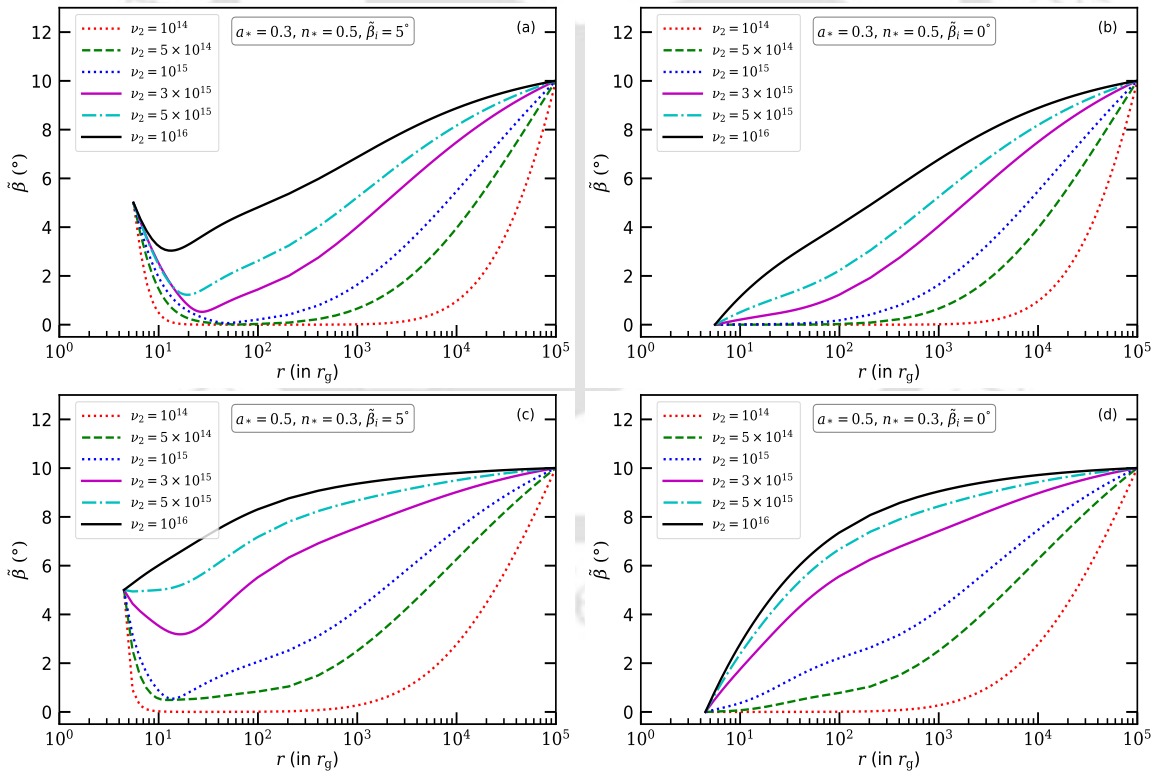

Figure 6.5: Variation $\tilde{\beta}$ with r for different values of ν_2 with a fixed $M_{\rm BH} = 10M_\odot, \tilde{\eta} = 0.25$ and $z_{\rm in} = 0.75$. The values of a_* and n_* are mentioned in the inset. See the text for details.

Fig. 6.5 portraits the variation of $\tilde{\beta}$ with respect to the radial coordinate for different values of ν_2 with some fixed parameters: $M_{\rm BH} = 10M_\odot, \eta = 0.25$ and $z_{\rm in} = 0.75$. The panels (a) and (b) depict scenarios where $(a_*, n_*) = (0.3, 0.5)$ with $\tilde{\beta}_i = 5^\circ$ and 0°,

respectively. Similarly, the panels (c) and (d) represent cases with $(a_*, n_*) = (0.5, 0.3)$ with $\tilde{\beta}_i$ values of 5° and 0°, respectively. Studying all the panels, we can infer that, the inner disk is more tilted for large $\tilde{\beta}_i$. Moreover, it is also seen that the tilting of the disk increases with the increment of ν_2.

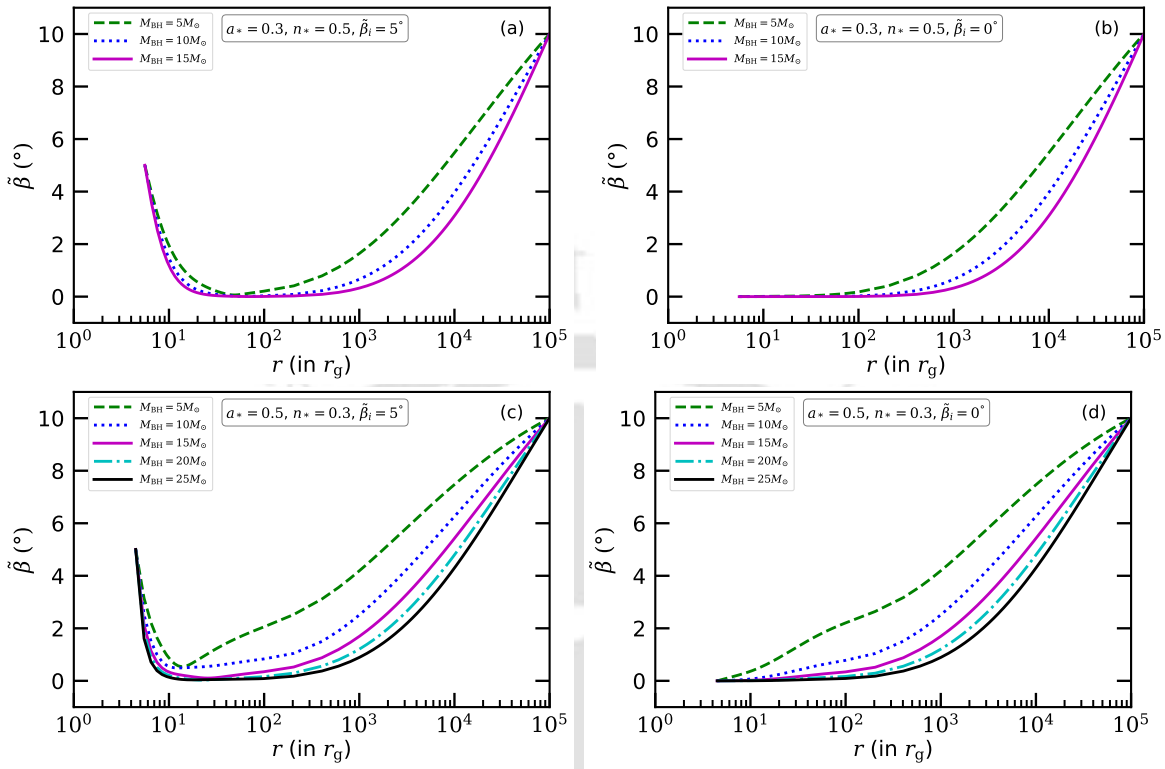

Figure 6.6: Variation of $\tilde{\beta}$ with r for different values of BH mass (M_{BH}) for a fixed $\nu_2 = 5 \times 10^{14}$ cm^{2}s^{-1}, $\tilde{\eta} = 0.25$ and $z_{in} = 0.75$. The values of a_* and n_* are mentioned in the inset. See the text for details.

Fig. 6.6 showcases the variation of $\tilde{\beta}$ with respect to the radial coordinate for different values of M_{BH}. Here we fix $\nu_2 = 5 \times 10^{14}$ cm^2 s^{-1}, $\eta = 0.25$ and $z_{in} = 0.75$. The panels (a) and (b) correspond to scenarios where $(a_*, n_*) = (0.3, 0.5)$ with $\tilde{\beta}_i = 5°$ and 0°, respectively. Similarly, the panels (c) and (d) represent cases with $(a_*, n_*) = (0.5, 0.3)$, with $\tilde{\beta}_i = 5°$ and 0°, respectively. Across all the subfigures, it is observed that the LT torque dominates for higher BH masses. This observation highlights the significance of the BH mass in determining the dominance of the LT torque and its effect on aligning the accretion disk with the BH's spin axis.

Fig. 6.7 is similar to Fig. 6.6 but for a different value of ν_2, i.e., $\nu_2 = 10^{15}$ cm^2 s^{-1}. Comparing Fig. 6.6 and Fig. 6.7, we can infer that when the viscosity parameter ν_2 (representing viscous torque) is higher, a more massive BH (higher M_{BH}) is needed to align the disk. This observation highlights the complex relation among the BH mass, viscous torque, and the alignment dynamics of the accretion disk.

6.3.3 Warp radius of the disk

It is seen from the above discussion that a disk is partially aligned for a set of parameter values. In such a case, one can consider a radius r_{align} up to which the disk remains aligned. It is higher for the higher values of the LT effect. In our computation, we

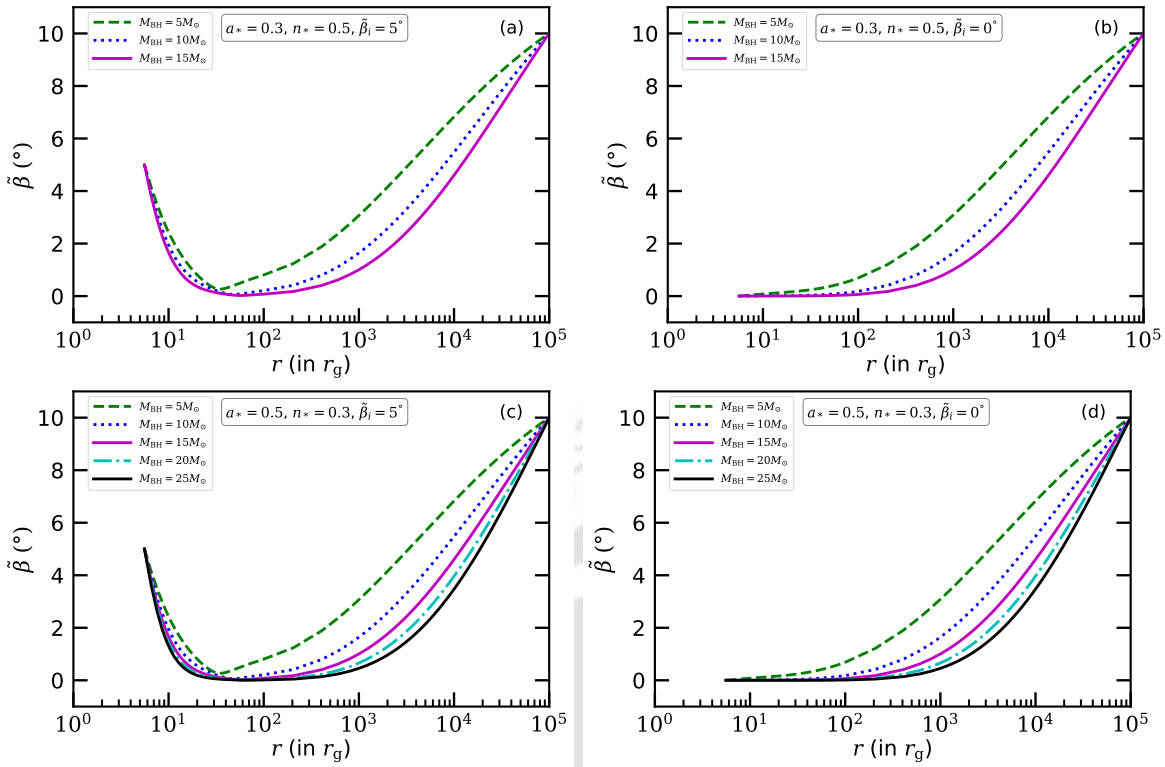

Figure 6.7: Similar to Fig. 6.6 but for a fixed $\nu_2 = 10^{15}$ cm^2 s^{-1}.See the text for details.

consider $r_{\rm align}$ as the radius up to which the tilt angle is less than 0.01° (Banerjee et al., 2019b). The characteristic warp radius ($r_{\rm warp}$) is defined as the radius inside which the LT effect dominates. It is calculated by equating the timescale for warp diffusion (i.e., r^2/ν_2) and the local LT precession timescale (i.e., $1/|\Omega_{\rm p}|$). Thus, one can solve the following equation

$$\left| \left(\frac{2a_* r_g}{r} - \frac{3a_*^2 r_g^{3/2}}{2r^{3/2}} - \frac{2n_*^2 r_g^{1/2}}{r^{1/2}} (1 - 2r_g/r)^2 \right) \right| = \frac{\nu_2}{c r_g}, \tag{6.24}$$

for $r = r_{\rm warp}$ to obtain the warp radius for our case. It gives $r_{\rm warp} = 2a_* c r_g^2/\nu_2$ for a Kerr BH, which resembles Eq. (45) of Banerjee et al. (2019b). When the LT effect due to n_* (3rd term of Eq. (6.24) dominates over the LT effect due to a_* (1st term of Eq. (6.24), one has to solve it by considering the negative sign in the right hand side of Eq. (6.24). Otherwise, it has to be considered as positive. Let us take an example from the plots of the panel (d) of Fig. 6.2 which corresponds to $\tilde{\beta}(r)$ for $M_{\rm BH} = 10M_\odot$, $a_* = 0.4$ and $\nu_2 = 10^{15}$ cm^2 s^{-1} with four different values of n_*. For $(a_*, n_*) = (0.4, 0.0)$, we obtain $r_{\rm warp} \sim 34 r_g$ by considering the above-mentioned positive sign. For this set of parameters, the disk cannot be in the situation where tilt angle $\tilde{\beta} < 0.01°$. This implies that $r_{\rm align}$ does not arise in this case. Therefore, we can say that the LT torque cannot overrule the viscous torque to make the disk aligned in the equatorial plane. Similarly, for $(a_*, n_*) = (0.4, 0.4)$ and $(0.4, 0.5)$, we obtain $r_{\rm warp} \sim 110 r_g$ and $\sim 411 r_g$ respectively, by considering the negative sign in Eq. (6.24). For $(a_*, n_*) = (0.4, 0.4)$ and $(0.4, 0.5)$, we obtain $r_{\rm align} \sim 53 r_g$ and $\sim 52 r_g$ respectively. The values of R_0 are obtained as $\sim 12 r_g$ and $\sim 8 r_g$, respectively, for the above mentioned cases. One obtains $r_{\rm warp} \sim 13 r_g$ for $(a_*, n_*) = (0.4, 0.3)$ by considering the positive sign. Note that the LT precession vanishes at $\tilde{r}_0 \sim 24.5 r_g$

in this particular case as mentioned earlier. It indicates that the LT effect lost its control over the disk for $r > 13r_g$. Let us consider another sample from panel (a) of Fig. 6.5. In this case, $\tilde{r}_0$ is located at $\sim 6.8r_g$ for $(a_*, n_*) = (0.3, 0.5)$. However, depending on the numerical values of ν_2, the locations of $r_{\rm warp}$ and $r_{\rm align}$ would be different. For instance, if we take $\nu_2 = 10^{14}$ cm^2 s^{-1}, we obtain $r_{\rm warp} \sim 48890r_g$ and $r_{\rm align} \sim 1127r_g$. On the other hand, $r_{\rm warp} \sim 1861r_g$ and $r_{\rm align} \sim 73r_g$ for $\nu_2 = 5 \times 10^{14}$ cm^2 s^{-1}. Similarly, for $\nu_2 = 10^{15}$ cm^2 s^{-1}, we obtain $r_{\rm warp} \sim 431r_g$ and $r_{\rm align} \sim 49r_g$. If we further increase the viscosity to $\nu_2 = 3 \times 10^{15}$ cm^2 s^{-1}, $r_{\rm warp}$ and $r_{\rm align}$ cannot be obtained, as $r_{\rm warp} < r_{\rm ISCO}$. Thus, we see that if we increase the viscosity, the viscous torque leads over the LT torque after a certain value of ν_2. As a result, the $r_{\rm warp}$ and $r_{\rm align}$ shift in the lower r, and beyond a particular ν_2, both of them cease to exist. This is also clear from the curves of the panel (a) of Fig. 6.5. Moreover, due to the higher viscous torque compared to the overall LT torque, it cannot take over the control of the disk for $r > \tilde{r}_0$. Eventually, the viscous torque dominates the overall LT torque, and the $\tilde{\beta}(r)$ curve starts to move upward. The relation between $r_{\rm align}$ and $r_{\rm warp}$ was found to be $r_{\rm align} = 0.165r_{\rm warp}$ (Natarajan & Armitage, 1999) for the Kerr BH. The proportionality factor was later obtained as ~ 0.094 in Banerjee et al. (2019b). However, due to the non-monotonous behaviour of the $\tilde{\beta}(r)$ curves in the KTN BH, the proportionality factor between $r_{\rm align}$ and $r_{\rm warp}$ does not remain fixed across the parameter space explored in this paper. The proportionality factor roughly varies within $0.03 - 0.45$, as obtained from our computations.

6.3.4 Justification for using the approximate expression for LT precession

We have considered here the approximate LT precession expression for the KTN BH and, hence, considered the numerical values of a_* and n_* up to 0.7 to calculate the tilt profiles. In general, the approximate expression ($\Omega_{\rm LT} \sim 2a_*M_{\rm BH}^2/r^3$) of LT precession in Kerr BH is used upto $a_* \to 1$ in many papers (Caproni et al., 2006). This is because the above-mentioned expression is not only applicable for the slowly-spinning ($a_* << 1$) Kerr BH, but it is also applicable to the Kerr BHs with high spin, if a_* is small enough than $r/M_{\rm BH}$ (i.e., a_*/r is much less than 1). This is also clear from Eq. (6.3). After a careful inspection, we find that if one uses that expression ($\Omega_{\rm LT} \sim 2a_*M_{\rm BH}^2/r^3$) for the Kerr BH with $a_* < 1$, no qualitative differences could be found in the tilt profiles. However, a quantitative difference (maximum upto $\sim 15\%$) in the tilt angle could appear at $r \sim 5r_g$ for $a_* = 0.7$, and tends to zero for $r > 9r_g$. For $a_* < 0.7$, the above-mentioned quantitative difference decreases significantly from $\sim 15\%$. It is expected because the LT effect in a Kerr BH is mainly governed by the inverse cube law of distance (i.e, a/r^3) for $a_* << r/M_{\rm BH}$, as explained above. Now, since the value of a_* for a Kerr BH is comparatively much less than $r/M_{\rm BH}$ (the minimum value of r is $r_{\rm ISCO}$) in reality, the difference in the numerical values obtained using the exact expression and the approximate expression of LT precession does not differ significantly. That is why, the approximate expression of LT precession is applied (Natarajan & Armitage, 1999; Nelson & Papaloizou, 2000; Fragile & Anninos, 2005; Caproni et al., 2006; Fragile et al., 2007; Martin et al., 2008; Li et al., 2013; Li et al., 2015; Banerjee et al., 2019b) even to the higher a_* values for calculating the tilt profile. Note that the qualitative and substantial quantitative differences can be seen only for those a_* values which represent the Kerr naked singularities, i.e., $a_* > 1$. This is because, a_* becomes

comparable to r/M, or, even $a_* > r/M_{\rm BH}$ at $r_{\rm ISCO}$ and close to that radii for some values of a_* (Chakraborty et al., 2017). Due to the same (above-mentioned) reason, we have also used here the approximate expression of LT precession (Eq. (6.4)) for calculating the tilt profile and applied it to the KTN BH with the value of n_* up to 0.7 along with $a_* = 0.7$. In addition, Eq. (6.4) reveals that the dominant contribution (due to the presence of GMM) comes from $n^2/r^{5/2}$ by neglecting the higher order terms for $n_* << r/M_{\rm BH}$. Although no qualitative differences appear in the tilt profiles calculated using the exact and approximate expressions (i.e., for $a_* << r/M_{\rm BH}$ and $n_* << r/M_{\rm BH}$) of LT precession frequency in the KTN BH, a quantitative difference (maximum upto $\sim 11\%$) in the tilt angle could appear at $r \sim 8.4 r_g$ for $(a_*, n_*) = (0.7, 0.7)$, and tends to zero for $r > 16 r_g$. Comparatively for the lower values of (a_*, n_*), the above-mentioned quantitative differences are expected to be less than 11%. However, the qualitative and substantial quantitative differences are supposed to be seen if one of the parameters (a_*, n_*) or both are greater than or very close to 1. In such a case, one has to use the full LT precession frequency expression (Eq. (6.2)) to solve the coupled differential equations similar to Eqs. (6.19-6.20), the left hand sides of which would also be obtained as a function of a_* and n_*. This means that the left hand side of Eq. (6.7) should be modified. Actually, the assumptions that lead to Eq. (6.7) are valid only within the parameter space where the effects of general relativity are sufficiently weak. This enables us to express the angular frequency using the Newtonian formula. We demand $r > r_g$ in this instance, such that one can expand Eq. (6.2) to obtain the expression of $\Omega_{\rm p}$ (Eq. 6.4), since $a_*/(r/r_g)$ is inevitably small in this regime. The exact formulation of a tilted thin accretion disk around the Kerr and KTN spacetime (valid for both BHs and naked singularities (Chakraborty et al., 2017; Chakraborty & Bhattacharyya, 2018; Chakraborty & Bhattacharyya, 2019)) is necessary to study the tilted accretion disk around GRO J1655-40 and some other astrophysical collapsed objects

6.4 Chapter conclusions

In this chapter, we numerically solve the warped accretion disk equations in the viscous regime for a KTN BH. Taking into account the inner disk contribution, we obtain the radial profile of the tilted disk around the said BH starting from the outer edge of the disk upto ISCO radius. We analyze the radial profile of the tilted disk as a function of the several parameters from our numerical results. We find that the inner disk could be entirely misaligned for a reasonable range of parameter values, which could confront with the astrophysical observations. For specific values of $M_{\rm BH}$ and ν_2, there are combinations of (a_*, n_*), where the disk begins to align with the direction of the BH spin, indicating that the Bardeen-Petterson effects could be observed. We summarise the key takeaways from the parameter sweep below.

The alignment of the disk strongly depends on the tug-of-war between the viscous torque (controlled by ν_2) and the LT torque (controlled by $M_{\rm BH}$, a_* and n_*). In case of the KTN BH, the LT precession does not monotonically increase with the decrement of r towards $r_{\rm ISCO}$, unlike a Kerr BH. Instead, if the value of r decreases from the outer orbit to ISCO, the modulus of LT precession frequency first increases, attains a peak, then decreases to zero, and increases again depending on the numerical values of (a_*, n_*) and the location of ISCO. Therefore, it is evident that the interplay between

the LT effects due to a_* and n_* is also important in this case.

Since, the radial profile of $\tilde{\beta}$ is affected by the LT effect, the behavior of all the curves for $\tilde{\beta}(r)$ is non-monotonous. For the same reason, the proportionality factor between $r_{\rm align}$ and $r_{\rm warp}$ for the various $\tilde{\beta}(r)$ curves does not remain fixed for the KTN BHs. It is interesting to see that the LT torue due to GMM is extended comparatively to the outer disk than the LT effect produced by the Kerr parameter, as it varies $R^{-5/2}$ in case of the KTN BHs.

The $\tilde{\beta}(r)$ curves for $n_* < a_*$ are located at the upper portion of the $n_* = a_*$ curve in the $\tilde{\beta} - r$ plane, whereas they are located at the lower portion of the same plane for $n_* > a_*$, in the case of larger r. This indicates that the LT torque becomes stronger for the higher value of n_* in that range of r. However, the above-mentioned trend is not necessarily true at the inner disk, as the dominant LT torque term switches from being the a_* term to the n_* term at $\tilde{r}_0$. Moreover, for every combination of a_*, n_* and $M_{\rm BH}$ (ν_2), there is a specific value of ν_2 ($M_{\rm BH}$), above (below) which the inner edge of the disk remains misaligned.

Certainly, the study of inner accretion disk plays an important role to probe the strong gravity regime. Tilting of the inner accretion disk with respect to the BH spin axis affects the spectral and timing properties of the X-ray emission through the LT precession, and therefore, it is useful to study the same in strong gravity regime. In fact, C-type low frequency QPO frequency is identified as the LT precision frequency (Stella & Vietri, 1998, 1999; Ingram & Motta, 2014), and shown to be emerged from the inner accretion disk. Therefore, our solution for the radial profile of the tilted disk around a KTN BH could be useful to probe the strong gravity regime as well as the existence of GMM in nature. Although some degeneracies could appear in the tilt profiles between a Kerr BH and a KTN BH with some specific combinations of (a_*, n_*) in some values of r, it is unlikely to match both of the tilt profiles exactly as a whole at each and every value of r for these two different type of BHs. This is because the functional dependence of the LT precession frequency as well as the tilt profile on a_*, n_* and ν_2 for all values of r could not be exactly the same for a Kerr and a KTN BH. However, probing the strong gravity regime with the accurate measurements of the tilt profile can help to break the degeneracies (if any) between the different BH metrics.

Indian Institute of Technology Guwahati

Chapter 7

Summary and future prospects

7.1 Summary of thesis

Accretion is one of the main sources of commonly observed high energetic astrophysical phenomena in quasars, XRBs and AGNs. Therefore, in this thesis, we explore the relativistic accretion flow around BHs and WHs in various astrophysical scenarios, such as hydrodynamical flow, magnetohydrodynamical flow and accretion flow in a tilted disk. In addition to that, we study hydrodynamical flow properties around galactic BHs surrounded by DM halos.

In Chapter 2, we have studied relativistic advective accretion flows around KTN BHs, considering both shock-free and shock-induced accretion solutions. In this regard, we have solved the governing hydrodynamical equations with a relativistic EoS to obtain global accretion solutions, which depend on the flow energy ($\mathcal{E}$), angular momentum (λ), and BH parameters, such as spin parameter ($a_{\rm k}$), and NUT parameter (n). Depending on the parameters, the flow may admit one or multiple critical points. The inflowing rotating matter encounters a centrifugal barrier, and when the relativistic Rankine-Hugoniot conditions are satisfied, shock transitions occur. As the shock-induced solutions contain higher entropy than the shock-free solutions, they are thermodynamically favourable. From our findings, it is evident that shock-induced solutions are not the isolated ones, these span a wide range in λ-$\mathcal{E}$ parameter space. The two BH parameters, $a_{\rm k}$ and n, affect oppositely on the shock properties (shock location (r_s), compression ratio (R), and shock strength (S)) and shock parameter space. Our study portrays that the maximum value of NUT parameter ($n^{\rm max}$), which allows shock solutions, increases with $a_{\rm k}$, and interestingly, shock can exist even for $a_{\rm k} > 1$ in KTN BH, which is unlike in Kerr BH. Finally, we have calculated Bremsstrahlung luminosity for shocked and shock-free solutions, and the results reveal that shock-induced accretion solutions give rise to higher luminosity than shock-free solutions.

Having explored the properties of shock-induced relativistic accretion flows around a compact object that is a KTN BH, we have extended our investigation to the ECOs. Among various ECOs, the rotating Kerr-like WH serves as a potential candidate to mimic the rotating Kerr BH away from the central objects, even though it has a different spacetime geometry. The defining property of this spacetime is the existence of the throat radius ($r_{\rm Th}$), which connects two different zones. Therefore, there is a possibility that the accretion flow may be influenced due to the properties of spacetime and may have distinguishing signatures on the astrophysical observables. With this motivation, in Chapter 3, we have investigated low angular momentum, inviscid, advective accretion flows around this stationary, axisymmetric Kerr-like WH spacetime. The steady state solutions are obtained by solving the governing flow equations, and we have examined the roles of $a_{\rm k}$ and β in regulating the accretion dynamics. We have obtained the complete set of transonic solutions (O, A, W, and I-type) around WHs by varying $\mathcal{E}$, λ, $a_{\rm k}$, and β, and retrace their domains in the $\lambda - \mathcal{E}$ plane. With this, the results show that $a_{\rm k}$ and β also influence the solution topologies as well as their properties. In addition to the transonic flow, subsonic solutions also exist in this spacetime, but due to their lower entropy than transonic flows, they are not thermodynamically favourable. Focusing on the I-type transonic solutions, which passes through the inner critical point ($r_{\rm in}$), the density, pressure, and temperature follow approximate power laws as $\rho \propto r^{-(n+2/5)}$, $p \propto r^{-(n+1)}$, and $T \propto r^{-(n-1/3)}$ with $n \sim 1$, which deviates from self-similarity near $r_{\rm Th}$ because of some non-linearity present in the spacetime. Furthermore, our result shows that Bremsstrahlung luminosity (L) increases with $a_{\rm k}$ and β for both I and O-type solutions and I-type solutions generate higher luminosity. Most interestingly, our model can reproduce the observed high luminosity of Cygnus X-3 in its hypersoft state, which suggests the accretion around a WH is also a viable mechanism of energetic X-ray emissions.

In Chapter 2 and Chapter 3, we have explored the dynamics of accretion flows around KTN BHs and Kerr-like WHs and showed the influences of the spacetime geometries on the infalling matter as well as observational signatures. However, such analyses were done by neglecting the astrophysical environment. Various observational evidence, such as galaxy rotation curves, gravitational lensing, anisotropies in the CMB, strongly indicate the presence of non-luminous DM as a dominant mass component of the Universe. Since supermassive BHs in galactic nuclei are expected to reside within dense DM halos, their gravitational influence cannot be ignored while modelling the surrounding spacetime. Therefore, in Chapter 4, we have investigated advection dominated, inviscid, transonic hot accretion flows onto a galactic SMBH embedded in a DM halo. The SMBH is modelled as a central Schwarzschild BH surrounded by a spherically symmetric cold collisionless anisotropic DM distribution. For the comparative analysis, we have considered Hernquist, NFW, Einasto profiles and a fully relativistic Hernquist-type DM spike formed via adiabatic growth of a central BH. By influencing the gravitational potential, the DM halo can alter the properties of the accretion flow, including its topology, thermodynamic properties, and emitted radiation. Since the dominant luminosity in I-type accretion solutions originates from the inner disk, the deviations of the luminosity from vacuum Schwarzschild geometry are strongly influenced by the DM spike, which reflects the nature of the DM spike. The variations of the luminosity of the emitted radiation from the accretion flow increase with the mass and compactness of the DM halo. Both the bolometric luminosity and SED show distinct departures from the vacuum Schwarzschild BH, with stronger

deviations for more massive and compact halos. In the HQ-type DM spike model, the nonlinear dependence of the density profile significantly changes the flow properties and emission properties.

We have already studied the relativistic hydrodynamical flow around KTN BH, Kerr-like WH, and Schwarzschild BH surrounded by a DM halo. The presence of magnetic fields is very common in astrophysical scenarios and plays a crucial role in accretion dynamics by transporting angular momentum, energy dissipation, and launching the jet. Recent observations of the polarimetric image of the Sgr A* by EHT collaborations and GRMHD simulations provide constraints on the accretion flow properties, including the BH spin, the mass accretion rate, and the magnetic field strengths at different radii close to the BH. These measurements infer the critical role of magnetic fields in the dynamics of the near horizon region and favoured the MAD scenario, which demonstrates the dynamic role of strong magnetic fields in the observed emissions from SMBHs. These motivate us to study the GRMHD flow around a BH in light of EHT observations. Therefore, in Chapter 5, we have intended to obtain the magnetized accretion solutions and their properties around a Kerr BH by solving the GRMHD equations in steady state, which can match the EHT constrained magnetic field distribution near Sgr A*. Within this model framework, we have derived steady state GRMHD solutions that match the magnetic field strengths measured by the EHT collaboration to within $\pm 10\%$ error at $7.3r_{\rm g}$ and $4r_{\rm g}$ for a Kerr black hole of mass $4 \times 10^6 M_\odot$, mass accretion rate $10^{-8} M_\odot {\rm yr}^{-1}$, and spin $a_{\rm k} = 0.94$. Finally we have successfully showed that, depending on the flow parameters, namely energy ($\mathcal{E}$), angular momentum ($\mathcal{L}$), magnetic flux (Φ) and isorotation parameter (I), there is a family of solutions, which simultaneously match the magnetic field at both radii with an accuracy of approximately 10%. Therefore, our results indicate that the present study provides a self-consistent theoretical framework based on GRMHD accretion flows to explain the nature of magnetized accretion flows around Sgr A*.

So far, we have examined hydrodynamical and magnetohydrodynamical accretion flows around various BHs and WHs, mostly assuming disks on the equatorial plane of the central object. In realistic scenarios, an accretion disk may be tilted when the angular momentum of the inflowing matter is misaligned with the compact object's spin. Moreover, the observational evidences from various astrophysical sources like H1743-322, GRO J1655-40, M87* indicate that accretion disks are not always perfectly aligned with the spin axis of the central compact objects. In addition to that, observables of GRO J1655-40 are explained better considering the KTN BH rather than the Kerr BH. Therefore, to complete the overall understanding of the relativistic accretion flow, we have extensively studied the LT precession in the tilted accretion disk around KTN BH in Chapter 6. Here, we have numerically solved the warped accretion disk equations in the viscous regime. Considering the inner disk contribution, we have computed the radial tilt profile from the outer disk edge to the ISCO radius. Our results show that the inner disk may be aligned or misaligned depending upon the flow parameters and BH properties. Therefore, disk alignment is governed by the competition between viscous torque (ν_2) and LT torque ($M_{\rm BH}$, a_*, n_*). For specific $M_{\rm BH}$ and ν_2, certain (a_*, n_*) combinations lead to the alignment, which is in agreement with the BP effect. In KTN spacetimes, unlike Kerr, the LT precession does not increase monotonically toward $r_{\rm ISCO}$, as there is a competition between a_* and n_* at each radial coordinate. For each $(a_*, n_*, M_{\rm BH}, \nu_2)$ set, there exists a critical ν_2 ($M_{\rm BH}$), above (below) which the inner edge remains misaligned. Therefore, this

theoretical analysis of the tilted nature of the accretion disk around KTN BH, along with observations, can probe the strong gravity and indicate the existence of the NUT parameter in the spacetime.

7.2 Future prospects

In this thesis, we have explored relativistic accretion around compact objects and ECOs. These studies include the shock-induced accretion solutions around a broader class of stationary and axisymmetric BHs, namely KTN BHs and their implications on observational features, the relativistic hydrodynamic solutions in the context of Kerr-like WHs and around SMBHs immersed in various DM halos. Furthermore, we have studied magnetized accretion flows onto Kerr BHs in steady state and the dynamics of tilted accretion disks around KTN BHs. Collectively, these investigations open up several interesting possibilities for future research.

We have shown that the formation of shocks in accretion flows is not a disjoint event but rather a self-consistent outcome depending on the flow parameters and spacetime geometry. Depending on the flow parameters, the shock transition may appear as stationary (standing) or oscillatory in nature. In the present thesis, we discuss the properties of standing shocks in hydrodynamical system. Mitra & Das (2024) investigated the existence of shock-induced accretion solutions around Kerr BHs in steady state GRMHD framework. Furthermore, according to Molteni et al. (1996), oscillatory shocks may naturally arise when the cooling timescale becomes comparable to the infall timescale. Such oscillations trigger Quasi-periodic modulations in the emitted light curves of accreting systems such as AGN and XRBs, which are observed as QPOs in their power density spectra (PDS). Motivated by this, in future, we want to incorporate detailed radiative cooling processes, including Bremsstrahlung, Synchrotron, and Comptonization into the framework of GRMHD accretion flows around Kerr and KTN BHs. This will enable us to self-consistently generate QPOs from shock-induced accretion solutions and investigate the combined effect of the magnetic field, the BH parameters, and cooling mechanisms on both QPO frequencies and luminosities. These theoretical predictions, along with observational data, will provide valuable insights into the properties of compact objects and the dynamics of accretion flows. In addition, Jana & Das (2024) have recently shown that the PSC can act as a source of outflows in magnetized flows around Kerr BHs due to the excess thermal pressure gradient in the post-shock region. GRMHD simulations further support the formation of relativistic jets/outflows from the accretion around compact objects (Mościbrodzka et al., 2016; Dihingia & Vaidya, 2022; Mizuno, 2022). Therefore, we plan to investigate the formation of jet/outflow from shock-induced accretion solutions within the GRMHD framework around various compact objects under steady state conditions.

We have also studied the nature of transonic accretion solutions around SMBHs embedded in DM halos, where the BHs are static and spherically symmetric objects. Recently, Mitra et al. (2025); Fernandes & Cardoso (2025) investigated the rotating BHs in astrophysical environments. Therefore, it is expected that the presence of a rotating DM spike could also influence transonic accretion flows and modify their radiative properties. Hence, we want to extend our study regarding the accretion flow for a rotating DM spike around a Kerr BH and provide a valuable diagnostic of the nature and distribution of DM halos surrounding this. Even though we have not

considered the accretion of DM around the compact object till now. However, the accretion of baryonic matter as well as DM (Mach & Odrzywo, 2021) is inevitable and also affects the mass of the compact objects and the observables as well. Therefore, we intend to incorporate the DM accretion along with the baryonic matter accretion around compact objects.

Very recently, Combi et al. (2024) carried out GRMHD simulations of a spherically symmetric traversable wormhole (Simpson–Visser) and showed that magneto-rotational instability (MRI) aids matter accretion on one side of the wormhole and powers a mildly relativistic thermal wind to the other side of it. Therefore, as we have studied the accretion flow in one side of Kerr-like WH, we want to study how the matter is coming out from the other side of the WH throat and what observational evidence we can get from this. With this, we also investigate the accretion flow around other ECOs such as gravastars, boson stars, quark stars (see section 1.2) and difference in the astrophysical obvervables.

We have investigated the dynamics of tilted accretion disks around KTN BHs, and demonstrated that the inner disk tilt angle depends on the BH parameters and the flow parameters. Ghasemi-Nodehi et al. (2021) examined the possibility of a non-zero NUT parameter in the case of M87* using EHT observations. On the other hand, M87 provides a unique laboratory to study the interplay between SMBHs and relativistic jets. With a baseline of 17 years of observations, it has been found that there was a shift in the jet's transverse position. Cui et al. (2023) reported a period of about 11 years for the changes in the jet's angle based on the collected data over 22 years. However, the origin of these variations remains unclear. Therefore, the LT precession may be a plausible explanation of this jet precession. Motivated by this, as a future goal, we want to study jet precession arising from tilted accretion flows around KTN BH.

Indian Institute of Technology Guwahati

Appendix A

Appendix A

Effect of general relativity on disk emission

The frequency shift of an emitted photon due to the general relativistic effects is expressed in terms of redshift factor z as,

$$\frac{\nu_{\rm o}}{\nu_{\rm e}} = \frac{E_{\rm o}}{E_{\rm e}} = \frac{(p_\mu u^\mu)_{\rm o}}{(p_\mu u^\mu)_{\rm e}} = \frac{1}{1+z}, \tag{A.1}$$

where, $\nu_{\rm o}$ is the observed frequency, $\nu_{\rm e}$ is the emitted frequency, $E_{\rm o}$ is the observed energy, $E_{\rm e}$ is the emitted energy, and p_μ is the 4-momentum of the photon.

The energy of the emitted photon is given by,

$$E_{\rm e} = p_t u^t + p_\phi u^\phi = p_t u^t \left(1 + \Omega \frac{p_\phi}{p_t}\right), \tag{A.2}$$

where, Ω $(= u^\phi/u^t)$ is the angular velocity of the particle around the BH, and p_ϕ/p_t refers the impact parameter of the photon around Z-axis (see Fig. A.1) which is given by,

$$\frac{p_\phi}{p_t} = b \sin\alpha \sin\theta_0 \tag{A.3}$$

In Fig. A.1, the BH is placed at the origin (O) of the XYZ-coordinate system. A photon is emitted from the point R and being observed at the point P. OP refers the distance between the observer and the black hole. The observer's screen is perpendicular to OP and it is inclined with an angle θ_0 to the Z-axis. On the observer's screen, (b, α) are the coordinates of the intersection point of the tangential line to the photon trajectory. It is apparent that the effect of light bending generally diminishes provided the source of the emitted photon is located at far away distance from the observer. Considering this, we approximate $b \sin\alpha = r \sin\phi$ to calculate the redshift factor as,

$$1 + z = u^t \big(1 + \Omega r \sin\phi \sin\theta_0\big). \tag{A.4}$$

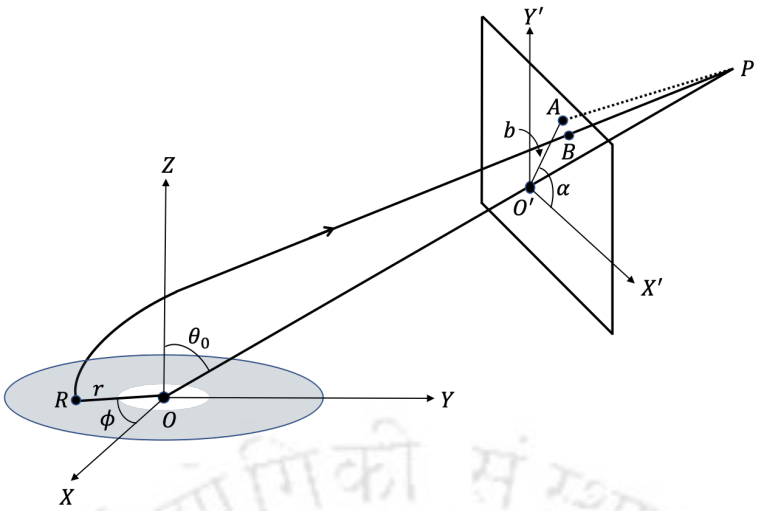

Figure A.1: Geometrical representation of a emitted photon from the accretion disk around a black hole. See text for details.

We use Eq. (A.4) to calculate the luminosity (L) corresponding to the Bremsstrahlung radiation.

Appendix B

Appendix B

B.1 Keplerian angular momentum

One of the key conditions for transonic hot accretion flow is that the constant flow angular momentum must be lower than the Keplerian angular momentum (λ_K). The Keplerian angular momentum is obtained by the vanishing gradient of the effective potential

$$\frac{d\Phi_e^{\rm eff}}{dr} = 0 \ . \tag{B.1}$$

This implies that matter rotating in a Keplerian orbit will stay in equilibrium as the centrifugal force balances the effective gravitational attraction. The variation of the Keplerian angular momentum for the different DM profiles is shown in Fig. B.1. We note that the presence of the DM halo always increases the Keplerian angular momentum from that of Schwarzschild BH. This implies that advection dominated transonic hot accretion flow in the presence of DM halo can have higher specific angular momentum. Except for highly compact halos, the Einasto distribution shows the highest Keplerian angular momentum at any radius.

The minima of the Keplerian angular momenta correspond to the radius of the marginally stable orbit (Abramowicz & Fragile, 2013; Rezzolla & Zanotti, 2013). We observe that the radius of the marginally stable orbit (ISCO, see Eq. (4.7)) shifts inwards due to the presence of the DM halo signalling a weaker inflow. This is consistent with the observation in (Heydari-Fard et al., 2025).

B.2 Hernquist-type DM spike

In this appendix, we plot the nonlinear dependence of the density profile of the HQ-type DM spike with the halo mass, the associated effective potential Eq. (4.23) in

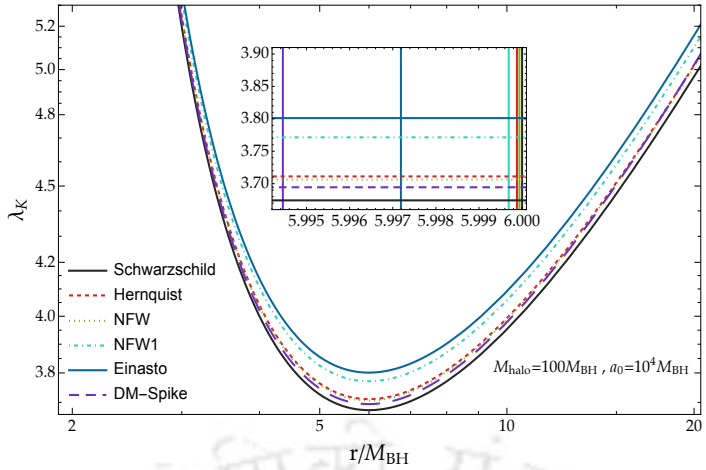

Figure B.1: Variation of the Keplerian angular momentum (λ_K) with the radial coordinate (r) in the unit of the BH mass for different DM halo profiles. The vertical lines in the inset show the location of the marginally stable orbit (minima of λ_K) of the corresponding DM halo distribution.

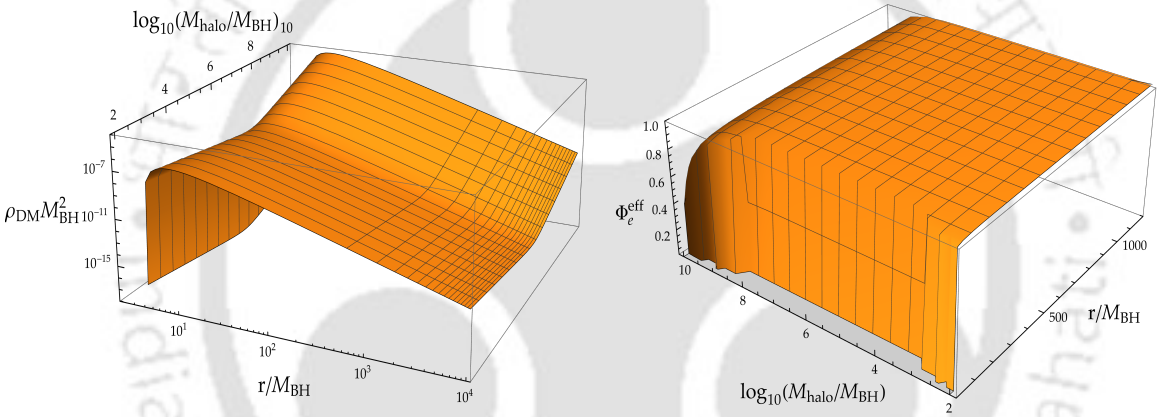

Figure B.2: Variation of the halo density and effective potential of HQ-type DM spike profile with the halo mass for a fixed DM halo compactness of 0.01.

Fig. B.2. The resulting changes in the location and temperature at the critical point for I-type accretion flow with $\mathcal{E} = 1.001$ and $\lambda = 3.674$ is shown in Fig. B.3. Fig. B.3 also shows the radius r_0 at which the aspect ratio becomes unity. Note that the maximum value of r_0 is set at $1000M_{BH}$ for the current analysis. Other flow properties strongly depend on the location and temperature of the critical point. This explains the nonlinear behaviour of the flow properties and luminosity of the HQ-type DM distribution shown in section 4.5 and section 4.6.

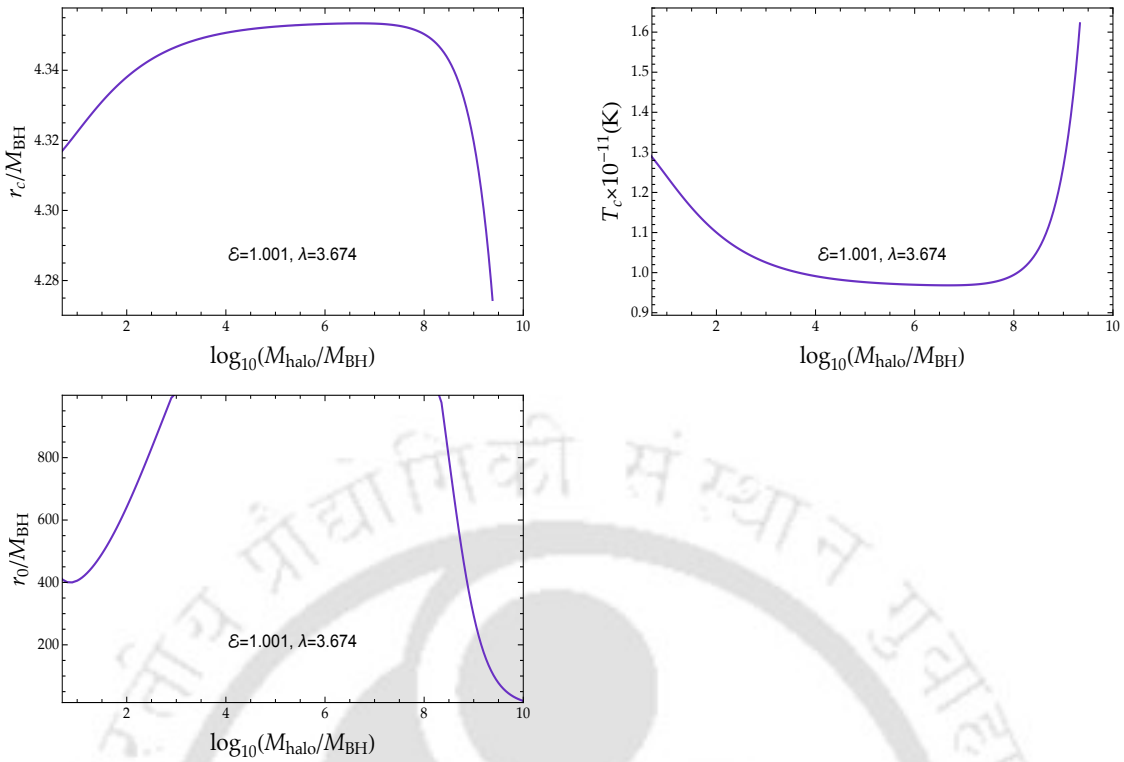

Figure B.3: Plot of the critical points (r_c) (top) and temperature (T_c) of the critical point (middle) for a Hernquist type DM halo with $M_{\rm halo}$ around a galactic SMBH with $\mathcal{E} = 1.001$ and $\lambda = 3.674$. In the bottom panel, variation of radial distance r_0 at which the relative disk height (H/r) becomes unity, is shown. Here, the maximum value of r_0 is set at 1000 $M_{\rm BH}$.

Appendix C

Appendix C

Conservation equations of energy and angular momentum, and radial momentum equation

Using the energy conservation equation (Eq. (5.6)), we get,

$$\frac{d\mathcal{E}}{dr} = \mathcal{E}_r + \mathcal{E}_v \frac{dv}{dr} + \mathcal{E}_\Theta \frac{d\Theta}{dr} + \mathcal{E}_\lambda \frac{d\lambda}{dr} = 0.$$

The coefficients $\mathcal{E}_r$, $\mathcal{E}_v$, $\mathcal{E}_\theta$, and $\mathcal{E}_\lambda$ are given by,

$$\begin{aligned}
\mathcal{E}_r =& -\frac{\partial h_{\rm tot}}{\partial r}u_t - h_{\rm tot}\frac{\partial u_t}{\partial r} + \frac{g_{t\phi}b^r\frac{\partial b^\phi}{\partial r}}{u^r\rho} + \frac{g_{tt}b^r\frac{\partial b^t}{\partial r}}{u^r\rho}\frac{b^r b^t\frac{dg_{tt}}{dr}}{u^r\rho} + \frac{b^r b^\phi\frac{dg_{t\phi}}{dr}}{u^r\rho} + \frac{3b^r(g_{tt}b^t+g_{t\phi}b^\phi)}{2ru^r\rho} \\
&+ \frac{\frac{\partial b^r}{\partial r}(g_{tt}b^t+g_{t\phi}b^\phi)}{u^r\rho} - \frac{\frac{\partial \mathcal{F}}{\partial r}b^r(g_{tt}b^t+g_{\phi\phi}b^\phi)}{2\mathcal{F}u^r\rho} + \frac{b^r\frac{d\Delta}{dr}(g_{tt}b^t+g_{t\phi}b^\phi)}{2\Delta u^r\rho} - \frac{b^r\frac{\partial u^r}{\partial r}(g_{tt}b^t+g_{t\phi}b^\phi)}{(u^r)^2\rho}, \\
\mathcal{E}_v =& -\frac{\partial h_{\rm tot}}{\partial v}u_t - h_{\rm tot}\frac{\partial u_t}{\partial v} + \frac{g_{tt}b^r\frac{\partial b^t}{\partial v}}{u^r\rho} + \frac{g_{t\phi}b^r\frac{\partial b^\phi}{\partial v}}{u^r\rho} + \frac{\frac{\partial b^r}{\partial v}(g_{tt}b^t+g_{t\phi}b^\phi)}{u^r\rho} - \frac{b^r\frac{\partial u^r}{\partial v}(g_{tt}b^t+g_{t\phi}b^\phi)}{(u^r)^2\rho} \\
&+ \frac{b^r(g_{tt}b^t+g_{t\phi})}{u^r\rho v} + \frac{b^r v\gamma_v^2(g_{tt}b^t+g_{t\phi}b^\phi)}{u^r\rho}, \\
\mathcal{E}_\Theta =& -\frac{\partial h_{\rm tot}}{\partial \Theta}u_t + \frac{b^r(g_{tt}b^t+g_{t\phi}b^\phi)}{ru^r\Theta\rho}, \\
\mathcal{E}_\lambda =& -\frac{\partial h_{\rm tot}}{\partial \lambda}u_t - h_{\rm tot}\frac{\partial u_t}{\partial \lambda} + \frac{g_{tt}b^r\frac{\partial b^t}{\partial \lambda}}{u^r\rho} + \frac{g_{t\phi}b^r\frac{\partial b^\phi}{\partial \lambda}}{u^r\rho} - \frac{\frac{\partial F}{\partial \lambda}b^r(g_{tt}b^t+g_{t\phi}b^\phi)}{2\mathcal{F}u^r\rho} - \frac{\frac{\partial b^r}{\partial \lambda}(g_{tt}b^t+g_{t\phi}b^\phi)}{u^r\rho}.
\end{aligned}$$

Applying the angular momentum conservation equation (Eq. (5.7)), we obtain,

$$\frac{d\mathcal{L}}{dr} = \mathcal{L}_r + \mathcal{L}_v\frac{dv}{dr} + \mathcal{L}_\Theta\frac{d\Theta}{dr} + \mathcal{L}_\lambda\frac{d\lambda}{dr} = 0,$$

where the coefficients $\mathcal{L}_r, \mathcal{L}_v$, $\mathcal{L}_\theta$ and $\mathcal{L}_\lambda$ are expressed as,

$$\begin{aligned}
\mathcal{L}_r =&\frac{\partial h_{\rm tot}}{\partial r}u_\phi + h_{\rm tot}\frac{\partial u_\phi}{\partial r} - \frac{g_{t\phi}b^r\frac{\partial b^t}{\partial r}}{u^r\rho} - \frac{3b^r(g_{t\phi}b^t+g_{\phi\phi}b^\phi)}{2ru^r\rho} + \frac{\frac{\partial\mathcal{F}}{\partial r}(g_{t\phi}b^t+g_{\phi\phi}b^\phi)}{2\mathcal{F}u^r\rho} - \frac{\frac{\partial b^r}{\partial r}(g_{t\phi}b^t+g_{\phi\phi}b^\phi)}{u^r\rho}\\
&+\frac{b^r\frac{\partial u^r}{\partial r}(g_{t\phi}b^t+g_{\phi\phi}b^\phi)}{(u^r)^2\rho} - \frac{g_{\phi\phi}b^r\frac{\partial b^\phi}{\partial r}}{u^r\rho} - \frac{b^rb^t\frac{dg_{t\phi}}{dr}}{u^r\rho} - \frac{b^rb^\phi\frac{dg_{\phi\phi}}{dr}}{u^r\rho} - \frac{b^r(g_{t\phi}b^t+g_{\phi\phi}b^\phi\frac{d\Delta}{dr})}{2\Delta u^r\rho},\\
\mathcal{L}_v =&\frac{\partial h_{\rm tot}}{\partial v}u_\phi + h_{\rm tot}\frac{\partial u_\phi}{\partial v} - \frac{g_{t\phi}b^r\frac{\partial b^t}{\partial v}}{u^r\rho} - \frac{g_{\phi\phi}b^r\frac{\partial b^\phi}{\partial v}}{u^r\rho} - \frac{\frac{\partial b^r}{\partial v}(g_{t\phi}b^t+g_{\phi\phi}b^\phi)}{u^r\rho} + \frac{b^r\frac{\partial u^r}{\partial v}(g_{t\phi}b^t+g_{\phi\phi}b^\phi)}{(u^r)^2\rho}\\
&-\frac{b^r(g_{t\phi}b^t+g_{\phi\phi}b^\phi)}{u^r\rho v} - \frac{b^rv\gamma_v^2(g_{t\phi}b^t+g_{\phi\phi}b^\phi)}{u^r\rho},\\
\mathcal{L}_\Theta =&\frac{\partial h_{\rm tot}}{\partial\Theta}u_\phi - \frac{b^r(g_{t\phi}b^t+g_{\phi\phi}b^\phi)}{2\Theta u^r\rho},\\
\mathcal{L}_\lambda =&\frac{\partial h_{\rm tot}}{\partial\lambda}u_\phi + h_{\rm tot}\frac{\partial u_\phi}{\partial\lambda} - \frac{g_{t\phi}b^r\frac{\partial b^t}{\partial\lambda}}{u^r\rho} - \frac{\frac{\partial b^r}{\partial\lambda}(g_{t\phi}b^t+g_{\phi\phi}b^\phi)}{u^r\rho} - \frac{g_{\phi\phi}b^r\frac{\partial b^\phi}{\partial\lambda}}{u^r\rho} + \frac{\frac{\partial\mathcal{F}}{\partial\lambda}b^r(g_{t\phi}b^t+g_{\phi\phi}b^\phi)}{2\mathcal{F}u^r\rho}.
\end{aligned}$$

The radial momentum equation (Eq. (5.10)) is written as,

$$\mathcal{R}_r + \mathcal{R}_v\frac{dv}{dr} + \mathcal{R}_\Theta\frac{d\Theta}{dr} + \mathcal{R}_\lambda\frac{d\lambda}{dr} = 0,$$

where the coefficients $\mathcal{R}_r$, $\mathcal{R}_v$, $\mathcal{R}_\theta$ and $\mathcal{R}_\lambda$ are given by,

$$\begin{aligned}
\mathcal{R}_r =&\frac{1}{h_{\rm tot}\left(\frac{1}{g_{rr}}+(u^r)^2\right)\rho}\Bigg[-2b^r\frac{\partial b^r}{\partial r} - g_{rr}b^r\frac{\partial b^r}{\partial r}(u^r)^2 + \frac{1}{2}\left(\frac{1}{g_{rr}}+(u^r)^2\right) + h_{\rm tot}u^r\frac{\partial u^r}{\partial r}\rho\\
&-\frac{3\left(\frac{1}{g_{rr}}+(u^r)^2\right)\Theta\rho}{r\tau} + \frac{\frac{\partial\mathcal{F}}{\partial r}\left(\frac{1}{g_{rr}}+(u^r)^2\right)\Theta\rho}{\tau\mathcal{F}} - b^ru^r\frac{\partial b^t}{\partial r}(g_{tt}u^t+g_{t\phi}u^\phi) - b^ru^r\frac{\partial b^\phi}{\partial r}(g_{t\phi b^t}+g_{\phi\phi}b^\phi)\\
&-\frac{(b^r)^2\frac{dg_{rr}}{dr}}{g_{rr}} - \frac{1}{2}(b^r)^2(u^r)^2\frac{dg_{rr}}{dr} + \frac{h_{\rm tot}(u^r)^2\rho\frac{dg_{rr}}{dr}}{2g_{rr}} + \frac{(b^t)^2\frac{dg_{tt}}{dr}}{2g_{rr}} + \frac{b^tb^\phi\frac{dg_{t\phi}}{dr}}{g_{rr}} - \frac{-(b^r)^2\frac{dg_{\theta\theta}}{dr}}{2g_{\theta\theta}}\\
&-(b^r)^2\left(\frac{g_{\phi\phi}\frac{dg_{tt}}{dr}}{2(-g_{t\phi}^2+g_{tt}g_{\phi\phi})} + \frac{g_{t\phi}\frac{dg_{t\phi}}{dr}}{2(g_{t\phi}^2-g_{tt}g_{\phi\phi})}\right) - g_{rr}(u^r)^2b^t\left(-\frac{b^t\frac{dg_{tt}}{dr}}{2g_{rr}} - \frac{b^\phi\frac{dg_{t\phi}}{dr}}{2g_{rr}}\right)\\
&-2b^ru^rb^t(g_{tt}u^t+g_{t\phi}u^\phi)\left(\frac{g_{\phi\phi}\frac{dg_{tt}}{dr}}{2(-g_{t\phi}^2+g_{tt}g_{\phi\phi})} + \frac{g_{t\phi}\frac{dg_{t\phi}}{dr}}{2(g_{t\phi}^2-g_{tt}g_{\phi\phi})}\right) + h_{\rm tot}u^t\rho\left(-\frac{u^t\frac{dg_{tt}}{dr}}{2g_{rr}} - \frac{u^\phi\frac{dg_{t\phi}}{dr}}{2g_{rr}}\right)\\
&-2b^ru^rb^t(g_{t\phi}u^t+g_{\phi\phi}u^\phi)\left(\frac{g_{t\phi}\frac{dg_{tt}}{dr}}{2(g_{t\phi}^2-g_{tt}g_{\phi\phi})} + \frac{g_{tt}\frac{dg_{t\phi}}{dr}}{2(-g_{t\phi}^2+g_{tt}g_{\phi\phi})}\right) + \frac{(b^\phi)^2\frac{dg_{\phi\phi}}{dr}}{2g_{rr}}\\
&-2b^ru^rb^\phi\left(g_{tt}u^t+g_{t\phi}u^\phi\right)\left(\frac{g_{\phi\phi}\frac{dg_{t\phi}}{dr}}{2(-g_{t\phi}^2+g_{tt}g_{\phi\phi})} + \frac{g_{t\phi}\frac{dg_{\phi\phi}}{dr}}{2(g_{t\phi}^2-g_{tt}g_{\phi\phi})}\right) + h_{\rm tot}u^t\rho\left(-\frac{u^t\frac{dg_{t\phi}}{dr}}{2g_{rr}} - \frac{u^\phi\frac{dg_{\phi\phi}}{dr}}{2g_{rr}}\right)\\
&-g_{rr}(u^r)^2b^\phi\left(-\frac{b^t\frac{dg_{t\phi}}{dr}}{2g_{rr}} - \frac{b^\phi\frac{dg_{\phi\phi}}{dr}}{2g_{rr}}\right) - (b^r)^2\left(\frac{g_{t\phi}\frac{dg_{t\phi}}{dr}}{2(g_{t\phi}^2-g_{tt}g_{\phi\phi})} + \frac{g_{tt}\frac{dg_{\phi\phi}}{dr}}{2(-g_{t\phi}^2+g_{tt}g_{\phi\phi})}\right)\\
&-2b^ru^rb^\phi\left(g_{t\phi}u^t+g_{\phi\phi}u^\phi\right)\left(\frac{g_{t\phi}\frac{dg_{t\phi}}{dr}}{2(g_{t\phi}^2-g_{tt}g_{\phi\phi})} + \frac{g_{tt}\frac{dg_{\phi\phi}}{dr}}{2(-g_{t\phi}^2+g_{tt}g_{\phi\phi})}\right) - \frac{\left(\frac{1}{g_{rr}}+(u^r)^2\right)\Theta\rho\frac{d\Delta}{dr}}{\tau\Delta}\Bigg],
\end{aligned}$$

$$\mathcal{R}_v = \frac{1}{h_{\rm tot}\left(\frac{1}{g_{rr}}+(u^r)^2\right)\rho}\Bigg[-b^r\frac{\partial b^r}{\partial r} - g_{rr}b^r\frac{\partial b^r}{\partial r}(u^r)^2 + \frac{1}{2}\frac{\partial (B^2)}{\partial v}\left(\frac{1}{g_{rr}}+(u^r)^2\right)$$
$$+ h_{\rm tot}u^r\frac{\partial u^r}{\partial v}\rho - \frac{2\left(\frac{1}{g_{rr}}+(u^r)^2\right)\Theta\rho}{\tau v} - \frac{2\left(\frac{1}{g_{rr}}+(u^r)^2\right)\Theta\rho v\gamma_v^2}{\tau} - b^r u^r\frac{\partial b^t}{\partial v}(g_{tt}u^t + g_{t\phi}u^\phi)$$
$$- b^r u^r\frac{\partial b^\phi}{\partial v}(g_{t\phi}u^t + g_{\phi\phi}u^\phi)\Bigg],$$

$$\mathcal{R}_\Theta = \frac{1}{\tau h_{\rm tot}},$$

$$\mathcal{R}_\lambda = \frac{1}{h_{\rm tot}\left(\frac{1}{g_{rr}}+(u^r)^2\right)\rho}\Bigg[-2b^r\frac{\partial b^r}{\partial \lambda} - g_{rr}b^r\frac{\partial b^r}{\partial \lambda} + \frac{1}{2}\left(\frac{1}{g_{rr}}+(u^r)^2\right)\frac{\frac{\partial \mathcal{F}}{\partial \lambda}\left(\frac{1}{g_{rr}}+(u^r)^2\right)\Theta\rho}{\tau\mathcal{F}}$$
$$- b^r u^r\frac{\partial b^t}{\partial \lambda}(g_{tt}u^t + g_{t\phi}u^\phi) - b^r u^r\frac{\partial b^\phi}{\partial \lambda}(g_{t\phi}u^t + g_{\phi\phi}u^\phi)\Bigg].$$

Bibliography

Abbott B. P., et al., 2017, Phys. Rev. Lett., 119, 161101

Abbott T. M. C., et al., 2018, Physical Review D, 98, 043526

Abdujabbarov A., Atamurotov F., Kucukakca Y., Ahmedov B., Camci U., 2013, Astrophysics and Space Science, 344, 429

Abramowicz M. A., Chakrabarti S. K., 1990, The Astrophysical Journal, 350, 281

Abramowicz M. A., Fragile P. C., 2013, Living Reviews in Relativity, 16, 1

Abramowicz M. A., Czerny B., Lasota J. P., Szuszkiewicz E., 1988, Astrophys. J. , 332, 646

Abramowicz M. A., Chen X., Kato S., Lasota J.-P., Regev O., 1995, Astrophysical Journal Letters, 438, L37

Abramowicz M. A., Chen X. M., Granath M., Lasota J. P., 1996, Astrophys. J., 471, 762

Abramowicz M. A., Lanza A., Percival M. J., 1997, Astrophys. J. , 479, 179

Abuter R., et al., 2019, Astron. Astrophys., 625

Acharyya R., Banerjee P., Kar S., 2024, JCAP, 04, 070

Adams W. S., 1914, Publ. Astron. Soc. Pacific , 26, 198

Adams W. S., 1915, Publications of the Astronomical Society of the Pacific, 27, 236

Aghanim N., et al., 2020, Astron. Astrophys., 641, A6

Agrawal P. C., Gokhale G. S., Iyengar V. S., Kunte P. K., Manchanda R. K., Sreekantan B. V., 1972, Astrophysics and Space Science, 18, 408

Akiyama K., et al., 2021, Astrophys. J. Lett., 910, L13

Akiyama K., et al., 2024a, The Astrophysical Journal Letters, 964, L25

Akiyama K., et al., 2024b, Astrophys. J. Lett., 964, L25

Akiyama K., et al., 2024c, The Astrophysical Journal Letters, 964, L26

Akiyama K., et al., 2024d, Astrophys. J. Lett., 964, L26

Akizuki C., Fukue J., 2006, Publications of the Astronomical Society of Japan, 58, 469

Aktar R., Das S., Nandi A., 2015, Mon. Not. Roy. Astron. Soc., 453, 3414

Aktar R., Das S., Nandi A., Sreehari H., 2017, Monthly Notices of the Royal Astronomical Society, 471, 4806

Alam S., et al., 2017, Monthly Notices of the Royal Astronomical Society, 470, 2617

Alcock C., Farhi E., Olinto A., 1986, Astrophys. J. , 310, 261

Ambartsumyan V. A., Saakyan G. S., 1960, Soviet Astronomy, 4, 187

Amir M., Jusufi K., Banerjee A., Hansraj S., 2019, Classical and Quantum Gravity, 36, 215007

Anile A., 1989, Relativistic Fluids and Magneto-fluids: With Applications in Astrophysics and Plasma Physics. Cambridge Monographs on Mathematical Physics, Cambridge University Press, https://books.google.co.in/books?id=0Z1_MFT1H44C

Anzer U., Boerner G., Meszaros P., 1976, Astron. Astrophys. , 50, 305

Appl S., Camenzind M., 1988, Astron. Astrophys. , 206, 258

Artemova I. V., Bjoernsson G., Novikov I. D., 1996, Astrophys. J. , 461, 565

Aschenbach B., 2004, Astronomy & Astrophysics, 425, 1075

Atri P., et al., 2025, Astron. Astrophys., 696, A223

Baade W., Zwicky F., 1934, Proc. Nat. Acad. Sci., 20, 254

Bacchini F., Mayerson D. R., Ripperda B., Davelaar J., Olivares H., Hertog T., Vercnocke B., 2021, Phys. Rev. Lett., 127, 171601

Baes M., Dejonghe H., 2002, Astron. Astrophys. , 393, 485

Balbus S. A., Hawley J. F., 1991, The Astrophysical Journal, 376, 214

Balbus S. A., Hawley J. F., 1998a, Reviews of Modern Physics, 70, 1

Balbus S. A., Hawley J. F., 1998b, in Holt S. S., Kallman T. R., eds, American Institute of Physics Conference Series Vol. 431, Accretion processes in Astrophysical Systems: Some like it hot! - eigth AstroPhysics Conference. AIP, pp 79–88, doi:10.1063/1.55947

Balick B., Brown R. L., 1974, The Astrophysical Journal, 194, 265

Banerjee S., Chakraborty C., Bhattacharyya S., 2019a, Monthly Notices of the Royal Astronomical Society, 487, 3488

Banerjee S., Chakraborty C., Bhattacharyya S., 2019b, The Astrophysical Journal, 870, 95

Barceló C., Liberati S., Sonego S., Visser M., 2009, Sci. Am., 301, 38

Barceló C., Carballo-Rubio R., Garay L. J., 2016, Universe, 2, 7

Bardeen J. M., Petterson J. A., 1975, Astrophys. J. Lett. , 195, L65

Bardeen J. M., Press W. H., Teukolsky S. A., 1972, Astrophys. J. , 178, 347

Baumgarte T. W., Shapiro S. L., 2003, Astrophys. J., 585, 921

Becker P. A., Kazanas D., 2001, Astrophys. J. , 546, 429

Becker P. A., Das S., Le T., 2008, Astrophys. J. Lett. , 677, L93

Begelman M. C., Pringle J. E., 2007, Monthly Notices of the Royal Astronomical Society, 375, 1070

Bertone G., Merritt D., 2005, Phys. Rev. D, 72, 103502

Bessel F. W., 1844, Monthly Notices of the Royal Astronomical Society, 6, 136

Betoule M., et al., 2014, Astronomy & Astrophysics, 568, A22

Biemond J., 2007, arXiv e-prints, p. arXiv:0706.0313

Birkhoff G. D., Langer R. E., 1923, Relativity and modern physics

Bisnovatyi-Kogan G. S., Ruzmaikin A. A., 1974, Astrophysics and Space Science, 28, 45

Bisnovatyi-Kogan G. S., Ruzmaikin A. A., 1976, Astrophysics and Space Science, 42, 401

Blaes O., Hirose S., Krolik J. H., 2007, The Astrophysical Journal, 664, 1057

Blandford R. D., Payne D. G., 1982, Monthly Notices of the Royal Astronomical Society, 199, 883

Blandford R. D., Znajek R. L., 1977, Mon. Not. R. Astron. Soc. , 179, 433

Bolton C. T., 1972, Nature, 235, 271

Bond G., 1862, Astronomische Nachrichten, 57, 131

Bond H. E., Bergeron P., Bédard A., 2017, Astrophys. J. , 848, 16

Bondi H., 1952, Monthly Notices of the Royal Astronomical Society, 112, 195

Bondi H., Hoyle F., 1944, Monthly Notices of the Royal Astronomical Society, 104, 273

Bonnor W. B., 1969, Math. Proc. Cambridge Phil. Soc., 66, 145

Boshkayev K., Idrissov A., Luongo O., Malafarina D., 2020, Mon. Not. Roy. Astron. Soc., 496, 1115

Bower G. C., Wright M. C. H., Falcke H., Backer D. C., 2003, Astrophys. J., 588, 331

Bower R. G., Benson A. J., Malbon R., Helly J. C., Frenk C. S., Baugh C. M., Cole S., Lacey C. G., 2006, Mon. Not. Roy. Astron. Soc., 370, 645

Boyer R. H., Lindquist R. W., 1967, Journal of Mathematical Physics, 8, 265

Britzen S., et al., 2018, Mon. Not. R. Astron. Soc. , 478, 3199

Buchdahl H. A., 1959, Phys. Rev., 116, 1027

Bueno P., Cano P. A., Goelen F., Hertog T., Vercnocke B., 2018, Physical Review D, 97, 024040

Cameron A. G., 1959, Astrophys. J. , 130, 884

Camilloni F., Rezzolla L., 2024, arXiv e-prints, p. arXiv:2411.04184

Caproni A., Abraham Z., Mosquera Cuesta H. J., 2006, The Astrophysical Journal, 638, 120

Cardoso V., Pani P., Cadoni M., Cavaglià M., 2008, Phys. Rev. D, 77, 124044

Cardoso V., Destounis K., Duque F., Macedo R. P., Maselli A., 2022a, Phys. Rev. D , 105, L061501

Cardoso V., Destounis K., Duque F., Panosso Macedo R., Maselli A., 2022b, Phys. Rev. Lett., 129, 241103

Cataldo M., del Campo S., Minning P., Salgado P., 2009, Phys. Rev. D, 79, 024005

Cecil G., et al., 2000, Astrophys. J. , 536, 675

Cen R., 2001, Astrophys. J. Lett. , 546, L77

Chakrabarti S. K., 1989a, Monthly Notices of the Royal Astronomical Society, 240, 7

Chakrabarti S. K., 1989b, Astrophysical Journal Letters, 337, L89

Chakrabarti S. K., 1989c, The Astrophysical Journal, 347, 365

Chakrabarti S. K., 1990a, Monthly Notices of the Royal Astronomical Society, 243, 610

Chakrabarti S. K., 1990b, Mon. Not. R. Astron. Soc. , 246, 134

Chakrabarti S. K., 1996a, Monthly Notices of the Royal Astronomical Society, 283, 325

Chakrabarti S. K., 1996b, Astrophysical Journal v. 464, p. 664, 464, 664

Chakrabarti S. K., 1999a, Astron. Astrophys. , 351, 185

Chakrabarti S. K., 1999b, Astronomy and Astrophysics, 351, 185

Chakrabarti S. K., Das S., 2004, Monthly Notices of the Royal Astronomical Society, 349, 649

Chakrabarti S. K., Khanna R., 1992, Mon. Not. R. Astron. Soc. , 256, 300

Chakrabarti S. K., Mandal S., 2006, APJL, 642, L49

Chakrabarti S. K., Mondal S., 2006, Mon. Not. R. Astron. Soc. , 369, 976

Chakrabarti S., Titarchuk L. G., 1995, The Astrophysical Journal, 455, 623

Chakrabarti S. K., Acharyya K., Molteni D., 2004, Astron. Astrophys. , 421, 1

Chakraborty C., 2014, European Physical Journal C, 74, 2759

Chakraborty C., Bhattacharyya S., 2017, Mon. Not. Roy. Astron. Soc., 469, 3062

Chakraborty C., Bhattacharyya S., 2018, Phys. Rev. D, 98, 043021

Chakraborty C., Bhattacharyya S., 2019, Journal of Cosmology and Astroparticle Physics, 2019, 034

Chakraborty C., Bhattacharyya S., 2022, Physical Review D, 106, 103028

Chakraborty C., Majumdar P., 2014, Classical and Quantum Gravity, 31, 075006

Chakraborty C., Kocherlakota P., Patil M., Bhattacharyya S., Joshi P. S., Królak A., 2017, Physical Review D, 95, 084024

Chakraborty S., Compère G., Machet L., 2024

Chandrasekhar S., 1931, Astrophys. J. , 74, 81

Chandrasekhar S., 1939, An introduction to the study of stellar structure

Chandrasekhar S., 1983, The mathematical theory of black holes

Chattopadhyay I., Chakrabarti S. K., 2002, Monthly Notices of the Royal Astronomical Society, 333, 454

Chattopadhyay I., Das S., 2007, New Astronomy, 12, 454

Chattopadhyay I., Kumar R., 2016, Mon. Not. Roy. Astron. Soc., 459, 3792

Chattopadhyay I., Ryu D., 2009, The Astrophysical Journal, 694, 492

Chattopadhyay I., Das S., Chakrabarti S. K., 2004, Mon. Not. R. Astron. Soc. , 348, 846

Chemin L., de Blok W. J. G., Mamon G. A., 2011, AJ, 142, 109

Chen R.-Y., Javed F., Mustafa D. G., Maurya S. K., Ray S., 2024, JHEAp, 44, 172

Chirenti C. B. M. H., Rezzolla L., 2008, Phys. Rev. D, 78, 084011

Colgate S. A., 1973, Astrophys. J. Lett. , 181, L53

Colín P., Avila-Reese V., Valenzuela O., 2000, Astrophys. J. , 542, 622

Collaboration E. H. T., 2019a, Astrophysical Journal Letters, 875, L1

Collaboration E. H. T., 2019b, Astrophysical Journal Letters, 875, L2

Collaboration E. H. T., 2019c, Astrophysical Journal Letters, 875, L3

Collaboration E. H. T., 2019d, Astrophysical Journal Letters, 875, L4

Collaboration E. H. T., 2019e, Astrophysical Journal Letters, 875, L5

Collaboration E. H. T., 2019f, Astrophysical Journal Letters, 875, L6

Collaboration E. H. T., 2022a, Astrophysical Journal Letters, 930, L12

Collaboration E. H. T., 2022b, Astrophysical Journal Letters, 930, L13

Collaboration E. H. T., 2022c, Astrophysical Journal Letters, 930, L14

Collaboration E. H. T., 2022d, Astrophysical Journal Letters, 930, L15

Collaboration E. H. T., 2022e, Astrophysical Journal Letters, 930, L16

Collaboration E. H. T., 2022f, Astrophysical Journal Letters, 930, L17

Collaboration T. E. H. T., et al., 2021, The Astrophysical Journal Letters, 910, L12

Combi L., Yang H., Gutierrez E., Noble S. C., Romero G. E., Campanelli M., 2024, Phys. Rev. D, 109, 103034

Cui Y., et al., 2023, Nature, 621, 711

Cunningham C. T., Bardeen J. M., 1973, The Astrophysical Journal, 183, 237

Dadhich N., Wiita P. J., 1982, Journal of Physics A Mathematical General, 15, 2645

Daly R. A., Donahue M., O'Dea C. P., Sebastian B., Haggard D., Lu A., 2023, Mon. Not. Roy. Astron. Soc., 527, 428

Damour T., Solodukhin S. N., 2007,] 10.1103/PhysRevD.76.024016, 76, 024016

Das S., 2007, Monthly Notices of the Royal Astronomical Society, 376, 1659

Das T. K., Chakrabarti S. K., 1999, Classical and Quantum Gravity, 16, 3879

Das S., Chakrabarti S. K., 2004, International Journal of Modern Physics D, 13, 1955

Das S., Chakrabarti S. K., 2007, Mon. Not. R. Astron. Soc. , 374, 729

Das S., Chakrabarti S. K., 2008, Monthly Notices of the Royal Astronomical Society, 389, 371

Das S., Chattopadhyay I., Nandi A., Chakrabarti S. K., 2001a, Astronomy & Astrophysics, 379, 683

Das S., Chattopadhyay I., Chakrabarti S. K., 2001b, The Astrophysical Journal, 557, 983

Das S., Chakrabarti S. K., Mondal S., 2010, Mon. Not. R. Astron. Soc. , 401, 2053

Das S., Chattopadhyay I., Nandi A., Molteni D., 2014, Monthly Notices of the Royal Astronomical Society, 442, 251

Das S., Nandi A., Agrawal V. K., Dihingia I. K., Majumder S., 2021, Monthly Notices of the Royal Astronomical Society, 507, 2777

Das S., Nandi A., Stalin C. S., Rakshit S., Dihingia I. K., Singh S., Aktar R., Mitra S., 2022, Monthly Notices of the Royal Astronomical Society, 514, 1940

Datta S., 2024, Phys. Rev. D, 109, 104042

De Villiers J.-P., Hawley J. F., Krolik J. H., 2003, The Astrophysical Journal, 599, 1238

Debnath D., 2024, in 45th COSPAR Scientific Assembly. Held 13-21 July. p. 1826

Debnath D., Pal P. S., Chakrabarti S. K., Mondal S., Jana A., Chatterjee D., Molla A. A., 2016, in 41st COSPAR Scientific Assembly. pp E1.6–13–16

Debnath D., Chatterjee K., Chatterjee D., Jana A., Chakrabarti S. K., 2021, Mon. Not. R. Astron. Soc. , 504, 4242

Demianski M., Ivanov P. B., 1997, Astronomy & Astrophysics, 324, 829

Demianski M., Newman E. T., 1966, Bulletin de l'Academie Polonaise des Sciences Series des Sciences Mathematiques Astronomiques et Physiques, 14, 653

Dexter J., Fragile P. C., 2011, Astrophys. J. , 730, 36

Dhar B. K., Williams L. L. R., 2012, Mon. Not. R. Astron. Soc. , 427, 204

Dihingia I. K., Vaidya B., 2022, J. Astrophys. Astron., 43, 23

Dihingia I. K., Das S., Maity D., Chakrabarti S., 2018, Phys. Rev. D, 98, 083004

Dihingia I. K., Das S., Nandi A., 2019a, Monthly Notices of the Royal Astronomical Society, 484, 3209

Dihingia I., Das S., Maity D., Nandi A., 2019b, Mon. Not. Roy. Astron. Soc., 488, 2412

Dihingia I. K., Maity D., Chakrabarti S., Das S., 2020a, Phys. Rev. D, 102, 023012

Dihingia I. K., Maity D., Chakrabarti S., Das S., 2020b, Phys. Rev. D, 102, 023012

Dihingia I. K., Das S., Prabhakar G., Mandal S., 2020c, Monthly Notices of the Royal Astronomical Society, 496, 3043

Dihingia I. K., Uniyal A., Mizuno Y., 2025, arXiv e-prints, p. arXiv:2507.23187

Dirac P. A. M., 1931, Proc. Roy. Soc. Lond. A, 133, 60

Do T., et al., 2019, Science, 365, 664

Dowker J. S., 1974, General Relativity and Gravitation, 5, 603

Droste J., 1917, Koninklijke Nederlandse Akademie van Wetenschappen Proceedings Series B Physical Sciences, 19, 197

Eardley D. M., Lightman A. P., 1975, Astrophysical Journal, 200, 187

Einasto J., 1965, Trudy Astrofizicheskogo Instituta Alma-Ata, 5, 87

Einasto J., 1969, Astrofizika, 5, 137

Einasto J., Kutuzov S. A., 1964, Tartu Astrofuusika Observatoorium Teated, 11, 11

Einstein A., 1916a, Sitzungsberichte der Königlich Preußischen Akademie der Wissenschaften, pp 688–696

Einstein A., 1916b, Annalen Phys., 49, 769

Einstein A., 1918, Sitzungsberichte der Königlich Preussischen Akademie der Wissenschaften, pp 154–167

Einstein A., 1939, Annals Math., 40, 922

Einstein A., Rosen N., 1935, Phys. Rev., 48, 73

Ekers R. D., Goss W. M., Schwarz U. J., Downes D., Rogstad D. H., 1975, Astronomy & Astrophysics, 43, 159

Fabian A. C., et al., 2012, Mon. Not. R. Astron. Soc. , 424, 217

Falle S. A. E. G., Wilson M. J., 1985, in Dyson J. E., ed., , Active Galactic Nuclei. pp 342–345

Faraji S., Rosa J. a. L., 2024, Effect of dark matter on the shadow of a distorted and deformed compact object (arXiv:2403.02597)

Fernandes P. G. S., Cardoso V., 2025

Figueiredo E., Maselli A., Cardoso V., 2023, Phys. Rev. D, 107, 104033

Flamm L., 1916, Physikalische Zeitschrift, 17, 448

Flores R. A., Primack J. R., 1994, Astrophys. J. Lett. , 427, L1

Fowler R. H., 1926, Mon. Not. R. Astron. Soc. , 87, 114

Fragile P. C., Anninos P., 2005, The Astrophysical Journal, 623, 347

Fragile P. C., Meier D. L., 2009, Astrophys. J., 693, 771

Fragile P. C., Blaes O. M., Anninos P., Salmonson J. D., 2007, The Astrophysical Journal, 668, 417

Frank J., King A., Raine D. J., 2002, Accretion Power in Astrophysics: Third Edition. Cambridge, UK: Cambridge University Press

Freese K., Rindler-Daller T., Spolyar D., Valluri M., 2016, Reports on Progress in Physics, 79, 066902

Frolov V. P., Zelnikov A., 2011, Introduction to black hole physics. OUP Oxford

Fukue J., 1983, Publ. Astron. Soc. Japan , 35, 355

Fukue J., 1987, Publ. Astron. Soc. Japan , 39, 309

Fukumura K., 2005, PhD thesis, Montana State University System

Fukumura K., Takahashi M., Tsuruta S., 2007, Astrophys. J. , 657, 415

Fuller R. W., Wheeler J. A., 1962, Phys. Rev., 128, 919

Galeev A. A., Rosner R., Vaiana G. S., 1979, Astrophys. J. , 229, 318

Gammie C. F., McKinney J. C., Tóth G., 2003, The Astrophysical Journal, 589, 444

Garain S. K., 2025, Astronomy and Computing, 53, 100974

Garain S. K., Ghosh H., Chakrabarti S. K., 2014, Mon. Not. R. Astron. Soc. , 437, 1329

Gell-Mann M., 1964, Physics Letters, 8, 214

Gelles Z., Prather B. S., Palumbo D. C. M., Johnson M. D., Wong G. N., Georgiev B., 2021, The Astrophysical Journal, 912, 39

Genzel R., Eisenhauer F., Gillessen S., 2010, Reviews of Modern Physics, 82, 3121

Geralico A., Pompi F., Ruffini R., 2012, Int. J. Mod. Phys. Conf. Ser., 12, 146

Ghasemi-Nodehi M., Chakraborty C., Yu Q., Lu Y., 2021, European Physical Journal C, 81, 939

Ghez A. M., et al., 2008, Astrophys. J. , 689, 1044

Ghoreyshi S. M., Shadmehri M., 2018, Mon. Not. R. Astron. Soc. , 476, 4830

Ghosh T., Rana V., 2021, Mon. Not. R. Astron. Soc. , 504, 974

Giacconi R., Gursky H., Paolini F. R., Rossi B. B., 1962, Physical Review Letters,, 9, 439

Giacconi R., Gorenstein P., Gursky H., Usher P. D., Waters J. R., Sandage A., Osmer P., Peach J. V., 1967, Astrophys. J. Lett. , 148, L129

Giacconi R., Gursky H., Kellogg E., Schreier E., Tananbaum H., 1971, Astrophys. J. Lett. , 167, L67

Giri K., Chakrabarti S. K., 2012, Monthly Notices of the Royal Astronomical Society, 421, 666

Gnedin O. Y., Primack J. R., 2004, Phys. Rev. Lett., 93, 061302

Gold T., 1969, Nature, 221, 25

Gondolo P., Silk J., 1999, Phys. Rev. Lett., 83, 1719

Govaerts J., 2023, Classical and Quantum Gravity, 40, 085010

Graham A. W., Merritt D., Moore B., Diemand J., Terzić B., 2006, AJ, 132, 2711

Grove J., Johnson W., Kroeger R., McNaron-Brown K., Skibo J., Phlips B., 1998, The Astrophysical Journal, 500, 899

Guzmán F. S., 2006, Physical Review D, 73, 021501

Gyulchev G., Kunz J., Nedkova P., Vetsov T., Yazadjiev S., 2020, European Physical Journal C, 80, 1017

Haardt F., Maraschi L., 1993, Astrophys. J. , 413, 507

Haensel P., Zdunik J. L., Schaefer R., 1986, Astron. Astrophys. , 160, 121

Harko T., Kovács Z., Lobo F. S. N., 2009a, Classical and Quantum Gravity, 26, 215006

Harko T., Kovács Z., Lobo F. S. N., 2009b, Phys. Rev. D, 79, 064001

Harko T., Kovács Z., Lobo F. S. N., 2010, Classical and Quantum Gravity, 27, 105010

Harko T., Lobo F. S., Mak M., Sushkov S. V., 2013, Physical Review D, 87, 067504

Harrison C. M., 2017, Nature Astronomy, 1, 0165

Hatchett S. P., Begelman M. C., Sarazin C. L., 1981, The Astrophysical Journal, 247, 677

Hawley J. F., 2001, Astrophys. J., 554, 534

Hawley J. F., Balbus S. A., 1995, Publications of the Astronomical Society of Australia, 12, 159

Hayasaki K., Sohn B. W., Okazaki A. T., Jung T., Zhao G., Naito T., 2015, Journal of Cosmology and Astro-Particle Physics, 2015, 005

Hernquist L., 1990, Astrophys. J., 356, 359

Hernquist L., 1993, Astrophys. J. Suppl. , 86, 389

Herschel W., 1785, Philosophical Transactions of the Royal Society of London Series I, 75, 40

Hertzsprung E., 1915, Astrophys. J. , 42, 111

Hewish A., Bell S. J., Pilkington J. D. H., Scott P. F., Collins R. A., 1968, Nature, 217, 709

Heydari-Fard M., 2010, Classical and Quantum Gravity, 27, 235004

Heydari-Fard M., Heydari-Fard M., Riazi N., 2025, Gen. Rel. Grav., 57, 49

Hirose S., Krolik J. H., De Villiers J.-P., Hawley J. F., 2004, The Astrophysical Journal, 606, 1083

Hjalmarsdotter L., Zdziarski A. A., Larsson S., Beckmann V., McCollough M., Hannikainen D. C., Vilhu O., 2008, Monthly Notices of the Royal Astronomical Society, 384, 278

Hjellming R. M., Rupen M. P., 1995, Nature, 375, 464

Hoyle F., Lyttleton R. A., 1939, Proceedings of the Cambridge Philosophical Society, 35, 405

Hoyle F., Lyttleton R. A., 1940, Proceedings of the Cambridge Philosophical Society, 36, 325

Hoyle F., Lyttleton R. A., 1941, Monthly Notices of the Royal Astronomical Society, 101, 227

Hu W., Barkana R., Gruzinov A., 2000, Physical Review Letters, 85, 1158

Hulse R. A., Taylor J. H., 1975, Astrophys. J. Lett. , 195, L51

Ichimaru S., 1976, Astrophysical Journal, 208, 701

Ichimaru S., 1977, The Astrophysical Journal, 214, 840

Igumenshchev I. V., Abramowicz M. A., 1999, Mon. Not. R. Astron. Soc. , 303, 309

Ingram A., Done C., 2012a, Mon. Not. R. Astron. Soc. , 419, 2369

Ingram A., Done C., 2012b, Mon. Not. R. Astron. Soc. , 427, 934

Ingram A., Motta S., 2014, Monthly Notices of the Royal Astronomical Society, 444, 2065

Ingram A., van der Klis M., Middleton M., Done C., Altamirano D., Heil L., Uttley P., Axelsson M., 2016, Monthly Notices of the Royal Astronomical Society, 461, 1967

Ioka K., Levinson A., Nakar E., 2019, Mon. Not. Roy. Astron. Soc., 484, 3502

Ito H., Levinson A., Nakar E., Nagataki S., 2025

Itoh N., 1970, Progress of Theoretical Physics, 44, 291

Ivanenko D. D., Kurdgelaidze D. F., 1965, Astrophysics, 1, 251

Ivanenko D., Kurdgelaidze D. F., 1969, Nuovo Cimento Lettere, 2, 13

Ivanov P. B., Illarionov A. F., 1997, Monthly Notices of the Royal Astronomical Society, 285, 394

Iyer N., Nandi A., Mandal S., 2015, The Astrophysical Journal, 807, 108

Jana C., Das S., 2024, Journal of Cosmology and Astroparticle Physics, 2024, 075

Jana A., Debnath D., Chakrabarti S. K., Chatterjee D., 2018, in 42nd COSPAR Scientific Assembly. pp E1.17–8–18

Jennison R. C., Das Gupta M. K., 1953, Nature, 172, 996

Jusufi K., Jamil M., Zhu T., 2020, Eur. Phys. J. C, 80, 354

Kagramanova V., Kunz J., Hackmann E., Lämmerzahl C., 2010, Phys. Rev. D, 81, 124044

Karimov R. K., Izmailov R. N., Nandi K. K., 2019, European Physical Journal C, 79, 952

Karzas W. J., Latter R., 1961, Astrophysical Journal Supplement, 6, 167

Kasuya S., Kobayashi M., 2021, Phys. Rev. D, 103, 104050

Kato S., Wu X.-B., Yang L.-T., Yang Z.-L., 1993, Monthly Notices of the Royal Astronomical Society, 260, 317

Kato Y., Mineshige S., Shibata K., 2004, Astrophys. J., 605, 307

Kaup D. J., 1968, Physical Review, 172, 1331

Kawanaka N., Mineshige S., Iwasawa K., 2005, The Astrophysical Journal, 635, 167

Kerr R. P., 1963, Physical Review Letters, 11, 237

Khanna R., Camenzind M., 1996, Astronomy & Astrophysics, 307, 665

Kim J., Garain S. K., Chakrabarti S. K., Balsara D. S., 2019, Monthly Notices of the Royal Astronomical Society, 482, 3636

King A. R., Pringle J. E., Livio M., 2007, Monthly Notices of the Royal Astronomical Society, 376, 1740

Kluzniak W., Abramowicz M. A., 2001, Acta Physica Polonica B, 32, 3605

Koljonen K. I. I., Maccarone T., McCollough M. L., Gurwell M., Trushkin S. A., Pooley G. G., Piano G., Tavani M., 2018, Astronomy & Astrophysics, 612, A27

Konoplya R. A., Zhidenko A., 2022, Astrophys. J., 933, 166

Kormendy J., Ho L. C., 2013, Ann. Rev. Astron. Astrophys., 51, 511

Kovács Z., Cheng K. S., Harko T., 2009, Monthly Notices of the Royal Astronomical Society, 400, 1632

Kraus P., Mathur S. D., 2015, Int. J. Mod. Phys. D, 24, 1543003

Krause F., Raedler K. H., 1980, Mean-field magnetohydrodynamics and dynamo theory

Kumar R., Chattopadhyay I., 2017, Mon. Not. Roy. Astron. Soc., 469, 4221

Kumar A., Chakrabarti S., Das S., 2025, Astrophys. J., 980, 68

Landau L. D., Lifschits E. M., 1975, The Classical Theory of Fields. Course of Theoretical Physics Vol. Volume 2, Pergamon Press, Oxford

Lasota J. P., 1994, in Duschl W. J., Frank J., Meyer F., Meyer-Hofmeister E., Tscharnuter W. M., eds, NATO Advanced Study Institute (ASI) Series C Vol. 417, Theory of Accretion Disks - 2. p. 341

Lawrence A., Elvis M., 2010, Astrophys. J. , 714, 561

Le T., Becker P. A., 2005, Astrophys. J. , 632, 476

Lee S.-J., Chattopadhyay I., Kumar R., Hyung S., Ryu D., 2016, The Astrophysical Journal, 831, 33

Lemos J. P. S., Lobo F. S. N., de Oliveira S. Q., 2003, Phys. Rev. D, 68, 064004

Lense J., Thirring H., 1918, Physikalische Zeitschrift, 19, 156

Li Y.-R., Wang J.-M., Cheng C., Qiu J., 2013, Astrophys. J. , 764, 16

Li Y.-R., Wang J.-M., Cheng C., Qiu J., 2015, Astrophys. J., 804, 45

Lightman A. P., Eardley D. M., 1974, Astrophys. J. Lett. , 187, L1

Lin F.-L., Patel A., Pu H.-Y., 2022, arXiv e-prints, p. arXiv:2202.13559

Liska M., Hesp C., Tchekhovskoy A., Ingram A., van der Klis M., Markoff S., 2018, Mon. Not. R. Astron. Soc. , 474, L81

Liu C., Yang S., Wu Q., Zhu T., 2022, Journal of Cosmology and Astroparticle Physics, 2022, 034

Lobo F. S. N., 2005, Phys. Rev. D, 71, 124022

Lu J. F., 1985, Astronomy & Astrophysics, 148, 176

Lu J.-F., Gu W.-M., Yuan F., 1999, Astrophys. J. , 523, 340

Lü H., Mei J., Pope C., 2009, Physical Review Letters, 103, 091301

Lubow S. H., Ogilvie G. I., Pringle J. E., 2002, Monthly Notices of the Royal Astronomical Society, 337, 706

Luminet J. P., 1979, The Astronomy and Astrophysics, 75, 228

Luyten W. J., 1922a, Publ. Astron. Soc. Pacific , 34, 132

Luyten W. J., 1922b, Publ. Astron. Soc. Pacific , 34, 356

Luyten W. J., 1923, Lick Observatory Bulletin, 11, 1

Lynden-Bell D., 1962, Mon. Not. R. Astron. Soc. , 123, 447

Lynden-Bell D., 1969, Nature, 223, 690

Lynden-Bell D., Nouri-Zonoz M., 1998, Rev. Mod. Phys., 70, 427

Lynden-Bell D., Rees M. J., 1971, Monthly Notices of the Royal Astronomical Society, 152, 461

Mach P., Odrzywo A., 2021, Phys. Rev. Lett., 126, 101104

Machida M., Nakamura K. E., Matsumoto R., 2006, Publications of the Astronomical Society of Japan, 58, 193

Maeda K.-i., Cardoso V., Wang A., 2025, Phys. Rev. D, 111, 044060

Magorrian J., et al., 1998, The Astronomical Journal, 115, 2285

Majumder S., Sreehari H., Aftab N., Katoch T., Das S., Nandi A., 2022, arXiv e-prints, p. arXiv:2203.02710

Majumder S., Das S., Agrawal V. K., Nandi A., 2023, Mon. Not. R. Astron. Soc. , 526, 2086

Mandal S., Chakrabarti S. K., 2005, Astronomy & Astrophysics, 434, 839

Maoz D., 2016, Astrophysics in a Nutshell. Second Edition

Marchesini D., D'Onghia E., Chincarini G., Firmani C., Conconi P., Molinari E., Zacchei A., 2002, Astrophys. J. , 575, 801

Marconi A., Hunt L. K., 2003, Astrophysical Journal Letters, 589, L21

Markwardt C. B., Swank J. H., Taam R. E., 1999, The Astrophysical Journal Letters, 513, L37

Marrone D. P., Moran J. M., Zhao J.-H., Rao R., 2006, Astrophys. J., 640, 308

Martin R. G., Reis R. C., Pringle J. E., 2008, Monthly Notices of the Royal Astronomical Society, 391, L15

Mathur S. D., 2005, Fortsch. Phys., 53, 793

Mathur S. D., 2010, Gen. Rel. Grav., 42, 113

Matsumoto R., Kato S., Fukue J., Okazaki A. T., 1984, Publications of the Astronomical Society of Japan, 36, 71

Mayer L., Kazantzidis S., Madau P., Colpi M., Quinn T. R., Wadsley J., 2007, Science, 316, 1874

Mazur P. O., Mottola E., 2004, Proceedings of the National Academy of Science, 101, 9545

McClintock J. E., Shafee R., Narayan R., Remillard R. A., Davis S. W., Li L.-X., 2006, Astrophys. J., 652, 518

McCollough M. L., Corrales L., Dunham M. M., 2016, Astrophysical Journal Letters, 830, L36

McCrea W. H., 1956, Astrophys. J. , 124, 461

McGaugh S. S., Schombert J. M., Lelli F., Franck J., 2024, Astrophys. J., 976, 13

McKinney J. C., Gammie C. F., 2004, The Astrophysical Journal, 611, 977

Mehdizadeh M. R., Ziaie A. H., 2017, Phys. Rev. D, 95, 064049

Mehdizadeh M. R., Zangeneh M. K., Lobo F. S. N., 2015,] 10.1103/PhysRevD.91.084004, 91, 084004

Melia F., Falcke H., 2001, Annual Review of Astronomy and Astrophysics, 39, 309

Merritt D., 2004, Phys. Rev. Lett., 92, 201304

Merritt D., Milosavljevic M., Verde L., Jimenez R., 2002, Phys. Rev. Lett., 88, 191301

Merritt D., Graham A. W., Moore B., Diemand J., Terzić B., 2006, AJ, 132, 2685

Meza M. R., Huang X., Davis S. W., Jiang Y.-F., 2025, arXiv e-prints, p. arXiv:2506.00109

Michel F. C., 1972, Astrophysics and Space Science, 15, 153

Migdal A., 1972, Sov. Phys. JETP, 34, 1184

Miller J. G., 1973, Journal of Mathematical Physics, 14, 486

Miller J. M., Homan J., Steeghs D., Rupen M., Hunstead R. W., Wijnands R., Charles P. A., Fabian A. C., 2006, The Astrophysical Journal, 653, 525

Mills B. S., Davis S. W., Middleton M. J., 2021, Astrophys. J. , 914, 6

Mineshige S., Kawaguchi T., Takeuchi M., Hayashida K., 2000, Publ. Astron. Soc. Japan , 52, 499

Mirabel I. F., Rodríguez L. F., 1994, Nature, 371, 46

Mirzaev T., Abdikamalov A. B., Abdujabbarov A. A., Ayzenberg D., Ahmedov B., Bambi C., 2022, arXiv e-prints, p. arXiv:2202.02122

Mishra B., Begelman M. C., Armitage P. J., Simon J. B., 2020, Monthly Notices of the Royal Astronomical Society, 492, 1855

Misner C. W., 1963, Journal of Mathematical Physics, 4, 924

Misner C. W., Taub A. H., 1969, Soviet Journal of Experimental and Theoretical Physics, 28, 122

Misner C. W., Wheeler J. A., 1957, Annals of Physics, 2, 525

Mitra S., Das S., 2024, Astrophys. J., 971, 28

Mitra S., Maity D., Dihingia I. K., Das S., 2022, Mon. Not. R. Astron. Soc. , 516, 5092

Mitra S., Speeney N., Chakraborty S., Berti E., 2025

Mizuno Y., 2022, Universe, 8, 85

Mizuno Y., Gomez J. L., Nishikawa K.-I., Meli A., Hardee P. E., Rezzolla L., 2015, Astrophys. J., 809, 38

Moffatt H. K., 1978, Magnetic field generation in electrically conducting fluids

Molchanov S. A., Ruzmaĭkin A. A., Sokolov D. D., 1985, Soviet Physics Uspekhi, 28, 307

Molla A. A., Debnath D., Chakrabarti S. K., Mondal S., Jana A., 2016, Mon. Not. R. Astron. Soc. , 460, 3163

Molteni D., Sponholz H., Chakrabarti S. K., 1996, Astrophys. J. , 457, 805

Mondal S., Debnath D., Chakrabarti S. K., 2014, Astrophys. J. , 786, 4

Montgomery C., Orchiston W., Whittingham I., 2009, Journal of Astronomical History and Heritage, 12, 90

Morag J., Irani I., Sapir N., Waxman E., 2024, Mon. Not. R. Astron. Soc. , 528, 7137

Morgan E. H., Remillard R. A., Greiner J., 1997, Astrophys. J. , 482, 993

Morganti R., 2017, Frontiers in Astronomy and Space Sciences, 4, 42

Morris D., Berge G. L., 1964, Astrophysical Journal, 139, 1388

Morris M. S., Thorne K. S., 1988, American Journal of Physics, 56, 395

Morsink S. M., Stella L., 1999, Astrophys. J. , 513, 827

Mościbrodzka M., Falcke H., Shiokawa H., 2016, Astron. Astrophys. , 586, A38

Motta S., Muñoz-Darias T., Casella P., Belloni T., Homan J., 2011, Mon. Not. R. Astron. Soc. , 418, 2292

Motta S. E., Munoz-Darias T., Sanna A., Fender R., Belloni T., Stella L., 2014, Mon. Not. R. Astron. Soc. , 439, L65

Mukhopadhyay B., 2002, Astrophys. J. , 581, 427

Nagakura H., Yamada S., 2008, Astrophys. J., 689, 391

Nandi A., Debnath D., Mandal S., Chakrabarti S. K., 2012, Astronomy & Astrophysics, 542, A56

Nandi A., et al., 2018, Astrophysics and Space Science, 363, 90

Narayan R., Yi I.-s., 1994, Astrophys. J. Lett., 428, L13

Narayan R., Yi I., 1995a, The Astrophysical Journal, 444, 231

Narayan R., Yi I., 1995b, The Astrophysical Journal, 452, 710

Narayan R., Kato S., Honma F., 1997, Astrophys. J., 476, 49

Narayan R., Igumenshchev I. V., Abramowicz M. A., 2000, Astrophys. J. , 539, 798

Narayan R., Sądowski A., Penna R. F., Kulkarni A. K., 2012, Monthly Notices of the Royal Astronomical Society, 426, 3241

Narayan R., et al., 2021, The Astrophysical Journal, 912, 35

Narzilloev B., Abdujabbarov A., Ahmedov B., Bambi C., 2023, Phys. Rev. D, 108, 103013

Natarajan P., 2002, The Shapes of Galaxies and Their Dark Halos. WORLD SCIENTIFIC (https://www.worldscientific.com/doi/pdf/10.1142/4886), doi:10.1142/4886, https://www.worldscientific.com/doi/abs/10.1142/4886

Natarajan P., Armitage P. J., 1999, Monthly Notices of the Royal Astronomical Society, 309, 961

Navarro J. F., Frenk C. S., White S. D. M., 1995, Mon. Not. Roy. Astron. Soc., 275, 720

Navarro J. F., Frenk C. S., White S. D. M., 1996, Astrophys. J. , 462, 563

Navarro J. F., Frenk C. S., White S. D. M., 1997, Astrophys. J., 490, 493

Navarro J. F., et al., 2004, Mon. Not. R. Astron. Soc. , 349, 1039

Nelson R. P., Papaloizou J. C. B., 2000, Monthly Notices of the Royal Astronomical Society, 315, 570

Newman E., Tamburino L., Unti T., 1963, Journal of Mathematical Physics, 4, 915

Newman E. T., Couch R., Chinnapared K., Exton A., Prakash A., Torrence R., 1965, J. Math. Phys., 6, 918

Nishikawa K.-I., Koide S., Sakai J.-i., Christodoulou D. M., Sol H., Mutel R. L., 1997, Astrophys. J. Lett. , 483, L45

Nixon C., King A., Price D., Frank J., 2012, Astrophys. J. Lett. , 757, L24

Nolting C., Ball J., Nguyen T. M., 2023, Astrophys. J., 948, 25

Nouri-Zonoz M., Lynden-Bell D., 1997, Monthly Notices of the Royal Astronomical Society, 292, 714

Novikov I. D., Thorne K. S., 1973, in Dewitt C., Dewitt B. S., eds, Black Holes (Les Astres Occlus). pp 343–450

Nowak M. A., Wagoner R. V., 1991, Astrophys. J. , 378, 656

Oda M., Gorenstein P., Gursky H., Kellogg E., Schreier E., Tananbaum H., Giacconi R., 1971, Astrophys. J. Lett. , 166, L1

Oda H., Machida M., Nakamura K. E., Matsumoto R., 2007, Publ. Astron. Soc. Jap., 59, 457

Oda H., Machida M., Nakamura K. E., Matsumoto R., 2010, Astrophys. J., 712, 639

Ogilvie G. I., 1999, Mon. Not. Roy. Astron. Soc., 304, 557

Okuda T., Das S., 2015, Mon. Not. R. Astron. Soc. , 453, 147

Okuda T., Singh C. B., Das S., Aktar R., Nandi A., Dal Pino E. M. d. G., 2019, Publications of the Astronomical Society of Japan, 71, 49

Oppenheimer J. R., Volkoff G. M., 1939, Phys. Rev., 55, 374

Oswalt T. D., Smith J. A., Wood M. A., Hintzen P., 1996, Nature, 382, 692

Pacini F., 1967, Nature, 216, 567

Paczyńsky B., Wiita P. J., 1980, Astronomy & Astrophysics, 88, 23

Page D. N., Thorne K. S., 1974, The Astrophysical Journal, 191, 499

Pahari M., et al., 2017, Astrophys. J. , 849, 16

Palumbo D. C. M., Wong G. N., Chael A., Johnson M. D., 2023, Astrophysical Journal Letters, 952, L31

Papaloizou J. C. B., Pringle J. E., 1983, Monthly Notices of the Royal Astronomical Society, 202, 1181

Parker E. N., 1955, The Astrophysical Journal, 122, 293

Parker E. N., 1958, Astrophys. J. , 128, 664

Parker E. N., 1966, Astrophysical Journal, 145, 811

Patra S., Majhi B. R., 2025, Effect of dark matter halo on transonic accretion flow around a galactic black hole (arXiv:2501.07456)

Patra S., Majhi B. R., Das S., 2022, Physics of the Dark Universe, 37, 101120

Patra S., Majhi B. R., Das S., 2024, Journal of High Energy Astrophysics, 44, 371

Peebles P. J. E., 2000, Astrophys. J. Lett. , 534, L127

Peitz J., Appl S., 1997, Monthly Notices of the Royal Astronomical Society, 286, 681

Penrose R., 1969, Nuovo Cimento Rivista Serie, 1, 252

Peskin M. E., Schroeder D. V., 1995, An Introduction to quantum field theory. Addison-Wesley, Reading, USA, doi:10.1201/9780429503559

Petterson J. A., 1977a, The Astrophysical Journal, 214, 550

Petterson J. A., 1977b, The Astrophysical Journal, 216, 827

Petterson J. A., Rothschild R. E., Gruber D. E., 1991, The Astrophysical Journal, 378, 696

Pezzella L., Destounis K., Maselli A., Cardoso V., 2024

Planck Collaboration et al., 2016, Astronomy & Astrophysics, 594, A13

Plebanski J. F., Demianski M., 1976, Annals Phys., 98, 98

Powell M. C., et al., 2022, Astrophys. J., 938, 77

Prada F., Klypin A. A., Simonneau E., Betancort-Rijo J., Patiri S., Gottlober S., Sanchez-Conde M. A., 2006, Astrophys. J., 645, 1001

Prendergast K. H., Burbidge G. R., 1968, Astrophysical Journal Letters, 151, L83

Pringle J. E., 1981, Annual review of astronomy and astrophysics, 19, 137

Pringle J. E., 1992, Monthly Notices of the Royal Astronomical Society, 258, 811

Pringle J. E., Rees M. J., 1972, Astronomy & Astrophysics, 21, 1

Pudritz R. E., 1981, Monthly Notices of the Royal Astronomical Society, 195, 881

Pun C. S. J., Kovács Z., Harko T., 2008, Phys. Rev. D, 78, 024043

Quataert E., 2002, The Astrophysical Journal, 575, 855

Raban D., Jaffe W., Röttgering H., Meisenheimer K., Tristram K. R. W., 2009, Mon. Not. R. Astron. Soc. , 394, 1325

Rahaman F., Kalam M., Sarker M., Ghosh A., Raychaudhuri B., 2007, General Relativity and Gravitation, 39, 145

Rahvar S., Nouri-Zonoz M., 2003, Monthly Notices of the Royal Astronomical Society, 338, 926

Ramaswamy S., Sen A., 1981, Journal of Mathematical Physics, 22, 2612

Ranjbar R., Olivares-Sánchez H. R., Abbassi S., 2025, Bondi-like Accretion Flow Dynamics: The Role of Gravitational Potential (arXiv:2502.12101)

Rees M. J., 1984, Annual review of astronomy and astrophysics, 22, 471

Remillard R. A., McClintock J. E., 2006, Ann. Rev. Astron. & Astrophys. , 44, 49

Renzini A., et al., 1996, Astrophys. J. Lett. , 465, L23

Retana-Montenegro E., van Hese E., Gentile G., Baes M., Frutos-Alfaro F., 2012, Astron. Astrophys. , 540, A70

Rezzolla L., Zanotti O., 2013, Relativistic Hydrodynamics. Oxford University Press, doi:10.1093/acprof:oso/9780198528906.001.0001

Richstone D., et al., 1998, Nature, 395, A14

Riffert H., Herold H., 1995, The Astrophysical Journal, 450, 508

Ripperda B., Bacchini F., Philippov A. A., 2020, The Astrophysical Journal, 900, 100

Rubin V. C., Ford Jr. W. K., Thonnard N., 1978, Astrophys. J. Lett. , 225, L107

Ruffini R., Bonazzola S., 1969, Physical Review, 187, 1767

Ruffini R., Wheeler J. A., 1971, Physics Today, 24, 30

Ruggiero M. L., 2024, Journal of Cosmology and Astroparticle Physics, 2024, 025

Russell H. N., 1914, Popular Astronomy, 22, 331

Ryu D., Chattopadhyay I., Choi E., 2006, The Astrophysical Journal Supplement Series, 166, 410

Ryu D., Chattopadhyay I., Jang H., 2011, in Pogorelov N. V., Audit E., Zank G. P., eds, Astronomical Society of the Pacific Conference Series Vol. 444, 5th International Conference of Numerical Modeling of Space Plasma Flows (ASTRONUM 2010). p. 248 (arXiv:1102.3223), doi:10.48550/arXiv.1102.3223

Sadeghian L., Ferrer F., Will C. M., 2013, Phys. Rev. D, 88, 063522

Samadi M., Abbassi S., Khajavi M., 2014, Mon. Not. Roy. Astron. Soc., 437, 3124

Sanders R. H., 2008, Mon. Not. Roy. Astron. Soc., 386, 1588

Sarkar B., Das S., 2016, Monthly Notices of the Royal Astronomical Society, 461, 190

Sarkar B., Das S., 2018, J. Astrophys. Astron., 39, 3

Sarkar B., Dihingia I. K., Misra R., 2025, New Astronomy, 118, 102377

Sawyer R. F., 1972, Physical Review Letters, 29, 382

Scheuer P. A. G., Feiler R., 1996, Monthly Notices of the Royal Astronomical Society, 282, 291

Schreier E., Gursky H., Kellogg E., Tananbaum H., Giacconi R., 1971, Astrophysical Journal Letters, 170, L21

Schunck F. E., Mielke E. W., 2003, Classical and Quantum Gravity, 20, R301

Schwarzschild K., 1916, Sitzungsberichte der Königlich Preussischen Akademie der Wissenschaften, pp 189–196

Semerák O., Karas V., 1999, Astron. Astrophys. , 343, 325

Sen G., Maity D., Das S., 2024, JCAP, 10, 068

Sérsic J. L., 1963, Boletin de la Asociacion Argentina de Astronomia La Plata Argentina, 6, 41

Shaikh R., 2018, Phys. Rev. D, 98, 064033

Shakura N. I., 1973, Soviet Astronomy, 16, 756

Shakura N. I., Sunyaev R. A., 1973, Astron. Astrophys. , 24, 337

Shakura N. I., Sunyaev R. A., 1976, Monthly Notices of the Royal Astronomical Society, 175, 613

Shapiro S. L., 1973, Astrophys. J. , 185, 69

Shapiro S. L., Shelton J., 2016, Phys. Rev. D, 93, 123510

Shapiro S. L., Teukolsky S. A., 1983, Black holes, white dwarfs and neutron stars. The physics of compact objects. Wiley-Interscience, doi:10.1002/9783527617661

Shapiro S. L., Lightman A. P., Eardley D. M., 1976, The Astrophysical Journal, 204, 187

Shen J. Q., 2002, Gen. Rel. Grav., 34, 1423

Shen Y., YuChih H.-Y., 2025, Physical Review D, 111, 023003

Shen Z., Wang A., Gong Y., Yin S., 2024, Phys. Lett. B, 855, 138797

Singh M., Das S., 2024, Astrophysics and Space Science, 369, 1

Singh M., Das S., 2025, Journal of Cosmology and Astro-Particle Physics, 2025, 068

Singh M., Jana C., Das S., 2025, Journal of Cosmology and Astro-Particle Physics, 2025, 055

Singha C., Biswas S., 2024, Phys. Rev. D, 109, 024043

Skordis C., Zlosnik T., 2021, Phys. Rev. Lett., 127, 161302

Smith D. M., Heindl W. A., Markwardt C. B., Swank J. H., 2001, ApJL, 554, L41

Smith D. M., Heindl W. A., Swank J. H., 2002, The Astrophysical Journal, 569, 362

Sofue Y., Rubin V., 2001, Annual review of astronomy and astrophysics, 39, 137

Speeney N., Antonelli A., Baibhav V., Berti E., 2022, Phys. Rev. D, 106, 044027

Speeney N., Berti E., Cardoso V., Maselli A., 2024, Phys. Rev. D, 109, 084068

Spergel D. N., Steinhardt P. J., 2000, Physical Review Letters, 84, 3760

Sreehari H., Ravishankar B. T., Iyer N., Agrawal V. K., Katoch T. B., Mandal S., Nandi A., 2019, Monthly Notices of the Royal Astronomical Society, 487, 928

Sreehari H., Nandi A., Das S., Agrawal V. K., Mandal S., Ramadevi M. C., Katoch T., 2020, Monthly Notices of the Royal Astronomical Society, 499, 5891

Stelea C., 2006

Stella L., Vietri M., 1998, Astrophysical Journal Letters, 492, L59

Stella L., Vietri M., 1999, Physical review letters, 82, 17

Stone J. M., Norman M. L., 1994, The Astrophysical Journal, 433, 746

Stone J. M., Pringle J. E., Begelman M. C., 1999, Monthly Notices of the Royal Astronomical Society, 310, 1002

Stuchlík Z., Vrba J., 2021, Universe, 7, 279

Sunyaev R. A., Titarchuk L. G., 1980, Astron. Astrophys. , 86, 121

Synge J. L., 1957, The Relativistic Gas. Vol. 32, North-Holland Publishing Co., Amsterdam

Szostek A., Zdziarski A. A., McCollough M. L., 2008, Mon. Not. R. Astron. Soc. , 388, 1001

Takahashi M., Rilett D., Fukumura K., Tsuruta S., 2002, Astrophys. J. , 572, 950

Takahashi M., Goto J., Fukumura K., Rilett D., Tsuruta S., 2006, Astrophys. J. , 645, 1408

Takasao S., Shuto Y., Wada K., 2022, The Astrophysical Journal, 926, 50

Tamburini F., Thidé B., Della Valle M., 2020, Mon. Not. Roy. Astron. Soc., 492, L22

Tananbaum H., Gursky H., Kellogg E. M., Levinson R., Schreier E., Giacconi R., 1972, Astrophys. J. Lett. , 174, L143

Taub A. H., 1948, Phys. Rev., 74, 328

Taub A. H., 1951, Annals of Mathematics, 53, 472

Taylor J. E., Silk J., 2003, Mon. Not. Roy. Astron. Soc., 339, 505

Thorne K. S., 1973, Astrophys. J. , 179, 897

Thorne K. S., Price R. H., 1975, Astrophys. J. Lett. , 195, L101

Titarchuk L., Seifina E., Soffiitta P., Makhinya D., 2025, arXiv e-prints, p. arXiv:2508.09692

Torkelsson U., Brandenburg A., 1994, Astronomy & Astrophysics, 283, 677

Torres D. F., 2002, Nuclear Physics B, 626, 377

Tremaine S., et al., 2002, The Astrophysical Journal, 574, 740

Tulin S., Yu H.-B., 2018, Phys. Rept., 730, 1

Tully R. B., Fisher J. R., 1977, Astronomy and Astrophysics, 54, 661

Ullio P., Zhao H., Kamionkowski M., 2001, Phys. Rev. D, 64, 043504

Vasiliev E., 2007, Phys. Rev. D, 76, 103532

Veledina A., et al., 2023, arXiv e-prints, p. arXiv:2303.01174

Vietri M., 2008, Foundations of high-energy astrophysics. University of Chicago Press

Virmani A., 2011, Physical Review D, 84, 064034

Visser M., 1995, Lorentzian wormholes. From Einstein to Hawking. Woodbury, N.Y.: American Institute of Physics

Volonteri M., 2010, The Astronomy and Astrophysics Review, 18, 279

Volonteri M., Rees M. J., 2005, Astrophys. J., 633, 624

Wald R. M., 1984, General Relativity

Watarai K.-y., Fukue J., Takeuchi M., Mineshige S., 2000, Publ. Astron. Soc. Japan , 52, 133

Watarai K.-y., Mizuno T., Mineshige S., 2001, Astrophys. J. Lett. , 549, L77

Weaver T. A., 1976, Astrophys. J. Suppl. , 32, 233

Weaver T., Chapline G., Wood L., Silk J., 1974, in Bulletin of the American Astronomical Society. p. 274

Webb G. M., Axford W. I., Forman M. A., 1985, Astrophys. J. , 298, 684

Weber E. J., Davis Jr. L., 1967, Astrophys. J. , 148, 217

Webster B. L., Murdin P., 1972, Nature, 235, 37

Wentzel D. G., 1963, Annual Review of Astronomy and Astrophysics, 1, 195

Wheeler J. A., 1955, Phys. Rev., 97, 511

Wheeler J. A., 1968, American Scientist, 56, 1

Wiita P. J., Vishveshwara C. V., Siah M. J., Iyer B. R., 1983, Journal of Physics A Mathematical General, 16, 2077

Wu X.-B., Liu F. K., 2004, Astrophys. J., 614, 91

Xu R.-x., Qiao G.-j., 1998, Chinese Physics Letters, 15, 934

Yamasaki T., 1997, Publ. Astron. Soc. Japan , 49, 227

Yang R., Kafatos M., 1995, Astron. Astrophys. , 295, 238

Yang J., et al., 2023, Mon. Not. R. Astron. Soc. , 526, L1

Yarza R., Wong G. N., Ryan B. R., Gammie C. F., 2020, Astrophys. J., 898, 50

Yuan F., Narayan R., 2014, Ann. Rev. Astron. Astrophys., 52, 529

Yuan F., Quataert E., Narayan R., 2003, Astrophys. J. , 598, 301

Zdziarski A. A., Maitra C., Frankowski A., Skinner G. K., Misra R., 2012, Mon. Not. Roy. Astron. Soc., 426, 1031

Zdziarski A. A., Mikolajewska J., Belczynski K., 2013, Monthly Notices of the Royal Astronomical Society, 429, L104

Zdziarski A. A., et al., 2024, Astrophys. J. Lett. , 967, L9

Zeldovich Y. B., Sunyaev R., 1969, Astrophysics and Space Science, 4, 301

Zeng X.-X., Li G.-P., He K.-J., 2022, Nuclear Physics B, 974, 115639

Zhang Z.-C., Tang Y., 2024, Phys. Rev. D, 110, 103008

Zimmerman R. L., Shahir B. Y., 1989, Gen. Rel. Grav., 21, 821

Zweig G., 1964,] 10.17181/CERN-TH-401

Zwicky F., 1933, Helvetica Physica Acta, 6, 110

Zwicky F., 1937, The Astrophysical Journal, 86, 217

Zwicky F., 2009, General Relativity and Gravitation, 41, 207

de Vaucouleurs G., 1948, Annales d'Astrophysique, 11, 247